AUGMENTED MISE-À-LA-MASSE INTERPRETATION USING RAPID NUMERICAL METHODS

HASHIM CAREY

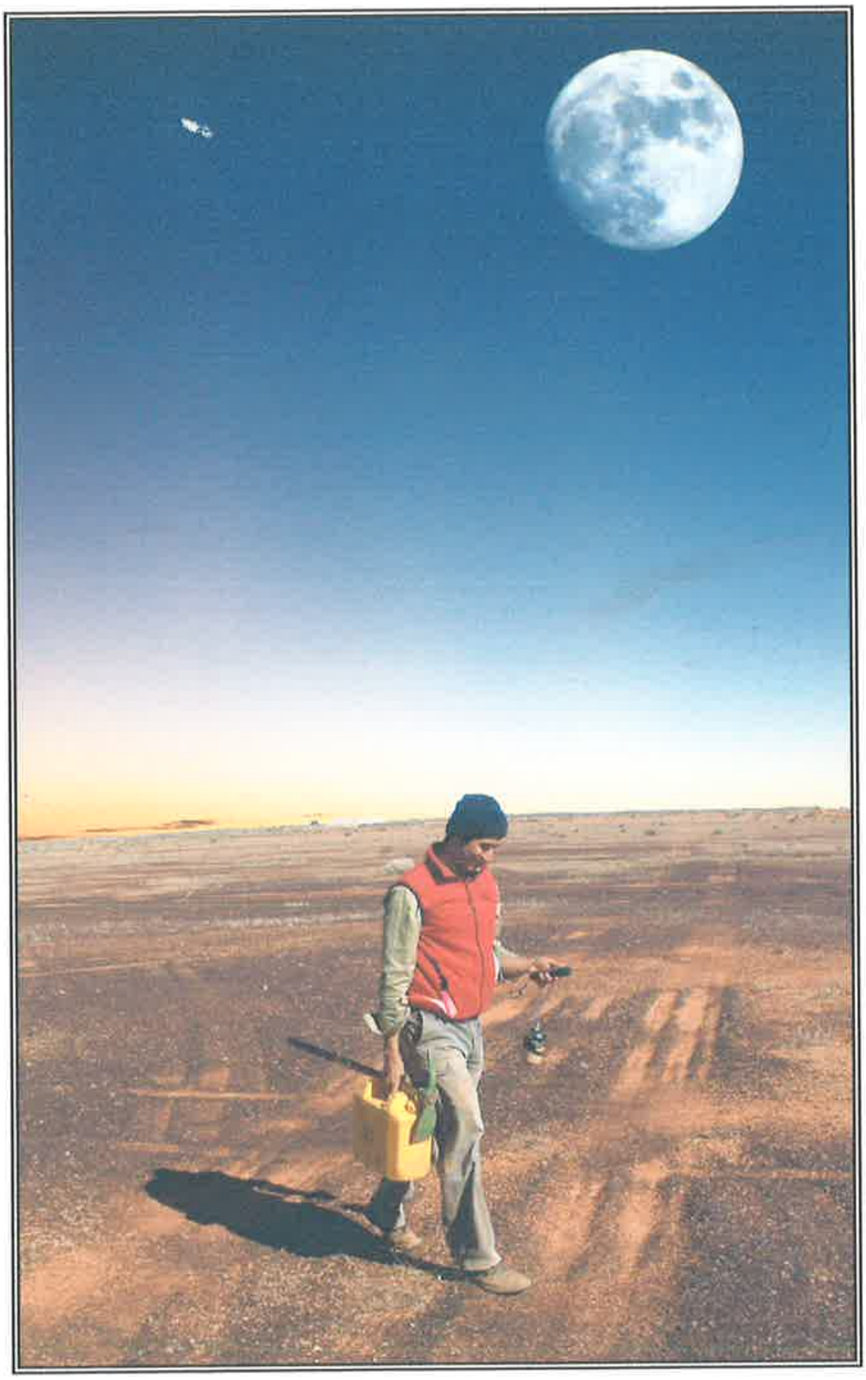

SCHOOL OF EARTH AND ENVIRONMENTAL SCIENCE
DISCIPLINE OF GEOLOGY AND GEOPHYSICS
THE UNIVERSITY OF ADELAIDE

Contents

Abstract

The applied potential, mise-à-la-masse (MALM) method, is used in the exploration of base metal deposits (Golden Grove, Western Australia and Prominent Hill, South Australia), where MALM data was collected. The method maps surface potentials (or voltages) associated with resistivity contrasts intrinsically linked with the geology. Information pertaining to the structural geometry and electrical connectivity of the conductive targets can be deduced from the surface potentials with the traditional placement of the source electrode in contact with the conductive body. However, in many cases, boreholes do not intersect the mineralisation. Such boreholes can still be used if the mineralisation is close and the surface potentials have similar anomaly patterns to the in-mineralisation responses. For electrodes in these "near-miss" positions, at shallow depths, the surface potentials are, however, dominated by potentials associated with the proximity of the source electrode. Two new numerical methods have been developed to analyse surface potentials of MALM data from a VMS deposit at Golden Grove, WA and a Cu-Au deposit at Prominent Hill, SA.

A finite element method modelling program developed by Zhou and Greenhalgh (2001) modelled the physical characteristics of a conductive body and in a resistive half-space for various locations of the down-hole electrodes. Parameters including varying resistivity contrasts, volume and dip of the conductor were investigated. Other models studied the effects of near-miss electrode positions and associated surface responses. The methods developed here aid in the interpretation of MALM data by firstly separating the electrode response from surface potentials, leaving the conductive body response and secondly by developing a three-dimensional image approximation of the resistivity contrasts to assist in geological interpretation. To enhance the potentials attributed to resistivity contrasts, a method of numerically calculating the potentials produced by the source electrode and subtracting it from MALM surface potentials yields residual potentials that better represent the subsurface geology. This method was most effective with surveys that had surface potentials distorted by the electrode response, particularly for shallow near-miss electrode positions. To image the subsurface in three dimensions, a modified version of Hämmann et al.'s (1997) image reconstruction algorithm was adapted to use the MALM surface potentials. The method represents the surface potentials by the super-positioning and correlation of elementary point sources of electrical potential. The imaging proved to be sensitive to changes in the distribution of the surface potentials and aided in MALM analysis.

These two methods used in combination with *a priori* geologic/geophysical of the field sites information aided in the interpretation of MALM field data sets. The outcomes of the method showed that the combined use of the electrode effect removal and subsurface approximation better approximated the geology than the unprocessed MALM data.

Declaration

This work contains no material which has been accepted for the award of any other degree or diploma in any university or other tertiary institution and, to the best of my knowledge and belief, contains no material previously published or written by another person, except where due reference has been made in the text.

I give consent to this copy of my thesis being available for loan and photocopying when deposited in the University Library.

15-04-2004

Hashim Carey

Dated

Acknowledgements

I am indebted for the guidance and assistance provided by my supervisors Graham Heinson and Mike Sexton throughout the course of this work. Both have helped to keep the project on target by stoking the fire and stirring the pot whenever I needed encouragement.

Thankyou to those involved at both Newmont Mining and the CRC for Landscapes Environment and Mineral Exploration for endeavouring to find the financial assets needed for the bursary, project field costs and the costs associated with presenting at SEG 2003, Dallas, TX. Without their efforts, this project would not have been completed.

John Hart of Minotaur Resources tutored the geology of the Prominent Hill Prospect in South Australia and organised the use of a drill hole for the purposes of conducting my field work. John and Minotaur were very gracious even when I fouled their drill-hole, my thanks and apologies. Thankyou to Brendan Coleman of Tensor Geophysical Services for his assistance in the data acquisition.

I am grateful to the geoscientists of the specific field sites for their invaluable discussions into the geology and geophysics of their respective areas (Marcel Van Eck, Terry Hoschke for Golden Grove and Hamish Freeman for Prominent Hill).

Thanks to Graham and Linda Deer for their efforts in the arduous task of identifying and correcting the violations of grammatical parlance in addition to astutely advising me of my disseminated dyslexia.

Thankyou to my parents, friends and Linda for being especially patient with me and all the other day to day things they do that I take too much for granted.

> "The life which is unexamined is not worth living."
>
> Plato

CHAPTER 1 - PREFACE

1.1 APPLIED POTENTIAL METHODS – MISE-À-LA-MASSE

Electrical potential methods are widely applicable within geoscience, in particular, mineral exploration. The two main forms are self-potential (SP) methods and applied potential methods. SP methods are used to detect anomalous patterns in the spontaneous electrical field within the earth. These are derived from various sources examined by Sato and Mooney (1960), Keller and Frischknecht (1966) and Telford et al. (1990).

Applied potential methods use an artificial electrical source to generate an electric current within the subsurface. Information on the resistivity structure of the earth is obtained by measuring the potentials caused by the applied current. Applied potential methods include resistivity sounding, profiling and voltage mapping or Mise-à-la-Masse (Alfano, 1959; Keller and Frischknecht, 1966; Parasnis, 1966; Zohdy et al., 1973).

The Mise-à-la-Masse (MALM) method has been used in mineral exploration to target conductive bodies, for example volcanogenic massive sulphides (VMS) (Ascough, 1999; Bhattacharya et al., 2001) and other base metal mineralisations (Parasnis, 1967; Ketola, 1972; Bowker, 1991; Hattula and Rekola, 2000). Other applications include coal exploration (Rodríguez and Rodríguez, 2000) and environmental and civil engineering investigations such as tracking contamination plumes and other hydrogeologic investigations (Beasley and Ward, 1986; Reynolds, 1997; Osiensky, 1997; Nimmer and Osiensky, 2002).

MALM is conducted by the electrical excitation of a conductive mass within the earth by a source electrode placed in contact with the conductive mass via a drill hole or at an outcrop when available (Figure 1.1). With the mass energised, surface potentials are mapped using a single potential electrode. The configuration of the electrodes is detailed in Section 2.3 (Array configuration – pole-pole and pole-dipole, p23). Data from a MALM survey can delineate the areal extent of the conductive mass that has been excited and can also highlight the electrical interconnections between mineralisation lenses. Information on the structural geometry of the conductive body can be deduced from the surface potential maps.

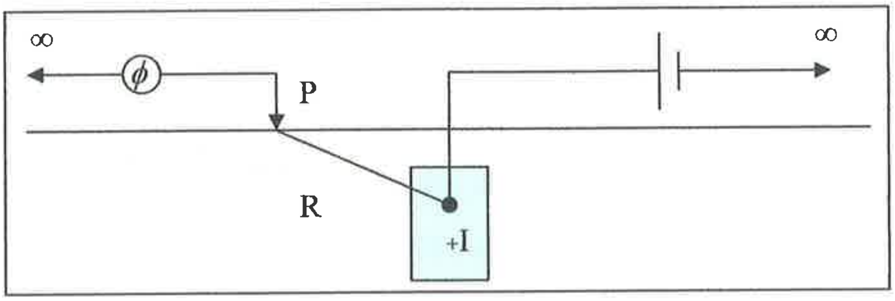

Figure 1.1: Mise-à-la-Masse pole-pole configuration, where I is the current input electrode, P is the potential measuring electrode, R is the distance between the two electrodes, ϕ is the potential with respect to a base station at that distance. (Eloranta, 1985)

1.2 SIGNIFICANCE / PROJECT GOALS

Mise-à-la-Masse is a low cost geophysical method which garners information on target bodies. Whilst MALM is a method capable of determining the extent of mineralisation, much of the interpretations of the data are qualitative, based on the surface potential maps recorded, or with minor processing, i.e. a horizontal gradient filter. Improvements in the analysis of MALM data enable increased geological knowledge to be derived from this uncomplicated method. If these investigations of the MALM method are able to extract further tangible information from the same data, then expenditure on more costly methods may not be necessary or applicable.

Not all of the acquired field data have been obtained in the classical MALM electrode configuration. Some source electrodes have been placed in positions where there is no significant mineralisation, but close to known mineralisation. These "near-miss" configurations yield data which share similarities with the in-mineralisation MALM data sets. The nature of these source electrode positions have been investigated through modelling.

The use of three-dimensional (3D) Finite Element Method (FEM) forward modelling software (Zhou and Greenhalgh, 2001) allows an insight to the interaction of the electrical potential field with the conductive structures and the overburden. Synthesised 3D responses of models which replicate basic geological features can be used in two ways. Firstly, idealised models advance the understanding of the potential field about conductive body both in 3D and across the surface, allowing the development of a set of axioms to help in the interpretation of MALM data. Secondly, idealised synthetic responses can aid in the development and interpretation of new techniques and the data generated by them.

Numerical processes can assist in the analysis of MALM surveys by removing or reducing unwanted elements within the data (Daniels, 1983; Oppliger, 1984; Bowker, 1987). MALM surface potentials are the result of potential contributions from two sources. One contribution is from the induced charges at resistivity contrasts within the subsurface and the second is the current divergence from the source electrode itself (expanded upon in Section 2.6, p29). The potential response of an electrode in a homogenous, isotropic half-space with no resistivity anomaly can be analytically calculated. These electrode effect potentials can be subtracted from the MALM data. The resulting potential map is representative of the residual potentials generated by the resistivity contrasts in the earth. Residual potentials assist in the analysis of MALM data by revealing more information on the subsurface geology than unprocessed MALM data.

Existing techniques of inverting 3D potential and resistivity data are computationally intensive and time consuming. Algorithms which approximate SP data have been used with success in the investigation of geothermal fluid movement (Di Maio and Patella, 1994; Patella 1997) and ground water flow (Hämmann et al., 1997). An algorithm that does not require full 3D parameterisation for the MALM method would allow for the rapid appraisal of MALM data.

An appreciation of the MALM responses in regolith covered regions is of significance as much of Australia is under a weathered mantle that inhibits exploration for mineral deposits (Doyle, 1981; Taylor and Eggleton, 2001). Morphology of the regolith can notably affect the MALM data by distorting or displacing surface potentials due to the near-surface resistivity contrasts within the regolith. However, it has not been ascertained to what extent these near-surface resistivity contrasts affect MALM data. The effects of weathered cover on MALM can be studied using 3D FEM modelling to simulate some basic profiles that may occur in an inhomogeneous, isotropic weathered layer.

The foremost goal of this project is to develop and apply novel analytical methods to improve the interpretation of MALM data in weathered terrains. Other major goals of this project are to:

- acquire data sets from two field locations using MALM to investigate two types of conductive base metals mineralisation. One field site is Golden Grove, Western Australia, the other is Prominent Hill, South Australia;
- generate synthetic forwards models for the investigation of effects that basic geological and geophysical parameters have on the MALM response. These parameters include resistivity contrast, dip, volume, depth from surface and near-miss electrode positions. Various regolith features were modelled to assess the effect on surface potentials. FEM models constrained by the known geology for each field site were generated. These simplified models of the field areas attempt to simulate the potential fields about the synthetic conductive bodies;
- develop a numerical method to remove the effect of the electrode potential, thus leaving residual potentials due to the resistivity structure within the earth. This technique is applied to the idealised models and field geology models and used to better quantify the acquired field data;
- modify and further develop the algorithm used by Hämmann et al. (1997) for use in the rapid evaluation of MALM data in 3D. The responses from the FEM models are assessed using this modified algorithm as are the field MALM results. The algorithm will be combined with the electrode effect removal to enhance interpretations of MALM data.

1.3 FIELD SITES/LOCALE

Two field sites were investigated using the techniques developed in this paper. At Golden Grove, in Western Australia, MALM has been used to explore for continuity of mineralisation away from an existing mine. The Scuddles/Gossan Hill mine has been operational for over ten years, hence significant information on the geology of the area is known from abundant drill holes as well as from the mine itself (M. Van Eck pers comm., 2003). The other site, Prominent Hill, in South Australia, is a more recent exploration prospect which is still under development through the investigation of targets with a variety of geophysical techniques (Hart and Freeman, 2003b).

Golden Grove

Field location

Golden Grove is a base metals operation conducted by Newmont Australia in Western Australia. It lies in the southern Murchison Province of the Archaean Yilgarn Craton. The terrain is semi-arid with low relief. Vegetation is predominately mulga scrub with a sparse ground cover of grasses and shrubs. There are two operational mines, Scuddles and Gossan Hill, and processing facilities are present at the site. The Scuddles Cu-Zn deposit was first discovered in 1979, with production beginning in 1990 (Robinson and Belford, 1991). The mines are located 200 kilometres inland from Geraldton, or 60 kilometres south of Yalgoo (Figure 1.2).

Background geology

Geology of this system is described in further detail by Frater (1983), and Ashley et al. (1988). The geology of the area strikes north-north-westerly, with dips vertical or very steeply to the west (Figure 1.3). The VMS deposits lie within the Gossan Hill Group, which consists of weakly metamorphosed volcanics, pelitic and felsic sediments. This sequence of felsic volcaniclastics lie in contact with granitoid rocks to the east and is capped by a unit of banded iron formation to the west (Robinson and Belford, 1991). The sequence is intruded by both steeply dipping and flat-lying dolerite dykes (Ashley et al., 1988).

At Golden Grove the mineralisation is thought to be strata-bound (Frater, 1983) and demonstrates VMS zonation with intense stringer ore in the footwall. Mineralisation consists of highly conductive massive pyrite and pyrite-chalcopyrite ores that dip to the west at approximately 80 degrees, and plunge to the north at an angle of 5 degrees (Figure 1.3). Both Scuddles and Gossan Hill have a similar geological setting. These traits are also shared by the potential deposits at Catalpa prospect, north of Gossan Hill. There is no expression of the mineralisation at the surface save for a thin horizon of lamellate mineralised chert that is correlated to the chert found in the upper region of the mineralised horizon at depth (Craven et al., 1985). The area has a thick regolith mantle, ranging from 80 to 100 metres thick (Frater, 1983). The mineralisation is thought to be effectively insulated electrically from this conductive weathered layer by the resistive host rock as the main mineralised horizon begins at a depth of 120 to 200 metres below the surface (Craven et al., 1985).

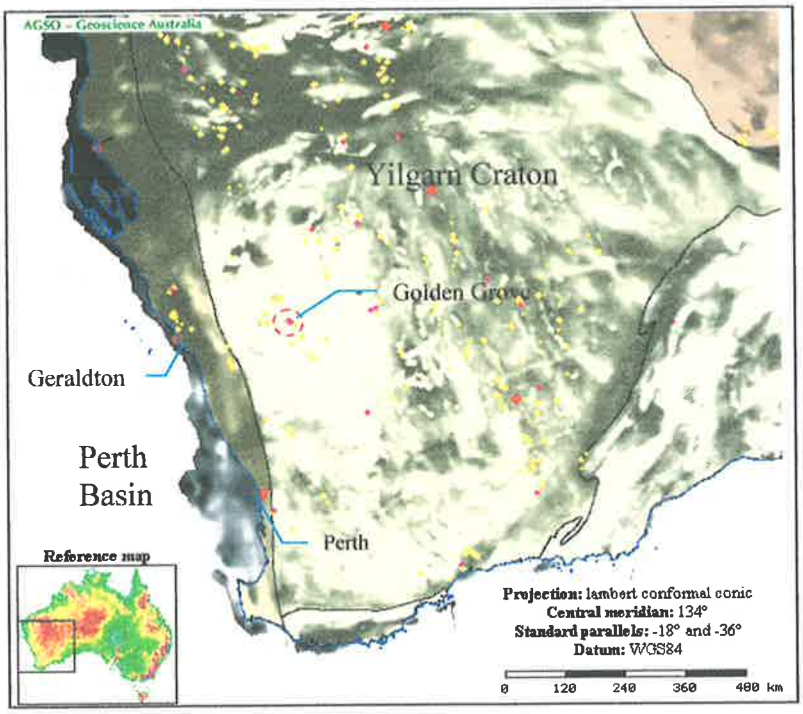

Figure 1.2: Location map of Golden Grove superimposed on an aeromagnetic image of the Yilgarn Craton. The purple dots located in the centre of the dashed circle represent the Golden Grove deposit. Other yellow and purple dots indicate Cu – Zn - Pb deposits. (Courtesy of Geoscience Australia website)

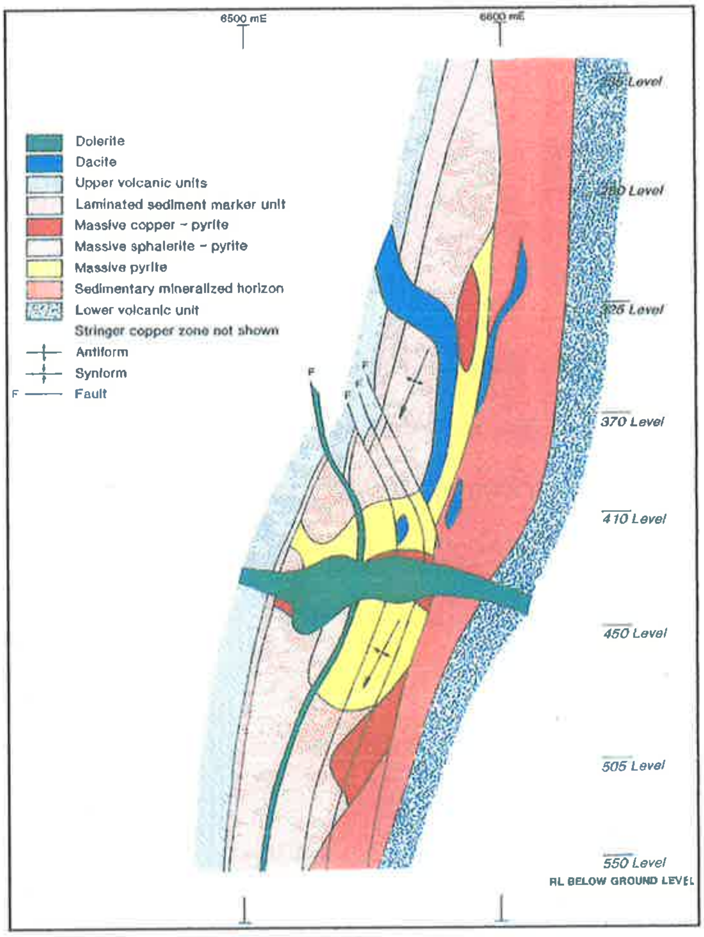

Figure 1.3: Cross-section, looking mine grid north, of the Scuddles deposit at Golden Grove, Western Australia. Note the vertical orientation of the overturned VMS deposit which is predominant in the Golden Grove deposits. After Boyd and Frankcombe (1994).

Background geophysics

A wealth of geophysical data has been acquired throughout the exploration history of the Golden Grove site. Such data range from aeromagentics to gradient Induced Polarisation (IP) and, of course, MALM.

The Scuddles and Gossan Hill deposits appear as discrete magnetic anomalies in the aeromagnetic survey completed in 1978 (Robinson and Belford, 1991). This survey was followed up by ground magnetic traverses. Other potential field measurements included gravity surveys conducted during the early nineties. Resolution for the gravity data were 40 by 80 metre spacing in the easterly and northerly directions respectively. Gravity surveying of the area has shown that an anomalous response is east of the surface projections of the mineralisation, which is thought to be caused by silicification of the footwall (Boyd and Frankcombe, 1994).

Gradient-array resistivity and IP surveys were carried out soon after the initial discovery. The resistivity data picked out the footwall silicification to the east of the Scuddles mineralisation, and there was a small chargeability response over the main Scuddles body (Boyd and Frankcombe, 1994). Various forms of electro-magnetic (EM) methods were used at Golden Grove. In general the mineralisation in the area is known to be conductive and responds to surface and down-hole EM techniques (Craven et al., 1985; Boyd and Frankcombe, 1994). EM surveys gave a strong anomalous response orientated along strike (north and south).

Boyd and Frankcombe (1994) conclude that transient EM (TEM) has been the most effective method at Scuddles, with IP and MALM proving also successful. Regional mapping was aided by the gravity and magnetic data sets.

Mise-à-la-Masse

The MALM method is being used by Newmont Australia to aid in their brownfields exploration of base metals in Golden Grove, delineating regions of low resistivity such as the extent of the VMS deposit at Golden Grove. MALM surveys were undertaken at Scuddles in the mid-1980s with a distinct anomalous response. Further surveys were conducted for exploration purposes in the 1990s and included the current data sets described below. There are two distinct areas that were investigated in this paper; Catalpa and Catalpa North (Figure 1.4), are part of the Catalpa prospect, north of the Gossan Hill Mine. Figure 1.5 is the longitudinal section of the known mineralisations projected to the vertical plane. The image is orientated mine-grid west with the Catalpa and Catalpa North survey areas on the right of the diagram. Frater (1983) detailed the geology for part of this region with surface geology maps and cross-sections. The mine grid used for in the surveys is aligned 52 degrees west of magnetic north. Further details on the MALM method for this study can be found in Section 3.2.

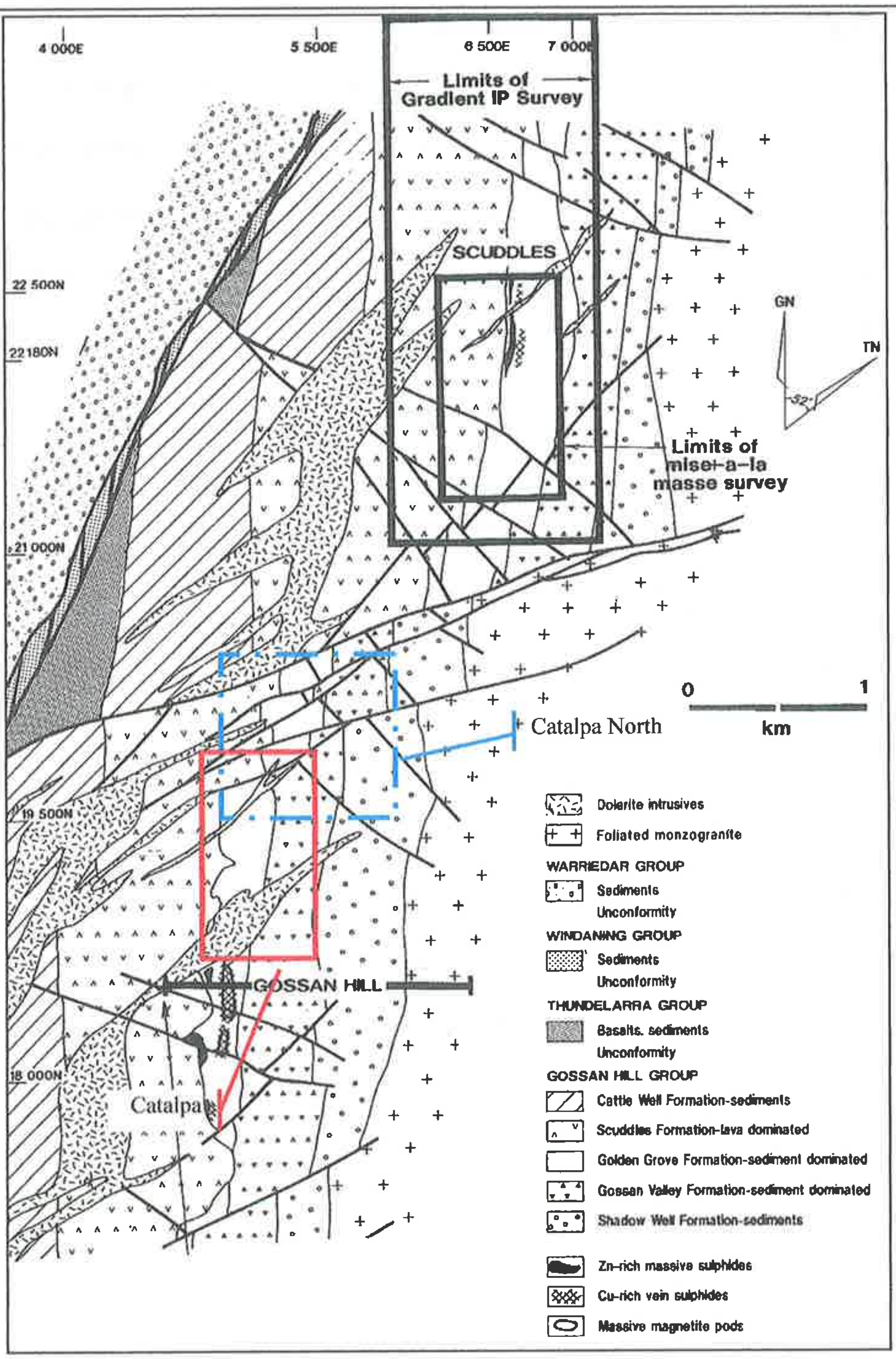

Figure 1.4: The Scuddles/Gossan Hill region with Catalpa and Catalpa North outlined by the quadrangles. The Catalpa North area (dashed outline) is riddled with faults, while to the south the Catalpa area (solid red rectangle) has only one fault of significance Note that grid north (GN) is offset 52 degrees to the west of magnetic north (TN) (after Boyd and Frankcombe, 1994).

Electrode position and drill hole deviation logs

The data from a Golden Grove MALM survey was accompanied by a drill hole deviation log for the drill hole used in the survey. This log gave the dip angles and azimuth directions for a depth down the drill hole. A program, *dlog.m*, (Appendix A, p146) was written in Matlab to resynthesise these logs into surface projections as well as 3D plots for both the drill hole trace and the down-hole source electrode position. This program takes into account the deviations of the drill hole and calculates an accurate X,Y position and depth from surface for the down-hole source electrode. In essence, it is a simplified, home-grown version of the "Wholeplot" module from the Oasis Montaj software suite.

For holes without the drill hole azimuth/declination logs a trigonometric calculation was performed to obtained surface coordinates. For such a survey the position information for the down-hole source electrode was given as the down-hole depth. The dip and direction of the drill hole (measured at the collar) were used, in combination with the down-hole electrode depth, to obtain the X,Y surface coordinates as well as its depth from surface for the source electrode These trigonometric calculations did not account for drill hole deviations, hence are not as accurate as the *dlog.m* derived positions.

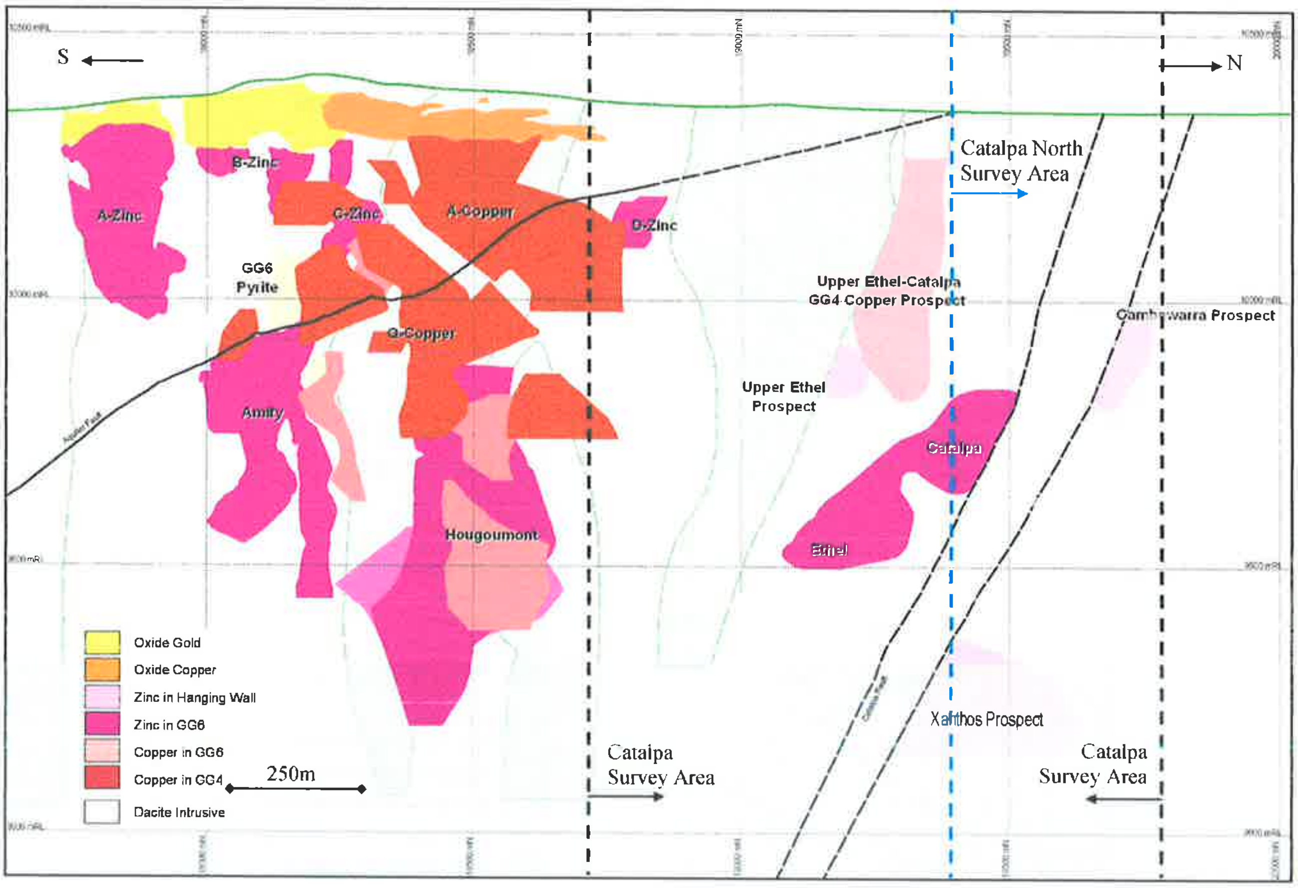

Figure 1.5: A longitude section of the Gossan Hill mine and the Catalpa and partial Catalpa North prospects north of the mine. This section is the projection of the interpreted mineralised bodies and prospects. Note that depths are given in terms mRL and that 1mRL = 1 metre. The dashed lines indicate the boundaries of the MALM survey areas Catalpa and Catalpa North.

Catalpa

Four surveys were undertaken within the Catalpa region shown in Figure 1.4; in these surveys the source electrode was placed in drill hole RHDD018 and at three different positions in drill holeRHDD020 (Foley, 1999). Of interest are the different positions of the source electrode in RHDD020, two near-miss surveys and one in-mineralisation. In the north of the area is a major dextral fault which runs NNE to SSW (magnetic north), around the 19600N northing.

Table 1-1 lists the collar position and down-hole depths for the drill holes in the area. The electrode position in X,Y,Z (Table 1-1) was determined via the *dlog.m* program (Appendix A, p146) and are plotted as surface projections along with the drill hole traces in Figure 1.6.

Selection of these down-hole depths is detailed in the Field data collection method section (p76). The electrode depths for RHDD018 and RHDD020 Setup A intersect mineralisation whilst RHDD020 Setup B and C did not intersect the mineralisation (Foley, 1999).

Drill hole	Collar		Down-hole	Electrode Position		
	Easting	Northing	Depth (m)	Easting	Northing	Depth (m)
RHDD018	4698	19372	**688**	4981	19322	**624**
RHDD020 Setup A	4685	19320	**697**	4998	19254	**617**
RHDD020 Setup B	4685	19320	**481**	4886	19278	**434**
RHDD020 Setup C	4685	19320	**920**	5122	19221	**800**

Table 1-1: Drill hole collar and electrode positions for the Catalpa area. The positions in X, Y and Z for the electrodes were obtained from the dlog.m program. These positions were used for the models and electrode effect removal.

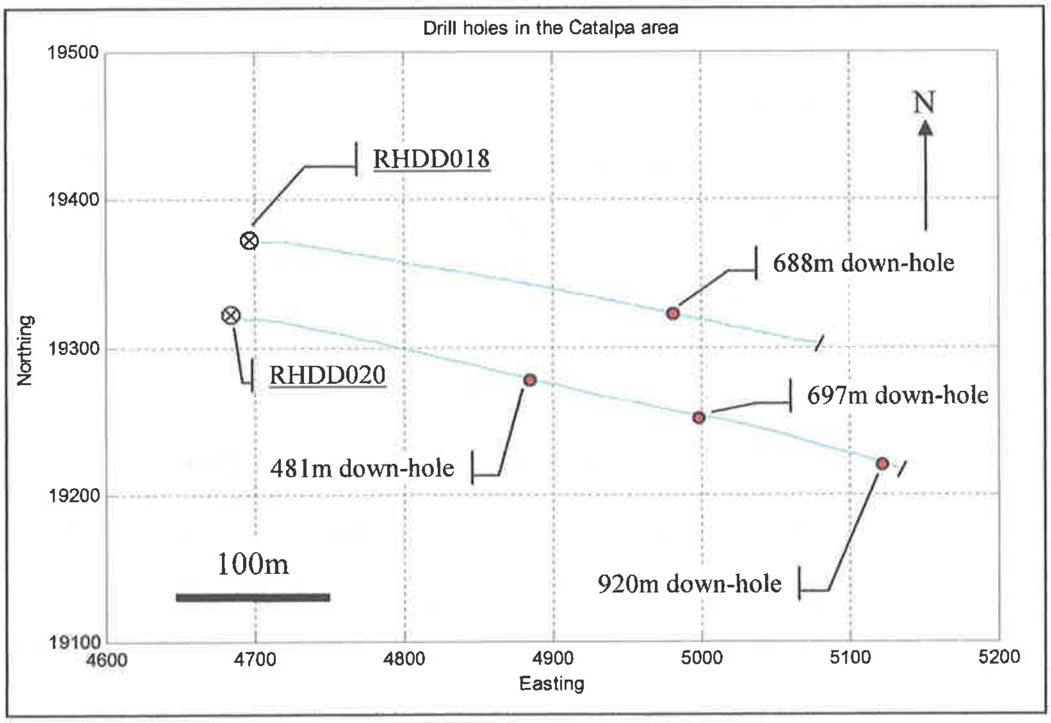

Figure 1.6: Surface projections of drill holes RHDD018 and RHDD020. The electrode for RHDD018 was placed at a down-hole depth of 688 metres. Down-hole electrode depths for RHDD020 Setup A B and C are 697, 481 and 920 metres respectively.

Catalpa North

The simplified geology of the area in Craven et al. (1985) defines two main faults, these being the Catalpa/Luisini Fault and the Racehorse Fault. The faults in this area makes for an interesting MALM survey area as the faults may act as electrical conductors, linking the displaced conductive structures together (Bowker, 1991).

Catalpa North had four surveys in three drill holes. RHDD010, RHDD038 and RHDD040 Setup 1 were of similar depths whilst RHDD040 Setup 2 was much deeper (Table 1-2). *dlog.m* gave depth from surface values for the electrode positions, plotted with the surface projections of the drill holes in Figure 1.7.

Discussions with the geological staff at Golden Grove has identified that RHDD010 did not have the electrode connected to any sulphides at 430 metres, hence is an out-of-mineralisation survey. RHDD038 had trace amounts of disseminated pyrite at 416 metres, and is classed as an out-of-mineralisation survey. Both electrode depths in hole RHDD040 did not intersect any sulphides either. In short, none of these electrode depths have been placed in contact with significant sulphides (M. Van Eck pers comm., 2003).

Drill hole	Collar		Down-hole Depth (m)	Electrode Position		
	Easting	Northing		Easting	Northing	Depth (m)
RHDD010	5164	20311	**430**	5379	20286	**371**
RHDD038	4877	19921	**416**	5024	19920	**390**
RHDD040 Setup 1	4911	20105	**455**	5068	20112	**429**
RHDD040 Setup 2	4911	20105	**975**	5278	20096	**904**

Table 1-2: Drill hole collar and electrode positions for the Catalpa North area. The positions for the electrodes were obtained from the dlog.m program. These positions were used for the models and electrode effect removal.

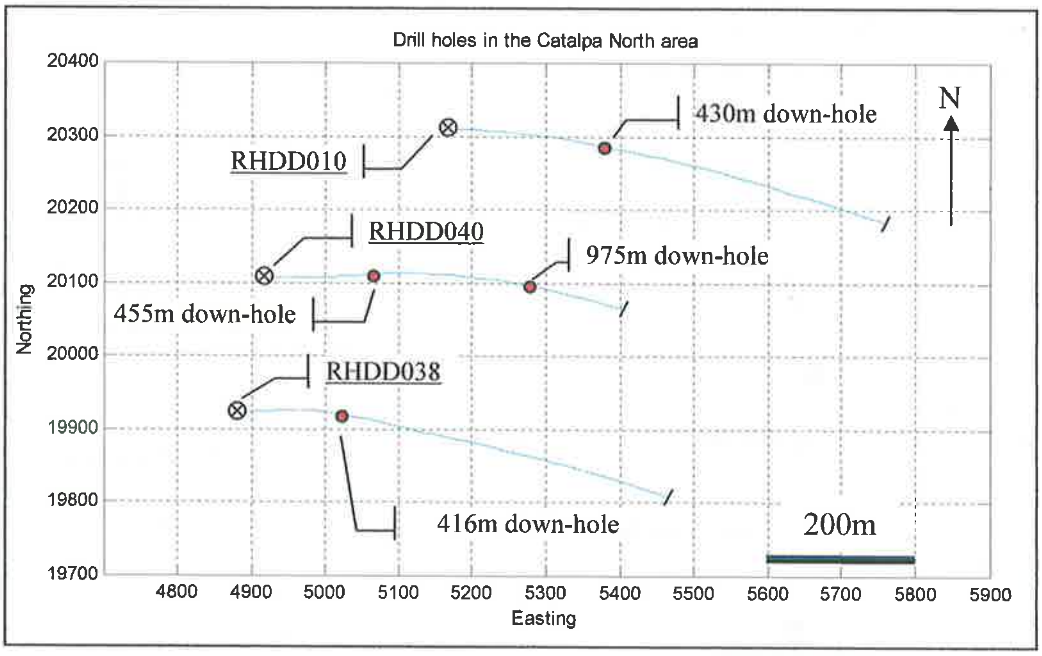

Figure 1.7: Surface projections of drill holes RHDD010, RHDD038 and RHDD040. The down-hole electrode depth for RHDD010 and RHDD038 was 430 and 416 metres respectively. Down-hole electrode depths for RHDD040 Setup 1 and 2 are 455 and 975 metres respectively.

Prominent Hill

Field location

Prominent Hill is a Cu-Au-U-Rare Earth Elements (REE) prospect in the central-north of South Australia. The prospect is approximately 630 km northwest of Adelaide and 100 kilometres southwest of Coober Pedy. Operated by Minotaur Resources Ltd, the prospect lies within the Mount Woods Joint Venture (Figure 1.8). The area is semi-arid with meagre vegetation ranging from low shrubs to sparse ground cover. The vegetation exhibits banding or "tiger-striping", indicative of sheet water flow (A. Brown pers comm., 2003)

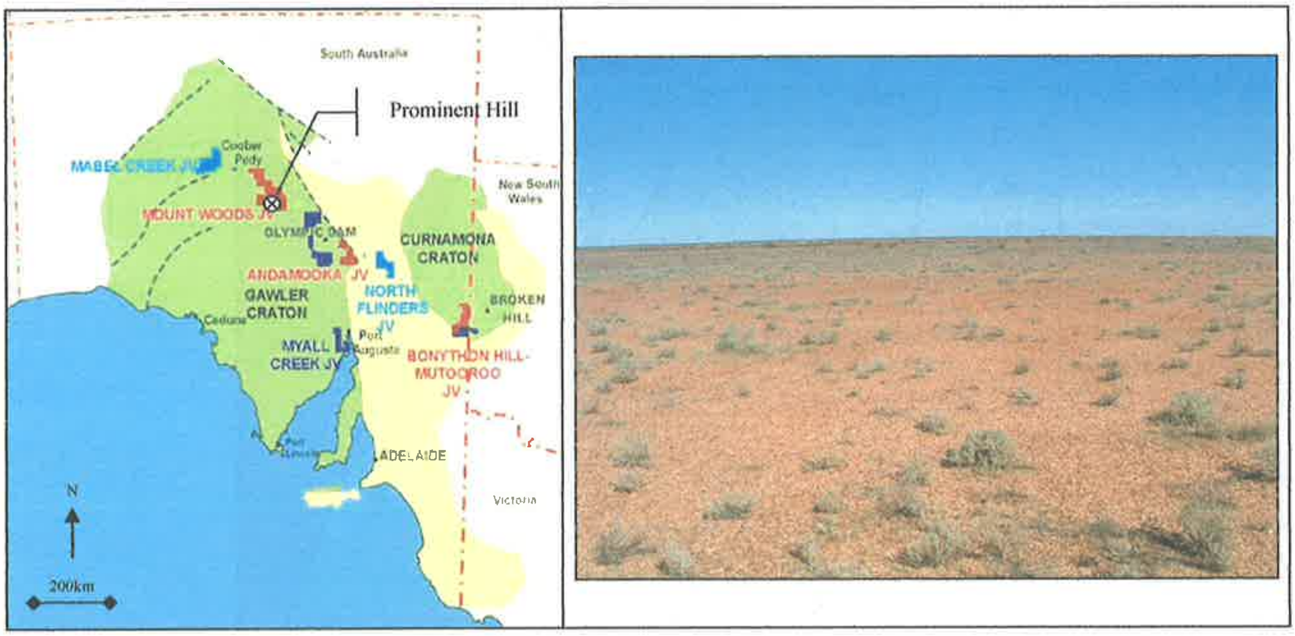

Figure 1.8: (left) Location map of the Mount Woods Joint Venture in the mid-north of South Australia, 630 km north-west of Adelaide. (Belperio, 2002). (right) Terrain or lack there of, on the exploration grid at 555500E, 6712300N looking south.

Background geology

The Mount Woods Inlier is located on the eastern margin of the Gawler Craton and is Paleo- to Mesoproterozoic in age (Hart and Freeman, 2003a). Outcrop in this region has shown the basement to consist of quartzofeldspathic and garnetiferous gneisses, migmatite, quartzite and quartz-biotite schists (Daly et al., 1998; Hart and Freeman, 2003b). Prominent Hill is located towards the southern extent of the Mount Woods Inlier. Basement in the area comprises basalts and andesite, equivalent to the Gawler Range Volcanics. The discovery hole URN001 was drilled in 2001 which intersected a massive haematite breccia containing copper, gold and uranium. Mineralisation is associated with haematitic breccias that were intruded into a sedimentary pile (Hart and Freeman, 2003a). The main zone of mineralisation is contained in a sequence of unmetamorphosed sediments and volcanics of significant width (Hart and Freeman, 2003b). The mineralisation is constrained by an east-west trending structural zone, plunging to the west beneath volcano-sedimentary cover (Figure 1.9a). The Fe-Cu-Au mineralisation at Prominent Hill are similar in style and metal assemblage to the copper mineralisation at Olympic Dam, South Australia (H. Freeman pers comm., 2003).

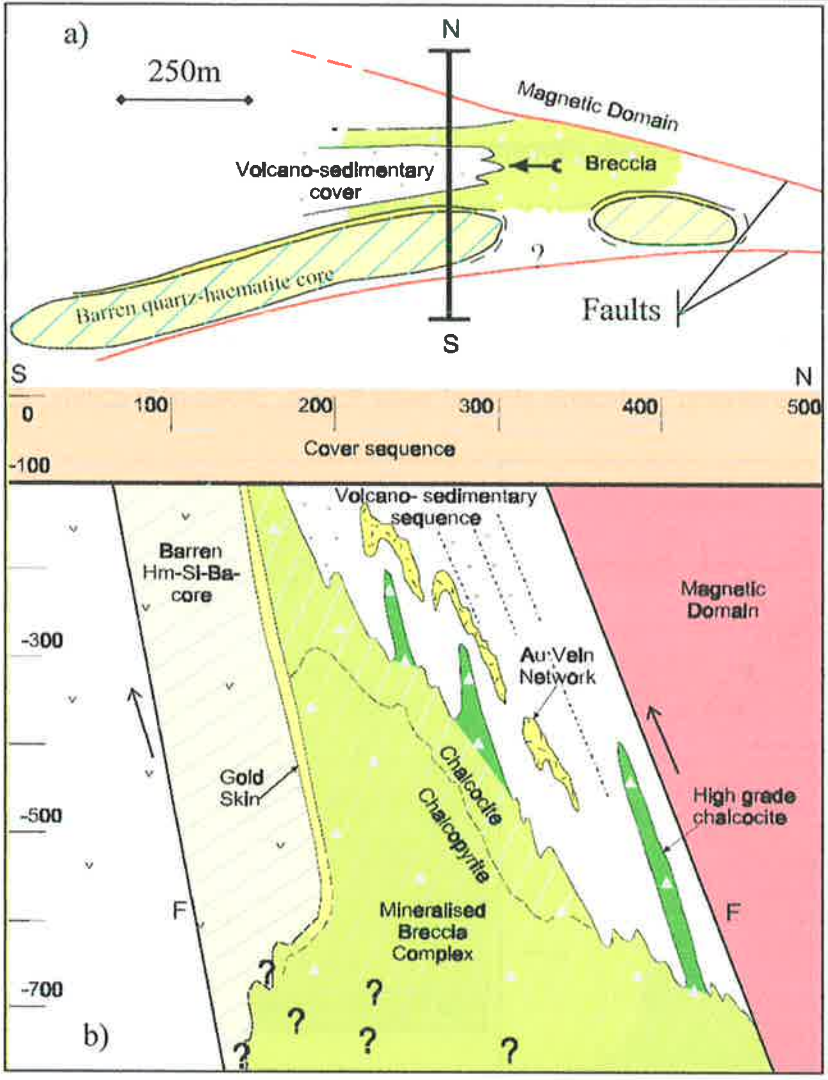

Figure 1.9: Interpretative geological model of the Prominent Hill deposit, a) (top) shows the model in plan view, with the faults bounding the mineralised zone to the north and south. b) is the cross-section (along the line in N-S) of the mineralisation which shows a near vertical orientation of mineralised and barren bodies (after Belperio, 2002).

Regolith cover

The Prominent Hill prospect is covered by a variable regolith sequence up to 120 metres thick (Figure 1.9b), it is separated into three distinct layers which can be identified in drill holes (Figure 1.10) (J. Hart pers comm., 2003). The uppermost section is a sandy cover that is increasingly leached of its iron oxide staining with depth; this layer extends down to approximately 40 metres (Figure 1.10). The Bulldog Shale is a 20 metre thick, highly conductive ($\rho \sim 2$ ohm.m) black shale which hampers electrical methods (Hart and Freeman, 2003b). Below this is another sandy layer which is more resistive ($\rho \sim 1000$ ohm.m) than the upper section ($\rho \sim 100$ ohm.m). The lower layer continues to the basement, and is approximately 40 metres thick. A thin layer of ferruginous lag covers the surface (Taylor and Eggleton, 2001)

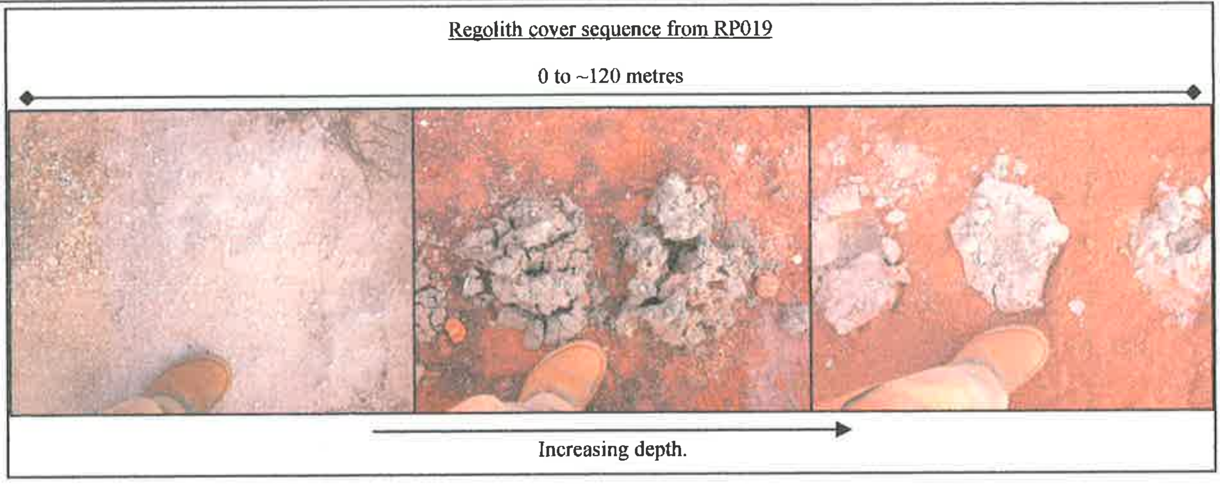

Figure 1.10: Drill scavenges from a recent hole RP019. (left) Sandy upper regolith cover, leached of ferruginous colouring with depth, extends from 0 to 40 metres. (centre) The Bulldog shale is dark grey and highly conductive (40 to 60 metres depth). Lower sandy regolith cover (right) is more resistive than the upper layer (From 60m to basement).

Background geophysics

As with Golden Grove, various forms of geophysical data were collected at Prominent Hill. These included potential field data, surface and down-hole electrical and EM data. The initial discovery hole targeted a gravity anomaly from a coarse-grid gravity survey, with a grid of 400 by 200 metres (Hart and Freeman, 2003b). A follow up detailed gravity survey (100 by 100 metre grid), separated the original anomaly into three main bodies (Figure 1.11). The ground magnetics anomaly corresponds with the northern gravity anomaly and there is no magnetic response from the southern gravity bodies (Figure 1.11).

IP/Resistivity data were collected both down-hole and across the surface. The down-hole surveys had resistivity lows that corresponded with peaks in the drill hole copper assays. The surface IP resistivity inversions identified a shallow conductive unit which coincides with the Bulldog Shale (Hart and Freeman, 2003a). The IP chargeability data also correlates with the Bouguer gravity anomaly. Surface TEM and down-hole EM data also highlighted the Bulldog shale, with anomalies in the mid-time windows coincident with those seen in the IP data, and only subtle responses that coincide with the mineralised breccias. A Mise-à-la-Masse survey was conducted at Prominent Hill prior to this study, but specifics of the survey and the data are not yet public domain.

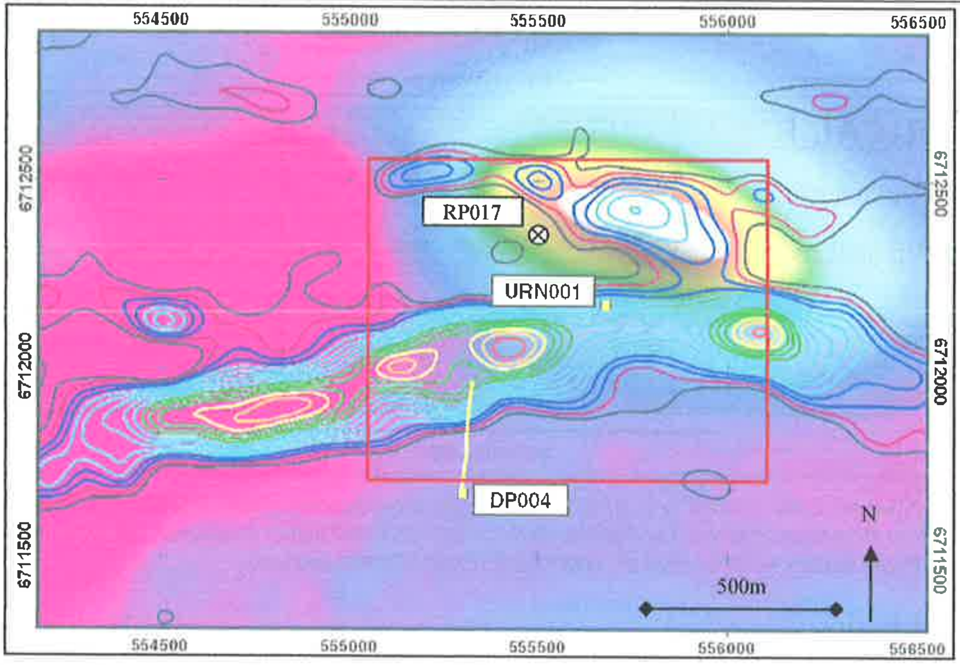

Figure 1.11: Potential field data; contours represent the 2^{nd} horizontal derivative of Bouguer gravity, and the colour surface is the ground magnetics data. URN001 is between gravity anomalies as a result of the coarse gravity survey (after Hart and Freeman, 2003a). The red rectangle encompasses the MALM survey area conducted in this study.

RP017 drill hole and survey area.

The area for the survey conducted at Prominent Hill was based around the RP017 drill hole. RP017 is an inclined hole, bearing 180 degrees from north at a declination of 60 degrees (J. Hart pers comm., 2003). The collar of the hole is to the north-west of the initial discovery hole URN001 (Table 1-3). The survey area for this study covers both the gravity and magnetic anomalies. From Figure 1.9 (a and b), the area encloses two faults which bound the mineralisation to the north and to the south. Specifics of the MALM survey for this study are expounded in Section 3.2.

Drill hole	Collar		Down-hole Depth (m)	Electrode Position		
	Easting	Northing		Easting	Northing	Depth (m)
RP017	555500E	6712340N	405	555500	6712137	351

Table 1-3: Collar and electrode position in terms of Easting, Northing and vertical depth. The electrode position was calculated from the declination and azimuth of the hole at the collar.

2.1 ELECTRICAL RESISTIVITY THEORY AND PRINCIPLES

The basis for all geoelectric theory begins with the four equations of Maxwell. These equations are mathematical interpretations of Faraday's and Ampere's Laws which interrelate the electric and magnetic fields.

$$\nabla \times \mathbf{E} = -\frac{\partial \mathbf{B}}{\partial t} \qquad \textit{Equation 2.1}$$

$$\nabla \times \mathbf{H} = \mathbf{J} + \frac{\partial \mathbf{D}}{\partial t} \qquad \textit{Equation 2.2}$$

$$\nabla \cdot \mathbf{B} = 0 \qquad \textit{Equation 2.3}$$

$$\nabla \cdot \mathbf{D} = \mathbf{Q} \qquad \textit{Equation 2.4}$$

Where, **E** is the electric field vector (V/m), **H** is the magnetic field vector (A/m), **B** is the induction field vector or magnetic flux density (webers/m^2 or T), **J** is the current density vector (A/m^2) and **D** is the electric displacement vector (C/m^2) (Keller and Frischknecht, 1966).

Equations 2.1 and 2.2 are expressions of Faraday's Law and Ampere's Law respectively. Using the vector identity, $\nabla \cdot \nabla \times \mathbf{A} = 0$, with these two equations yields Equations 2.3 and 2.4 respectively (Telford et al., 1990) where **Q** is the electric charge density. In regions of finite and constant resistivity, charge does not accumulate during current flow, thus **Q** = 0.

Therefore from Equation 2.4 and the vector identity, the divergence of the current density, which is equal to the (negative) rate of accumulation of **Q**, also equals zero for every place but the current source. The divergence condition for an isotropic, homogenous ground is as follows (Telford et al., 1990):

$$\nabla \cdot \mathbf{J} = -\frac{\partial}{\partial t}(\nabla \cdot \mathbf{D}) = -\frac{\partial \mathbf{Q}}{\partial t} = 0 \qquad \textit{Equation 2.5}$$

The electric displacement vector, **D**, and the current density vector, **J**, can be expressed in terms of the electric field vector, **E**, using the dielectric permittivity, ε, and electrical resistivity, ρ (Keller and Frischknecht, 1966).

$$\mathbf{D} = \varepsilon \mathbf{E} \qquad \textit{Equation 2.6}$$

$$\mathbf{J} = \frac{\mathbf{E}}{\rho} \qquad \textit{Equation 2.7}$$

Similarly, the magnetic induction, **B**, can be written in terms of the magnetic field strength, **H**, and the magnetic permeability, μ.

$$\mathbf{B} = \mu \mathbf{H} \qquad \textit{Equation 2.8}$$

The proportionality constants, ε and μ, establish the correlation of their two associated vector quantities. Full definitions of these constants are in Halliday et al. (1993). Equation 2.7 is Ohm's Law expressed in terms of **J**, **E** and ρ. Within the Earth, this equation generalises that the resistivity of the subsurface, ρ, governs the magnitude of the electrical field, **E**, for an applied current density, **J**.

Assuming the physical properties of the subsurface static in respect to time and space, **B** and **D** can now be removed from Maxwell's equations to give the equations in terms of **E** and **H** (Keller and Frischknecht, 1966):

$$\nabla \times \mathbf{E} = -\mu \frac{\partial \mathbf{H}}{\partial t} \qquad \textit{Equation 2.9}$$

$$\nabla \times \mathbf{H} = \frac{\mathbf{E}}{\rho} + \varepsilon \frac{\partial \mathbf{E}}{\partial t} \qquad \textit{Equation 2.10}$$

$$\nabla \cdot \mathbf{H} = 0 \qquad \textit{Equation 2.11}$$

$$\nabla \cdot \mathbf{E} = \frac{\mathbf{Q}}{\varepsilon} \qquad \textit{Equation 2.12}$$

For most geophysical EM methods, Equation 2.10 reduces to Equation 2.10b , as the second term is negligible for frequencies, $f < 10^5$Hz.

$$\nabla \times \mathbf{H} = \frac{\mathbf{E}}{\rho} \qquad \textit{Equation 2.10b}$$

Equations 2.9 and 2.10b can be rewritten to show that electric and magnetic fields obey the Diffusion Equation.

Buried source electrode in an infinite, homogenous, isotropic earth.

In considering MALM and other Direct Current (DC) resistivity methods (where the displacement currents are insignificant), the time variant derivatives in Equations 2.9 and 2.10 reduce to zero. Thus if considering the electric field or its gradient, only Equation 2.12 remains of significance.

The electric field vector, **E**, is also the gradient of a scalar potential, *V*, (Dey and Morrison, 1979).

$$\mathbf{E} = -\nabla V$$

which combined with Equation 2.7 gives

$$\mathbf{J} = -\frac{\nabla V}{\rho} \qquad \textit{Equation 2.13}$$

The above equation, substituted into Equation 2.5, the divergence condition, yields a Laplace's Equation for homogenous isotropic ground (Keller and Frischknecht, 1966):

$$\nabla \cdot \mathbf{J} = \frac{1}{\rho} \nabla \cdot \mathbf{E} = \frac{1}{\rho} \nabla^2 V = 0 \qquad \textit{Equation 2.14}$$

The MALM method can be thought of as a single buried electrode, which acts as a point source. In homogenous ground, the symmetry of the system dictates that the potential, V, is a function of the distance, r, from the point source. It is usual to define $V = 0$ as r tends to infinity.

Equation 2.14 can be expressed in polar coordinates as a function of r, (Keller and Frischknecht, 1966):

$$\frac{\partial}{\partial r}\left(r^2 \frac{\partial V}{\partial r}\right) + \frac{1}{r^2 \sin\theta}\frac{\partial}{\partial\theta}\left(\sin\theta \frac{\partial V}{\partial r}\right) + \frac{1}{r^2 \sin^2\theta}\frac{\partial^2 V}{\partial\psi^2} = 0$$

from the implied spherical symmetry, the terms with θ, and ψ, are negated and therefore reduces to:

$$\Rightarrow \frac{\partial}{\partial r}\left(r^2 \frac{\partial V}{\partial r}\right) = 0,$$ *integrating and rearranging gives:*

$$\frac{\partial V}{\partial r} = \frac{A}{r^2}$$ *Equation 2.15*

Integrating again gives Equation 2.16, the scalar potential, V, which is dependent on the distance from the point source, r and two integration constants A and B (Keller and Frischknecht, 1966):

$$V = -\frac{A}{r} + B$$ *Equation 2.16*

As r, tends to ∞, V, equals zero and therefore B equals zero. Since current diverges radially outwards from the source, the total current, I, crossing a spherical surface can be expressed in terms of A, using Equations 2.13 and 2.15:

$$I = 4\pi r^2 \mathbf{J} = -\frac{4\pi r^2}{\rho}\frac{\partial V}{\partial r} + B = -\frac{4\pi r^2}{\rho} A$$ *, which rearranges to* $A = -\frac{I\rho}{4\pi}$

The above can be substituted back into Equation 2.16 to give the total potential V, at a distance, r, from the single point source in a homogenous, isotropic full-space (Telford et al., 1990). Equation 2.17 is the potential function, V, is a principal building block of MALM theory but is insufficient for the Electrode Effect as discussed in Section 2.6:

$$V = \left(\frac{I\rho}{4\pi}\right)\frac{1}{r}$$ *Equation 2.17*

This function forms concentric spheres of equipotential surfaces at a radius, r, centred about the source electrode. This is partly the mathematical calculation for the homogenous electrode response shown in Figure 2.1 (Parasnis, 1966; Parasnis, 1967; Reynolds, 1997). This holds for an infinite full-space of constant resistivity which is an inadequate earth model.

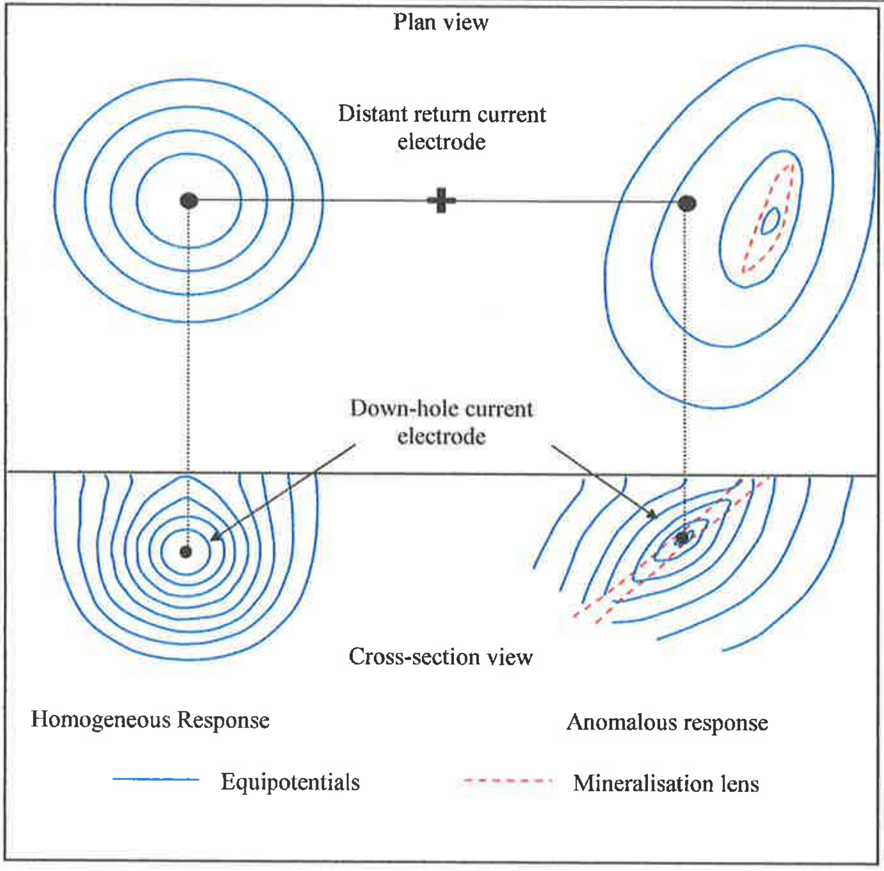

Figure 2.1: Homogenous media versus anomalous potential response from the MALM method, displaying the distorting and displacing effects of a lens of mineralisation on the electrical equipotentials about the down-hole electrode, both on the surface and in cross-section (after Parasnis, 1966).

Buried source electrode in a semi-infinite, homogenous, isotropic earth.

In order to be of use, the electrical potential calculated in Equation 2.17 must be placed in the context of a real world paradigm. The earth can be represented as a half-space, a semi-infinite homogeneous isotropic medium. The simplicity of this scenario allows the use of geometric optics to calculate the potential function (Keller and Frischknecht, 1966; Telford et al., 1990).

The semi-infinite half-space model has a bounding plan which separates media of two different resistivities; in this case it is the air/earth interface. For the optics analogy to be applicable, the potential function, V, must abide by both the following conditions (expounded to a greater degree in Keller and Frischknecht (1966) and Dey and Morrison (1979));

- V must be continuous across the bounding plane between the two media (conservation of potential, Ohm's Law).
- The *normal* component of current flow through the bounding plane must be continuous (conservation of charge).

The schematic in Figure 2.2 establishes this optics analogy. The half-space bounded at the air/earth interface, with the earth extending infinitely from this bounding plane. A source electrode, M, is buried at a depth, *h*, from the bounding plane. The earth resistivity is ρ_1 and the resistivity of air is ρ_2.

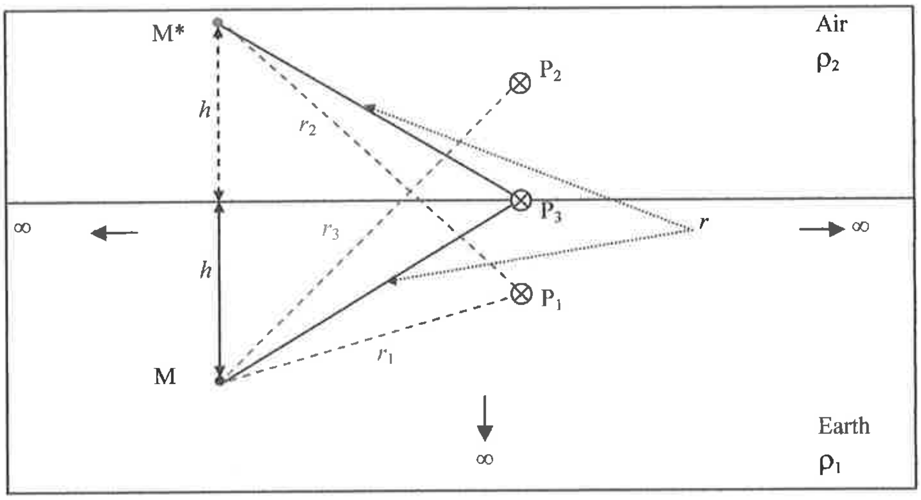

Figure 2.2: The semi-infinite earth is bounded at the air/earth interface. In this half-space, potential can be measured at three different locations, P1, P2 and P3. The source, M, is buried at a depth, h, within the earth of resistivity ρ1. At P1 and P3, the total potential can be calculated using the analogy of geometric optics. The total potential is the sum of the potential contributions from the source M and the reflected image source M caused by the bounding plane.*

The potential within the earth, at P_1, is given by, $V(P_1)$. This can be expressed as two potential contributions. The primary contribution, direct from the source electrode, M, is the same as the full-space potential (Equation 2.17). This has resistivity, ρ_1, and current, I. The other is from the image source, M*, caused by the reflection in the bounding plane (resistivity is the same, current equals I*) (Keller and Frischknecht, 1966):

$$V(P_1) = \frac{\rho_1 I}{4\pi r_1} + \frac{\rho_1 I^*}{4\pi r_2} \qquad \textit{Equation 2.18}$$

The potential above the bounding plane, $V(P_2)$, is due to the primary current source but obscured by the bounding plane with intensity I** (Telford et al., 1990):

$$V(P_2) = \frac{\rho_2 I^{**}}{4\pi r_3} \qquad \textit{Equation 2.19}$$

The potentials on at the bounding plane must uphold the first condition. Therefore, $V(P_3)$ equals $V(P_1)$ which must equal $V(P_2)$. The distance from the source and image source, r_1, r_2 and r_3, to the bounding plane are equal and simplify to (Keller and Frischknecht, 1966):

$$V(P_3) = \frac{\rho_1 I}{4\pi r_1} + \frac{\rho_1 I^*}{4\pi r_2} = \frac{\rho_2 I^{**}}{4\pi r_3} \rightarrow \rho_1 I + \rho_1 I^* = \rho_2 I^{**} \qquad \textit{Equation 2.20}$$

The second boundary condition must also hold, therefore the component normal to the bounding plane of current density vector, **J**, for both $V(P_1)$ and $V(P_2)$ must be equal (current density is related to potential via

Ohm's Law, Equation 2.13). $V(P_1)$ has two components, one from the primary source and the other from the image source. $V(P_2)$ has the direct component only.

Keller and Frischknecht (1966) expand on the normal component of, **J**, however the second condition can be summarised to the following expression due to the distance r_1, r_2 and r_3 being equal at the bounding plane:

$$I^{**} = I + I^{*} \qquad \textit{Equation 2.21}$$

The optics analogy treats the bounding plane as a semi-opaque mirror with a reflection coefficient K and a transmission coefficient of 1 – K (Giancoli, 1991). From Equations 2.20 and 2.21, these coefficients can be derived in terms of the resistivities of the media separated by the bounding plane (Telford et al., 1990):

Substituting 2.21 into 2.20 gives, $I^{*} = \frac{\rho_2 - \rho_1}{\rho_2 + \rho_1} I = KI$ *Equation 2.22*

Hence the reflection coefficient, $K = \frac{\rho_2 - \rho_1}{\rho_2 + \rho_1}$

I** can be eliminated by substituting Equation 2.22 into 2.21 and deriving I** in terms of the transmission coefficient, 1 – K, and total current, I, (Keller and Frischknecht, 1966):

$$I^{**} = I + IK = (1 - K)I \qquad \textit{Equation 2.23}$$

By substituting Equation 2.23 into to the respective equations for $V(P_1)$ and $V(P_2)$, these potentials can now be expressed in terms of the total current, I.

The validity of the method of images has been established. The potential, $V(P_3)$, at the surface of a semi-infinite half-space with a buried source electrode can be defined in terms of the earth resistivity and the total current and the distance, r, from M to P_3 (Equation 2.20, Figure 2.2):

$$V(P_3) = \frac{\rho_1 I}{4\pi r} + \frac{\rho_1 K I}{4\pi r}$$

As the resistivity of the air, ρ_2, tends to ∞, the reflection coefficient tends to 1, and the potential on the surface of the half-space can be reduced to:

$$V(P_3) = 2 * \frac{\rho_1 I}{4\pi r} \qquad \textit{Equation 2.24}$$

This gives the numerical calculation for surface potentials due to a homogeneous, isotropic half-space, which is used to calculate the Electrode Effect discussed in Section 2.6.

Buried source electrode in a semi-infinite inhomogeneous, isotropic earth

The anomalous response requires another expression in addition to Equation 2.24, in order to distort the equipotentials. Figure 2.1 (right) represents the MALM response due to inhomogeneous ground, which will now be mathematically derived. Laplace's Equation (Equation 2.14) addresses the Earth as a homogeneous ground. This stems from the constant resistivity where the divergence condition must equal zero hence charge, **Q**, does not accumulate (Equation 2.5) (Parasnis, 1986).

However, Equation 2.5 does not equal zero when the Earth has resistivity gradients where charge will accumulate. From Ohm's Law (Equation 2.7) and $\mathbf{E} = -\nabla V$, the divergence of the current density, **J**, must be zero everywhere except at the current source. A second term is required in equation 2.14when the resistivity is not constant (Alfano, 1959):

$$\nabla \cdot \mathbf{J} == -\frac{1}{\rho}\nabla^2 V - \nabla V \cdot \nabla \frac{1}{\rho} = 0\text{, } \textit{rearranges to give,}$$

$$\nabla^2 V == -\rho\left[\nabla \cdot \mathbf{J} + \nabla V \cdot \nabla \frac{1}{\rho}\right] \qquad \textit{Equation 2.25}$$

Equation 2.25 is Poisson's equation, which differs from Laplace's harmonic by the inclusion of the second term, $\nabla V \cdot \nabla \frac{1}{\rho}$, which is the potential contribution from charge accumulations at resistivity variations (Alfano, 1959; Keller and Frischknecht, 1966). Equation 2.25 equals zero when the resistivity is constant (there is no resistivity gradient), hence the second term disappears leaving the first term. The first term is the divergence of the current density vector which is zero.

The solution to Poisson's Equation takes the form of Poisson's Integral (Equation 2.26) via Gauss's Theorem which relates the equality between surface and volume integrals. The total potential, V_{total}, (Equation 2.26) is a function of the distance, *r*, which is the distance from the observation point of V_{total} to the position in the semi-infinite space where equation 2.25 is being calculated. The potential function, V_{total}, is integrated over the volume of the half-space, U, (Keller and Frischknecht, 1966):

$$V_{\text{total}} = \frac{1}{2\pi}\int_U \frac{-\rho\left[\nabla \cdot \mathbf{J} + \nabla V \cdot \nabla \frac{1}{\rho}\right]}{r}\,dU$$

This expands and simplifies with the substitution of $\mathbf{E} = -\nabla V$ to the following;

$$V_{\text{total}} = -\frac{1}{2\pi}\int_U \frac{\rho\nabla \cdot \mathbf{J}}{r}\,dU + \frac{1}{2\pi}\int_U \frac{\mathbf{E} \cdot \nabla \rho}{\rho r}\,dU \qquad \textit{Equation 2.26}$$

The first integral of Equation 2.26 is the potential due to a single current source in a uniform, homogenous half-space with resistivity, ρ. This normal potential is the same as that calculated via the image method in section 2.1.2, Equation 2.24 (Keller and Frischknecht, 1966).

The second integral of Equation 2.26 is the potential due to a charge distribution accumulating at discrete resistivity discontinuities. These discontinuities surfaces occur at the contacts between volumes of isotropic material of constant resistivity. By this definition, the potential contribution to V_{total} due to the second integral can be expressed in terms of the surfaces where these resistivity discontinuities occur. This is further explained by Keller and Frischknecht (1966).

2.2 ANISOTROPY

Thus far, only a homogeneous and isotropic half-space has been considered. The geological medium is more thoroughly defined by expressing Ohm's Law in dyadic (tensorial) form (Li and Pedersen, 1991; Lindell et al., 1993). The effects of electrical anisotropy on the MALM method are not insignificant (Eloranta, 1988; Li and Uren, 1997a), but do complicate the calculations for modelling the electrical potentials about a single point charge. Ohm's Law (Equation 2.7) holds for a linear anisotropic medium, and in Cartesian space Equation 2.7 can be expressed in vector components;

$$\mathbf{E} = \rho \mathbf{J} \Rightarrow \begin{bmatrix} E_x \\ E_y \\ E_z \end{bmatrix} = \begin{bmatrix} \rho_{xx} & \rho_{xy} & \rho_{xz} \\ \rho_{yx} & \rho_{yy} & \rho_{yz} \\ \rho_{zx} & \rho_{zy} & \rho_{zz} \end{bmatrix} \begin{bmatrix} J_x \\ J_y \\ J_z \end{bmatrix} \qquad \textit{Equation 2.27}$$

ρ is defined by the 3 by 3 resistivity tensor matrix in Equation 2.27. In an isotropic case, the diagonal resistivities ρ_{xx}, ρ_{yy}, ρ_{zz} are assumed to be equal, that is;

$$\rho_{isotropic} = \begin{bmatrix} \rho & 0 & 0 \\ 0 & \rho & 0 \\ 0 & 0 & \rho \end{bmatrix}$$

However, when the ground is anisotropic it is assumed that $\rho_{xx} \neq \rho_{yy} \neq \rho_{zz}$ and the resistivity tensor is given by;

$$\rho_{anisotropic} = \begin{bmatrix} \rho_{xx} & 0 & 0 \\ 0 & \rho_{yy} & 0 \\ 0 & 0 & \rho_{zz} \end{bmatrix}$$

This is the minimum number of components required to describe a resistivity tensor in 3D, in this case the tensor axes are parallel to the axes of the 3D space. The full nine component tensor accounts for the dip, azimuth and rotation angles of the anisotropy, but is much more difficult to compute (Li and Uren, 1997a).

The method of images can be used to model anisotropy (Asten, 1974; Lindell et al., 1993), however Eloranta (1988) uses an integral equation method to calculate the anisotropy, but one of the principal axes of the resistivity tensor is parallel to the earth's surface therefore limiting it to a 2D plane. The integral equation method that Li and Uren (1997a) developed allowed for complete arbitrary 3D resistivity tensor in a 3D half-space using all nine components. Li and Uren (1997b) extend this to include a weathered layer.

Although anisotropy could be considered, there are currently no constraints on it at either field site and therefore cannot be integrated into the models. Since modelling the isotropic earth is already non-unique; models requiring more complex parameterisations (i.e. anisotropic earth models) become increasingly hard to justify. Therefore the principle of parsimony advocates the simpler solution of an isotropic earth.

2.3 ARRAY CONFIGURATION – POLE-POLE AND POLE-DIPOLE

The electrode configuration most commonly used in MALM is the pole-pole array (Figure 1.1, p1). This array consists of a current electrode placed in electrical contact with the target conductive body, usually in the subsurface via a drill hole or at an outcrop of the target, if available. A second potential electrode is used to map the electric potential values about the conductive structure. These measurements usually occur at the surface but can be taken in drill holes as well (Bowker, 1991; Leney, 1966; Parasnis, 1967; Pietilä, 1991).

In the pole-pole configuration the earthing for the transmission circuit is made by a distant return current electrode which has a negligible effect on the measurements (Ketola, 1972; Mansinha and Mwenifumbo, 1983). The direction of the return current electrode relative to the survey area has been found to be inconsequential when placed at a distance (Mansinha and Mwenifumbo, 1983). This also holds for the return potential electrode which is also placed at distance.

Eloranta (1985) has shown through modelling that the placement of the buried source electrode within the conductive body has an influence on the surface potentials observed. However, these changes are nominal relative to variations due to resistivity or geometry (Beasley and Ward, 1985).

In most cases the electrical potentials measured are absolute potential, in reference to the distant remote potential electrode. However Ketola (1972) used a potential electrode earthing within the survey area. This gives a "relative" electrical potential which is harder to interpret as opposed to the absolute potential obtained by the configuration in Figure 1.1.

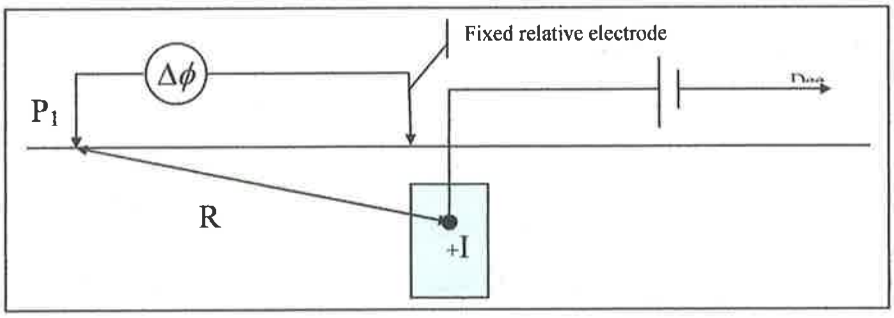

Figure 2.3: "Relative" potential measurement array used by Ketola (1972). The fixed position relative electrode is situated in the survey area. P_1 is moved to map the surface potentials in the survey area.

Alternatively, MALM can be carried out using a pole-dipole array (Figure 2.4) (Snyder and Merkel, 1973; Le Masne and Poirmeur, 1988). In this configuration, the current electrode is placed exactly the same for the pole-pole array, but the potential electrodes are arranged such that they are separated at a constant spacing and the pair are used to survey the area. This configuration measures the potential gradient which is assigned to the midpoint between two potential electrodes.

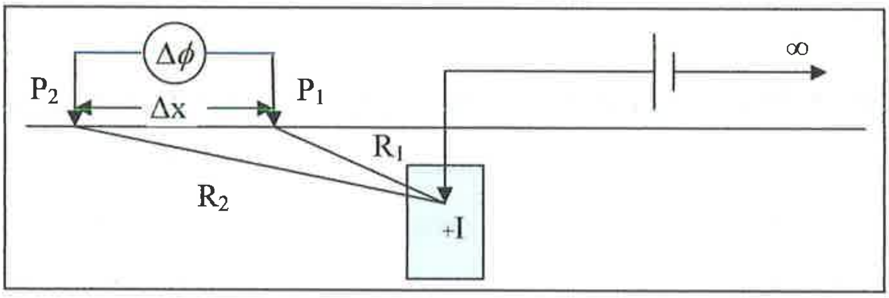

Figure 2.4: Mise-à-la-Masse pole-dipole configuration, I is the current input electrode, P_1 and P_2 are the potential measuring electrodes, R_1 and R_2 are the distances between the two potential electrodes and the current electrodes $\Delta\phi$ is the potential gradient with respect to some distant base station. Δx is the distance between the two potential electrodes. (after Eloranta, 1985)

From Eloranta (1985), the modelling of MALM using the pole-dipole arrangement was effective in discerning the dip of a body and the presence of nearby bodies. However, Eloranta (1985) states that in practice, geological noise from near-surface electrical resistivity heterogeneities overwhelms the anomaly response because the potential gradients are generally small and the results are therefore unreliable. As a consequence the potential anomaly technique (pole-pole) is the most reliable form of MALM anomaly presentation. In terms of field use, once deployed, the pole-pole technique is quicker for routine applications.

In addition to the surface mapping technique used frequently in MALM surveys, 3D techniques are also useful. 3D MALM surveys are an extension of the existing method that can include the potentials derived down boreholes. These cross-hole measurements can establish the continuity or otherwise of the conducting ore (Greenhalgh and Cao, 1998). Case studies (Beasley and Ward, 1986; Bowker, 1991; Parasnis, 1967; Pietilä, 1991; Hattula and Rekola, 2000) exhibit the potential for this form of MALM. Such measurements yield information about a target body and can be used effectively if there is a large number of boreholes in the region.

Near-miss/barren hole scenario

Daniels (1983) states that the MALM method is applicable to mapping resistivity anomalies in an otherwise laterally isotropic setting. In an instance where a drill hole has not intersected mineralisation but has passed very close (a near-miss scenario) the MALM method can still be of use. Whilst it is not common practice, the use of non-intersecting/barren drill holes for MALM can yield information on the conductive mineralisation. Despite not being in electrical contact, a near-miss electrode position still energises the conductive body such that it produces an anomalous surface potential response. Beasley and Ward (1986) and Greenhalgh and

Cao (1998) investigated via modelling the effects of the source electrode positioned near the body but isolated from it. Li and Uren (1997a) identified the effects of anisotropy on a near-miss electrode response.

In general, increasing the distance between the source electrode and the conductive body results in a decrease in the anomalous response, reverting to a homogeneous pattern of equipotentials at large separations (Figure 2.1). Beasley and Ward (1986) suggested that a near-miss scenario shares similar traits to the in-body situation for horizontal or shallowly dipping conductor. Also the results are similar for a horizontal or near horizontal conductor, when the near-miss electrode is above or below the body. However this changes for a steeply dipping conductive structure (Beasley and Ward, 1986). Bowker (1987) used the near-miss arrangement of the MALM source electrode to measure a bulk host-rock resistivity.

2.4 COMPUTER MODELLING

The literature pertaining to electrical potential modelling includes forward calculations and inversion schemes. These various methods can be used to model the MALM/applied potential method, each with its advantages and disadvantages. The main methods include;

Finite Difference Method (FDM) (Greenhalgh and Cao, 1998);

Finite Element Method (FEM) (Zhou and Greenhalgh, 2001);

Integral Equation Method (IEM) (Eloranta, 1984; Oppliger, 1984; Soininen, 1987).

Other approaches have used DC alpha centres (Wang et al., 1991) and conjugate gradients (Ellis and Oldenburg, 1994). It is interesting to note that with increased computational facilities over time there is a change in approach, allowing full 3D methods to be employed to 3D datasets. However, at present, even the most modern of desktop workstations are unable to model or invert complex 3D structure in realistic times.

Algorithms from other potential field methods are also applicable to mathematically model applied electrical potential scenarios. There are algorithms which side-step the time-consuming modelling approach by implementing a computationally less intensive method of imaging the subsurface. This takes the form of approximations; such an approach has been adopted by Hämmann et al. (1997), Di Maio and Patella (1994) and Patella (1997) for use with Self-Potential anomalies, but is equally applicable to applied potential scenarios. The algorithm is based on the assumption that a surface potential signal can represent the subsurface unambiguously through the superposition of multiple elementary sources and pattern matching.

2.5 MALM ELECTRICAL POTENTIAL RESPONSES

Resistivity contrasts

MALM anomalies are a result of resistivity contrasts within the earth, between the conducting body and host rock. The greater the contrast between the resistivity of the body and the medium surrounding it, the larger the anomaly (Beasley and Ward, 1986). An inhomogeneous medium also generates a distorted response (Bowker, 1987). In these cases, the peaks shift towards the medium of greater resistivity rather than being centred over the mass.

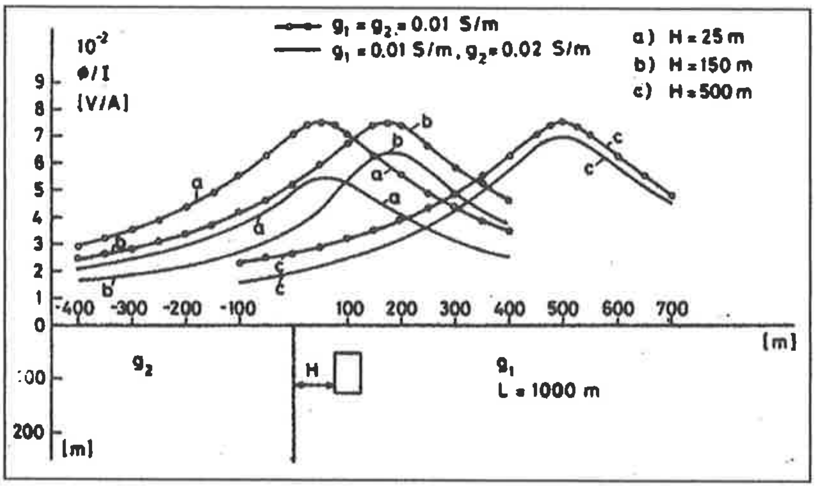

Figure 2.5: The effect of variation in the distance of the conductive body from the vertical contact. In one set of models there is no resistivity contrast between the two media. L, is the strike extent of the body. Another set has a resistivity contrast of 1:2 (g2:g1). (After Eloranta, 1986).

The effect of a conductive body near a vertical contact between two contrasting media was shown by Eloranta (1986). It has also been established that distance of the target from this vertical contact also plays a role in distortion of the equipotentials' epicentre, with the effect of the vertical contact being less evident with increased distance (Figure 2.5). The depth of the body also affects the response seen on the surface with a decay in values and a broadening of the peak. This was also part of further modelling experiments by Eloranta (1986).

Body near vertical structural change

Eloranta (1986) has also shown that inhomogeneities (Figure 2.6) in the earth are more evident if the electrode and body are positioned in the medium of greater resistivity. If $\rho_{\text{medium 1}} < \rho_{\text{medium 2}}$ the potentials generated by a constant resistivity body are greater when the body is in medium 2, so the vertical contact between media will be evident if the electrode and charged body are in medium 1. If the electrode and body were both in the medium of lesser resistivity (i.e. medium 1) then the effect of the inhomogeneity is not as pronounced. With the conductive body in medium 1, there is a substantial shift in the peak values of the surface potential away from the vertical change with increasing resistivity of medium 2.

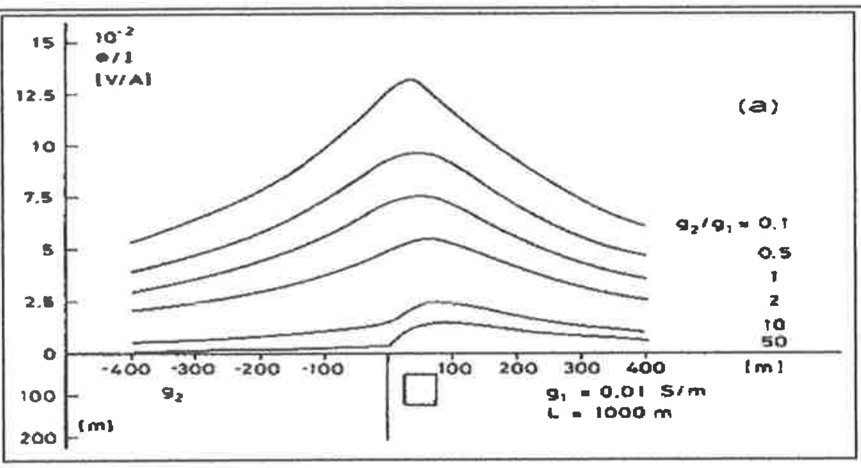

Figure 2.6. Ground surface profiles of Mise-à-la-Masse anomalies as a function of resistivity contrasts g2/g1 between media 1 and 2 separated by a vertical contact. L, is the strike extent of the body. (After Eloranta, 1986)

Depth of conductive body

Depth to the upper surface of a conductive body also plays a significant effect on the broadness of the peaks; with the shallower body depths, the amplitude of the anomaly increases (Bowker, 1987; Le Masne and Poirmeur, 1988). Ambiguity arises when changes in anomaly amplitude due to depth are compared with those changes due to anomaly volume. Eloranta (1986) observed that with a decreased amplitude of the anomaly, other influences will affect its surface expression. Deeper conducting bodies are more prone to interference from near-surface resistivity contrasts. In particular an overlying conductor of equal or proportionate resistivity (such as a regolith layer) can have the effect of damping or masking the effect of the charged mass (Bowker 1991; Eskola and Hongisto, 1981).

Dip of conductive body

The effect of a dipping conductive body is also important. With increasing dip, the largest potential would be centred above the upper surface of a conductor: this implies that in a mass with a high conductivity contrast, the peaks will shift up-dip of the centre of mass although the intensity of the anomaly is reduced (Eloranta, 1986). Once the dip of the body is greater than 45 degrees, the anomaly appears on the surface as a vertical body (Beasley and Ward, 1986). Dip angles below 45 degrees trend towards the anomaly of a horizontal conductive body.

Volume of conductive body

The volume of the conductive body has been shown through modelling (Eloranta, 1986) to affect the response of the surface potentials. These are, in turn, affected by resistivity discontinuities such as the vertical contact in Eloranta's models (1986), as shown in Figure 2.7. Curves on the left of the figure represent the potential response without a vertical resistivity contrast and those on the right are with a resistivity ratio of five to one. Different curves are due to the changes in volume through the parameter H. With increasing volume there is a decrease in the intensity of the response. The vertical contact has the effect of introducing an asymmetry to the curves as well as a peak value change compared to the uniform half-space model. The decrease in peak potentials are also echoed in vertical profiles taken at x = -50 metres.

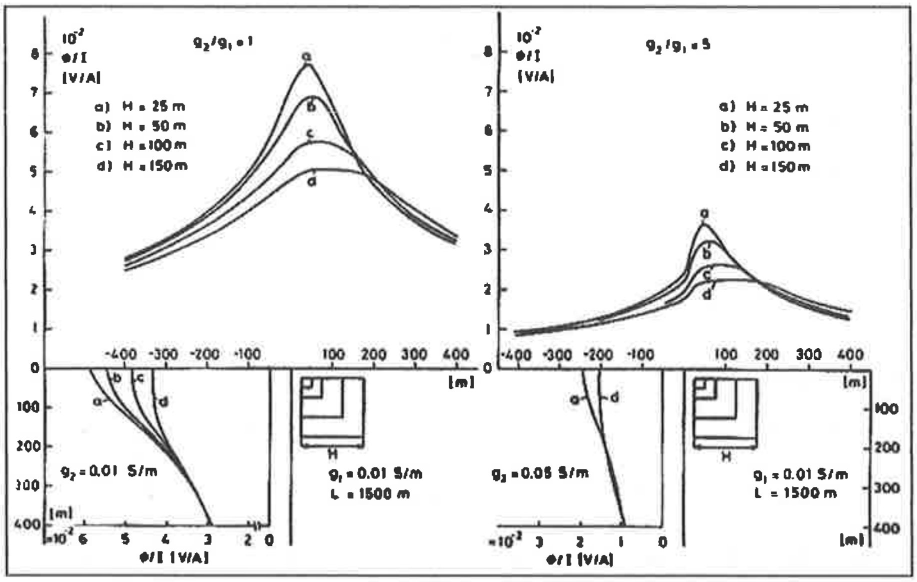

Figure 2.7. Variations in volume of the conductive body. Depth of the upper surface and distance from the contact vertical contact is fixed. Vertical profile anomalies produced at x = -50 m in the lower part of the figure. (After Eloranta, 1986).

Two bodies

Multiple conductive bodies in close proximity to the target body are hard to distinguish from the anomalous effect generated by a single charged body. This is especially true when the charged target is the shallowest conductive structure (Eloranta, 1985). If a source electrode is placed in the lower conductor, the uncharged body is observed as an perturbation in the surface potentials of the charged body. An overlying body adds to the anomalous effect, as seen in Eskola and Hongisto (1981). Faulting of a conductive body will cause a discontinuity of the body, thus generating multiple bodies. Bowker (1991) suggests that a fault plane favours a preferential current follow which electrically links and energises multiple bodies from one current source.

Topography

Topography variations can also affect the results of the MALM method as the current flow is parallel to the air/earth boundary (Fox et al., 1980; Telford et al., 1990). At topographical highs, the current flow lines are dispersed resulting in current density lows at hills. The opposite phenomena occur at topographical lows with the current flow lines converging in valleys (Telford et al., 1990). The potential field is distorted due to these changes of the current flow patterns. However, for cases where the surface relief gradients are less than 10 degrees, the effect of terrain on potentials and apparent resistivity is said to be insignificant (Fox et al., 1980). Potential/resistivity modelling can be used to correct for terrain and reduce the topography to a flat earth model (Oppliger, 1984; Spiegel et al., 1980). However, for the topography at Golden Grove and Prominent Hill do not warrant corrections to the MALM data, as any terrain effects would be inconsequential due to low surface relief.

2.6 ELECTRODE EFFECT AND BASIS FOR REMOVAL

Forward models of a layered earth model can be used to calculate apparent resistivities and subtracted them from observed field data (Daniels, 1983). The resultant residual apparent resistivity values served the purpose of accentuating the spatial extent of the anomalies. However, Eloranta (1985) states that using apparent resistivity data for MALM is not as reliable as absolute electrical potentials for positioning the body.

Daniels' (1983) residual apparent resistivity calculation is complicated by the use of multiple layers to represent horizontal strata. Whilst this can represent many geologic terrains, it is not valid for highly deformed geologies, especially those at Golden Grove where the geology has be deformed to a near vertical orientation (Frater, 1983). However it maybe applicable to the modelling/removal of the thick regolith mantle that covers the Golden Grove and Prominent Hill deposit, assuming that the layer is horizontal and is of constant thickness.

This study simplifies this process further by removing the potential of a buried source electrode from the surface potential data of the MALM method. From Equation 2.26, the first integral is the potential contribution at the point of measurement, of a buried source electrode.

$$V_{\text{total}} = -\frac{1}{2\pi}\int_U \frac{\rho\nabla\cdot\mathbf{J}}{r}dU + \frac{1}{2\pi}\int_U \frac{\mathbf{E}\cdot\nabla\rho}{\rho r}dU \qquad \textit{Equation 2.26}$$

By subtracting the effect of the first integral, the "residual" potentials will be that of the second integral in Equation 2.26, the potential contribution due to resistivity changes within the subsurface. Rather than using integration to calculate the potential contribution from the source electrode, the calculation can be performed numerically and simply, by using the principle of images in Equation 2.24. This equation is the electrical potential due to a buried source and its image in a semi-infinite homogeneous, isotropic half-space.

$$V_{\text{total}} - 2\left(\frac{\rho I}{4\pi r}\right) = \frac{1}{2\pi}\int_U \frac{\mathbf{E}\cdot\nabla\rho}{\rho r}dU \qquad \textit{Equation 2.28}$$

This method is coined the Electrode Effect Removal (EER) (Equation 2.28). In theory, the residual potential distribution is produced by the inhomogeneities within the subsurface, including the regolith. This distribution is therefore reflective of the geology of the survey area.

2.7 REGOLITH

Taylor and Eggleton (2001) describe in great detail the various regolith scenarios and morphologies that can occur. Regolith profiles can be separated into *in situ* weathered materials and transported weathered materials. *In situ* weathering profiles are initially caused by the physical process of mechanical weathering (i.e. abrasion, erosion, diurnal expansion and contraction). Such weathering leads to fissures and openings for chemical processes to occur as groundwater solutes penetrate the profile. A transported regolith profile is due to the weathering and transportation of material from its place of origin via physical processes such as colluvial, alluvial, aeolian or glacial weathering. Such material can then be deposited over an *in situ* profile and sometimes may be indistinguishable from it. These profiles are labelled polygenetic weathering profiles (Taylor and Eggleton, 2001).

A typical regolith profile (Figure 2.8) consists of three basic units: fresh rock, saprolith and pedolith. These can be further broken into sub categories. Nomenclature for these subcategories is dependent on an author's interpretation of the profile (Taylor and Eggleton, 2001).

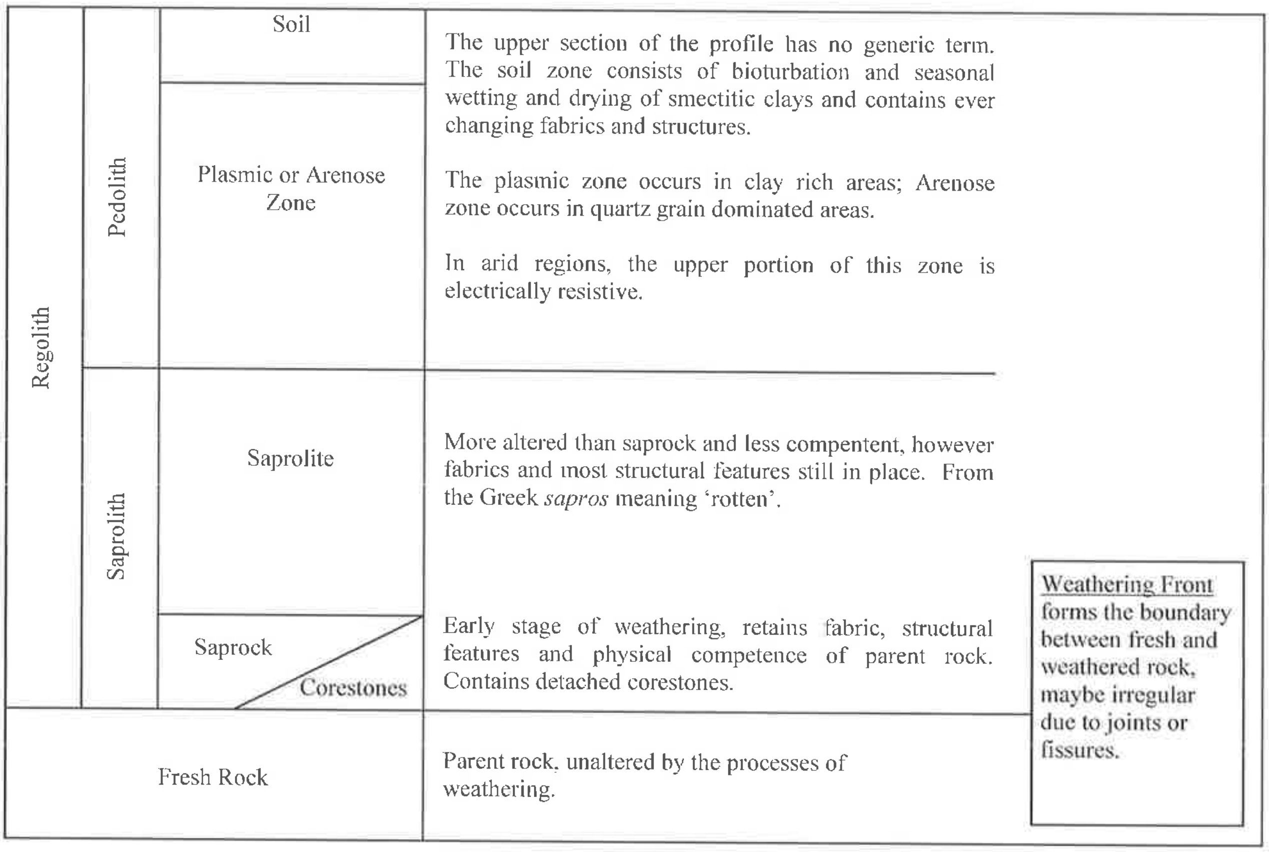

The upper section of the profile has no generic term. The soil zone consists of bioturbation and seasonal wetting and drying of smectitic clays and contains ever changing fabrics and structures.

The plasmic zone occurs in clay rich areas; Arenose zone occurs in quartz grain dominated areas.

In arid regions, the upper portion of this zone is electrically resistive.

More altered than saprock and less compentent, however fabrics and most structural features still in place. From the Greek *sapros* meaning 'rotten'.

Early stage of weathering, retains fabric, structural features and physical competence of parent rock. Contains detached corestones.

Parent rock, unaltered by the processes of weathering.

Weathering Front forms the boundary between fresh and weathered rock, maybe irregular due to joints or fissures.

Figure 2.8: General terms used to describe regolith units and the properties associated with those units (Taylor and Eggleton, 2001).

Weathering of sulphides acidifies the groundwater making it more reactive with the surrounding rocks hence increasing the rate of chemical weathering (Taylor and Eggleton, 2001). This scenario is prevalent at both Golden Grove, Western Australia and Prominent Hill, South Australia. Resistivity variations in the regolith can be caused by groundwater saturation and salinity since the weathered layer is highly porous and permeable (Emerson et al., 2000; Taylor and Eggleton, 2001).

An insight from these generalised regolith profiles indicate there can be rapid changes in regolith morphology within a small area, implying the regolith is far from a uniform layer as it is usually modelled (Merkel, 1971; Daniels, 1983).

Doyle (1981) summarises some of the effects of a deep, conducting, weathered layer on geophysical methods: those applicable to electrical or electromagnetic surveying are listed below:

- Overall depth to target is increased due to regolith layer compared to unweathered terrains; this reduces the amplitude of an anomalous signal;
- Targets are electrically screened by the regolith as current concentrates in the conductive surface layer; this lowers the anomalous amplitude response;
- Conversely, if the target is electrically connected to the regolith layer, current is channelled into the target, increasing the target anomaly (Webster, 1981);
- False electrical anomalies arise as a result of variation in thickness or electrical resistivity within the overburden, since the weathering front is conductive and highly variable in depth (Butt, 1981).

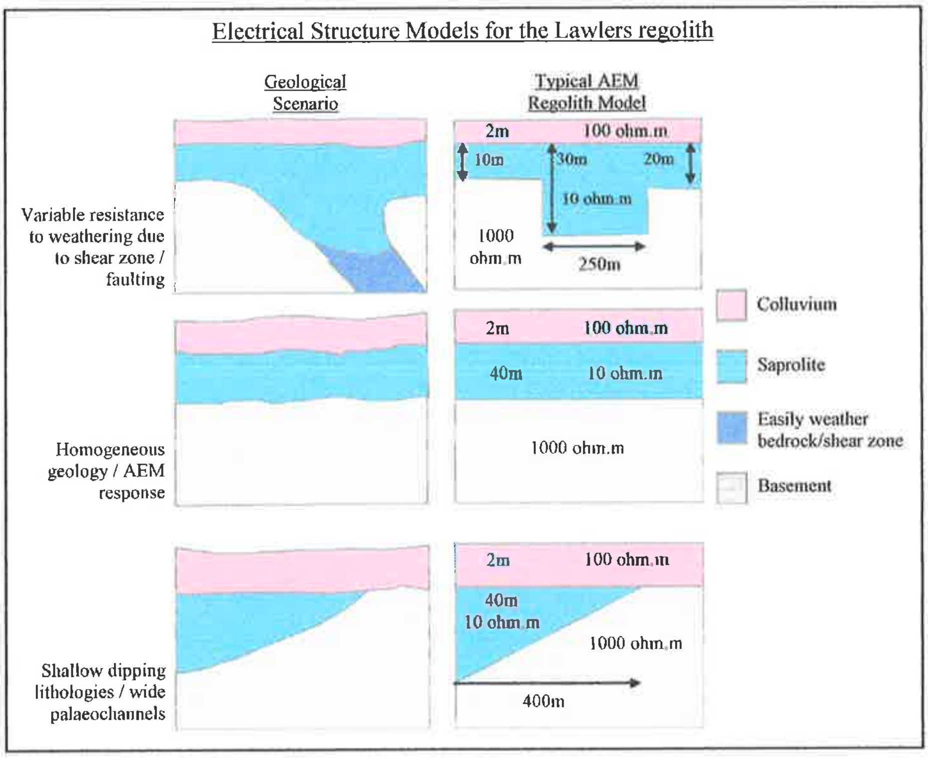

Figure 2.9: Some of the electrical models that describe near surface regolith geology in the Lawlers district, WA. Macnae et al. (2001) have attributed localised AEM regolith anomalies to these models and others (after Macnae et al., 2001).

Bishop et al. (2001) define typical resistivity values and thickness for the regolith units in the Lawlers district of Western Australia. The study found that airborne electromagnetic (AEM) data resolved three distinct layers in the regolith, as opposed to the six layers observed in pit exposures and drill holes. The three layers seen in the AEM models were reclassified as a thin resistive colluvium, a conductive saprolite and resistive basement.

Macnae et al. (2001) proposed models based on simplified electrical structures using these three layers. The models included a homogeneous regolith, a wedging model, a palaeochannel and a variable resistance to weathering models (Figure 2.9). Macnae et al. (2001) concluded that a number of simple regolith structures can cause local AEM anomalies with short spatial wavelengths. Modelling of these structures (Figure 2.9) has resulted in responses qualitatively similar to AEM profiles. It appears that a detectable regolith response comes from structures that exceed 100 metres in width. These models were simulated in this study to examine their effects on electrical potentials and the surface potentials of the MALM method (regolith modelling, p50).

The methods used in this investigation can be broken down into two main parts, a theoretical section and a field procedure section. A variety of theoretical and numerical techniques have been utilised to investigate the maximum benefit of the MALM method. These mathematical procedures have been used prior to data collection, in order to anticipate a probable MALM response (Prominent Hill, SA). The procedures have also been used subsequent to data collection as a means of enhancing the data acquired, and evaluating it quantitatively (both field sites). The field methods were carried out in a consistent manner between surveys and between field sites to minimise uncertainties caused by non-systematic field procedures.

3.1 THEORETICAL MODELLING/NUMERICAL ANALYSIS

Three primary methods were investigated for use in MALM analysis. These were a 3D FEM forward modelling code (Zhou and Greenhalgh, 2001), a numerical removal of the electrode effect (Telford et al., 1990), and a subsurface approximation algorithm by Hämmann et al. (1997), originally used for SP investigations.

3D Finite element method modelling

The 3D FEM software developed by Zhou and Greenhalgh (2001) served as a means of artificially generating MALM responses. The code allows for the general placement of up to two current and two potential electrodes. In this paper, it was used exclusively in the pole-pole mode of operation, along with simplified computer models of the subsurface that would reflect a surface potential response for a given geological model. In simulating a MALM response, the source electrode was embedded within the half-space, whilst the potential electrodes were placed on the surface/air boundary. The modelling program calculated potentials from a unit current source, hence all results are current normalised. The software has the capability to explore the potentials generated at buried potential electrode locations, a scenario which was not thoroughly explored as the project deals with surface MALM measurements.

The primary aims/uses for the 3D FEM software were to:

- Create idealised models to test the Electrode Effect Removal and Subsurface Approximation code;
- Aid in understanding the regolith response through the use of simple resistivity models; and
- Numerically actualise the MALM response for the specific field sites and electrode positions.

The input for the software creates a 3D matrix of resistivity values. This is defined by the length of the matrix in the X, Y and Z directions as well as the mesh grid spacing which is uniform for each dimension; for example, a 700 by 700 by 700 metre model with a model mesh resolution, ΔX, ΔY, ΔZ, of 50 by 50 by 25 metres. This gives the model space 5488 uniform tetrahedral blocks of dimensions 50 by 50 by 25 metres that can have resistivity values assigned to them by the user. As such, a "stair case" conductor was defined for dipping conductors, whereby the volume of the body is made constant, whilst changing the dip angle of the body/contact. The usable angles of such a stair case conductor are therefore limited by the mesh resolution ΔX, ΔY, ΔZ. Given the number of models generated, the results of each series of FEM models are published immediately after the description of the methodology.

Basic Idealised models

All simple body models were parameterised using the same model space. The model space used was 700 by 700 by 700 metres, with the model mesh being 25 by 25 by 25 metres. The potential electrodes on the surface were placed on a 50 by 50 metre grid. The models for this section were kept simple with a coarse grid in order to accommodate the time and computational resource constraints. According to Zhou and Greenhalgh (2001), when the grid nodes are doubled in each direction, there is a significant increase in computation time and storage requirements. Computation time increases with additional electrode positions. Consistency between each model also simplified comparisons.

Each model took approximately 10 minutes to calculate with this configuration on a 1.58 Ghz Athlon XP PC system, equipped with 512 Mb of RAM. The maximum memory used in each instance was approximately 80 Mb. The relatively quick calculation time with these conservative settings allowed for numerous models to be calculated in quick succession.

The FEM program calculated potentials at every node in the grid, including, the defined electrode positions. This allows the potential field about the model to be observed. The electrodes can be placed anywhere in the 3D model space, but for this study, their positions were limited to the air/earth boundary.

Resistivity Contrast

A conductive body measuring 125 by 400 by 250 metres was centred in the model space (Figure 3.1), at a depth of 100 metres. By systematically changing the resistivity contrast between the conductive body and the homogenous half-space, different surface potential values are observed across the body. The source electrode was placed at the centre of the conductive body, at location 350, 350, 225 metres. Resistivity of the half-space was 1000 ohm.m, whilst the resistivity of the conductive body was modelled with values of 0.1, 1, 10, 100 and 500 ohm.m.

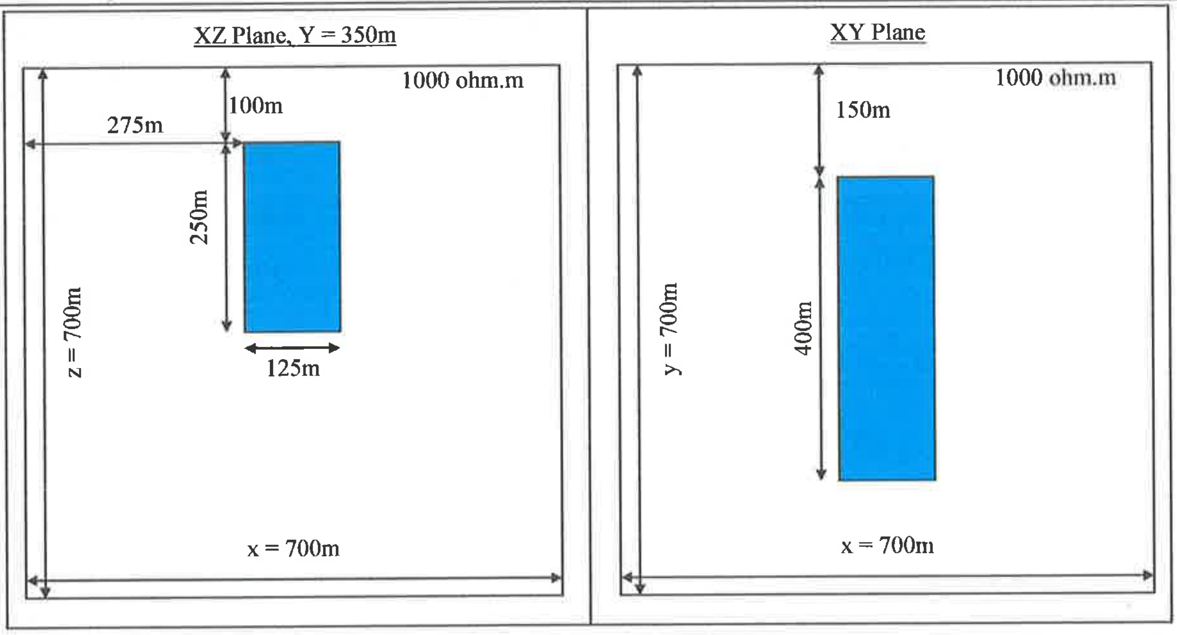

Figure 3.1: The above diagram shows the dimensions for the model space used in the 3D FEM models. The XZ plane (left) is take through the middle of the model at Y = 350 metres and looks to the "north". The XY plane (right), looks down on the model and shows the outline of any explicit feature.

Results:

Figure 3.2 are the profiles associated with the aforementioned resistivity values assigned to the conductive body. The highest potential value attained is when there is the least contrast in resistivities (where the body resistivity equals 500 ohm.m). From Figure 3.2, it is difficult to explain why the surface potential values rise when the resistivity ratio is 10000:1 (host: body). This effect is elucidated by viewing the surface potentials as contour maps. Figure 3.3 shows the potential response changing from a homogeneous response (Figure 2.1) to a distorted anomalous response with increased resistivity contrast.

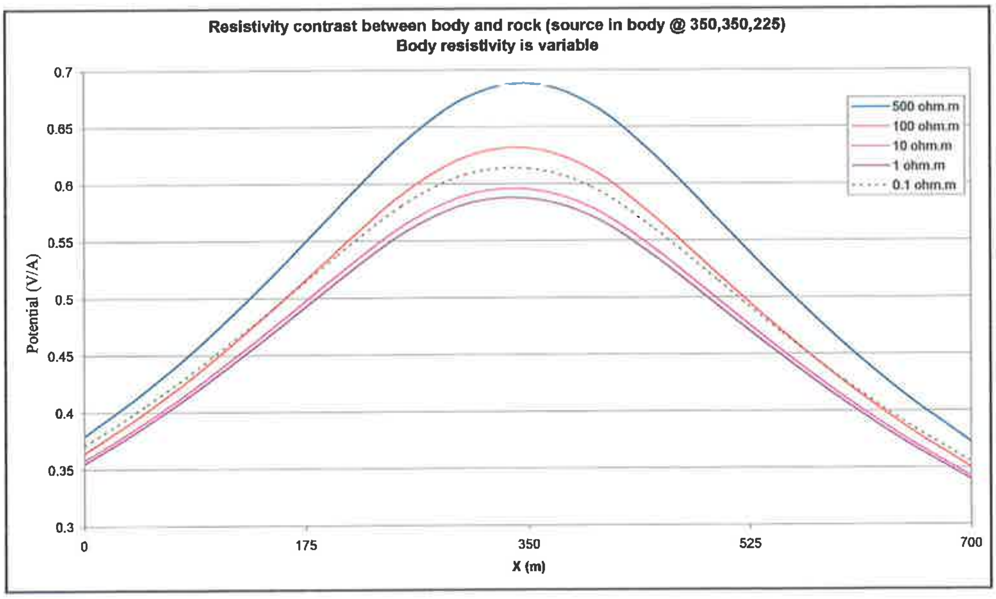

Figure 3.2: The surface potential values at Y = 350m, this shows the ambiguity of MALM if single line profiles are used to map the anomaly. The highest potential values are achieved when the resistivity of the body is 500 ohm.m.

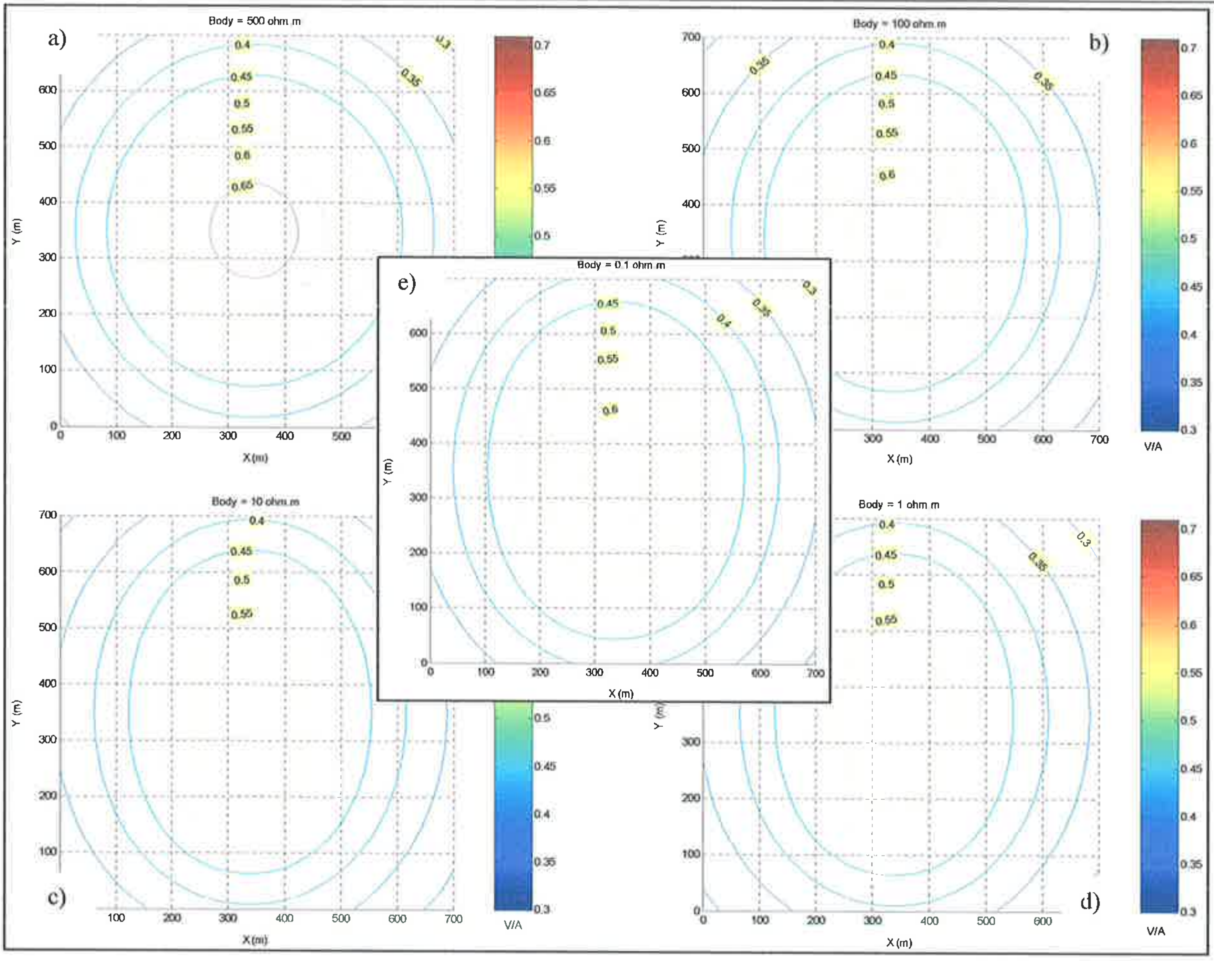

Figure 3.3: Contour maps of the surface potentials, for the resistivity contrast models a) ρ_{body} = 500 ohm.m, b) ρ_{body} = 100 ohm.m, c) ρ_{body} = 10 ohm.m, d) ρ_{body} = 1 ohm.m and e) ρ_{body} = 0.1 ohm.m. Colour scale for each map is the same as for Figure 3.2 (0.3 – 0.7 V/A).

The effect, which is readily evident in Figure 3.3, cannot be easily seen from surface potential profiles along a line; hence care must be taken in looking at line profiles. The change from a homogeneous to anomalous response due to increased resistivity contrast is best summarised in Beasley and Ward (1986). This observation is that, increasing the resistivity contrast results in an increased percentage of the anomalous response relative to the background potentials.

Conductive Body – Depth, Dip and Volume

Effect depth to upper surface of the conductive body

The depth to the upper surface of a target body has a significant impact on the surface potential response. This sequence of models deals with a single body of the same dimensions as the resistivity contrast models (Figure 3.1), centred in the model space with a source electrode placed in the centre of the body. The depth to the upper surface of the body is changed in each model of this sequence. Depths values used for these models are at 25 metre intervals from 75 metres to 425 metres (Figure 3.4). The half-space resistivity is 1000 ohm.m and the conductive body resistivity is 1 ohm.m. The current electrode is in electrical contact with the conductive body at location 350,350,125 metres for the shallowest body.

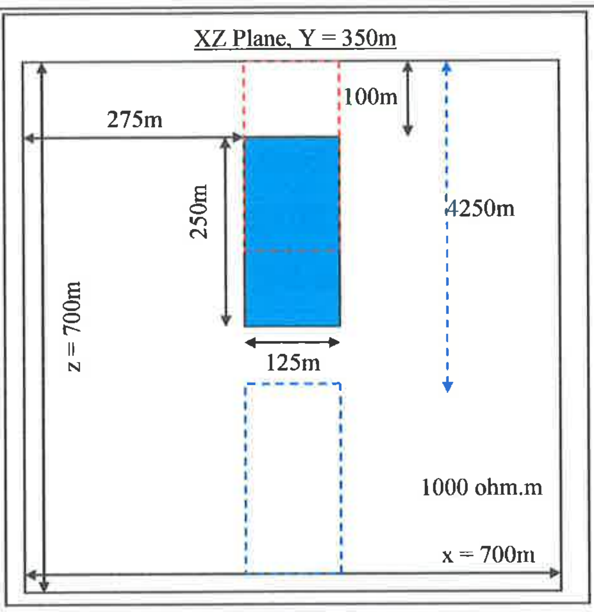

Figure 3.4: The conductive body was placed successively deeper, from 0 metres to 450 metres from the surface. The current electrode was always centred in the conductive body.

Results:

The intensity of the anomaly is decreased with increased depth. The results in Figure 3.5 follow Eloranta's (1986) modelling, although without the influence of the vertical contact modelled by Eloranta. Le Masne and Poimeur (1988) also achieved similar results, and emphasise that the effect is similar to that is seen when the electrode depth is decreased in a homogeneous half-space with no conductive body. The asymmetry of the response is cause by the FEM modelling software through the use of a coarse mesh grid to minimise calculation time

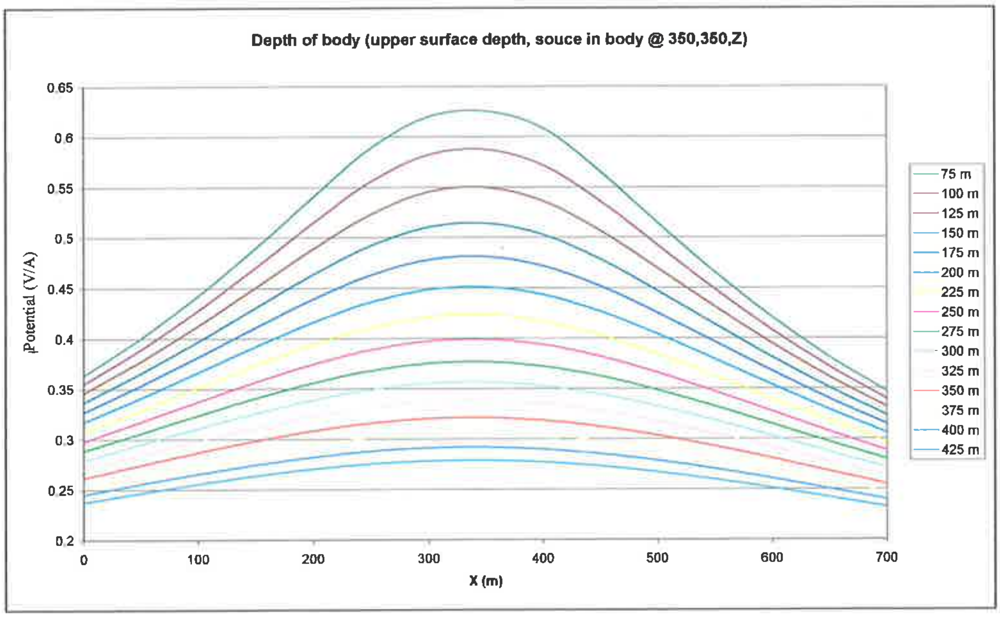

Figure 3.5: As the depth of the increases the body, the anomalous peak blends with the background potentials

Effect of dip of the conductive body

A constant upper surface position allows for similar models to be readily compared. In this case the upper surface was positioned to the right of the volume space. The models began with the same body used thus far, 125 by 400 by 250 metres. With each subsequent model, the dip was changed from a vertical 90 degrees to the following angles, 60, 45 and 30 degrees (Figure 3.6). The half-space resistivity was 1000 ohm.m and the conductive body was 1 ohm.m. The use of a staircase conductor allows the volume to be kept constant. The source electrode was at a depth of 225 metres, with the x-axis position varying with the dip of the body; it was placed 75 metres from the left edge of the body (Table 3-1). The y-axis position was constant at 350 metres.

Dip of conductive body	Electrode position along X-axis
30 degrees	375m
45 degrees	475m
60 degrees	525m
90 degrees	575m

Table 3-1: Electrode positions along the x-axis for the in-mineralisation dipping conductive bodies, at 225m depth and Y=350m.

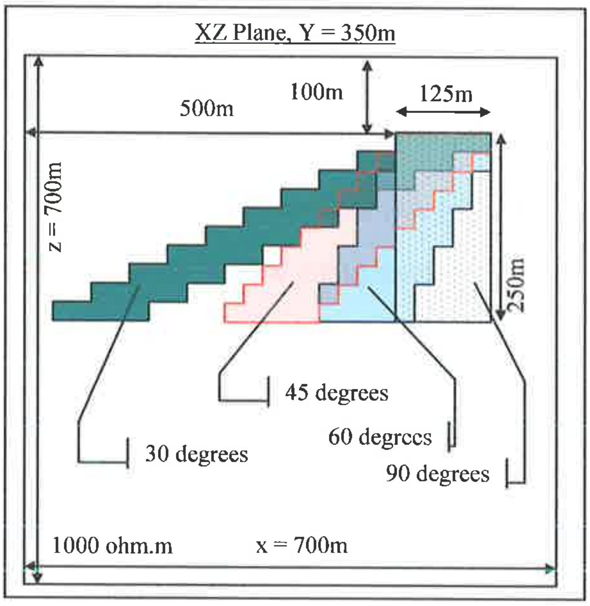

Figure 3.6: The models used in contrast to the vertical body. The dips for the body are as marked, 30, 45 and 60 degrees. The position of upper surface is a constant. The body has a resistivity of 1 ohm.m. All conductive bodies have the same volume.

Results:

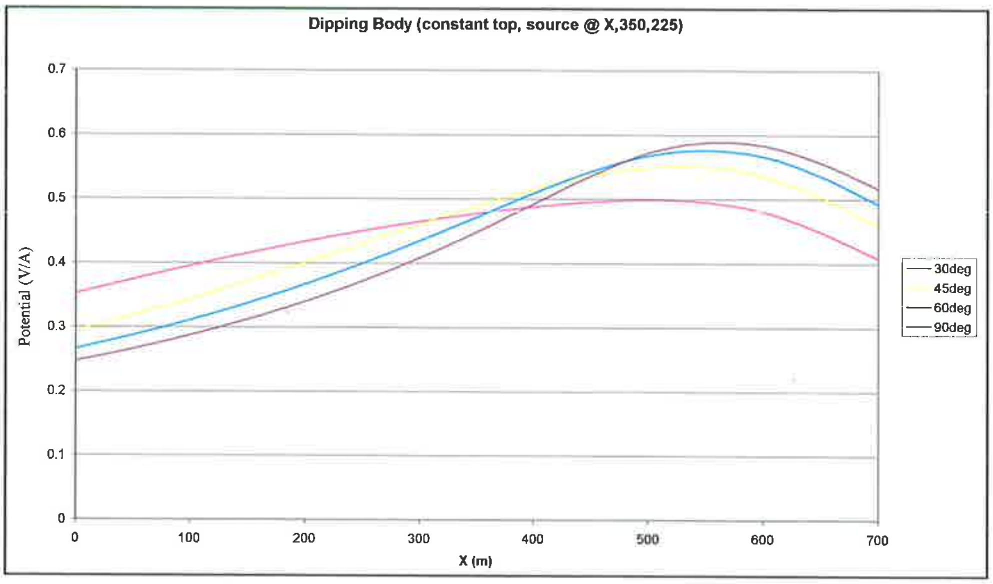

Figure 3.7: 4 models were created with differently dipping conductive bodies. The upper surface of the body was in a constant position.

As found by Eloranta (1986) and Beasley and Ward (1986), the conductive body at angle of 45 degrees and above, have a response similar to a vertical body. With decreasing dip angle, the peak is shifted towards the dip direction, as well as decreased peak anomaly values (Figure 3.7).

Volume change of the conductive body

The change in volume of a body was conducted by using a base model, i.e. the same model as the resistivity contrast of 1 ohm.m to 1000 ohm.m. The resistivities for the half-space and conductive body were the same for all models of this series, that is, 1000 ohm.m for the half-space and 1 ohm.m for the conductive body. The responses due changes in volume were compared to this initial model. The dimensions of the conductive body were only changed in the X and Z directions (Eloranta, 1986) with Y dimension being constrained to 400 metres (Figure 3.8). The Table 3-2 lists the dimensions and the volume in metres cubed.

Model #	X dimension (m)	Y dimension (m)	Z dimension (m)	Volume (m^3)
1	75	400	200	6000000
2	125	400	250	12500000
3	175	400	300	21000000
4	225	400	350	31500000
5	275	400	400	44000000

Table 3-2: Lists the X,Y and Z dimensions, and the corresponding volume for the models investigating changes in volume.

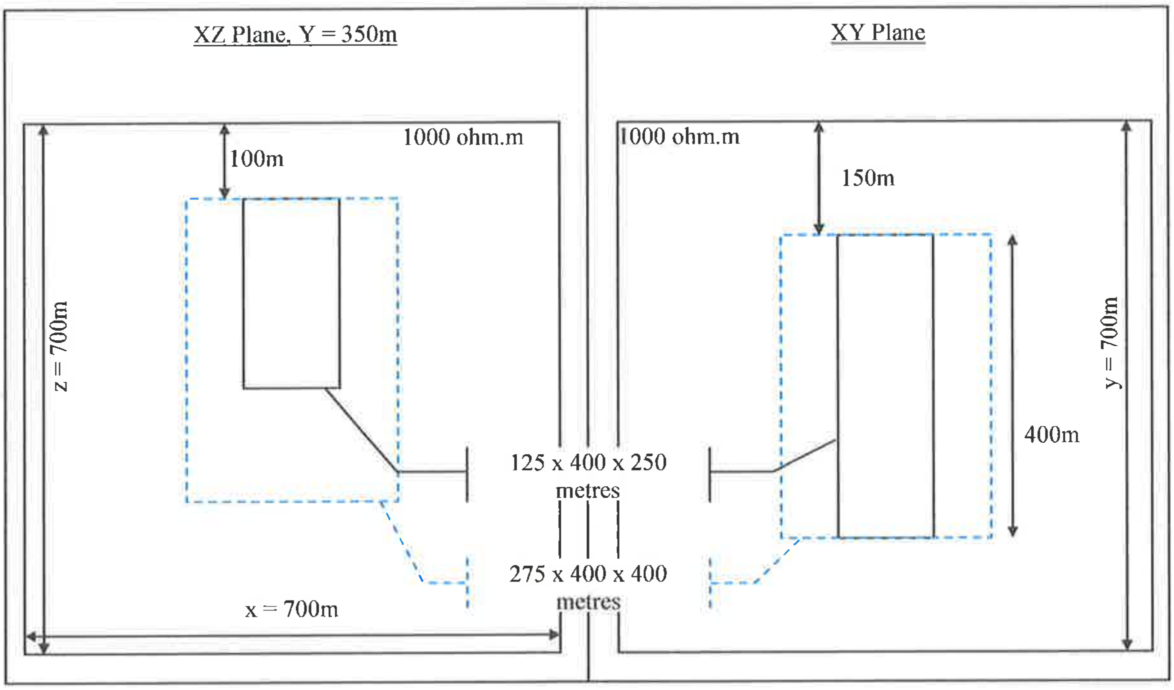

Figure 3.8: The volume of the models was increased by 7 times from the smallest to the largest (blue dashed lines). The solid black outline represents the basis model (model #2). The body has resistivity of 1 ohm.m.

The conductive body was centred in the model half-space with the upper surface depth at a constant 100 metres. The electrode was centred in the body, so whilst the X,Y position does not change, the depth of the electrode is dependent on the size of the body in Z.

Results:

Figure 3.9 concurs with the models of Eloranta (1986). With increased volume of the conductive body, the peak surface potential value decreases. The broadness of the anomaly is a function of the width of the conductive body.

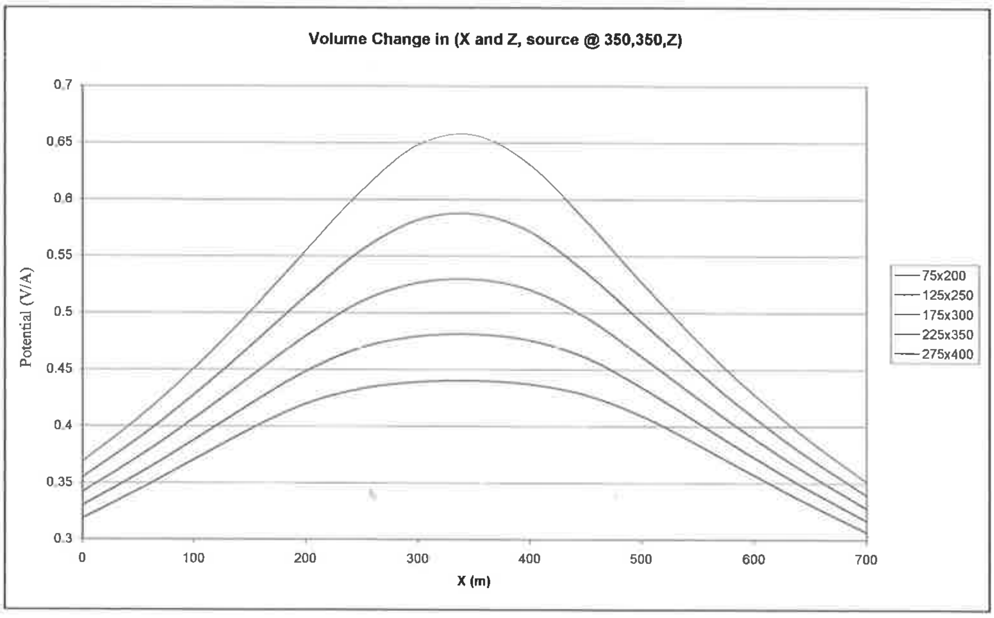

Figure 3.9: Volume change affects the intensity of anomaly. With increasing volume the peak potential response of a body decreases.

Two bodies

There were two series of two body models, one dealing with the depth of the second body and another looking at the separation between the two bodies. All bodies are centred along the Y-axis, therefore the body's edge is 150 metres from the northern boundary of the model. Both bodies have the same dimensions, i.e. 125 by 400 by 250 metres, therefore no volume difference exists between the two bodies to affect the surface potential response. These dimensions are the same as the resistivity contrast series of models and others. In this sequence of models the homogenous half-space had a resistivity of 1000 ohm.m and both conductive bodies had a resistivity of 1 ohm.m.

Depth of second body

One series of two body models had the current electrode in the second body. The first body was placed in the same location as that of the above resistivity contrast models. The second conductive body was placed 75 metres to the right of the first. These models were conducted with the source electrode placed at X,Y positions, 550,350 metres in the second body. The depths for the second body are 100, 150, 200, 250, 300 and 350 metres (Figure 3.10). The depth of the source varied with the second body's depth, at 225, 275, 325, 375, 425 and 475 metres.

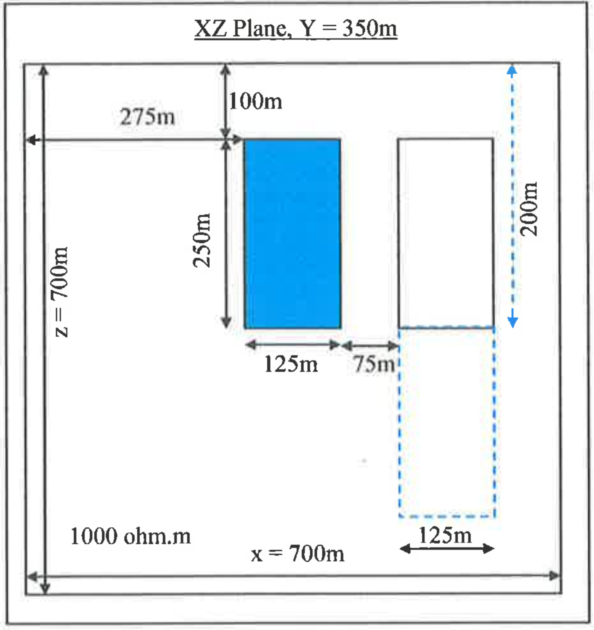

Figure 3.10: This schematic represents the depth models for the two body scenario. The second body (on the right) is moved from 100m (black outline) down to 350m (blue dashed outline). The half-space resistivity is 1000 ohm.m and both bodies have 1 ohm.m resistivities.

Results:

Figure 3.11 is the results of placing the source electrode in the second body which is moved vertically through the model space. Evidence of the first body in the surface potential profiles appears when the top of the second body (and source electrode) is at a depth equal to or greater than that of the top of the first body.

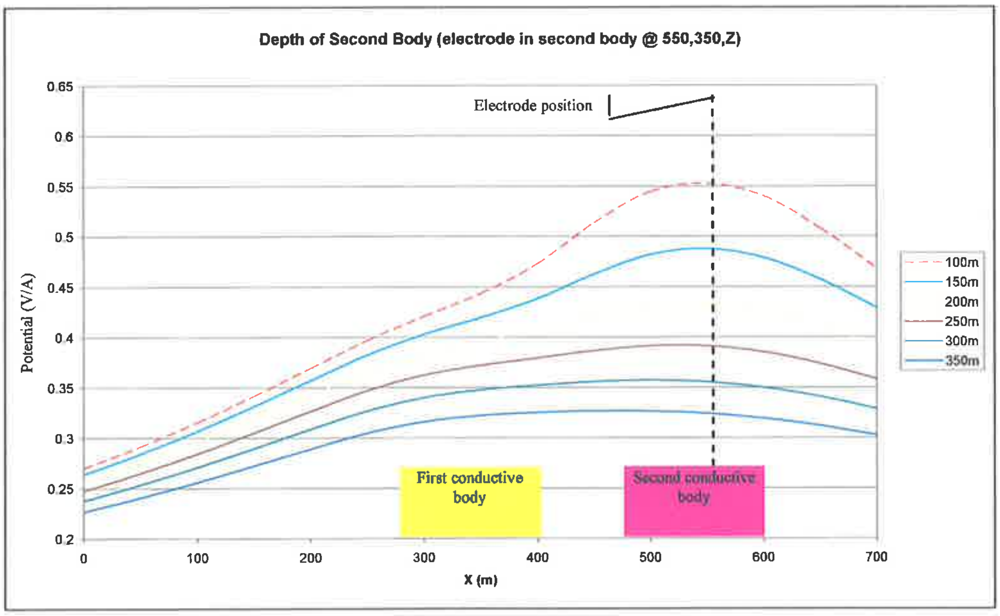

Figure 3.11: Source electrode in 2^{nd} body (550,350,Z). The electrode is kept in the same position within the 2^{nd} body. The 1^{st} body (centre) can be seen as a deflection of the surface potential profile.

Separation of second body

This series of models sees the bodies rearranged slightly (Figure 3.12). The first body is moved to the left to accommodate greater spacings between the two bodies. It is 75 metres from the edge of the model space, but otherwise its dimensions and the depth from the surface remain the same.

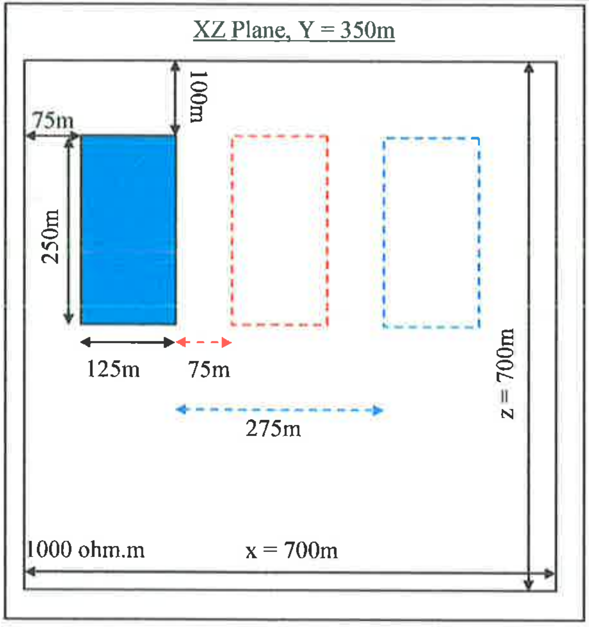

Figure 3.12: Two bodies separated by a variable distance. The first body (blue rectangle) contains the source electrode. The second body (dashed outline) has the same dimensions as the first and is also at the same depth. Both bodies have a resistivity value of 1 ohm.m, the half-space resistivity is 1000 ohm.m.

The source electrode is placed in the first body, at 150,350,225 metres and is kept the same for this series of models. In this scenario, the depth of the second body is kept the same as the first body at 100 metres. The distance between the two bodies was changed for each model, with the separation being 25, 75 125, 175 and 225 metres.

Results:

A second body is less evident in the potential profiles with increased separation from the first body (energised by source electrode, Figure 3.13). The highest peak potentials were observed when the bodies are furthest apart. The asymmetry of the potential profile is greatest when the bodies are closest together.

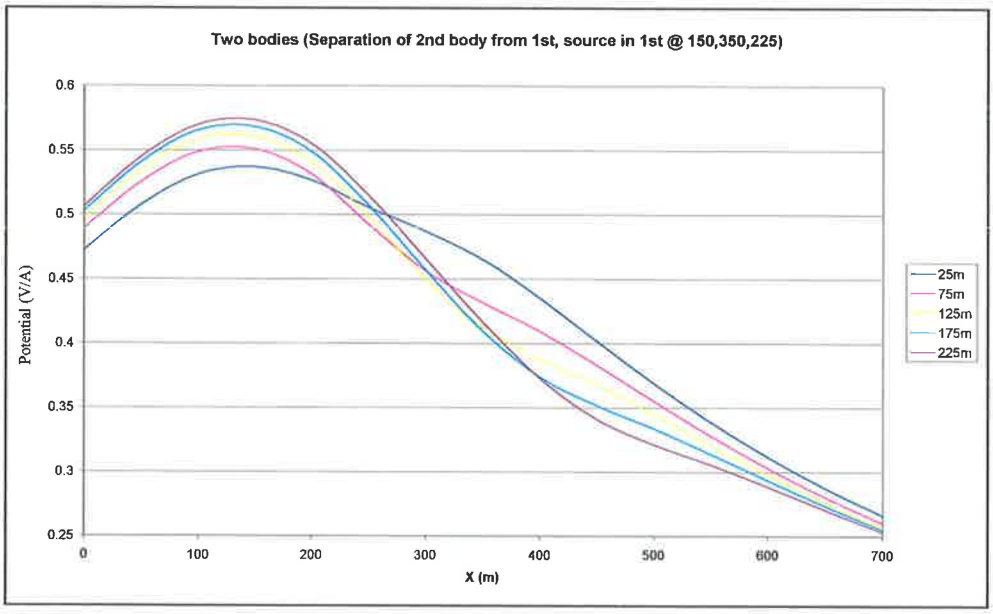

Figure 3.13: With increasing separation between two bodies, the second, non-energised body is less prominent in the surface potential profiles.

Near-miss electrode positions

The near-miss scenario was investigated by placing the source electrode out of contact with the conductive body. These series of models begins with the electrode within the body to show an in-mineralisation response (as seen in the modelling thus far). The source electrode is then placed outside of the conductive body and is placed progressively further from the conductive body with each successive model.

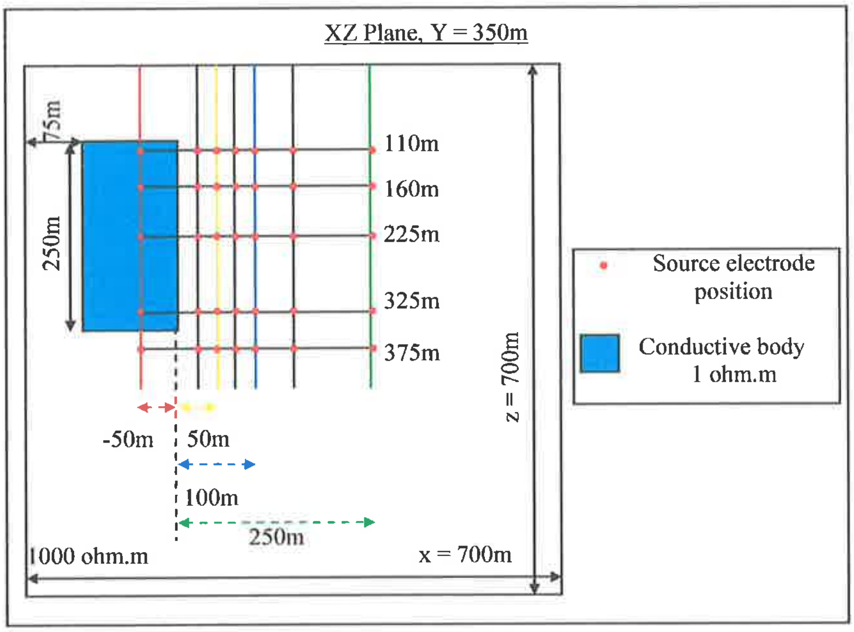

Figure 3.14: Near-miss electrode positions. The source electrode was positioned at depths 110, 160, 225, 325 and 375m. The distance of the electrode from the edge of the body ranged from -50 (in-mineralisation), 25, 50, 75, 100, 150, and 250m.

A conductive body was placed 75 metres from the edge of a half-space of 1000 ohm.m resistivity, 100 metres below the surface. The resistivity of the body was 1 ohm.m and the dimensions are 125 by 400 by 250 metres (Figure 3.14). Of interest is the relationship between the separation of the source electrode from the body and the ratio between the depth of the body and the depth of the source electrode.

A sequence of source electrode positions is used for the models (Figure 3.14). These positions are relative to the right hand edge of the conductive body (situated at x = 200m). The in-mineralisation position is negative 50 metres from the edge of the body (at x = 150m). The near-miss placements are 25, 50, 75, 100, 150, and 250 metres from the edge of the body (x = 225, 250, 275, 300, 350 and 450 metres respectively). These electrode positions were used at five different depths, 110, 160, 225, 325, and 375 metres. For the source electrode at the negative 50 metre position, at 375 metres depth, the source electrode is 25 metres below the lower surface of the conductive body.

Results:

In-mineralisation comparisons

Modelling shows that depth of the source electrode within the conductive body has a small effect on the surface response (Figure 3.15). However, the variations are negligible compared to a near-miss scenario or a resistivity or geometry change (Beasley and Ward, 1985). The near-miss curve for the electrode depth 375 metres shows a similar shape with a lower peak potential, despite missing the body by 25 metres.

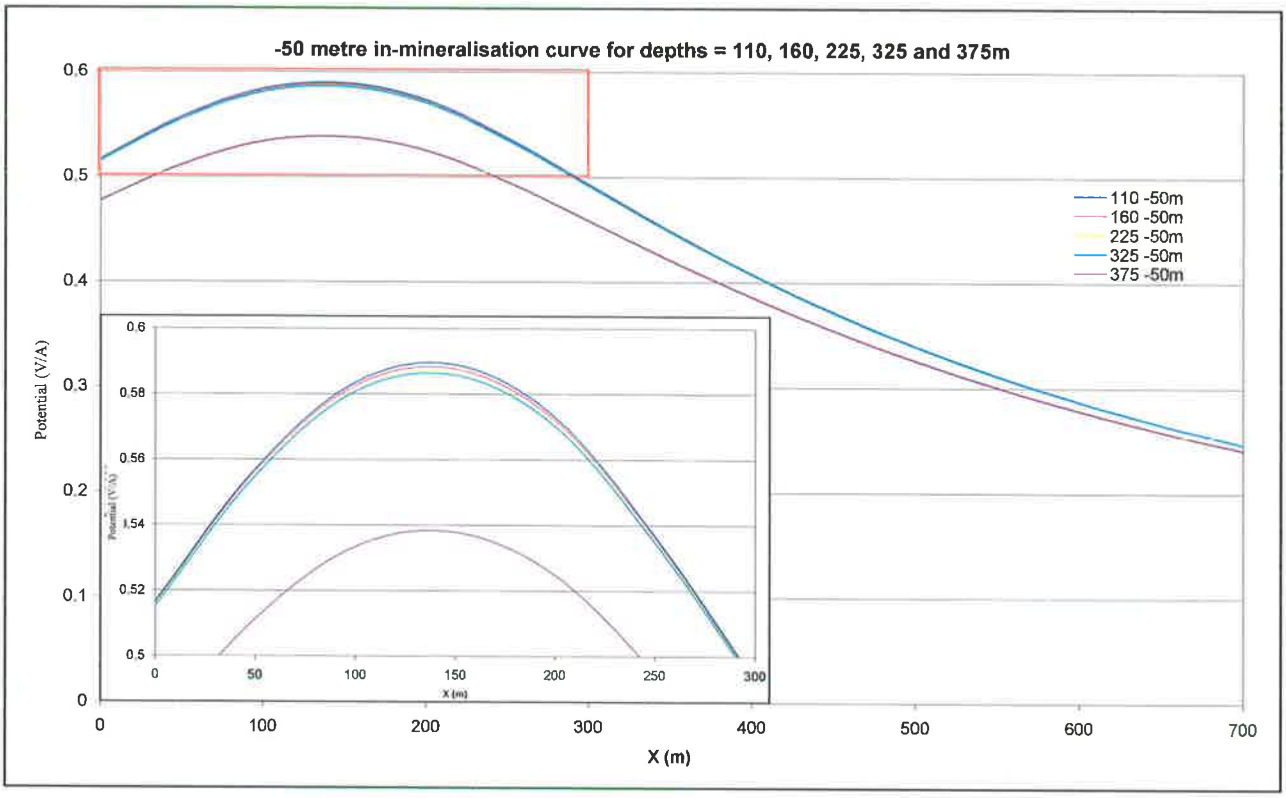

Figure 3.15: In-mineralisation (with electrode at x = 150) curves for the four depths where the source electrode intersects the body and the 375m depth near-miss electrode (out of mineralisation). The curves in the main chart show a minimal variation between the peaks, and the similarity of the curves regardless of electrode depth. The sub chart is of the area bounded by the red box.

Electrode depth 110m:

Results for the electrode placement at a depth of 110 metres (Figure 3.16) shows that the near-miss scenario changes to a homogeneous electrode effect with increased distance. Relative to the deeper electrodes, this change occurs within a short distance from the edge of the body.

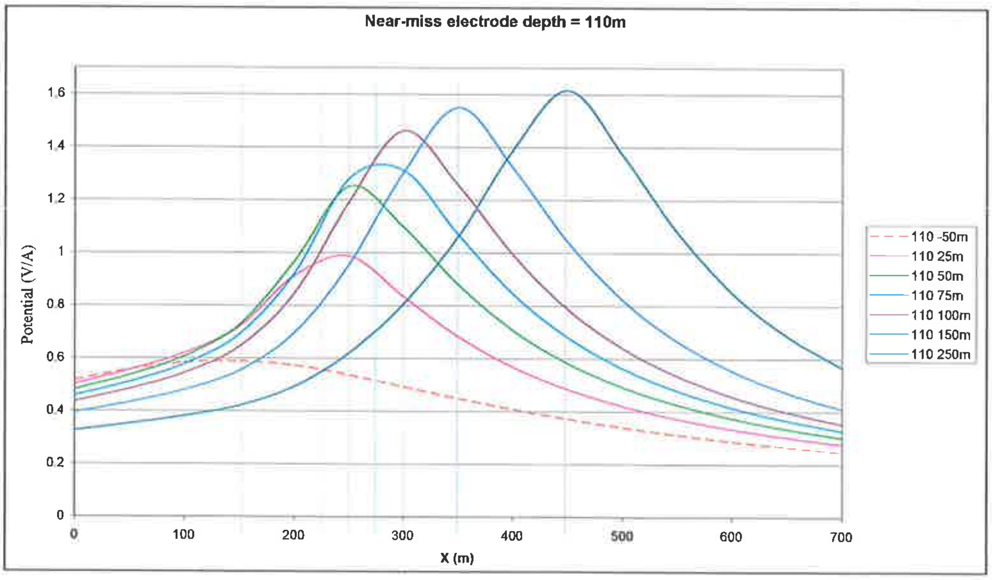

Figure 3.16: Near-miss electrode positions for depth 110m. The in-mineralisation case is very different from the near-miss cases. The peak response increases in amplitude with increased electrode separation from the conductive body.

For the electrode position at 25 metres from the body, the anomaly curve is asymmetrical with the peak not centred over the electrode position (Figure 3.16). 50 metres from the body, the response still slightly asymmetrical but the peak values is high. For distances greater than 50 metres, the amplitude of the homogeneous electrode response increases.

Electrode depth 160m

The amplitude response of the near-miss electrode positions is greater than the in-mineralisation case. For this depth, the affect of the conductive body can be seen as an asymmetry in the near-miss potential curves. This asymmetry can be seen in all curves except for the 150 and 250 metre separations (Figure 3.17).

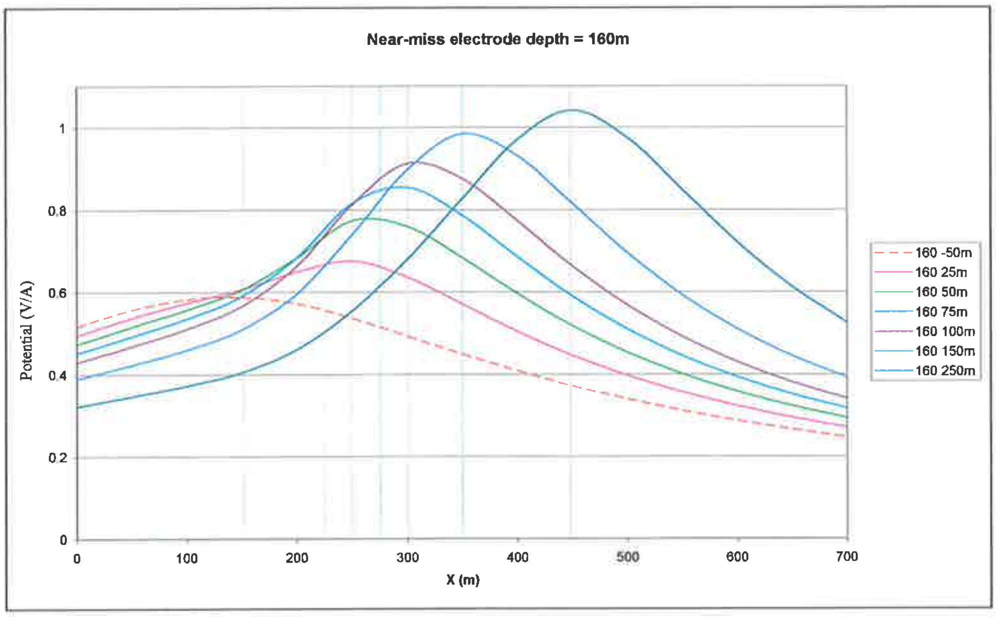

Figure 3.17: Near-miss electrode positions for depth 160m. The near-miss response of the conductive body is evident for greater separations. This can be seen in the asymmetric curves.

Electrode depth 225m

At this depth, asymmetry due to the conductive body is seen in all near-miss electrode positions (Figure 3.18). The peak values for both in-mineralisation and near-miss scenarios are comparatively equal. The electrodes which are closer to the conductive body, at 25, 50, and 75 metres, exhibit the greatest asymmetry in the surface potential curves. The peak response is shifted towards the conductive body for an electrode at 25 metres from the edge of the body.

Electrode depth 325m

The in-mineralisation response for this electrode depth is greater than any of the near-miss responses (Figure 3.19). Asymmetry due to the conductive body is evident in all profiles. The peak values exhibit a shift towards the conductive body for electrode positions less than 75 metres from the body.

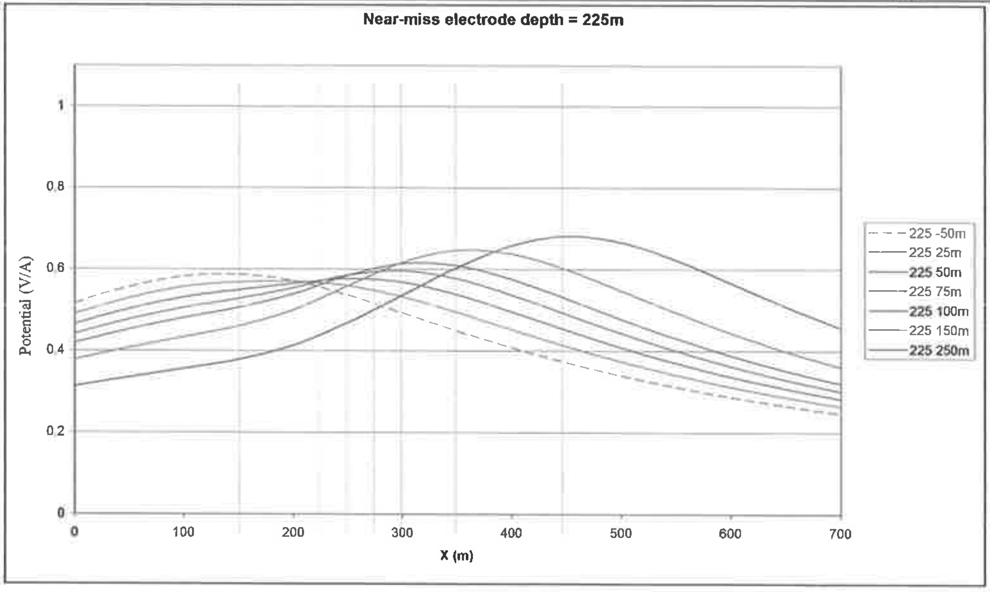

Figure 3.18: Near-miss electrode positions for depth 225m. Asymmetry due to the conductive body is present in all the surface potential profiles.

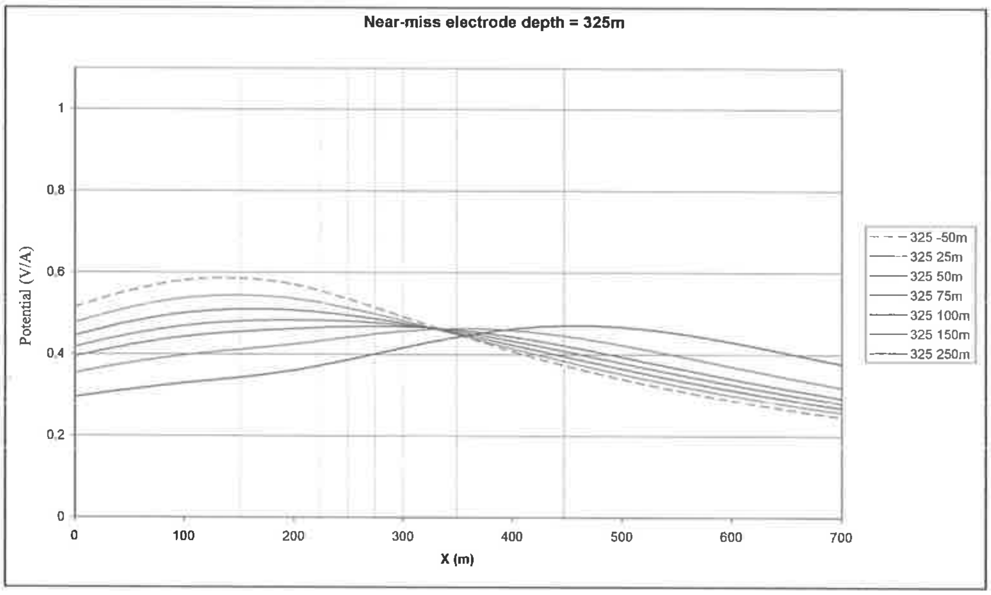

Figure 3.19: Near-miss electrode positions for depth 325m. Asymmetry is seen in all the surface potential profiles for this depth. The peak values for all near-miss electrode positions is subdued compared to the in-mineralisation response.

Electrode depth 375m

For this electrode depth, all positions are near-miss scenarios. The negative 50 metres position is separated from the bottom surface of the conductive body and has the highest peak value. This depth associated near-miss position has a response which is the same as the in-mineralisation cases, the difference being subdued amplitude response. This result agrees with Beasley and Ward (1985). The lateral near-miss positions all show asymmetry in the surface potential profiles. The peaks for electrode positions less than 100 metres shift towards the conductive body and away from the position of the electrode. A deeper electrode position has resulted in a significantly lower near-miss response.

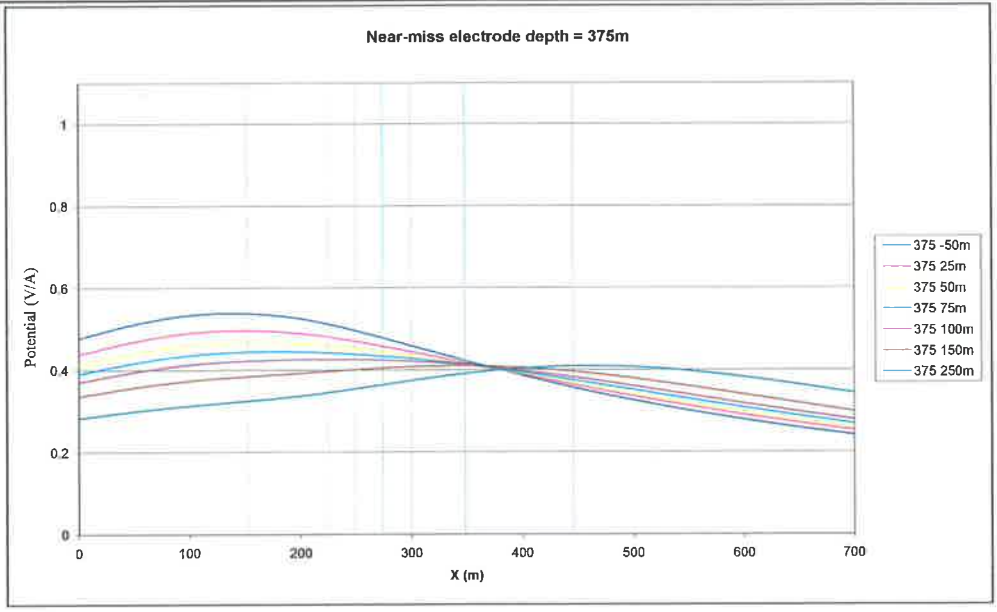

Figure 3.20: Near-miss electrode positions for depth 375m. All electrode positions are near-miss cases. The -50m position is directly beneath the conductive body, separated from the bottom surface by 25m.

Dipping Near-miss models

Using the dipping conductive body models created in the "Effect of dip of the conductive body" (p37), two series of models were examined using near-miss source positions. The conductive body in the models dips towards the west, with source positions to the west of the body defined as shallow near-miss (vertically above the body) and those to the east as deep near-miss positions (vertically below the body) (Figure 3.21). The source electrodes have been placed 50 metres from edge of the conductive body for all dip angles at a depth of 225 metres along the line Y equals 350 metres. Table 3-3 lists the X position of the near-miss electrodes.

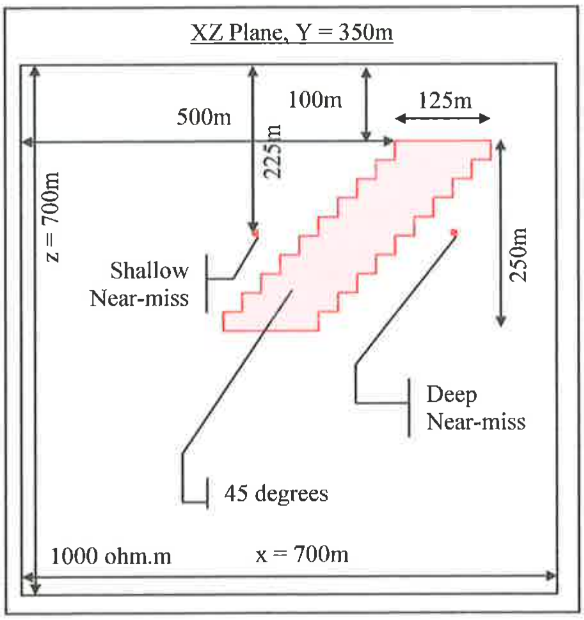

Figure 3.21: Dipping conductive body with near-miss electrode positions. Those positions to the west are shallow near-miss positions as they are above the body. Positions to the east are deep near-misses as they occur below the body. Only the 45 degree dipping conductive body is shown.

Dip of conductive body	Electrode position along X-axis	
	Shallow near-miss	Deep near-miss
30 degrees	250m	475m
45 degrees	350m	575m
60 degrees	400m	625m
90 degrees	450m	675m

Table 3-3: The near-miss electrode position along the x-axis, changes with varying dip. The shallow and deep near-miss positions are 50m from the left and right edge of the body. Depth of the electrode is 225m and Y = 350m.

Results:

The 30 degree dipping conductor acts like a horizontal body. Both the near-miss electrodes have a lower amplitude than the in-mineralisation response (Figure 3.22). There is little to distinguish between the near-miss profiles and the in-mineralisation case.

The 45 degree body has greater disparity between the near-miss cases. The shallower near-miss electrode maximum potential almost equals the peak amplitude of the in-mineralisation profile, but this is offset to the west of the upper surface of the body. The deep near-miss electrode has overall lower amplitudes to the in-mineralisation case and the curve is similar in shape, with the peaks being in approximately the same position (Figure 3.22).

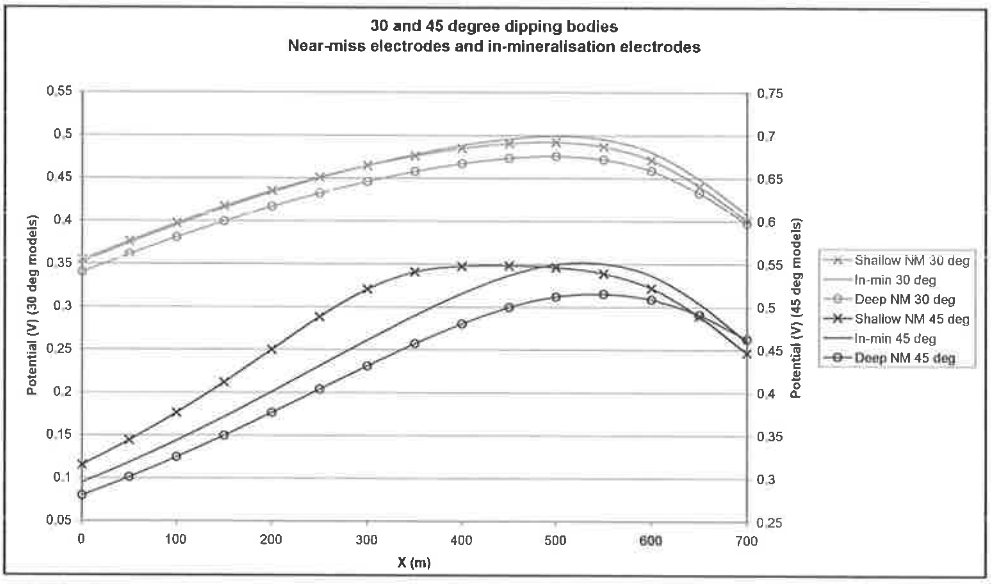

Figure 3.22: Near-miss and in-mineralisation profiles for the 30 degree dip body (plotted on the left vertical scale) and the 45 degree dip body (plotted on the right vertical scale). The near-miss positions are very similar to the in-mineralisation case for the 30 degree body and dissimilar for the 45 degree body.

Figure 3.23 shows greater difference amongst the near-miss cases for the 60 degree body. The shallow near-miss does not have its peak in the same position as the in-mineralisation case. The deep near-miss shares a greater similarity to the in-mineralisation case.

The near-miss positions and profiles for the vertical body are the same as those presented for the 50 metre near-miss cases at 225 metres depth about a vertical body (p45). The peaks are offset from the conductive body position (Figure 3.23). Asymmetries in the direction towards the body in the near-miss curves indicate the presence of a body.

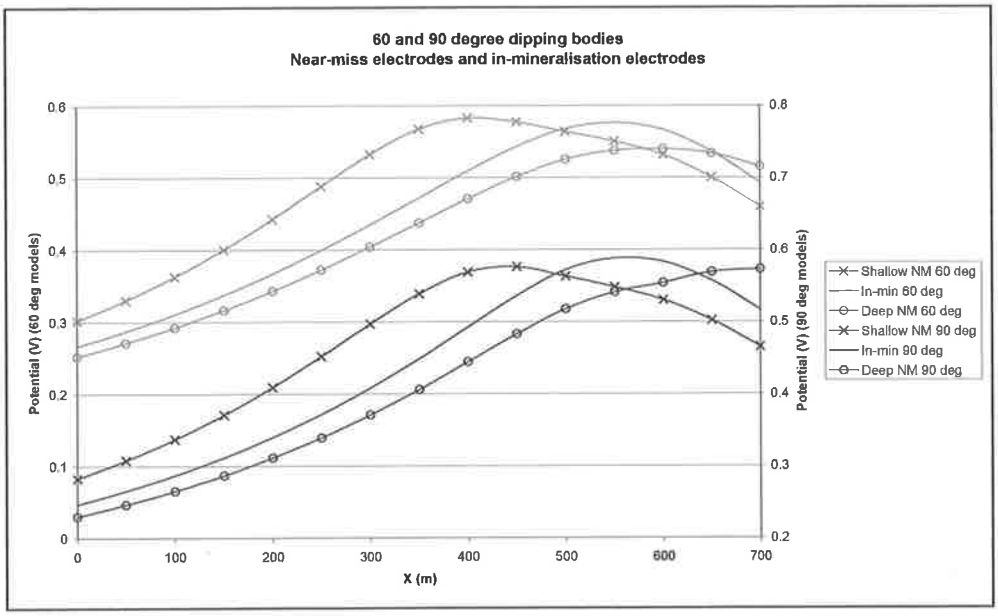

Figure 3.23: Near-miss and in-mineralisation profiles for the 60 degree dip body (plotted on the left vertical scale), and the 90 degree dip body (plotted on the right vertical scale).

The near-miss modelling identifies a relationship between the separation of the electrode from the conductive body and the ratio of the conductive body and electrode depth. At shallow depths, the transition from near-miss scenario to a homogeneous electrode scenario occurs within a small separation from the conductive body. At depth, the near-miss style response persists for greater separations.

The dip of the body greatly affects the near-miss responses of a shallow electrode position. The response of a shallowly dipping body is nearly the same regardless of the near-miss position above or below the body. A deep near-miss, where the electrode is below the conductive body, has a peak potential response due to conductive body rather the source electrode. This effect diminishes with increased dip.

Forward regolith model

The previous series of models did not include a regolith layer to keep the response simple and easy to interpret. This next sequence of models outlines the idealised regolith models studied. These models include slab-like weathering layers, weathered mineralisation profiles, and wedging profiles.

Basic Uniform Regolith Scenarios

The model space used is the same as those described previously of 700 by 700 by 700 metres with a model mesh resolution of 25 by 25 by 25 metres. These models deal with changes within a slab-like weathering model, where the upper portion of the model is defines as the regolith sequence which uniformly covers the model (Figure 3.24).

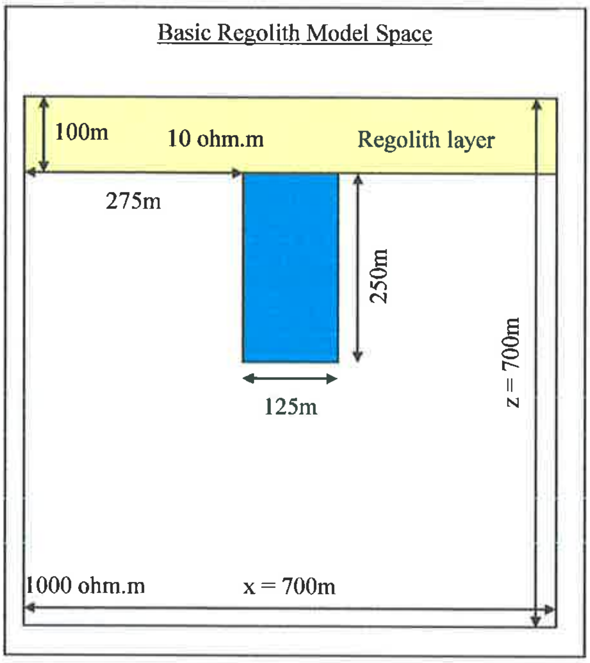

Figure 3.24: The basic regolith model space is the same as those for the idealised models but it includes a regolith layer, in this case 100 metres thick, with a 10 ohm.m resistivity. This model space applies for the Regoith Thickness and Regolith Resistivity Contrast models.

Regolith Thickness

The basic model is an electrode within the half-space with no conductive body. This electrode is at position 350,350,225 metres in a half-space of 1000 ohm.m. A regolith layer of 10 ohm.m is introduced, beginning with a thickness of 25 metres. The regolith thickness is increased incrementally by 25 metres with each model, to a maximum thickness of 200 metres.

Results:

With increasing thickness of the conductive regolith layer, the peak surface potential response decreases for the same source electrode depth (Figure 3.25). In other words, the greater the depth to basement, the greater the attenuation of signal.

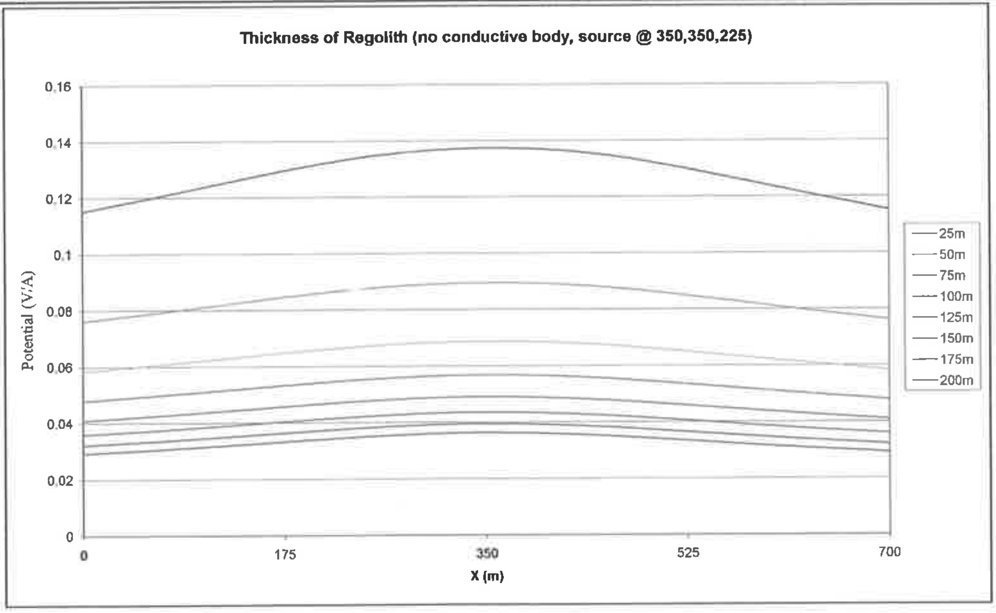

Figure 3.25: Thickness of regolith layer. There is no conductive body within the half-space, just the source electrode at a depth of 225 metres.

Regolith Resistivity Contrast

Two sets of models look at resistivity changes within the regolith relative to the host rock and the conductive body. Both sets have a uniformly thick 100 metre regolith layer with different resistivity values 0.1, 1, 10 and 100 ohm.m, in contrast to 1000 ohm.m resistivity of the half-space. One set of models looks at the MALM surface potential response of a source electrode in a two layered earth without a conductive body, this electrode is at 350 by 350 by 225 metres. The other set examines with the same model however with a conductive body of 125 by 400 by 250 metres of 1 ohm.m. The conductive target was centred in the model space and the electrode embedded within the body at 350 by 350 by 225 metres.

Results:

Figure 3.26 is similar in respect to Figure 3.25, in that a highly conductive regolith layer has the same effect as a thick regolith layer, both suppress surface potential amplitudes. A low resistivity contrast between the regolith layer and the basement results in elevated surface potentials relative the potentials due to a high resistivity contrast between the two media. A change in the magnitude of relative resistivities has a profound effect on the surface potentials; hence variations in resistivity of the near surface regolith are of consequence.

The introduction of a constant resistivity conductive body (1 ohm.m) that is in contact with the regolith layer elevates the surface potentials as the current is channelled into the weathered layer. However the amount of increase of the target response changes with the resistivity of the weathered layers, since the body is in contact (Figure 3.26). With increasing resistivity contrast between the regolith layer and conductive body (i.e. when regolith layer is 100 ohm.m), there is a subtle decrease in potentials of the models with a body relative to the models with no conductive body. If the body was isolated from the regolith, this would not occur.

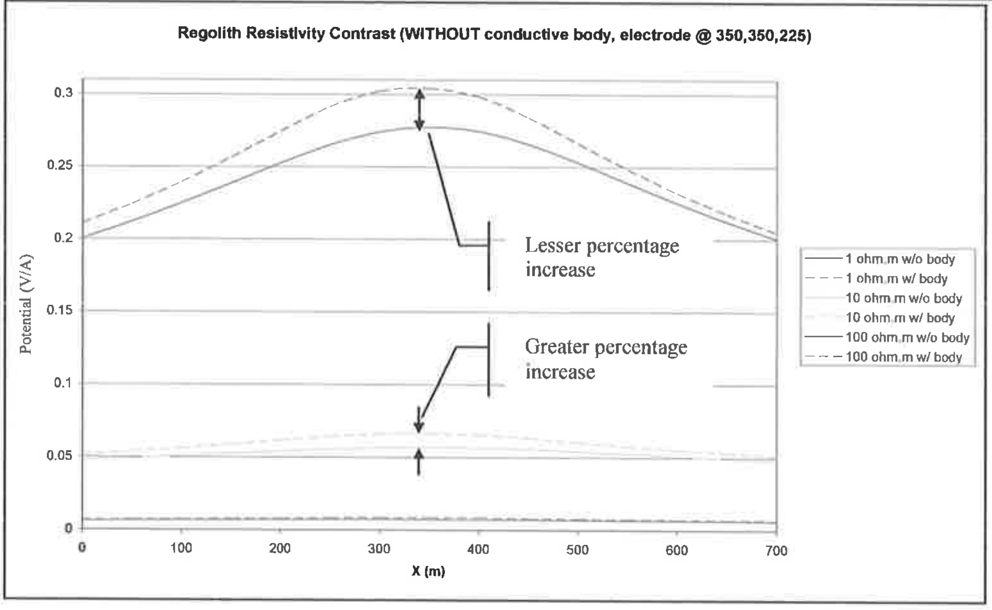

Figure 3.26: Change in regolith resistivity. Peak surface potentials are increased with decreased resistivity contrast between the regolith and basement.

Variable regolith scenarios

These more complex scenario models use a different model space as those used in basic scenario series. This alternate model space was used to accommodate a higher depth resolution. The measurements are 700 by 1050 by 1000 metres and the model mesh resolution was 50 by 50 by 5 metres. This allowed for more variability to be modelled in the regolith layer, since the upper section of the model can be defined by more depth slices. All bodies were centred in the Y-axis.

Weathered mineralisation models

These models simulate a conductive mineralisation that has weathered *in situ*, with lower resistivities in the regolith cover directly over the top of the unweathered mineralisation. This was taken a step further by layering the regolith cover above the mineralisation to simulate a leaching front that has moved from the surface down. The conductive body has the dimensions 200 by 700 by 450 metres and is buried at a depth of 100 metres with a resistivity of 1 ohm.m. The source electrode (at 350,525,325) is placed in the conductive body which is in electrical contact with the regolith immediately above it. These models highlight the disparity in rates of weathering can occur both laterally and vertically in the regolith layer.

As a comparison, the surface potential response for a model (Figure 3.27 A) with a uniform regolith layer (100 metres thick, and resistivity of 15 ohm.m) was calculated. This has no weathered mineralisation variation in the regolith cover.

A weathered mineralisation model has the same conductive body and regolith sequence; however the regolith layer directly above the body has a resistivity value of 5 ohm.m (Figure 3.27 B). This portion of the regolith has the same XY dimensions as the body, i.e. 200 by 700 metres, and is 100 metres thick.

A variation on the above model has the weathered regolith split into two parts; a leached upper portion affected by meteoric water with resistivity of 10 ohm.m, down to a depth of 25 metres. The lower portion is weathered to a lesser extent with resistivity of 5 ohm.m, to simulate a saprorock. This lower section extends from 25 metres to the top of the conductive body at 100 metres (Figure 3.27 C).

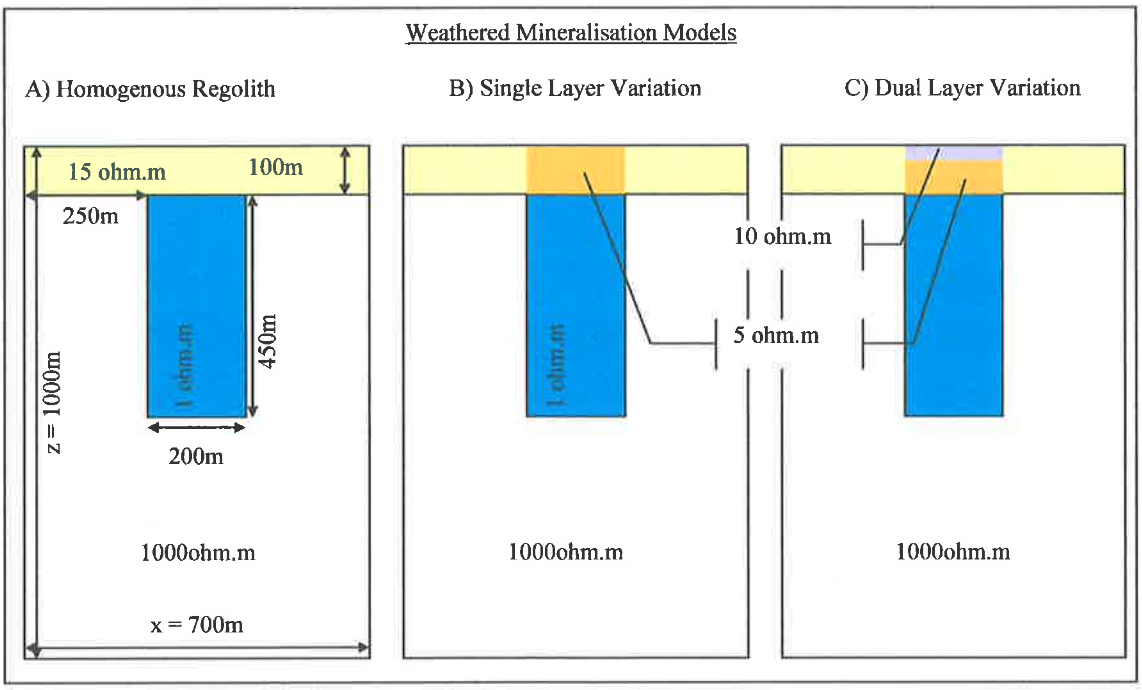

Figure 3.27: A) This model contains a homogenous regolith layer in comparison to B) with a single layer, regolith variation over the conductive body and to C) a dual Layer regolith variation. The half-space has resistivity of 1000 ohm.m metres and the conductive body has resistivity of 1 ohm.m.

Results:

The weathered mineralisation models identified that subtle changes can occur in the surface electrical potentials due to the different rates of weathering over the top of mineralisation (Figure 3.28). These nuances are very minor in comparison to the resistivity contrast caused by mineralisation.

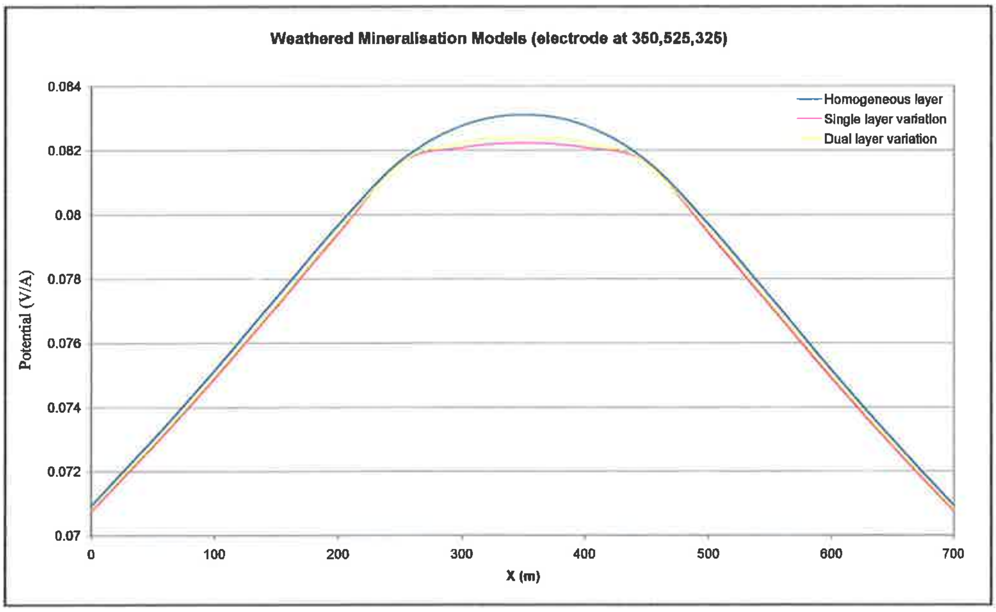

Figure 3.28: Subtle variations in surface electrical potentials due to minor changes in resistivity in the reoglith layer, both laterally and vertically.

Wedging regolith models

The wedging regolith models are studies on the effects of a regolith profile where variations in resistivity are defined by an angular contact. Such a scenario can manifest itself physically as in transported regolith, where newer material has covered an older regolith profile (i.e. paleochannel banks) or basement (Macnae et al. 2001). This process can be driven by either be alluvial or aeolian modes of weathering (Taylor and Eggleton, 2001). Alternatively, this change in resistivity is due to *in situ* weathering in the subsurface due to chemical interaction with groundwater. The angular contact could be caused by impermeable ground, preferential groundwater flow paths or by a hydraulic gradient.

Regolith/basement contact models

One paradigm studied is the regolith wedge lying atop unweathered basement rock. Such a scenario can be envisaged as a colluvium wedge accumulating from an elevated basement outcrop. There are two models generated which belong to this group, the only difference being the position of the conductive body along the X-axis. The dimensions of the conductive body are 100 by 750 by 400 metres, 150 metres from the northern edge of the model space. The depth of the body is a constant 150 metres below the surface. In one model, RBA (Figure 3.29 A), the conductive body is 100 metres from the western edge of the model space, in the other, RBB (Figure 3.29 B), it is 450 metres.

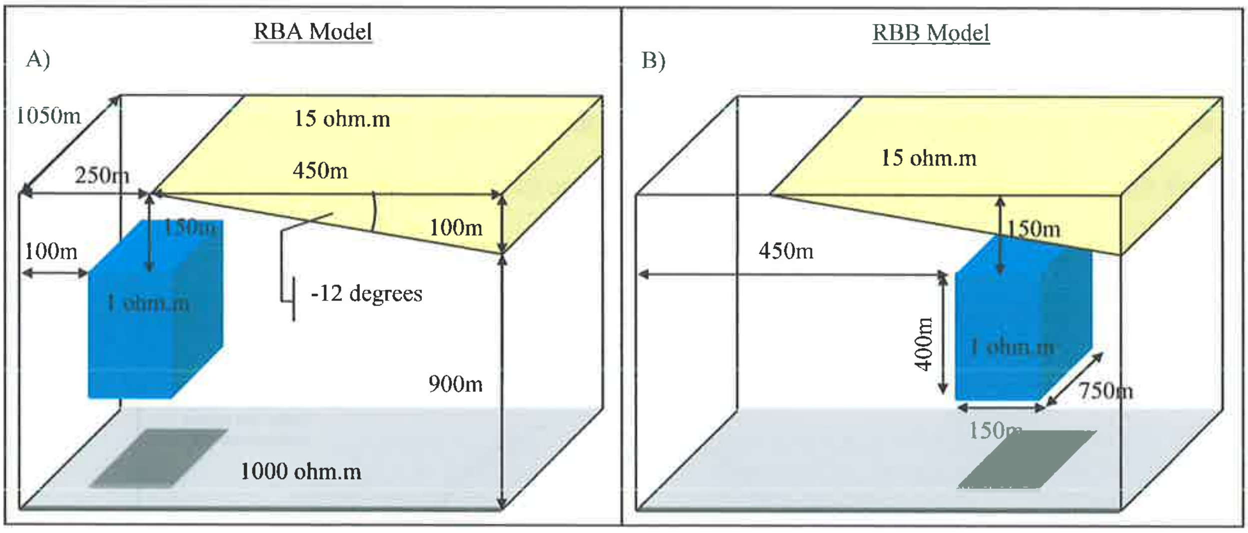

Figure 3.29: Regolith/basement wedge models, these simulate transported sediment collecting in a basin A) RBA model, with the conductive body 100m from the left edge of the model space and B) RBB model with body 450m from the edge.

The contact between the regolith and the basement rock is angled at negative 12 degrees; beginning 250 metres from the left edge of the model space, and extending for 450 metres. The maximum depth of the regolith is 100 metres; therefore the conductive body is not in contact with the regolith in either model. The angle of negative 12 degrees is achievable due to the higher depth resolution incorporated in these models. In RBA the body is directly under the surface transition from basement to regolith, whereas RBB has the model beneath the regolith wedge bulk. The source electrode is connected to the body in both models.

Results:

The sharp contact between the high resistivity basement and low resistivity regolith wedge can be seen at 250 metre (Figure 3.30) in the RBA model where the conductive body is situated beneath the surface position of the exposed bed rock. The peak surface potential of the RBA model is higher than that of the RBB model. The equipotential contours in Figure 3.31a indicates the strike direction of the conductive body and the regolith/basement contact is apparent in the contours. However the peak is offset to the west of the body position, the up-dip direction of the contact.

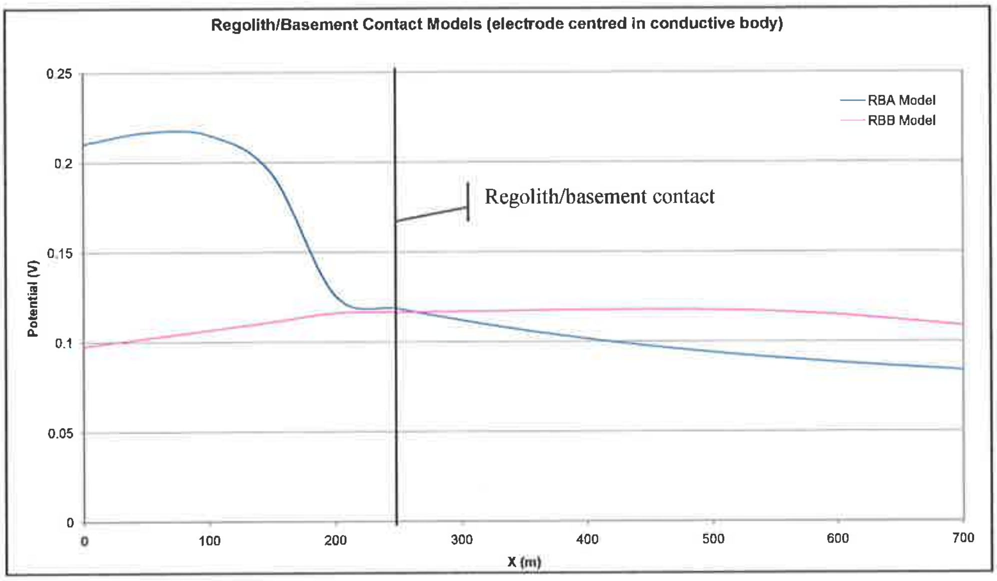

Figure 3.30: The RBA model has a high surface potential value due to the modelled surface exposure of resistive basement. The contact can be seen in the rapid decrease of surface potentials of the RBA model The RBB model has resulted in a broad peak with a relatively low peak potential, the position of the contact is not easily picked.

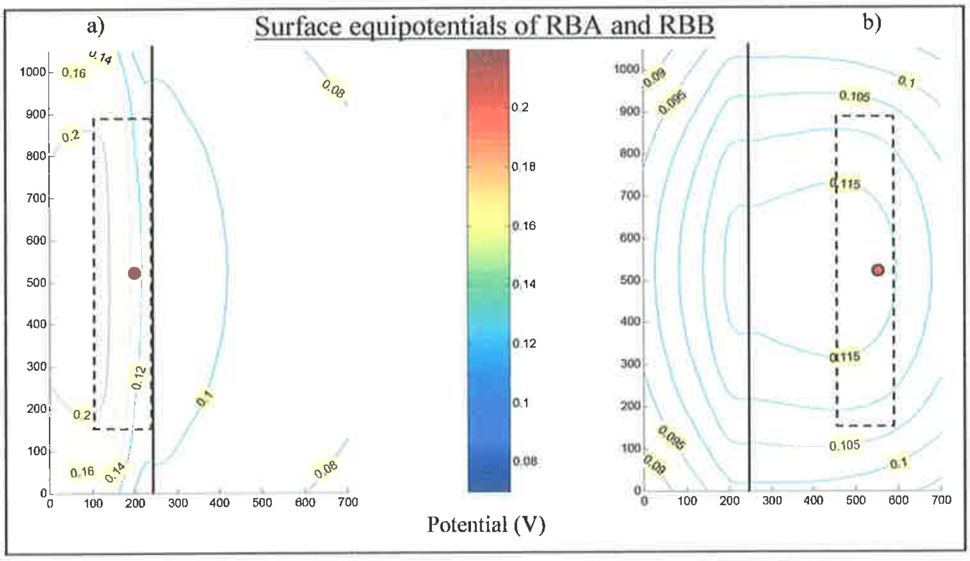

Figure 3.31: The solid line at 250m indicates the surface position of the regolith/basement contact and the dashed outline is the surface projection of the conductive structure. The red dot is the position of the surface electrode. a) (left) the high resistivity basement exposure alludes to the strike direction of the conductive body. b) (right) the equipotentials of the body positioned beneath the conductive regolith wedge does not give any indication of strike direction.

Figure 3.31b the contact is not as readily apparent when the body is placed beneath the bulk of the regolith wedge, the peak surface potentials are also shifted in the up-dip direction of the regolith/basement contact.

The RBB potential profile curve in Figure 3.30 does not distinguish the position of the regolith/basement contact readily. In comparison, the contact is easily identified in the plan view of the surface potentials. This is due in part to the simplicity of the models and the sharp contrast of resistivities. This would not be as simple to identify in field data due to more complex geometries and gradational resistivity transitions from regolith to basement.

Regolith/regolith contact models

The following models are simplified examples to explore changes in MALM responses due to the lateral variability within a regolith profile. The regolith is separated in to two rectangular prisms. The model WMA (Figure 3.32 A), has the resistivity of 10 ohm.m in the left prism, whilst the right has resistivity 15 ohm.m. The models are identical save for the resistivities in the regolith being swapped around in the second model (Model WMB, Figure 3.32 B).

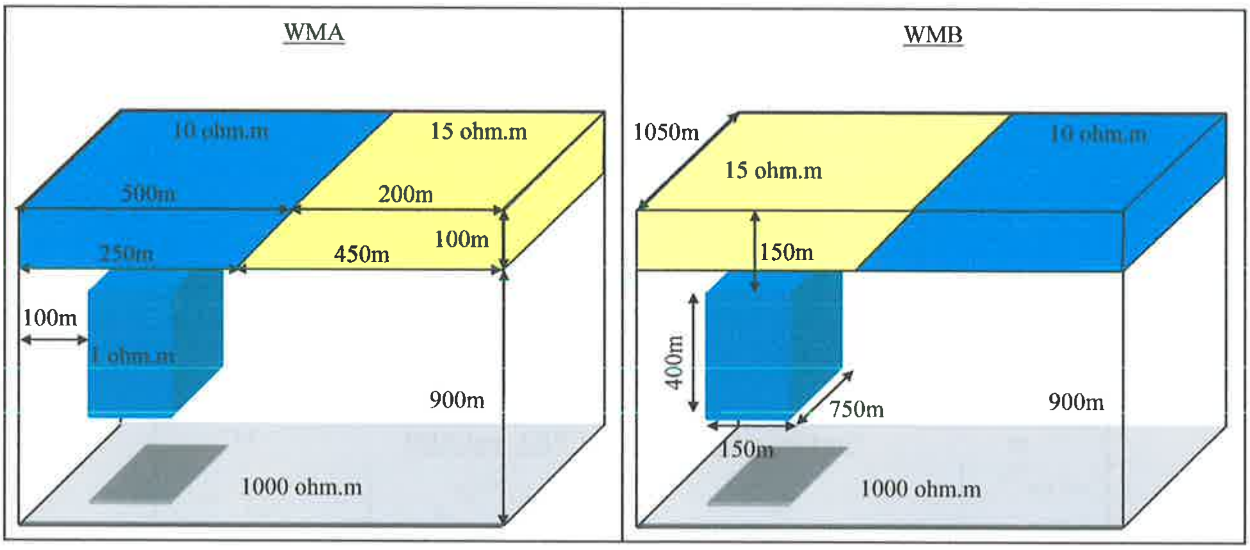

Figure 3.32: The regolith/regolith models are identical except for A) WMA, has the in the regolith resistivities from B) WMB swapped, such that the regolith layer has 10 ohm.m on the left rather than the right. The body is in the same position with the source electrode connected to the body.

The conductive body is the same as the Regolith/Basement model (i.e. 150 by 750 by 400 metres) and is placed at a depth of 150 metres in both models. The body is situated 100 metres from the left edge of the model. The source electrode is placed in contact with the body at the centre of the body.

Results:

When a more resistive regolith cover is overlying the conductive body there is a subtle change in surface potentials as seen in Figure 3.33 with a decrease in peak potentials of 0.0177 volts. This difference is not inconceivable as the change in resistivities is only 5 ohm.m. Whilst this subtle variation in potential does not seem like much, the surface position of the peaks has a significant change. The peak of the WMB is offset 50 metres to the west relative to the peak of WMA (Figure 3.33), this distance in substantial considering the minor change in resistivities.

The surface position of the contact between the two regolith materials is not identifiable in either model's surface potentials.

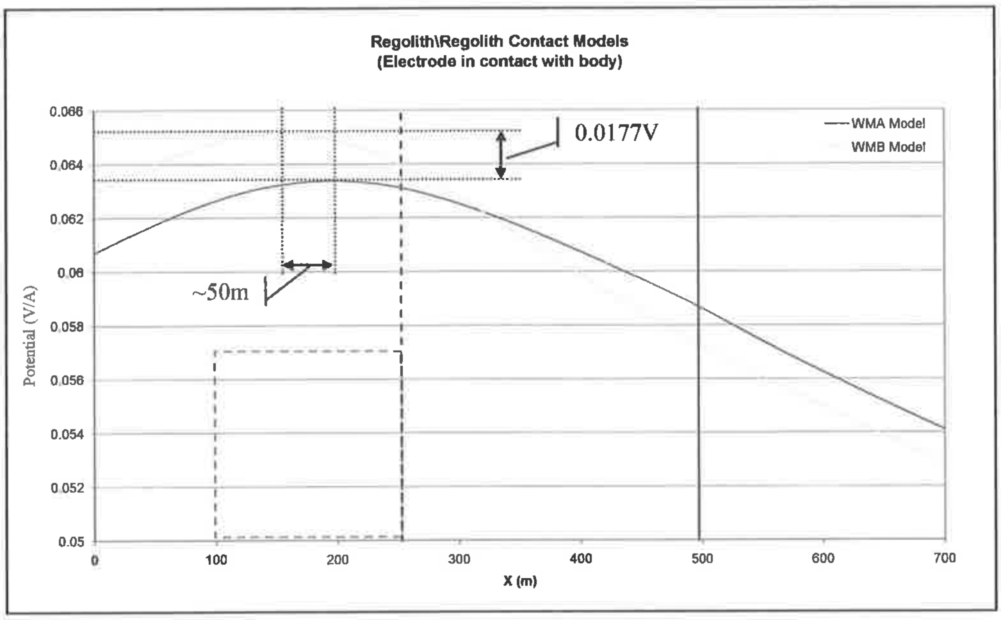

Figure 3.33: Solid blue line is the surface position of the contact between the two different regolith resistivities and the dashed blue line is the position of the contact at the base of the regolith layer. The red dashed outline is the position of the conductive body.

Forward models of field sites

A forward model was used in two different circumstances when investigating the field sites. At Golden Grove, where data were collected prior to modelling, the model was used to validate the geological model by synthetically reproducing the MALM response. However at Prominent Hill, the FEM modeller was used in experiment design, by incorporating existing geologic information and generating a synthetic MALM response prior to the field survey.

Each source electrode position was linked to a model configuration to match the potential electrode coverage, or to optimise run times if the models were computationally intensive. However, when multiple source electrodes were in close vicinity, a single model was used with a half-space that accommodated all surface electrode positions. Although the software can replicate the exact location of the field potential electrodes, it was found simpler to generate an artificial uniform potential electrode grid array for minimum curvature gridding.

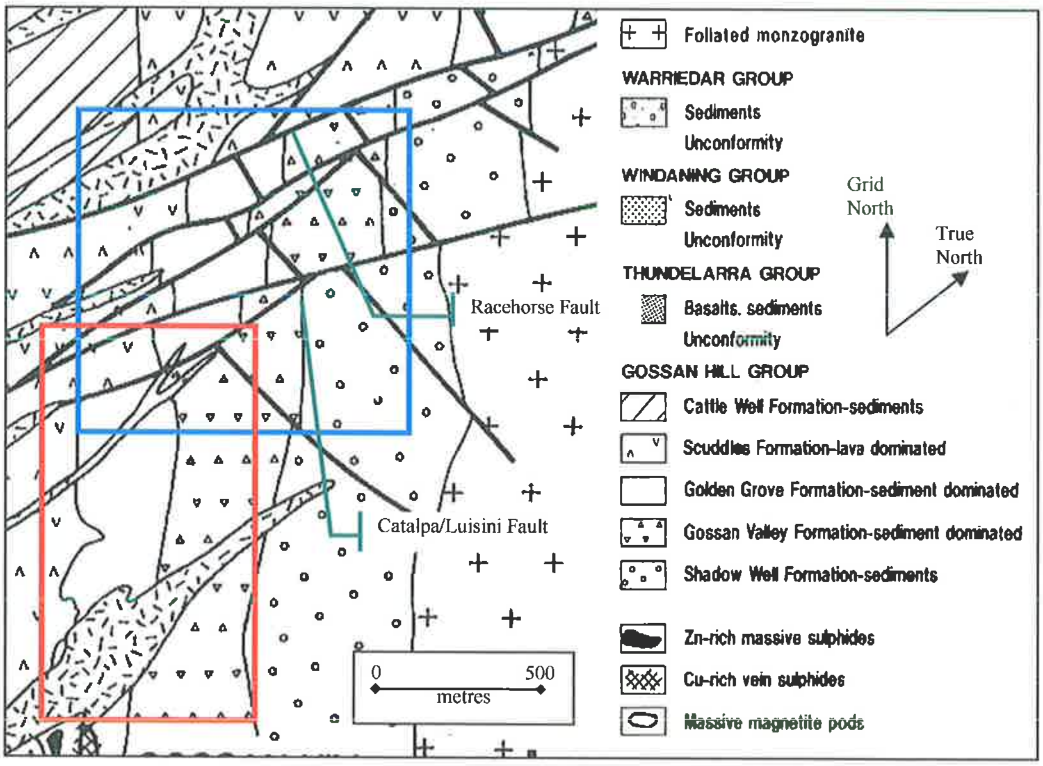

Figure 3.34: From Figure 1.4, a close up of the two areas at Golden Grove, Catalpa (red rectangle) has a singular fault to the north. Catalpa North (blue square) has multiple fault traces lying between the Catalpa/Luisini fault and the Racehorse Fault (after Boyd and Frankcombe, 1994). The MALM data that the models approximate are displayed in Section 4.1 ("Field MALM data results", p85).

Golden Grove, Western Australia

For Golden Grove, the FEM model was derived from the geological cross-section from Boyd and Frankcombe (1994) (Figure 1.3) and discussions with the mine geologists and geophysicist (M. Sexton et al., pers comm. 2002). The target body used in the FEM model is part of the conductive Golden Grove formation and is defined as a near vertical structure which has significantly lower resistivity than the surrounding host rock. The conductive body dips to the west at 80 degrees and has a uniform regolith cover that is 100 metres thick. Resistivities of the conductive body, half-space and regolith cover were set to 0.1 ohm.m, 1000 ohm.m and 10 ohm.m respectively based on field and lab measurements (Roach and Fitzpatrick, 2003) . This is the general description of features in the Golden Grove models (M. Van Eck, pers comm. 2003), which are split into two groups based on the two areas outlined previously in the field location description (Figure 3.34).

Catalpa

The model of the Catalpa region had dimensions of 1000 by 1000 by 1025 metres, with a mesh resolution of 20 by 50 by 25 metres. This volume encompassed all the areas of the four surveys conducted at Catalpa in drill holes RHDD018 and RHDD020 shown in Figure 3.34, with the only difference in the location of the source electrodes (Table 1-1, p9). For RHDD018 and RHDD020 Setup A were both in contact with the conductive body. RHDD020 Setup B and C were near-miss surveys, where the source electrode for the model duplicated the position *outside* of the body.

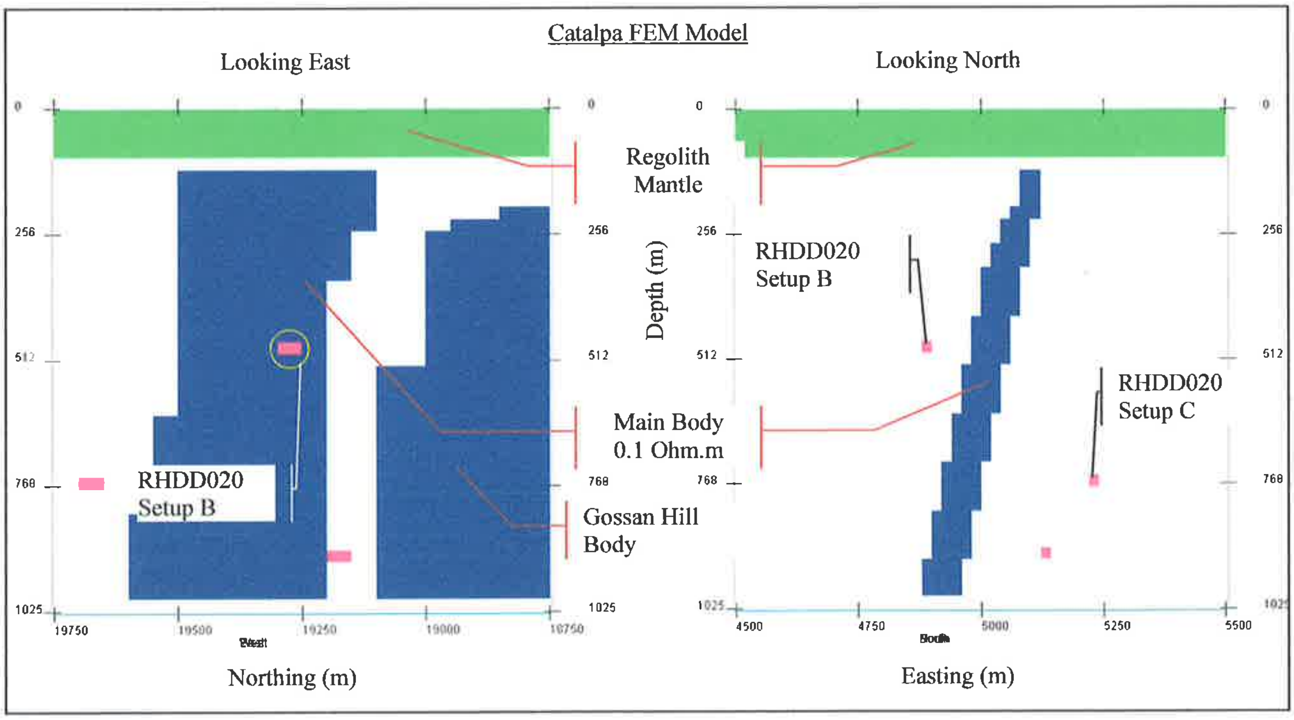

Figure 3.35: Catalpa FEM model, 100m of overburden separated by 25 m from the conductive target. To the south lies a possible Gossan Hill Mineralised body which in this model is electrically disconnected from the primary target. Note: the pink blocks that are not labelled are test electrode positions.

In Figure 3.35, the width of the main target body ranges from 40 metres, at the top of the body, to 80 metres at the base. This body represents the Catalpa ore body from the Gossan Hill long section (Figure 1.5, p8). To the south are the beginnings of the Gossan Hill suite of mineralisations. From the MALM response seen in RHDD020 Setup C, where the potentials open to the south, this body was included to investigate the possibility of a deep electrode position energising targets to the south of the Catalpa area. This assertion stems from the Gossan Hill system of mineralisation possibly being in close proximity with the Catalpa targets at depth.

A prominent geological feature in this location is the Catalpa/Luisini Fault (Figure 3.34) which lies to the north. This strike-slip fault has also been modelled, with the mineralisation terminating above 19650 N.

From the investigations of Craven et al. (1985), the conductive body is electrically isolated from conductive regolith. Depth for the uppermost part of the mineralisation was set at 125 metres below the surface, leaving a gap of 1000 ohm.m host between the conductive body and the regolith layer (Figure 3.35). A model was trialled with the conductive structure in contact with the regolith, but this response was not a good match to the actual MALM data collected (Figure 4.1 to Figure 4.4).

Results:

The subtleties of the MALM data cannot be reproduced entirely by a block body model as presented here, however there are qualitative comparisons to be made as trends seen in the MALM data are replicated in the FEM models. The peak potentials of the observed MALM data are much higher than those of the FEM models (Figure 3.36 cf. Figure 3.37). Perhaps this is due, in part, to the thick uniform conductive regolith layer used in the models which maybe incorrect for this site. There was a significant difference between the surveys RHDD018 and RHDD020 Setup A in the MALM data which has been lost in the FEM modelling (where RHDD018 and 020 Setup A are equal). This is no doubt due to the idealised nature of the model.

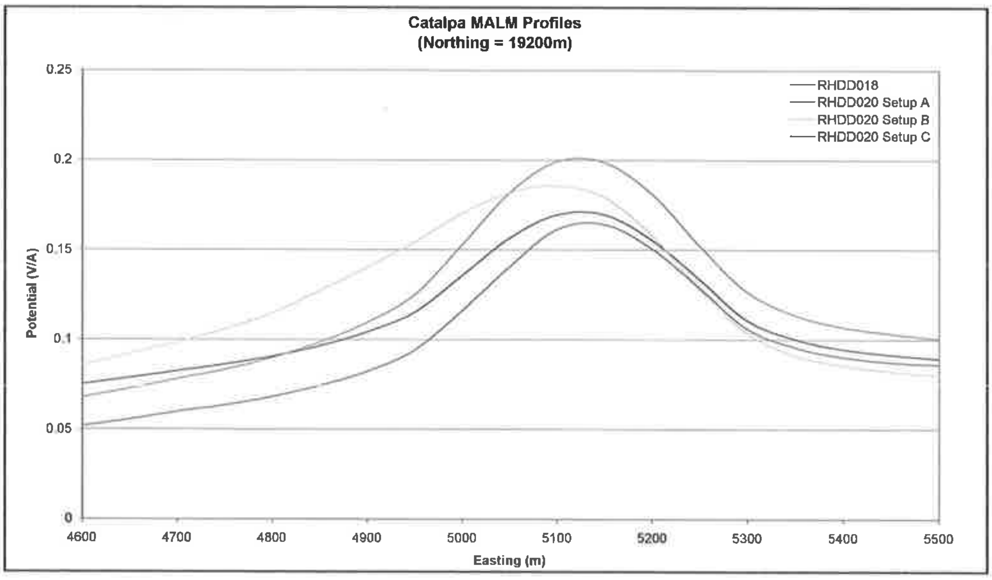

Figure 3.36: Surface potential profiles of the four MALM data sets from Catalpa. The profiles are those along the 19200m northing. The in-mineralisation models RHDD018 and RHDD020 have significantly different peak values at along this northing, but they share the same peak position. The near-miss positions of RHDD020 Setup B and C have a similar peak easting.

The most obvious similarities between the FEM models and the MALM data is the relative potentials of each of the surveys (Figure 3.36 cf. Figure 3.37). The surveys in RHDD020 from highest peak potentials to lowest are order as follows Setup A, Setup B then Setup C, which is partially related to the depth of the source electrode.

The asymmetry to the west of the RHDD020 Setup B (Figure 3.37) curve is due to the shallow near-miss position of the source electrode. From Figure 3.38b, at this position the electrode is contributing to the surface potentials in addition to the potentials due to current being channelled through the conductive body.

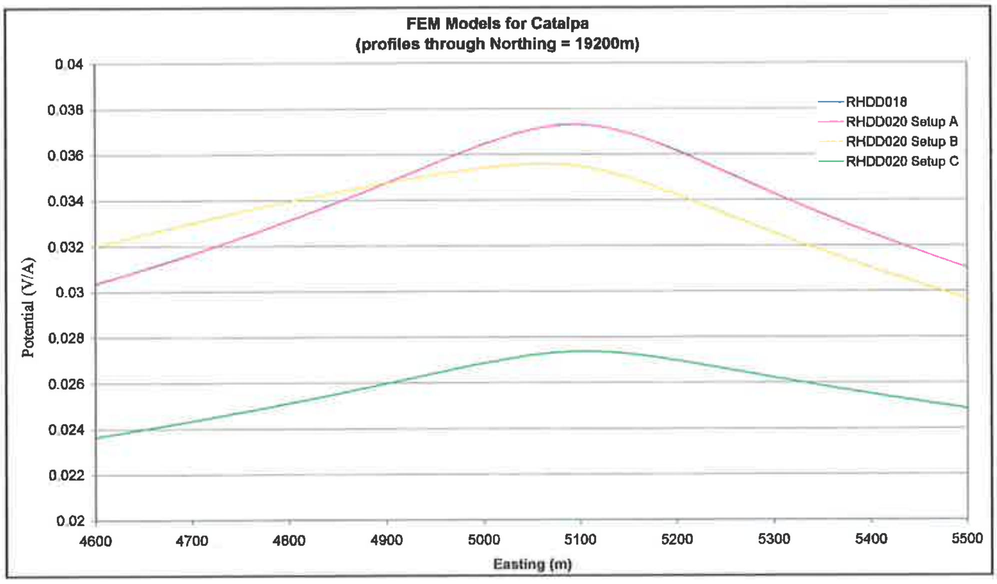

Figure 3.37: Catalpa FEM models' profiles along the 19200m northing. The asymmetries in the observed MALM data are also seen in the FEM model profiles. RHDD020 Setup B has an asymmetry to the west of the its peak.. The peak positions are a good approximation to those in Figure 3.36, but are much more subdued. Note: RHDD018 and RHDD020 Setup A share the same curve.

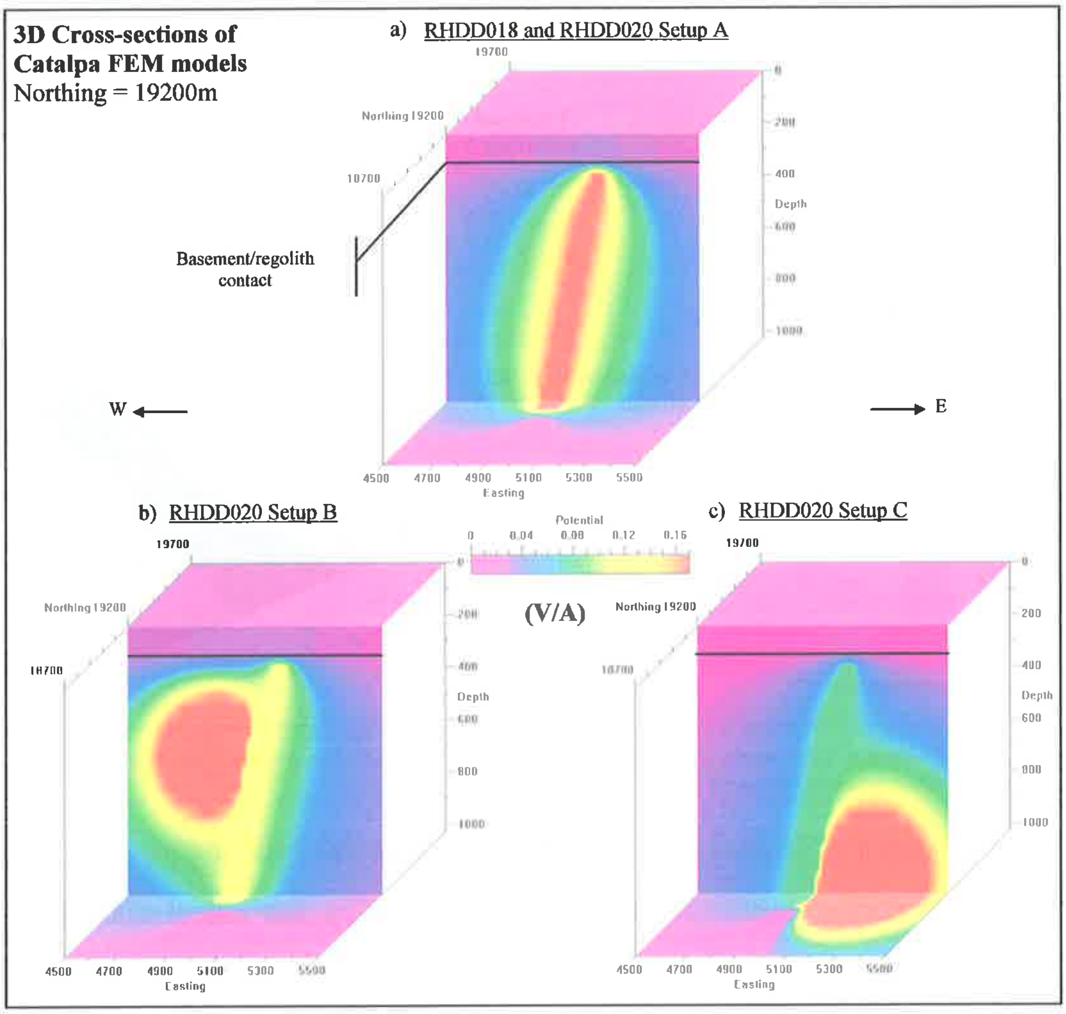

Figure 3.38: The solid black line indicates the contact between basement and regolith. a) (top) is the in-mineralisation FEM response of RHDD018 and RHDD020 Setup A. b) (left) is the shallow near-miss electrode position of RHDD020 Setup B. c) (right) RHDD020 Setup C with a near-miss electrode at depth. Cross-sections along 19200m northing.

This is not the case with Figure 3.38c where the upper surface of the conductive body is dominating the surface response. This is why the general potential profile of the deeper near-miss electrode is similar to that of the in-mineralisation electrode placement. This is seen in both the observed MALM and FEM potentials across the 19200m northing (Figure 3.36 and Figure 3.37).

Catalpa North

The modelling of the Catalpa North area was conducted after the acquisition of the data. From the Catalpa North MALM surveys (Section 4.1, p85), the potential high along the southern margin of all the Catalpa North data sets is associated with the anomaly seen in the Catalpa MALM. It would appear some similarities of the anomalies between surveys are due to an electrical connection of the conductive bodies, either along the fault planes or at depth. As such, this area was not as straightforward to model for it was not possible to synthetically reproduce the fault planes as it would require a much finer model mesh to delineate the faults, therefore more computer resources than available. The model used for Catalpa North consisted of a conductive body that extended to the north-west at depth. The electrodes were placed in accordance to the hole logs for each drill hole (Table 1-2, p9).

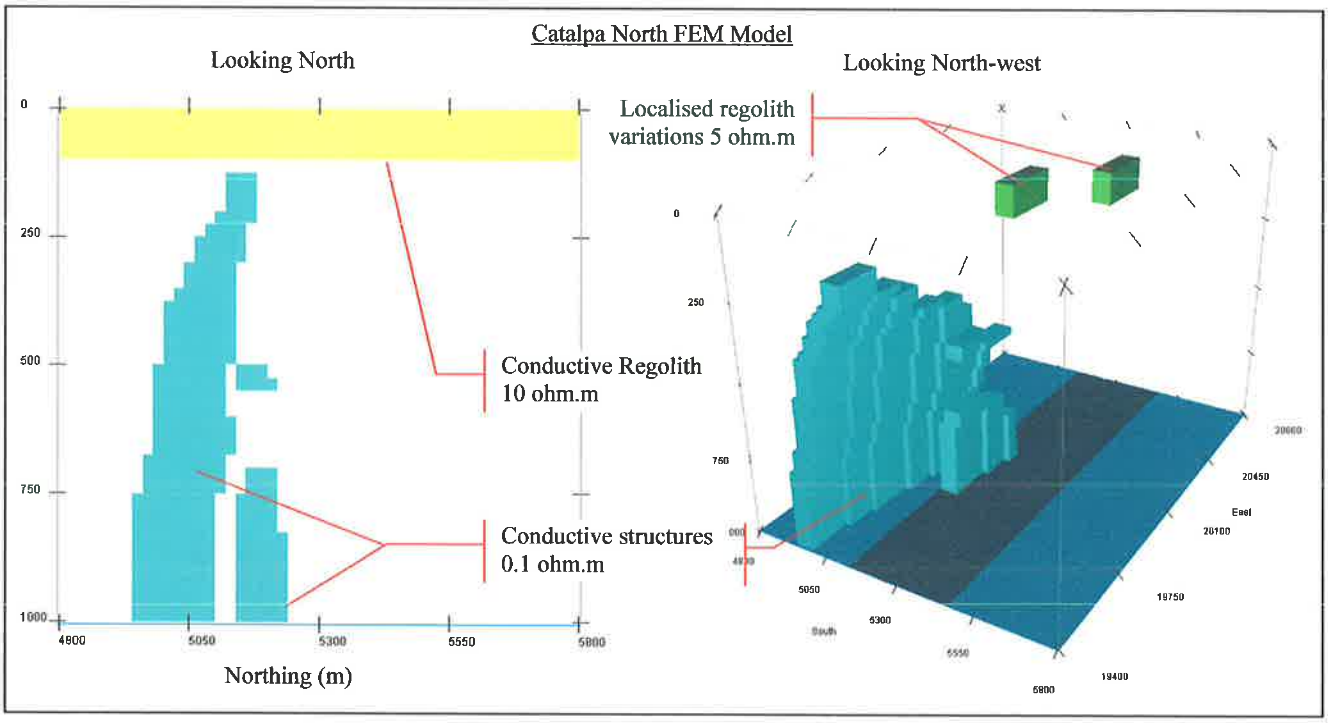

Figure 3.39: Views of the Catalpa North model (left) looking to the north, the conductive structure are near vertical. Looking N-W (right). The conductive body extends to the north.

Numerous faults between the Catalpa/Luisini Fault and the Racehorse Fault (Figure 3.34) make it more difficult to define the conductive structure in the Catalpa North area. The near vertical conductive body in the model (Figure 3.39) continued to the north-west at depth is an attempt to imitate the Catalpa/Xanthos ore bodies interpreted in the Gossan Hill Long section (Figure 1.5, p8). This deep main conductive body to the south endeavours to mimic the southern potential peak seen in the Catalpa North MALM data (Figure 4.6, Figure 4.7 and Figure 4.8 for RHDD038 and the two RHDD040 surveys)

As at Catalpa, the area is covered by 100 metres of homogeneous regolith of 10 ohm.m resistivity (Figure 3.39). The conductive body in this model had the same resistivity of 0.1 ohm.m. Within this regolith cover are two pods of lower resistivity materials (5 ohm.m). Since small changes in near-surface resistivity has been shown in modelling to affect the MALM response, these regolith variations were modelled in an attempt to replicate the response of RHDD010 (Figure 4.5) which has two low amplitude peaks

Results:

The Catalpa North modelling was unable to replicate the more complex geology and geophysical signiture of the area. Since the peaks to the south in the Catalpa North MALM surveys are associated with the peaks seen in the MALM data for Catalpa, it was assumed that any models of the Catalpa North area would be transference of the Catalpa models towards the north. Whilst every attempt was made to replicate the potential high to the south with near vertical block structures, the final model had to agree with the known geology and the four known drill holes.

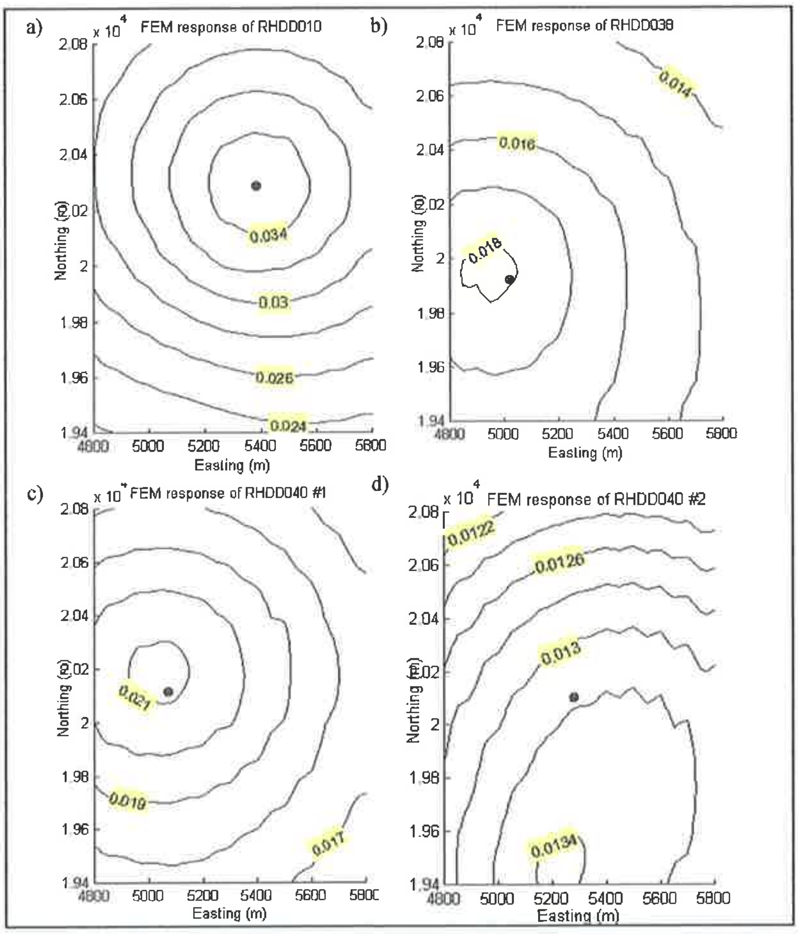

Figure 3.40: Catalpa North FEM surface potential responses of a) RHDD010, b) RHDD038, c) RHDD040 Setup 1 and d) RHDD040 Setup 2. Only the model for RHDD040 Setup2 reproduced a peak to the south, and at a much lower peak potential.

Without any significant mineralisation intersections at all 4 electrode placements (M. Van Eck pers comms., 2003, see Catalpa North MALM background, p9), the modelled electrode positions could not intersect the modelled body. All 4 models placed the source electrodes in an out-of-mineralisation position.

Figure 3.40a is the surface potentials for RHDD010 and its acquired MALM counter-part is Figure 4.5. From the results of the FEM regolith modelling, the two blocks of localised regolith variation seen in Figure 3.39 were used to mimic the double peak anomaly seen in Figure 4.5. These blocks measured 100 by 200 by 100 metres and represent variations in weathering rates or transported materials depositing in localised basins or channels. However from Figure 3.40a, this did not achieve the double peak anomaly when compared to the RHDD010 MALM survey (Figure 4.5). Both the FEM responses for RHDD038 and RHDD040 were dissimilar to the acquired MALM data for the same surveys. Figure 3.40b continues to the south, but does not have the high situated in the same position as Figure 4.6; rather the FEM surface potential peak is situated over the electrode position.

For RHDD040 Setup 1 (Figure 3.40c), there is no distortion of the surface potentials contours to the south, however, as with the acquired MALM survey, the surface potential anomaly is positioned over the electrode position. Only the model for RHDD040 Setup 2 (Figure 3.40d) shares qualitative similarities with its acquired MALM surface potentials. The peak in the FEM data approximates that seen in Figure 4.8, with the potentials continuing in a north-east direction from the peak.

The results of the Catalpa North modelling suggest that the geological interpretation in these models are not correct. The dissimilarity between the models and the acquired MALM data point to geoelectrical current flow paths (possibly due to the numerous faults) that cannot be modelled by block bodies.

Prominent Hill, South Australia

The model of Prominent Hill is derived from the geological interpretation of drill cores. Working from a simple block cross-section provided by Minotaur Resources, the modelling investigates scenarios in which viable data might be collected and calculated synthetic MALM responses prior to collecting the MALM data. Figure 3.41 is the cross-section that the models were derived from; the drill hole is inclined at 60 degrees from horizontal and dips to the south. The electrodes are placed at the locations given in Table 3-4.

The models examined the possible electrode positions in the main target, the chalcocite breccia. Two near-miss cases were also modelled, targeting regions about the chalcocite breccia, a deeper electrode overshooting the breccia and a shallower electrode that did not intercept the target. In all the models the host rock resistivity was set at a constant 1000 ohm.m, and the conductive shapes extended for 500 metres east and west. The regolith blanket was over the entire model half-space and split into three subgroups to model the 22 metre layer of black Bull Dog Shale of 2 ohm.m resistivity.

Source electrode position	Easting (m)	Northing (m)	Depth (m)
Chalcocite breccia	555500	6712138	380
Shallow near-miss chalcocite breccia	555500	6712194	350
Deep near-miss chalcocite breccia	555500	6712098	520

Table 3-4: FEM model electrode positions for the in-mineralisation and two near-miss electrode positions for the Prominent Hill model.

The width of the bodies was calculated from the drill hole intersections of each target and the inclination of the drill hole, this was also done for separation between the main targets. The haematite and magnetite rocks which bound the model to the north and south are set as per discussions with the geophysicist (J. Hart pers comm. 2003)

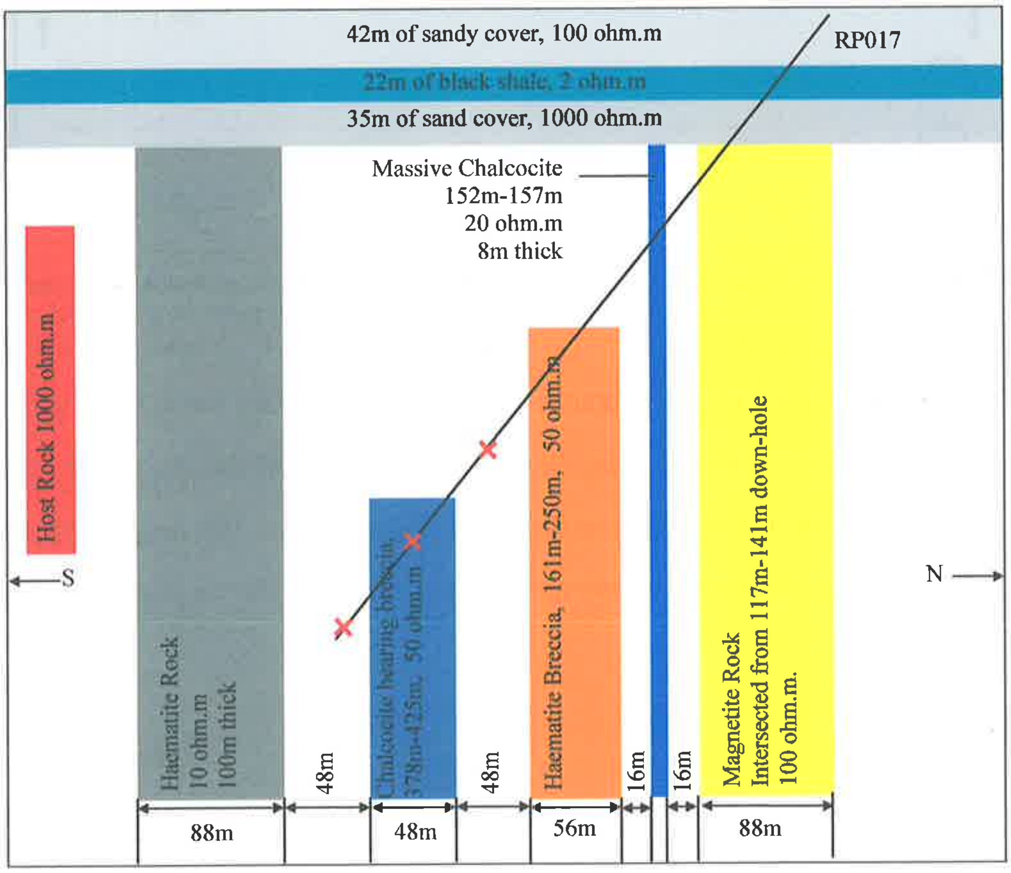

Figure 3.41: A simple cross-section representative of the Prominent Hill geology near RP017, this diagram also identifies the model dimensions and current electrode positions, demarcated by crosses along the drill hole. The bodies also give the mineralisation intersetions in terms of down-hole depths, this was translated into widths using the known drill hole inclination.

Results:

The FEM models for Prominent Hill have an order of magnitude higher values for the surface potentials than the actual MALM data acquired (Figure 3.42). However the shape of the FEM profiles in the north-south direction, appear to correlate with the MALM data. FEM models which were calculated prior to the survey, only spanned 500 metres north-south, whereas the observed data was collected over a larger area, extending a further 200 metres north and over 100 metres south.

Despite the dissimilarities between the amplitude the FEM models have revealed that the southern conductive haematite rock and the barren haematite breccia (north of the targeted chalcocite breccia) are conducting charge closer to the surface from the lower chalcocite breccia (Figure 3.43a). Whilst only one MALM data set was acquired, the FEM modelling allowed the synthesis of near-miss scenarios (relative to the chalcocite breccia).

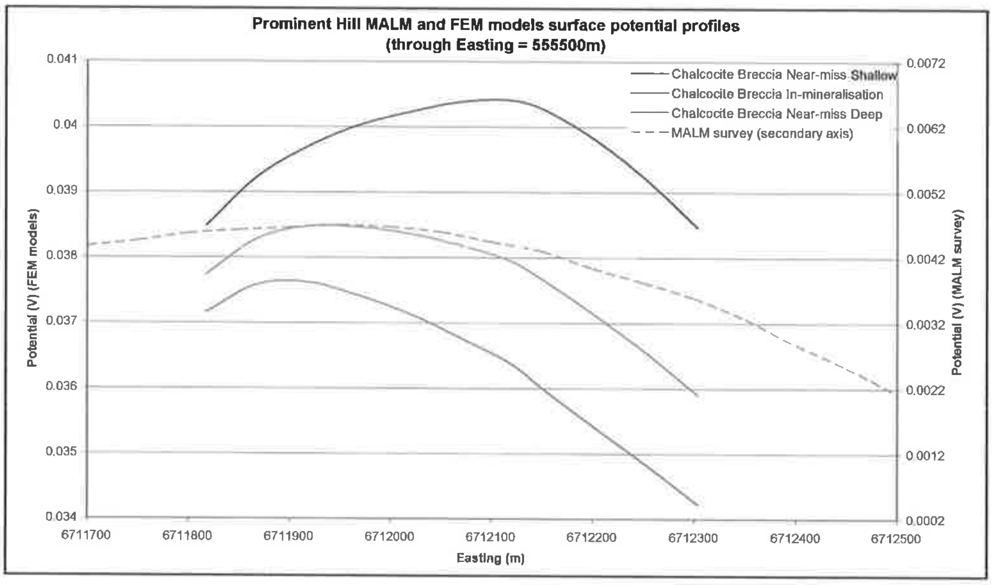

Figure 3.42: The three FEM models plotted on the primary scale (left) and the MALM data plotted on the secondary scale (right). The easting position of the peak of the observed data coincides with the peak of the in-mineralisation model, but the difference between the two is 0.0338 V.

From the FEM model, the shallow near-miss source electrode (Figure 3.43b) that is has a distinctly different profile (Figure 3.42) to the in-mineralisation case, as current is being channelled through the north conductive bodies (the haematite breccia and the massive chalcocite, Figure 3.41). The deeper near-miss scenario (Figure 3.43c) is more akin to the in-mineralisation model, as it highlights the conductive southern haematite rock.

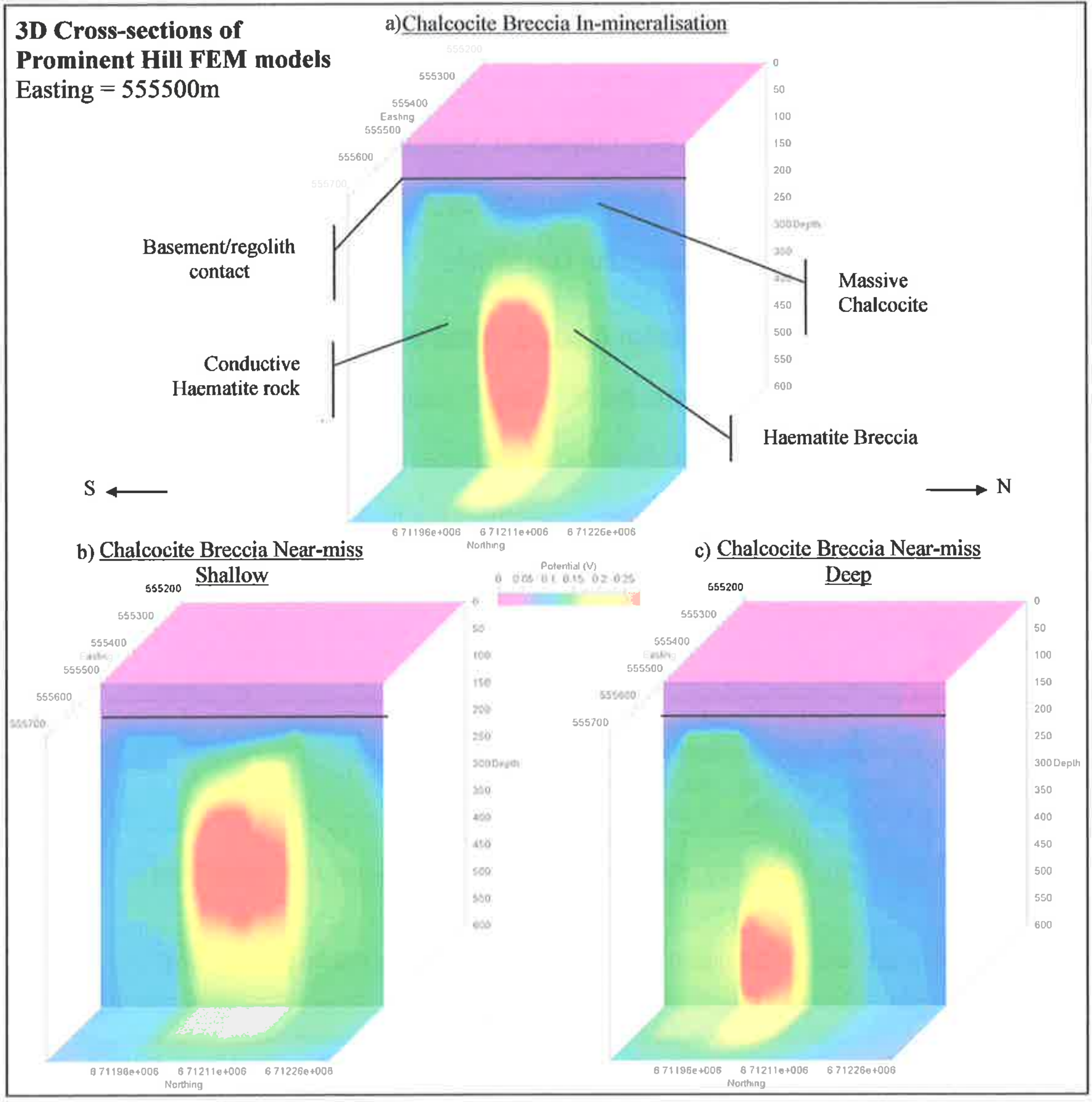

Figure 3.43: a) (top) in-mineralisation case for the chalcocite breccia where charge is channelled via the northern and southern flanking bodies. b) (left) a shallow near-miss source electrode energises the shallower northern bodies and the target chalcocite breccia. c) (right) a deep near-miss electrode position conducts charge closer to the surface via the southern haematite rock, but still excites the target chalcocite breccia as well.

Electrode Effect Removal (EER)

Theory and coding

The basis for the electrode removal has been outlined in Section 2.6 (p29). The EER uses the potential equation for a buried electrode in a semi-infinite, homogeneous, isotropic earth (Equation 2.24, p20), and subtracts it from the observed potential values of the MALM data.

Equation 2.24 was coded into a Matlab function (Code 3.1) and evaluated at the surface potential electrode positions. Input data for the function contains the X, Y and Z coordinates (xobs, yobs, zobs) of the potential electrodes and the potential values (pot) in volts at those positions. The main variables were source electrode position (c1x, c1y, and c1z), input current (tc), and resistivity of the half-space (rho). From Equation 2.24, *r* is the distance between the potential electrode position (xobs, yobs, zobs) and the source electrode position (c1x, c1y, c1z).

```
for i = 1:srow    % For the length of the data...
    a = abs(xobs(i)-c1x);    % Distance of c1x from data
    b = abs(yobs(i)-c1y);    % Distance of c1y from data
    c = abs(zobs(i)-(abs(c1z)));    % Distance of c1z from data
    ev(i) = 2*((tc*rho)/((4*pi)*(sqrt(a^2+b^2+c^2))));    % Calculation of Electrode Effect
end

resid = pot - ev;    % Calculation of residual data by subtracting ev from potential data.
```

Code 3.1: EER code, ev(i) is the value of Equation 2.24 at the i^{th} *potential electrode position (xobs, yobs, zobs). ev is a function of the distance of the source electrode position (c1x, c1y, c1z) from the potential electrode position and the variables tc and rho.*

The function accepts not only 2D data but 3D MALM data from other boreholes or mineshafts. The algorithm has been written to be able to examine non-current normalised MALM data (i.e. tc equals the transmitted current value).

Since the electrode effect (ev) is calculated at the potential electrode positions locations, it is a straightforward calculation to subtract ev from the observed potential data (pot), to give a residual potential value (resid) at the same positions as the input data (Code 3.1). The function outputs both resid and ev for gridding and display.

The residual potentials are the equivalent to the second integral of Equation 2.26; the potential contribution due to charge accumulations at resistivity boundaries within the subsurface of a semi-infinite, inhomogeneous, isotropic earth. The goal of the EER function is to recover the second integral contribution, therefore revealing charge distribution due to mineralogical and lithological changes in the geology of the area.

Application of the EER algorithm

The EER algorithm was applied to both field data and idealised FEM modelled response. All data has been current normalised (in the case of the FEM models, the responses were calculated with a unit source) and the remaining inputs for the EER functions are constants (i.e. position of source electrode hence the distance, r, the input current, tc = 1, and the scalar $4*\pi$). This simplified process of using the EER algorithm as the electrode effect became a function of the resistivity of the half-space, $\rho_{halfspace}$, for a given electrode position. Therefore the EER function scales linearly with the input resistivity for an electrode depth (Figure 3.44). For example, the electrode effect is large when $\rho_{halfspace}$ is large, such as in a near-miss scenarios where the electrode is placed in contact with the resistive host rock. The opposite occurs for an in-mineralisation scenario, where the low resistivity of the mineralisation results in a small electrode effect being removed. Thus, for conventional MALM, the residual potential does not reveal any more information.

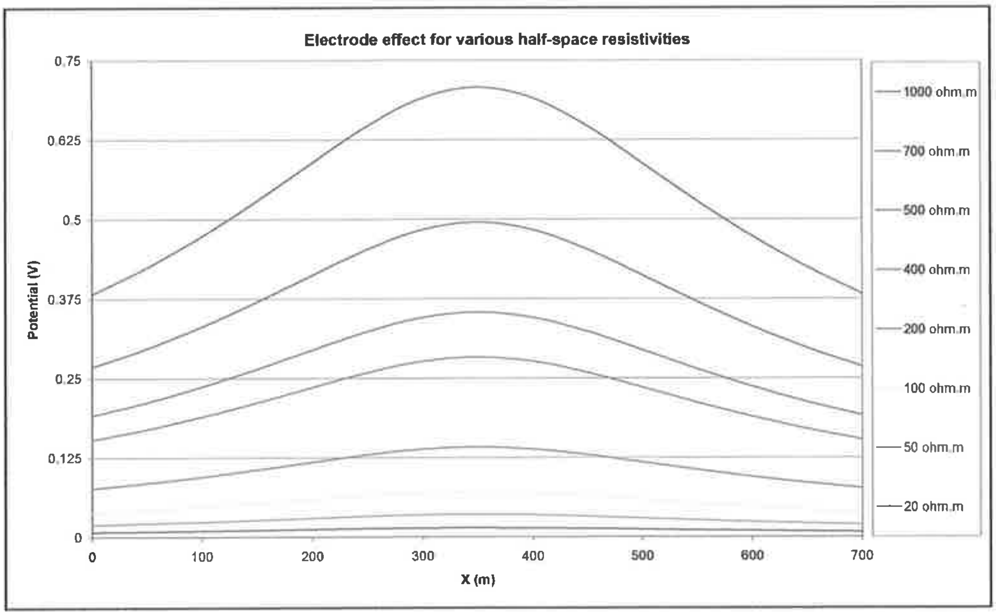

Figure 3.44: Electrode effect scales linearly with increasing resistivity for the same electrode depth. These are the symmetrical profiles generated by the EER function for resistivities 20, 50, 100, 200, 400, 500, 700 and 1000 ohm.m along X=350. The source is positioned at 350,350,225 m in a half-space of 700 by 700 by 700 metres.

The application of the EER function was reduced to a systematic search for the most appropriate resistivity, $\rho_{halfspace}$ that enhances the surface MALM potentials to reveal more information on the subsurface structures that exist in the earth/model.

Finite element modelling has been used to verify the EER methodology under simplified conditions. As the location and resistivities are precisely defined in the models it was a matter of finding a resistivity value for the EER function that resulted in surface potentials that better defined the models. This is highly applicable to the modelled near-miss scenarios as the peak of the anomaly was not always centred over the conductive structure as seen in the modelling. The resistivity values used were constrained such that no negative residual potentials occurred, that is the minium electrode effect potentials calculated cannot exceed the minimum modelled potentials. The idealised FEM models present in the "3D Finite element method modelling" section (p33) are passed through the EER function with the results detailed in Section 4.2, p92.

The EER function was also carried out for the FEM modelled field sites as a prelude to the application of the EER on the field data. Despite having only a qualitative similarity with the actual field data, these models helped identify what ranges of resistivities are applicable to the field site models. The aim of the EER function with the models based on simplified field geology was to deduce consistent residual potential anomalies between the different electrode positions that correlated to the modelled geology in each field area, Catalpa, Catalpa North and Prominent Hill.

The goal for the EER function applied to the field MALM data was to identify residual potential anomalies that correlated to the known geology as well as residual potentials from other surveys in the same field area. This implies that the EER function augments interpretations on a MALM data set by isolating those potentials associated with the subsurface geology.

Subsurface Approximation (SSA)

In general, no single unique model of the earth can be derived for potential field data (Keller and Frischknecht, 1966). For SP data, Di Maio and Patella (1994) developed a multiple-source location method to delineate hydrothermal fluid flow in active volcanic regions. Hämmann et al. (1997) used a modified version of this algorithm to investigate SP gradient anomalies associated with groundwater flow. The Image Reconstruction (IR) algorithm (Hämmann et al., 1997) and the algorithms developed by Di Maio and Patella (1994) and Patella (1997 a & b) make use of the horizontal components of the electric field. Super-positioning of numerous elementary sources can unambiguously represent SP data, with the spatial distribution of the sources determined by a pattern matching algorithm (Di Maio and Patella, 1994).

For the purposes of this investigation the IR algorithm (Hämmann et al., 1997) was modified to create the Subsurface Approximation (SSA) algorithm (Code 3.2). The SSA algorithm investigates absolute potentials (as opposed to electric field components in the IR algorithm) via super-positioning and correlating elementary point sources in 3D to the 2D MALM data.

The 3D SSA algorithm parallels the 2D IR algorithm, by executing:

a 3D volume scan of elementary source point positions;

a cross-correlation calculation of the super-positioned source points to the MALM data;

a normalisation of cross-correlations coefficients for sources at different depths.

SSA Algorithm and code

The SSA code accepts a 2D MALM data set and investigates the data as a distribution of point sources in 3D which satisfy the electrical potential field observed in the MALM method. Surface potentials can be described by elementary point sources, assuming a uniform and homogeneous background resistivity. Equation 2.24 is the potential due to a homogeneous, isotropic half-space via the method of images, where the distance, *r*, from the point source to *P*, is written in Cartesian distances, *x*, *y*, and *z*.

$$V(P) = \frac{2\rho I}{4\pi(\sqrt{x^2 + y^2 + z^2})}$$

Equation 3.1

The assumption of a uniform resistivity and elementary point source removes all constants and reduces Equation 3.1 to Equation 3.2, the potential, V_{ele}, at a position *P* due to an elementary point source, where *x*, *y* and *z* are the distances the source from *P* in their respective axes (Telford et al., 1990).

For an elementary source, Equation 2.24 reduces to;

$$V_{ele} = \frac{C}{\sqrt{x^2+y^2+z^2}}, \text{ where } C = \frac{2\rho I}{4\pi}, \qquad \textit{Equation 3.2}$$

The measured potential field, V_{meas} (Equation 3.3), can be overtly characterised by the super-position of potentials, V_{ele}, from numerous elementary sources.

$$V_{meas} = \sum_{i=1}^{n} V_{ele}^{i} \qquad \textit{Equation 3.3}$$

```
01  function [SSAtrix,XI,YI,ZI] = SSA(xdata,ydata,data);
02
03  amax = linspace(min(xdata),max(xdata),xlin);          %linear space of 100 points in X
04  bmax = linspace(min(ydata),max(ydata),ylin);          %linear space of 100 points in Y
05  cmax = linspace(-700,-0.0005,zlin);            %must not equal 0 to avoid div zero error
06  srow = length(data);
07
08  % correlation start
09  for a = 1:length(amax)             %For range of amax in x direction
10    for b = 1:length(bmax)           %For range of bmax in y direction
11      for c = 1:length(cmax)         %For range of cmax in z direction
12        for v = 1:srow               %Iterates through data points.
13          g(v)=1/sqrt((cmax(c))^2+(xdata(v)-amax(a))^2+(ydata(v)-bmax(b))^2);
14        end
15        chat = sum(g'.*data);
16        cnorm = sqrt( (sum(g.^2))*(sum(data.^2)));
17        SSAtrix(b,a,c)=chat/cnorm;
18      end
19    end
20  end
21
22  [i j k] = size(SSAtrix);
23  XI = linspace(min(xdata),max(xdata),j);
24  YI = linspace(min(ydata),max(ydata),i);
25  ZI = linspace(-700,-1,k);
```

Code 3.2: Matlab function SSA.m. From the inputs xdata, ydata and data, the function outputs a 3D matrix (SSAtrix), and three vectors (XI,YI,ZI) which describe the volume of the 3D matrix: these outputs are used by the graphics code "sliceomatic.m" a freely available Matlab function developed by Eric Ludlam of Mathswork. Line numbers have been added for ease of reference.

The function SSA.m accepts the *x* and *y* coordinate (*xdata, ydata*) for the MALM surface potential observations (*data*) (Code 3.2, line 1). The defined scanning function, *g*, relies on the dimensions in Equation 3.2.

$$g(x_i, y_j, a, b, c) = \frac{1}{\sqrt{(x_i-a)^2+(y_j-b)^2+c^2}}, \text{ where } c < 0 \qquad \textit{Equation 3.4}$$

Line 13 of Code 3.2 is the scanner function (Equation 3.4) defined using Equation 3.2, in which a subsurface elementary source point at position (*a,b,c*) generates a potential field at position (x_i,y_j) on the surface. This is done for numerous points within the volume beneath the MALM data. The limits in the *x* and *y* directions are defined by the extents of the surface data set (min/max *xdata* or *ydata*). The limits for the *z* direction are arbitrarily specified by the user, satisfying the condition such that *c* is less than zero. In all uses of the SSA algorithm, this depth range was specified to include the vertical depth of the source electrode, both in FEM idealised modelling and for the observed field site MALM surveys.

Lines 3, 4 and 5 generate linearly spaced points, the number of which is set by *xlin, ylin* and *zlin*, in the *x*, *y* and *z* directions respectively. These variables define the number of nodes for the output 3D matrix. The SSA algorithm takes longer to run with more nodes. An acceptable compromise between speed of execution and 3D matrix resolution was reached with *xlin, ylin* and *zlin* being equal to 20, 20, and 100 respectively or 40,000 nodes.

The multiple elementary source potentials, as defined by the scanner function $g(x_i,y_j,a,b,c)$, are super-positioned and correlated to the MALM surface data (Equation 3.5) (Hämmann et al., 1997).

$$\hat{C}(a,b,c)=\sum_i\sum_j g(x_i,y_j,a,b,c)V_{meas}(x_i,y_j) \qquad \textit{Equation 3.5}$$

By multiplying $g(x_i,y_j,a,b,c)$ with the potential data, V_{meas}, the resultant Ĉ is the sum of the observed potentials scaled by $g(x_i,y_j,a,b,c)$. Equation 3.4 equates to line 15 of Code 3.2. Hämmann et al. (1997) divided Ĉ by a normalisation factor based on the sum of the squared scanner function multiplied by the sum of the squared observed electric field. The IR algorithm yielded a C_{norm}.

$$C_{norm}(a,b,c)=\frac{\hat{C}(a,b,c)}{\left[\sum_i\sum_j g^2(x_i,y_j,a,b,c)\sum_i\sum_j V_{meas}^2(x_i,y_j)\right]^{\frac{1}{2}}} \qquad \textit{Equation 3.6}$$

The normalised and dimensionless correlations have values in the range of -1 to 1, where the minima and maxima of C_{norm} defined the positions of negative and positive elementary SP sources. In Equation 3.6, the same normalisation as used by Hämmann et al. (1997) is modified by replacing the squared observed electric field with the square of the observed MALM potentials.

C_{norm} for the SSA.m function (lines 16 and 17 of Code 3.2) results in dimensionless correlation values in the range of 0 to 1 (cf. IR algorithm output). The maxima of the SSA define positions of potential sources since the applied potential method results in no negative sources. Where the SSA outputs values close to zero (poor correlations to the data), these positions are unlikely to be elementary potential sources. SSAtrix (line 17) is the 40,000 node 3D matrix of correlation values with dimensions (xlin,ylin,zlin). The last four lines of Code 3.2 outputs axis dimensions (*XI*, *YI*, and *ZI*) for the volumetric display code sliceomatic.m (freeware written by Eric Ludlam, Mathsworks, 2002).

sliceomatic.m accepts the SSAtrix correlation matrix and the three variables for defining the correlation volume. This display function was used to analyse the output of SSA.m, and allows for slices to be made of the correlation volume, parallel to the 3 axes. Surfaces of equal correlation within the volume can also be defined and aid in the interpretation of the source points to the potential data set passed through the SSA algorithm.

Interpretation of the SSA algorithm

For electrical potential field data in general, a shallow source point produces a high frequency, high amplitude potential pattern which does not correlate well with the broad, low amplitude MALM data. Therefore shallow elementary source points are unlikely to have a high correlation (Figure 3.45). The potential field of the source has a lower frequency and amplitude with increased depth. Therefore the elementary sources at mid to lower depths have a higher correlation with the MALM data.

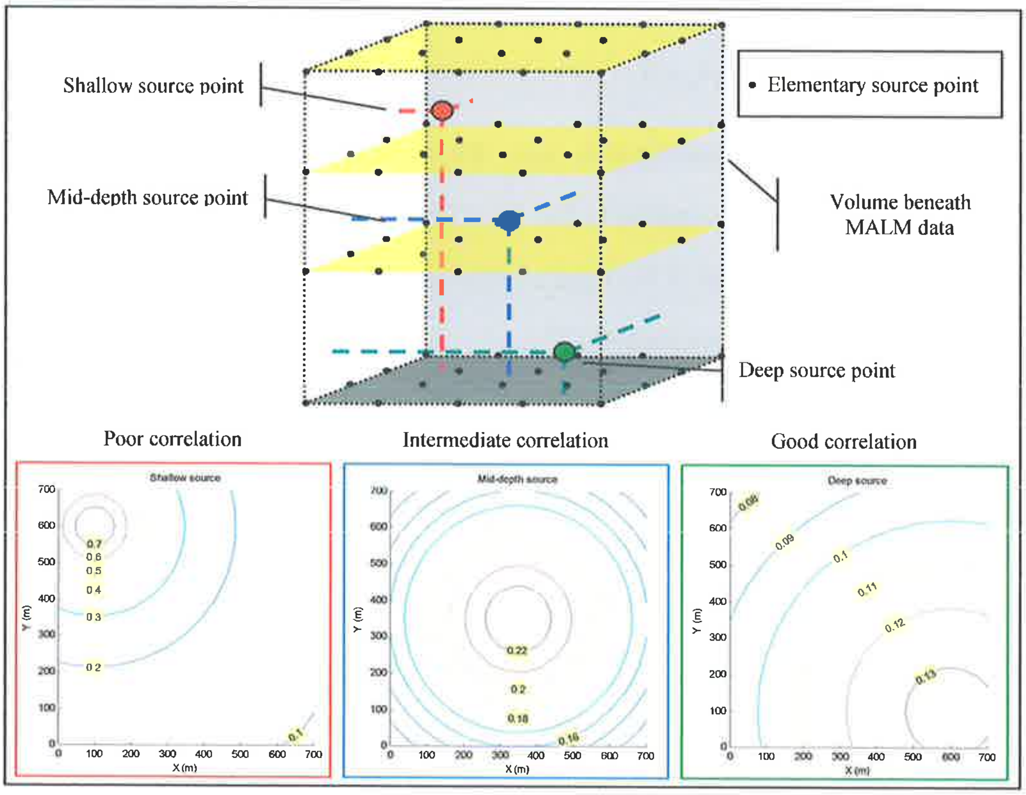

Figure 3.45: The top portion of this figure shows the volume beneath the MALM data being scanned with numerous elementary source points. The lower portion of the figure displays the potential fields created by elementary source points at various depths and locations in the volume. In general, shallow sources do not correlate well with broad MALM anomalies, the correlation increases with increased depth. This is dependent on the data.

These correlation coefficients are reflective of the geology which generates the MALM response as the positions of highest correlation are deemed to be the most likely sources of the electrical potential pattern seen in the MALM data.

Known limitations

Hämmann et al. (1997) identified several limitations for this algorithm. The primary limitation is the basic assumption of uniform background resistivity and elementary source super-positioning. If these two axioms are violated, the subsurface approximations are valueless. It is difficult to directly interpret geological features from the subsurface approximations, but when it is used in combination with other geological/geophysical information, the algorithm may provide useful, qualitative constraints on such features (Hämmann et al., 1997).

Application of the SSA algorithm

Idealised models allow for a simplified appraisal of the capabilities of the SSA algorithm. The surface potentials generated by the FEM program were passed through the SSA algorithm and the normalised correlation values qualitatively analysed for the best approximation of resistivity features in the models. Both iso-correlations and contoured slices of the correlation matrix are used in the investigation. The results from these models aided in the interpretation of more complicated geological scenarios such as the Golden Grove and Prominent Hill field site models and the acquired MALM data.

The FEM field site models are also analysed with the SSA algorithm for trends in the correlation matrix that can be associated with the modelled geology. As with the idealised models, interpretations of the correlation volume are made via iso-correlation surfaces and slices through the volume. It was of interest to compare the SSA output from the FEM models and their observed MALM counterparts to understand the similarities due to the qualitative trends seen in the response in both the modelled response and the observed data (see Forward models of field sites, p58). Data from the 9 field MALM surveys acquired were also passed through the SSA algorithm, 4 from Catalpa, 4 from Catalpa North and the single survey from Prominent Hill. The wide range of in-mineralisation, near-miss and out-of-mineralisation scenarios from this set of data along with the interpretations from FEM modelling allows for an in-depth investigation into the performance of the SSA algorithm on MALM data. Correlation matrices derived from the MALM data set were studied for connections to known geology, depth to target and lateral extent of conductive structures.

The combination of the Electrode Effect Removal and the Subsurface Approximation algorithms allows for the alternative evaluation of the EER function. Residual potentials are more representative of the resistivity contrasts within the earth, hence the distribution of elementary sources are affected by the subtraction of contributions from the source electrode.

3.2 FIELD DATA COLLECTION METHOD

Field MALM data were collected at Catalpa and Catalpa North, Golden Grove, Western Australia as well as at Prominent Hill, South Australia. The field methodology employed by Newmont in Western Australia was the main reference for all subsequent surveys undertaken both at Golden Grove and the single survey at Prominent Hill. The configuration at all field sites is a pole-pole array to measure absolute potentials.

Equipment

Equipment used included a 4KW IP transmitter, the VIP 4000 and an ELREC6 receiver both made by IRIS Instruments (Figure 3.46). The transmitter was powered by a 3 kVA, single-phase generator to produce at least 2A. The ELREC 6 receiver is capable of multi-channel receiver arrays, but for the purpose of this project only a single dipole was used. Approximately 7 kilometres of electrical wire was required for MALM (including 5.5 kilometres for the remote electrodes, 500 metres for the measuring electrode and enough wire to reach the desired down-hole depth). Measuring and remote potential electrodes were Zonge Engineering PPE/1 porous ceramic Cu-$CuSO_4$ pots. The Cu-$CuSO_4$ solution was consistently mixed up such that it was saturated.

A Crone DHEM hand winch aided in lowering and raising the down-hole source electrode (Figure 3.46) A sheave wheel and counter attached to the casing of the drill holes (bottom inset in Figure 3.47) measured the amount of wire lowered down the drill hole. The wheel aided in guiding the wire in the drill hole such that the wire did not rub against the PVC casing.

Figure 3.46: (left) IRIS VIP 4000 transmitter capable of delivering 4KW of power. (middle) ELREC 6 receiver, PPE/1 porous pot (circled) and operators at a measuring station. (right) Crone DHEM hand winch with cable reel and electrode attached and ready to deploy.

Drill holes and hole casing.

Drill holes in Golden Grove were cased for only the first tens of metres with PVC piping, with the rest of the drill hole length being uncased. This meant the source electrodes lowered into the holes were in direct contact with the mineralisation and ground water. Drill hole RP017 at Prominent Hill was cased in 50 millimetre diameter PVC piping for its entire length. The casing had 15 centimetre slots cut into the plastic every 40 to 50 centimetre, allowing ground water penetrate into the drill hole. This ground water served as the primary electrical connection to the conductive chalcocite breccia. This did not seem to have any adverse effects to the MALM result.

Figure 3.47: Casing used at drill hole RP017 (main) The red circles mark the positions of slots cut into the 50mm diameter PVC piping. (top inset) A slot in the PVC pipe with a pen for scale. (bottom inset) Installed PVC casing in RP017 with attached sheave

Electrode construction and configuration

Down-hole current electrode, positions and transmission values

The current electrode used at Golden Grove was a one metre length of steel piping, with the current carrying wire attached via a screw. The upper section of the pipe was bound in electrical tape, which tapered up the wire in an attempt to reduce the chances of snagging.

The construction of the Prominent Hill down-hole electrode involved a section of 20 millimetre diameter copper tubing, roughly one metre in length, drilled at one end to attach an 8 millimetre D-shackle. This shackle provided an attachment point for the wire which ran down the centre of the tube. A 20 millimetre Dynabolt, inserted at the other end of the tubing acted as a weight and was used to electrically secure the wire to the copper tubing. The upper section of the electrode, where the D-shackle was mounted was covered with electrical tape in an attempt to reduce the chances of snagging (Figure 3.48).

Figure 3.48: (top left) Shackle bound in electrical tape to reduce chances of snagging. (bottom left) Graph of resistances measured down-hole. (right) Prominent Hill electrode, 1m long, 20m diameter copper pipe with 20mm Dynabolt at the bottom and 8mm shackle at the top.

For all surveys at Golden Grove and Prominent Hill, the down-hole source electrode was placed at the depth of lowest resistance within a mineralised drill hole intersection. This was found by attaching a multimeter to the remote current electrode and to the down-hole current electrode and measuring the total resistance every ten metres down-hole. This distance was reduced to 1 metre when a resistance low depth region was encountered, allowing for a more accurate placement of the down-hole electrode. The resistance logs for the Golden Grove drill holes are unavailable as they were collected by a contractor.

The surveys at Catalpa were targeting a conductive body approximately 700 metres down-hole in RHDD018 and RHDD020. This massive pyrite/chalcopyrite has two in-mineralisation electrodes, RHDD018 and RHDD020 Setup A. RHDD020 also encompasses two near-miss surveys, one at the shallower depth of 481 metres, above the mineralisation intersection and another at a depth of 920 metres, well below the intersection. The direction and surface projection of these electrodes can be seen in Figure 1.6 (p9). Catalpa North had no significant mineral intersections but the electrodes were placed in zones of low resistivity caused by trace mineralisation. The drill holes and electrode projections for Catalpa North appear in Figure 1.7 (p10).

The target at Prominent Hill was the chalcocite breccia. Multimeter readings were taken from a down-hole depth of 370 metres to 440 metres at an interval of ten metres. The depth intervals were reduced to one metre spacings at the low values about 408 metres. The current electrode was placed at 405 metres down-hole depth as the resistance was 400 ohms. The down-hole resistance log for Prominent Hill is shown in Figure 3.48. This shows the large variability of resistances even within a few metres at this depth.

Transmission values

Table 3-5 lists the values for transmitted current at each survey's down-hole electrode position. This value remained constant throughout the survey.

Golden Grove		
Drill hole	**Down-hole Depth (m)**	**Transmitted Current (A)**
RHDD018	688	5.0
RHDD020 Setup A	697	5.0
RHDD020 Setup B	481	1.0
RHDD020 Setup C	920	3.8
RHDD010	430	4.5
RHDD038	416	2.2
RHDD040 Setup 1	455	3.0
RHDD040 Setup 2	975	3.0
Prominent Hill		
Drill hole	**Depth (m)**	**Transmitted Current (A)**
RP017	405	2.0

Table 3-5: Table of transmission values used at both field sites.

Measuring potential electrode

The roaming Cu-$CuSO_4$ measuring potential electrode was placed in a shallow hole filled with saline bore water to ensure a good coupling. A quick check on the receiver of the contact resistance was done at each station. If the contact resistance was greater than half a magnitude in difference to the last station, the hole was dug deeper and more water added to reduce the contact. The check for a consistently low contact resistance made sure the data were not degraded with electrode contact inconsistency. This is of importance as the voltages being measured are low, and the contact resistances have an impact on the measured potentials.

Remote electrode placement and construction

The literature states that as the remote electrodes are moved to greater distances, the effect on the potential measurement is reduced. Therefore, the placement of the remote electrodes along or across geological strike should be irrelevant. In the surveys conducted, the remote electrodes was found to be suitably isolated by placing both the remote electrodes at a distance approximately equal to 2 kilometres from the edges of the grid. The remote current electrode was placed across strike to the mineralisation (Ketola, 1972), whilst the remote potential electrode was placed along strike with the mineralisation (Parasnis, 1967).

The remote current electrode was at both sites was constructed by digging a shallow pit, lined with aluminium foil and covered with water and soil. This electrode makes for good contact to allow for a high transmitted current.

At Golden Grove, the remote current electrode positions were the same for each area (i.e. Catalpa, Catalpa North), that is, 2 kilometres west from the survey grid along grid road, no location data is available. The remote current electrode measured 2 by 2 by 0.2 metres. Three forty-four gallon drums of water poured into the electrode pit guaranteed the electrode would remain moist enough to transmit large currents for the multiple surveys which used that current electrode. The pit was refilled with water every six to seven days and the aluminium foil checked for degradation. This pit was placed to the west of the mineralisation as the strike direction was aligned north-south on the mine grid.

Figure 3.49: (left) A remote current electrode pit, with some of the aluminium foil exposed to connect to the wire leading back to the transmitter. (right) A buried and watered remote potential electrode (blue circle) with a GPS unit for scale, the pink wire leads back to the receiver.

At Prominent Hill, the remote current electrode pit measured 1 x 1 x 0.15 metres and was wetted with eighty litres of water over the period of two days. The electrode was placed across strike from the mineralisation (east-west), to the north of the grid at the coordinates 555492E, 6714463N, or 1913 metres from the northern edge of the grid.

The remote potential electrode was a PPE/1 porous ceramic Cu-$CuSO_4$ pot, placed in a shallow, bore-water filled hole. The remote potential electrode was deployed everyday and the pit refilled with water. It was also collected at the end of a day's surveying and the solution levels checked.

At Golden Grove, the remote potential electrode was placed 2 kilometres to the south, along strike of the mineralisation, no GPS reading was taken. At Prominent Hill, the remote potential electrode was placed along strike of mineralisation to the west of the grid at coordinates 553061E, 6712129N, or 1989 metres from the west edge of the grid.

Data collection

Survey grids

MALM data can be collected at non uniform points within a survey area. However for ease of processing and systematic field collection, a series of regular line and station intervals are helpful. Every attempt was made to make the coordinates of the station locations as accurate as possible. However, the smooth nature of the MALM response allowed a handheld GPS to be used to lay down the grid or by pacing fifty metres from station to station along a pre-cleared mine grid.

Golden Grove

The surveys at Golden Grove (Table 3-6) had a station-spacing of 50 metres, but the line spacing was variable, due in part to the use of cleared mine grid lines. Line spacing ranged from 80 to 180 metres. RHDD018 and the 3 RHDD020 surveys had lines which did not span the width of the survey, and were selectively placed to better resolve the anomaly.

RHDD010 does not conform to a regular grid pattern. The lines in this survey follow trends in the MALM response, attempting to map where the potentials close rather than the entire survey area. This is the only unusual sampling grid of the entire data set. This inconsistent data set was included to test the abilities the SSA algorithm to cope with non-uniform data sets. The number of MALM station readings for RHDD040 Setup 1 is less to the north and south in comparison to RHDD038.

Table 3-6: The survey areas used at the two field site, listed as origin and dimensions

Golden Grove	Minimum Value		Dimensions (m)		Figure Number
Drill hole	Easting	Northing	East - West	North - South	
RHDD018	4600	18700	900	1060	Figure 3.50(left)
RHDD020 (Setup A)	4600	18460	900	1300	Figure 3.50(left)
RHDD020 (Setup B and C)	4600	18700	900	1060	Figure 3.50(right)
RHDD010	4700	19400	1350	1400	Figure 3.51(left)
RHDD038	4750	19400	1000	1080	Figure 3.51(right)
RHDD040 (Setup 1)	4750	19500	1100	840	Figure 3.51(left)
RHDD040 (Setup 2)	4750	19400	1100	940	Figure 3.51(right)

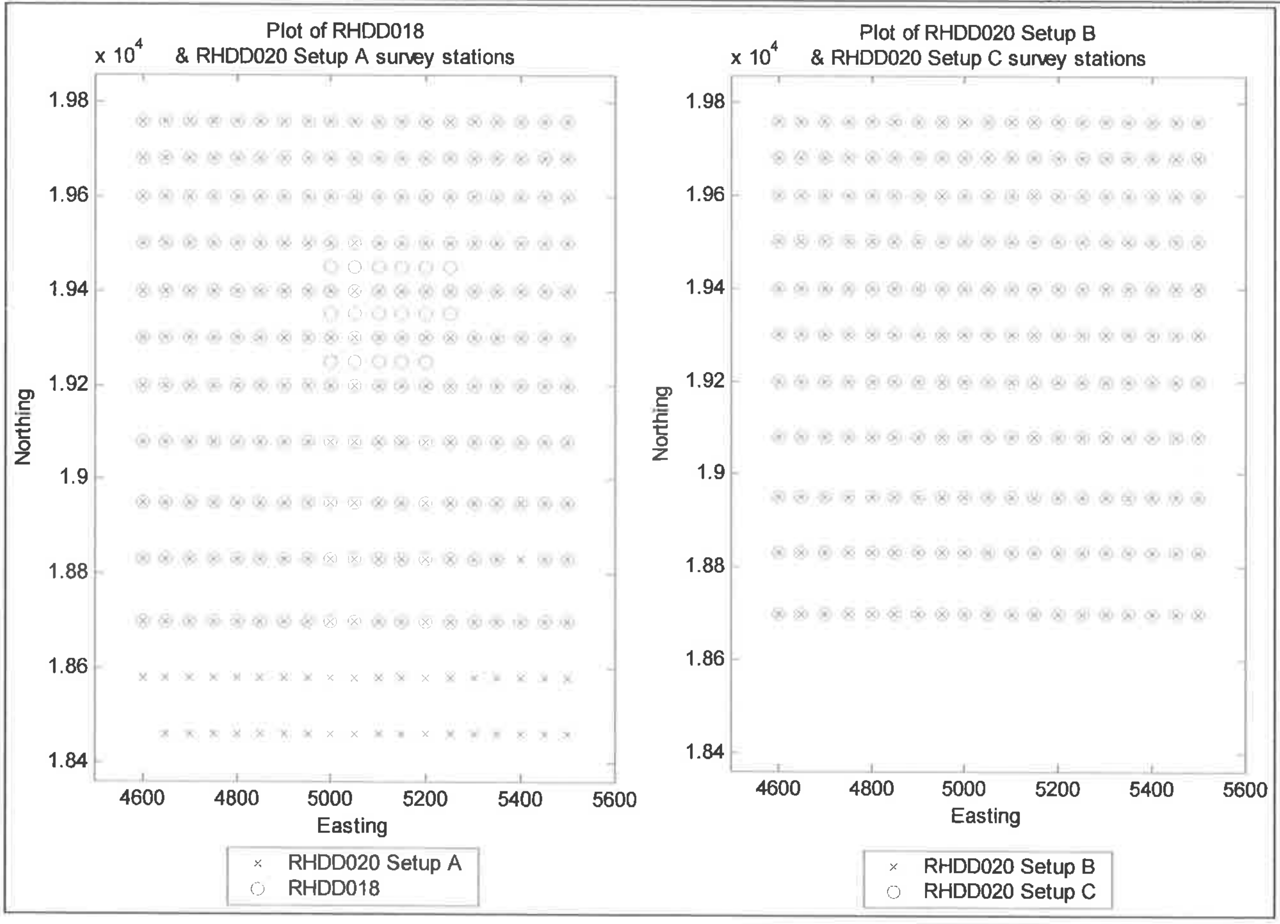

Figure 3.50: (left) Station positions for RHDD018 and RHDD020 Setup A. (right) Station positions for RHDD020 Setup B and C. Golden Grove, WA.

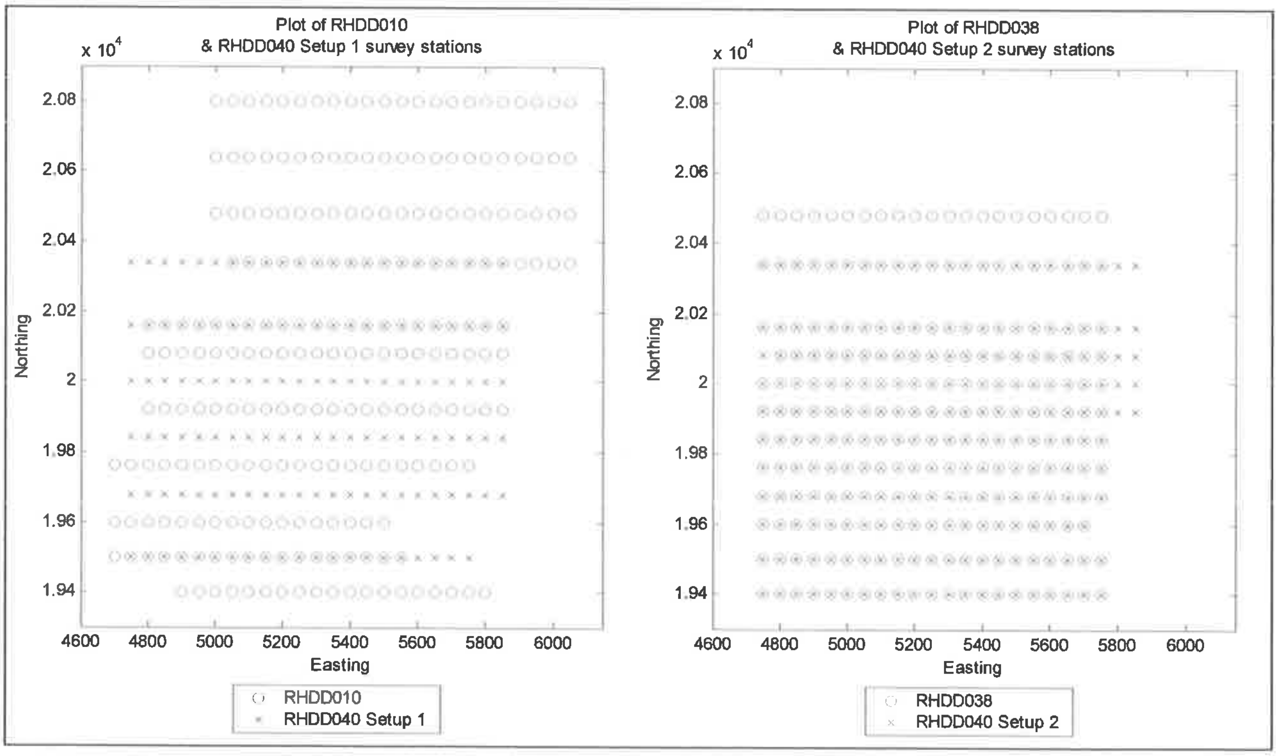

Figure 3.51: (left) Station positions for RHDD010 and RHDD040 Setup 1. (right) Station positions for RHDD038 and RHDD040 Setup 2. Golden Grove, WA.

Prominent Hill

The survey grid had line spacings of 150 metre and station spacings of 50 metre, set out with a GPS unit, akin to that used at Golden Grove (100m line spacing, 50m station spacing). Since the response from MALM is smooth, it is thought that this arrangement would be sufficient to cover the areal extent of the MALM anomaly. The grid is 1050 metres by 850 metres, centred on 556025E, 6712125N (Figure 3.52). The line 555350N was extended an extra two stations to the south to verify the closure of the anomaly to the south.

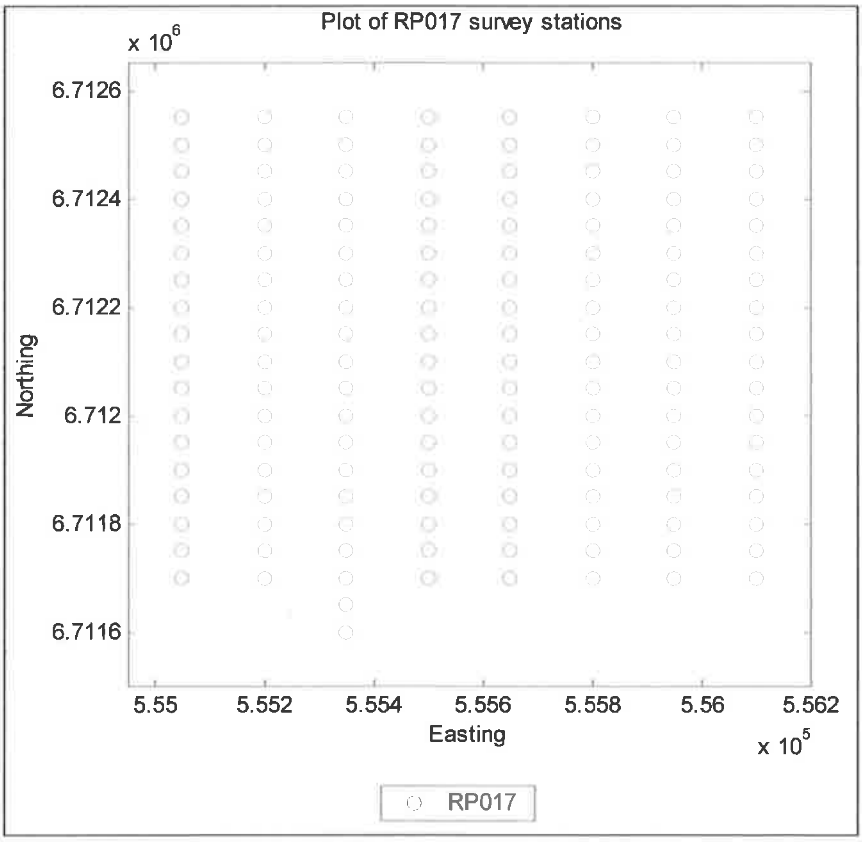

Figure 3.52: Station positions for RP017, Prominent Hill, SA.

Given the volume of results generated in this study, only the most pertinent sets of data are displayed/described. All potential voltages are shown in current normalised form for ease of comparison.

4.1 FIELD MALM DATA RESULTS

Golden Grove

The results for the MALM surveys conducted at the field sites, Catalpa and Catalpa North are displayed as colour maps of surface potentials with contours to enhance the subtleties in that are hard to pick in colour map. The colour scales for the images from Catalpa and Catalpa North have been normalised for each survey area. Therefore, the colour images are associated with potential amplitude and are comparable with other images in the same survey area. The colour scale limits for the two areas are listed in Table 4-1.

The surface electrode position is marked by a red circle on each image. All images are oriented with the mine grid north (52 degrees west of magnetic north) with the contour interval (CI) listed for each figure.

Drill hole	Potential Colour Scale Limits	
	Minimum (V)	Maximum (V)
Catalpa	0.047853	0.283793
Catalpa North	0.032187	0.099067

Table 4-1: The colour scale extents for Catalpa and Catalpa North. The normalised scale for each survey area allows for ease of interpretation of data from the same area.

Catalpa

RHDD018

The in-mineralisation MALM response for RHDD018 (Figure 4.1) has the peak of the anomaly offset to the east from the source electrode position and the anomaly is elongated in the strike direction (north-south). The contours of equipotential continue to the south toward Gossan Hill. This is an in-mineralisation response.

RHDD020

The in-mineralisation response (RHDD020 Setup A, Figure 4.2) is similar to that of RHDD018 but has a higher amplitude (see potential profiles, Figure 3.36, p60). As seen in Figure 4.2, the potentials are elongate in the strike direction with the peak of the anomaly in the same position as RHDD018. Figure 4.3 is the shallow near-miss response from RHDD020 Setup B. The westward extension of the anomaly towards the electrode position results from the near-miss electrode placement. The peak position is similar to RHDD018 and RHDD020 Setup A. The other near-miss position is RHDD020 Setup C (Figure 4.4). The peak position is in the same position as the others in Catalpa but the equipotentials increase towards the Gossan Hill in the south.

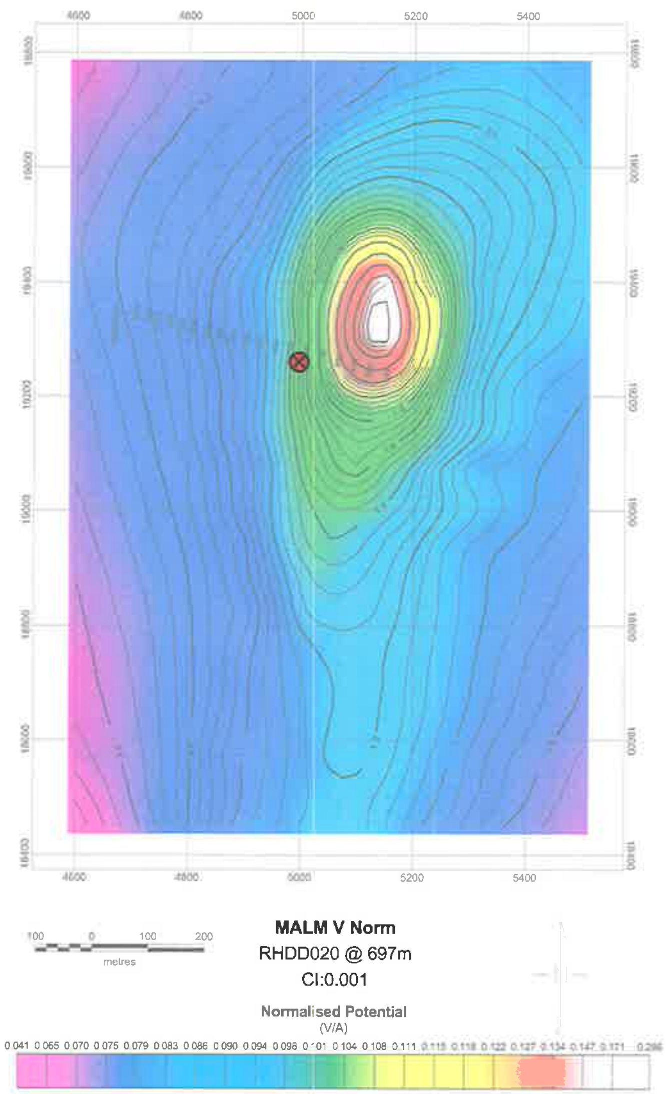

Figure 4.1: RHDD018 potential map. The peak is offset from the source electrode surface position and the equipotentials continue to the south. Depth from surface is 624 metres.

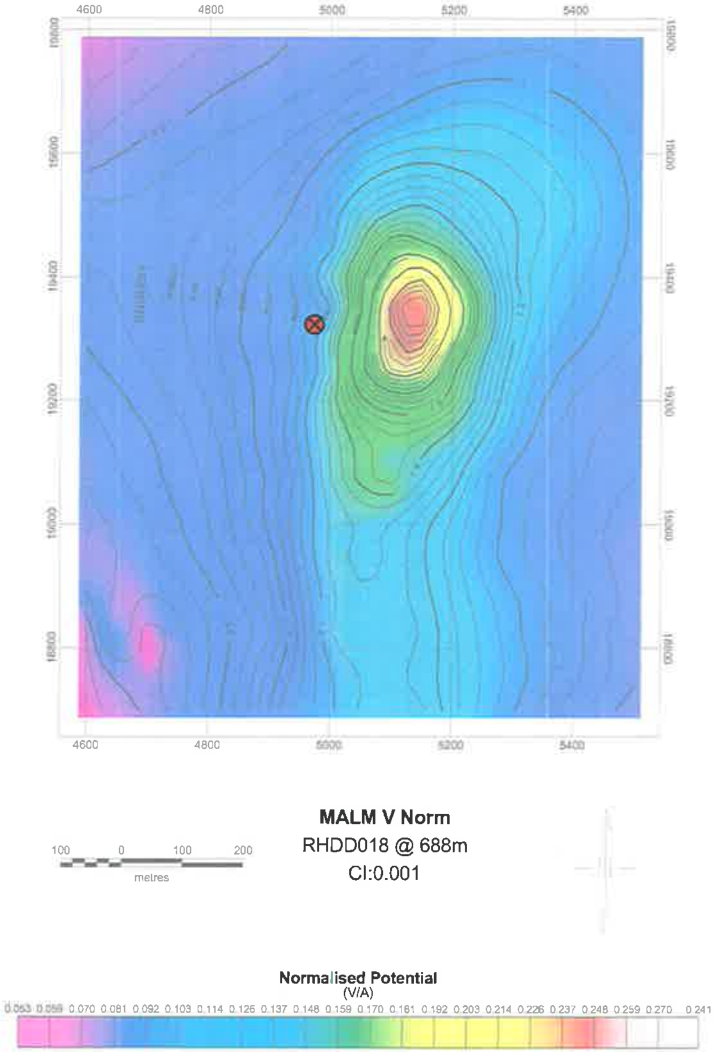

Figure 4.2: RHDD020 Setup A; electrode is a similar depth from surface as RHDD018, 617 metres. The peak value is higher than RHDD018 but in the same position.

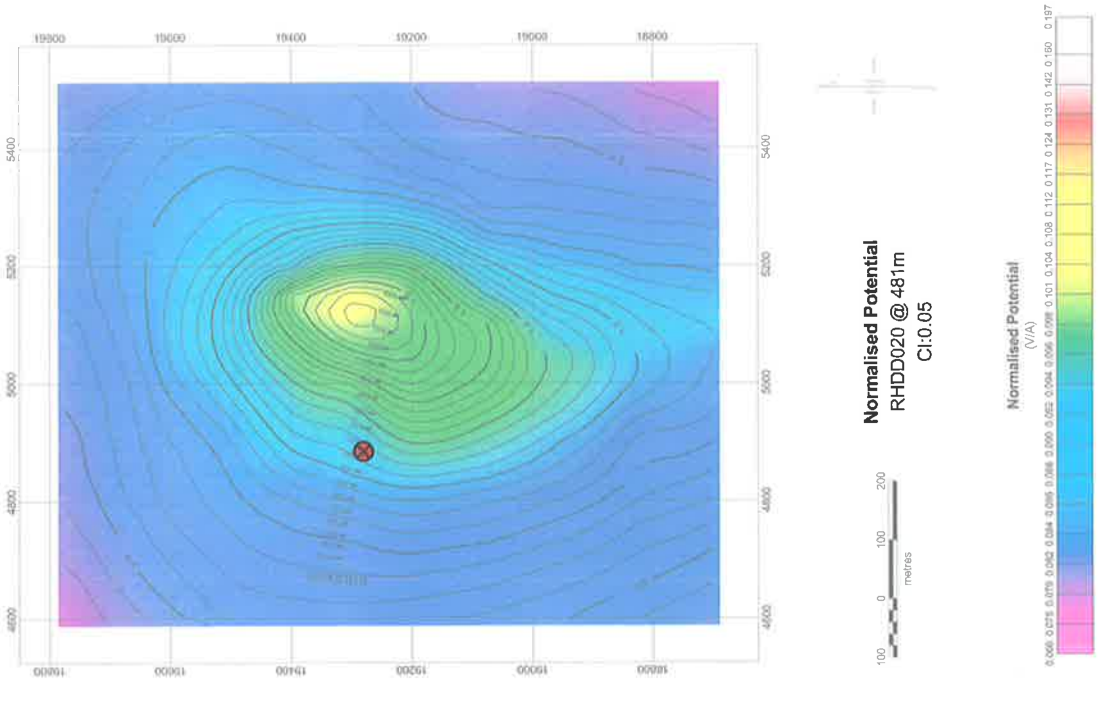

Figure 4.3: RHDD020 Setup B; the peak is in the same position as RHDD018 and RHDD020 Setup A. The anomaly extends to the west towards the electrode position, which is 434 metres below the surface.

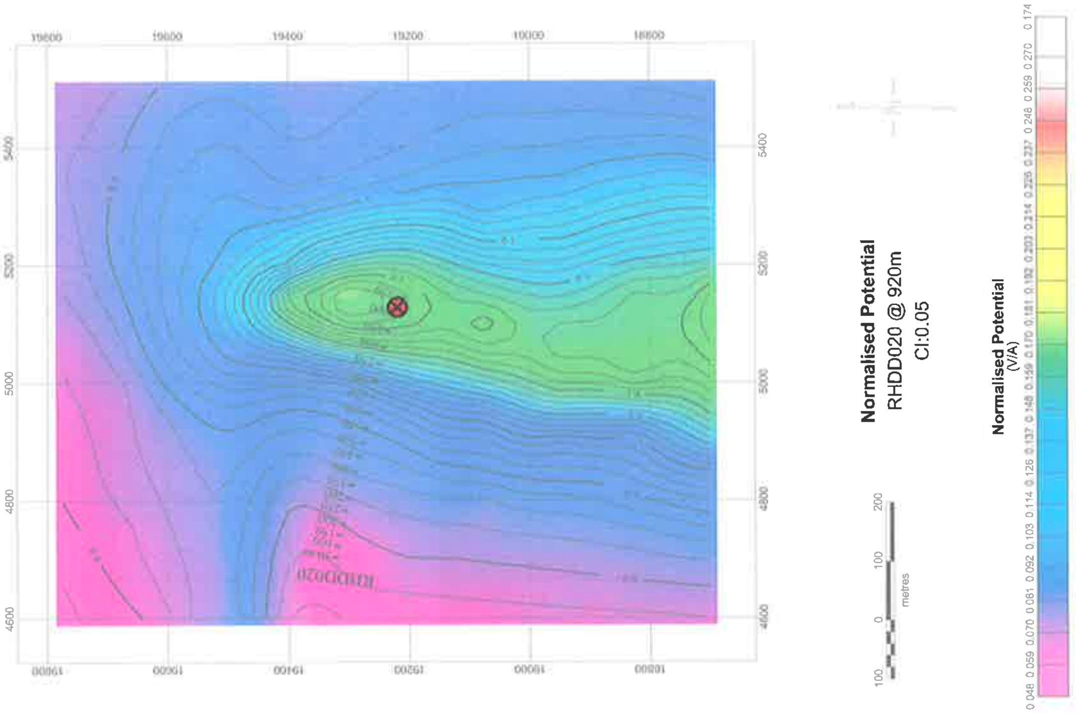

Figure 4.4: RHDD020 Setup C; the equipotentials open to the south in this survey with a deep electrode at 800 metres below the surface. This near-miss electrode setup is similar to RHDD018 and RHDD020 Setup A.

Catalpa North

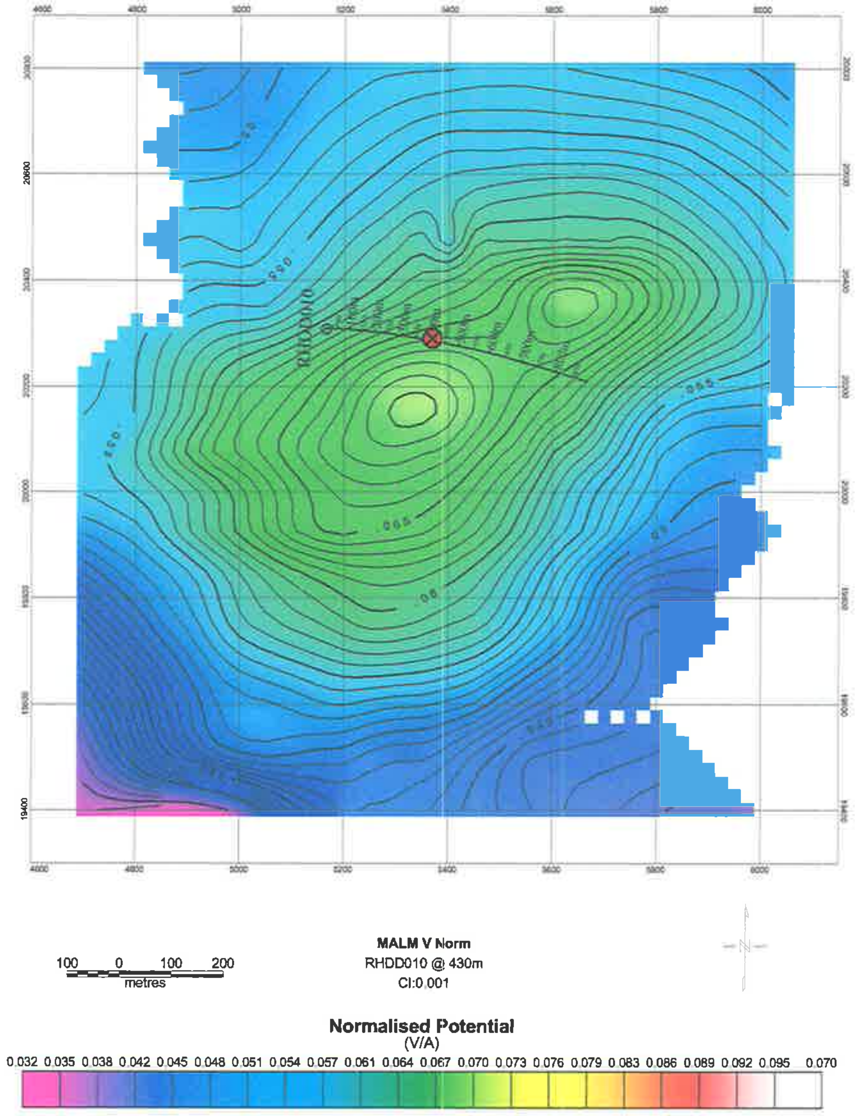

Figure 4.5: RHDD010 has the electrode at a depth of 371m below the surface. This survey has a double peak anomaly straddling the drill hole. The anomaly/ies are elongate in the ENE-WSW direction, which is different to the known strike of the geology.

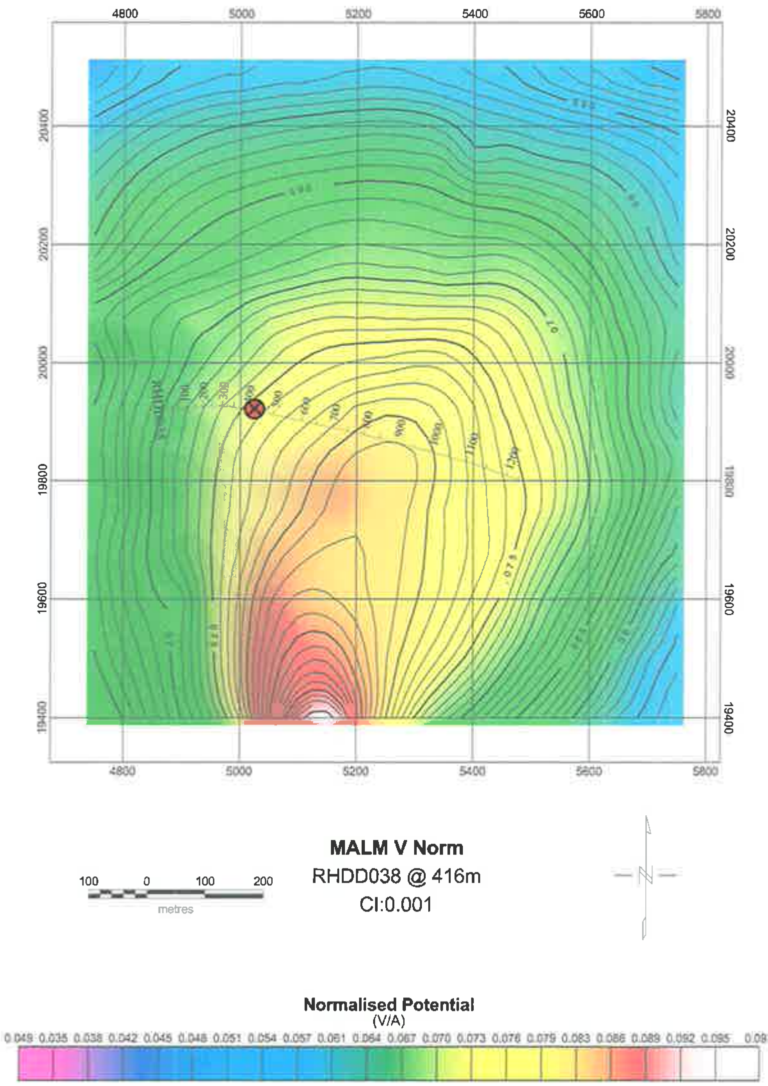

Figure 4.6: Potentials appear to be emanating from a subsurface source to the south of the electrode position. The anomaly fans out to the north and is a broad target. The electrode is not connected to any significant mineralisation.

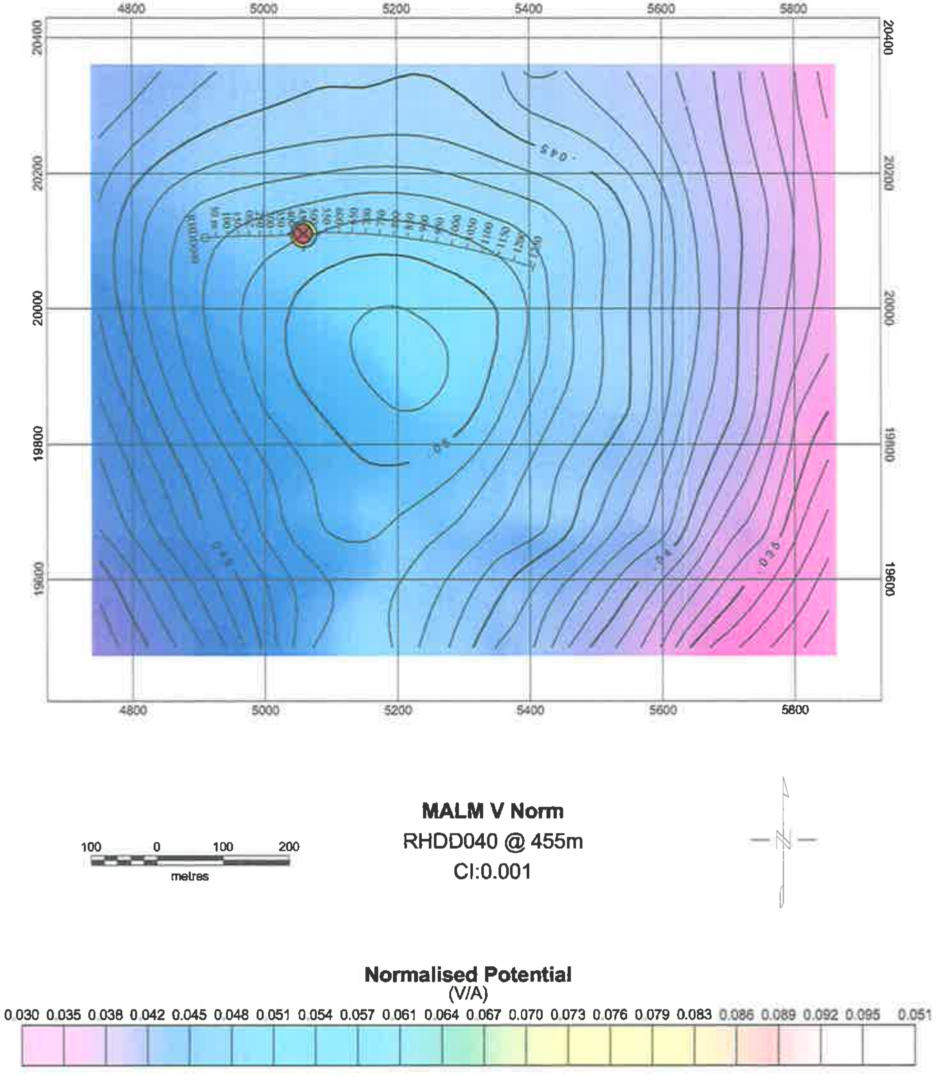

Figure 4.7: RHDD040 Setup 1 has the electrode at a depth of 429m below the surface. The peak of the anomaly is to the south east of the surface electrode position. The equipotentials open to the south as per RHDD038.

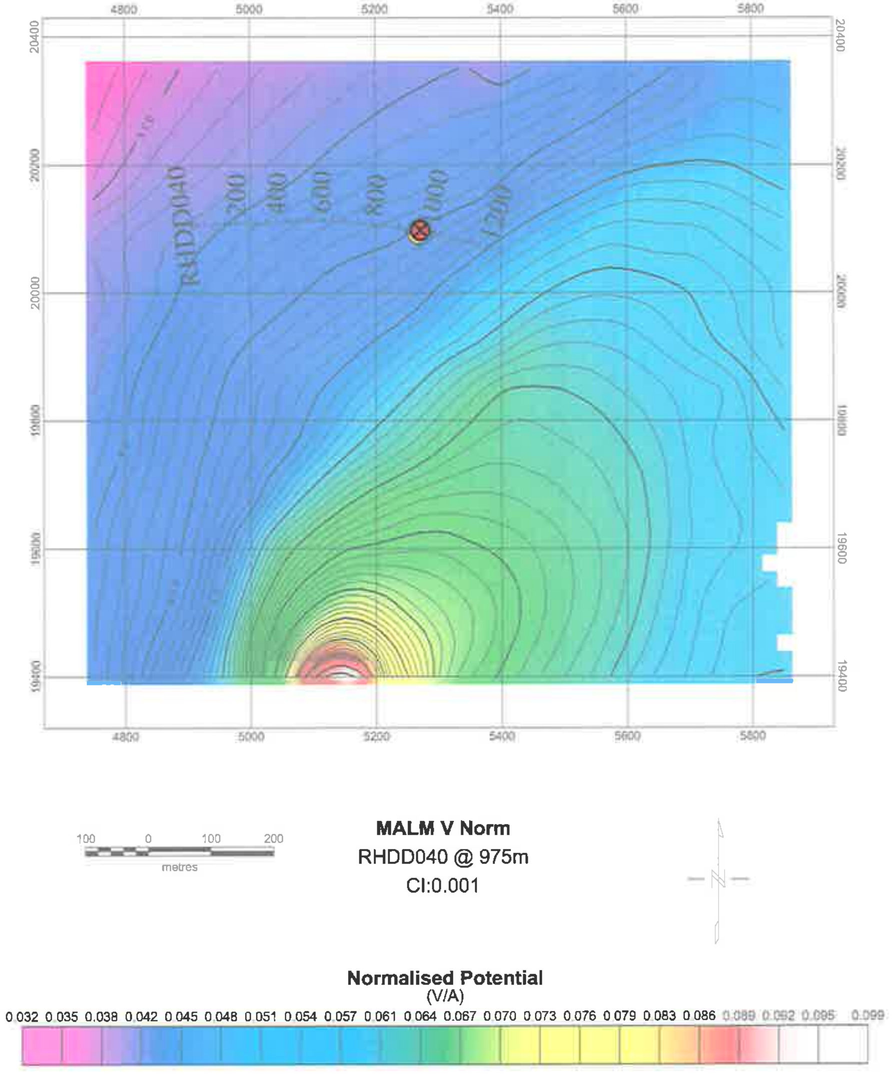

Figure 4.8: RHDD040 Setup 2 with a deep electrode at 904m below the surface. The potentials surround an anomaly to the south of the source position. This is peak has a similar position to that shown by RHDD038.

Catalpa North

RDD010

Figure 4.5 is a double peak anomaly which straddles the drill hole. The peaks are to the east and south of the current electrode position. This scenario is not in any known mineralisation and hence is regarded as an out-of-mineralisation case. The response from the RHDD010 survey is subdued in comparison to the other surveys in the Catalpa North area. This anomaly may be a result of the response from faults which juxtapose materials of differing resistivities, hence creating a resistivity contrast, or variations in the near surface resistivity.

RHDD038

The MALM response for the electrode position has a strong anomaly on the southern margin of the survey area (Figure 4.6). The position of the potential high is consistent in both surveys of RHDD040, indicating that the anomaly is not a collection error, but rather it emanates for the same peak anomaly seen in the RHDD018 and RHDD020 Setup A data (Figure 4.1 and Figure 4.2). The surface potentials radiate from this southern peak into a broad fan, stretching out towards the source electrode position. With only trace amounts of pyrite at the down-hole electrode position, this survey is classed as an out-of-mineralisation scenario. The disseminated pyrites are possibly allowing geoelectric connections which increase the influence of the source electrode.

RHDD040

RHDD040 Setup 1 is a shallow out-of-mineralisation source electrode placement with a large broad anomaly situated to the south-east of the electrode position (Figure 4.7). This broad and subdued response appears to extend to the south towards the peak seen in RHDD038 (Figure 4.6). The deeper electrode position in RHDD040 is different response (Figure 4.8) to the shallow electrode placement. The peak anomaly is in the same position on the southern margin of the survey grid which is associated with the anomaly seen in the RHDD038 survey and the Catalpa MALM surveys. From this peak, the potentials extend and fan out towards the north-east. The deeper source electrode position is not in contact with any known mineralisation. Although the initial appearance of the of the two survey suggests that the method is mapping two different targets, further investigation shows both surveys have an anomalous response to the south for the same hole, implying associated electrical connections for both electrode depths.

Prominent Hill

RP017

The Prominent Hill mineralisation response is offset to the south of the source electrode position and elongate in the direction of geological strike (Figure 4.9). This has the appearance of a classic MALM anomaly. However, due to current conducting, Cu-barren mineralisations adjacent to the energised chalcocite breccia to the south, survey appears to be mapping the position of the conductive barren haematite rock to the south of the target mineralisation. The colour scale for the map is a linear scale from the minimum to the maximum potential value.

By plotting the MALM data set against the gravity data previously obtained at Prominent Hill, it is apparent that the MALM is mapping the geoelectric response of the dense gravity anomaly seen in Figure 4.10. There is no MALM response from the northern magnetic/gravity anomaly (Figure 1.11) implying that the two are not electrically connected.

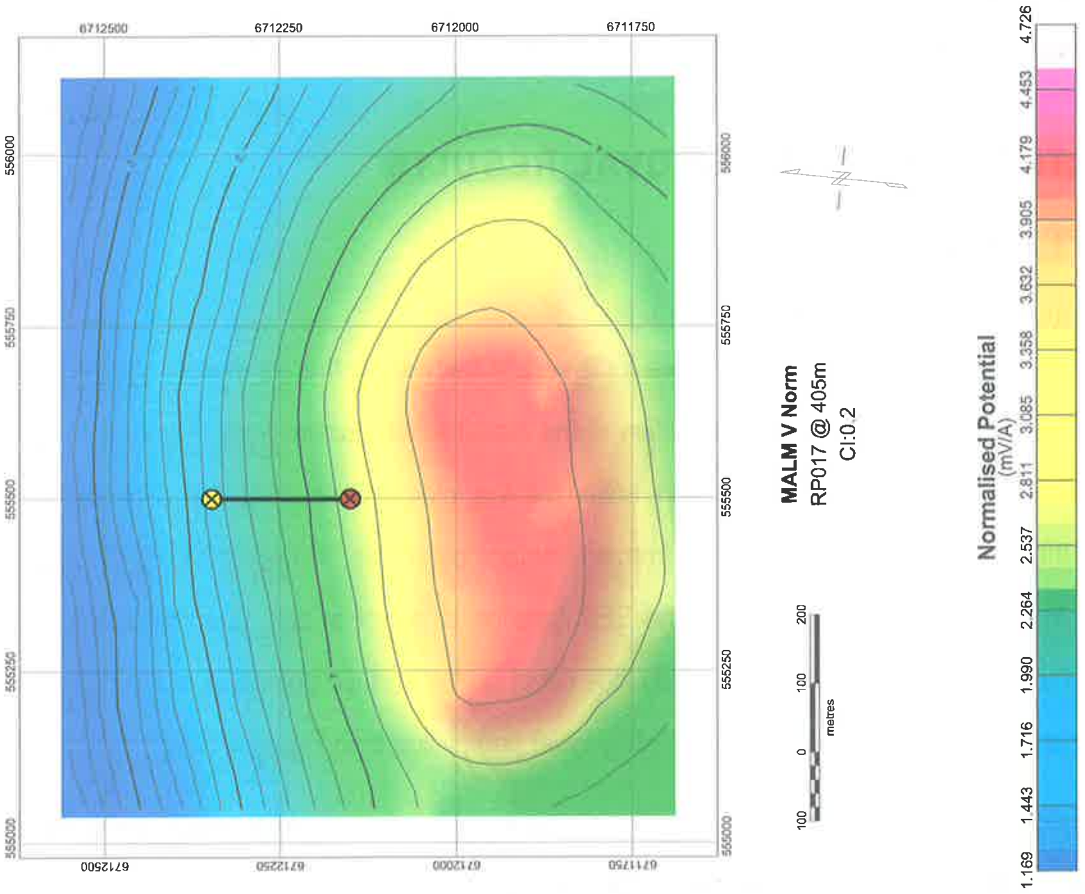

Figure 4.9: RP017 a calculated electrode depth of 351 metres. The red circle marks the surface electrode position and the yellow circle marks the drill hole collar. The anomaly is offset to the south and elongate in the strike direction, (east-west).

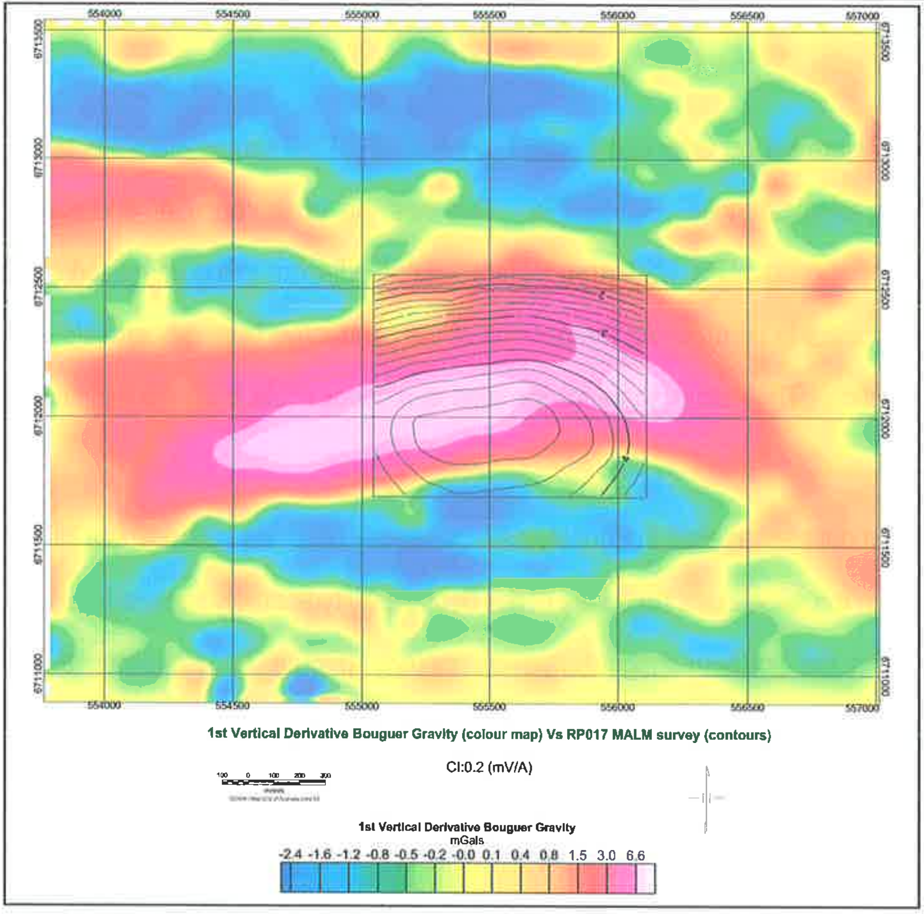

Figure 4.10: 1st vertical derivative of the Bouguer corrected gravity data (colour map, cf. with Figure 1.11) with the MALM survey data plotted as contours. From the background study of the geophysics at Prominent Hill (p13), the MALM anomaly coincides with the dense barren haematite core mapped by the gravity anomaly.

4.2 ELECTRODE EFFECT REMOVAL RESULTS

Idealised FEM models

In-mineralisation models - Vertical body models

Surface potentials generated by the FEM software for a vertical body show that for steeply dipping or vertical conductors, the anomaly outlines the strike direction of the modelled conductive body (Figure 4.11a). Using the EER function to calculate residual potentials enhances the interpretation of MALM data about vertical conductors as the electrode effect is eliminated from the surface potentials. However finding the appropriate $\rho_{halfspace}$ value for the half-space resistivity of the EER function is not clear-cut Low half-space resistivity values result in a low amplitude response that has little effect on the surface potentials of the FEM data; the residual potentials in Figure 4.11b and c have a slightly lower peak value than Figure 4.11a.

With an increased half-space resistivity, the surface potentials show the anomalous peak broadening (Figure 4.11d and e) and the maximum residual potential decreases. If too much electrode effect is removed, the residual surface potentials no longer look like the in-mineralised anomaly pattern (Figure 4.11f).

The reduction in amplitude increases with increasing EER and is clearly seen in the y-axis profiles of the same data (Figure 4.12). Along with the increased electrode removal, minimal shift in the x-axis position of the maximum residual potential, and only occurs shift occurs when too much electrode effect is removed (500 ohm.m resistivity EER function).

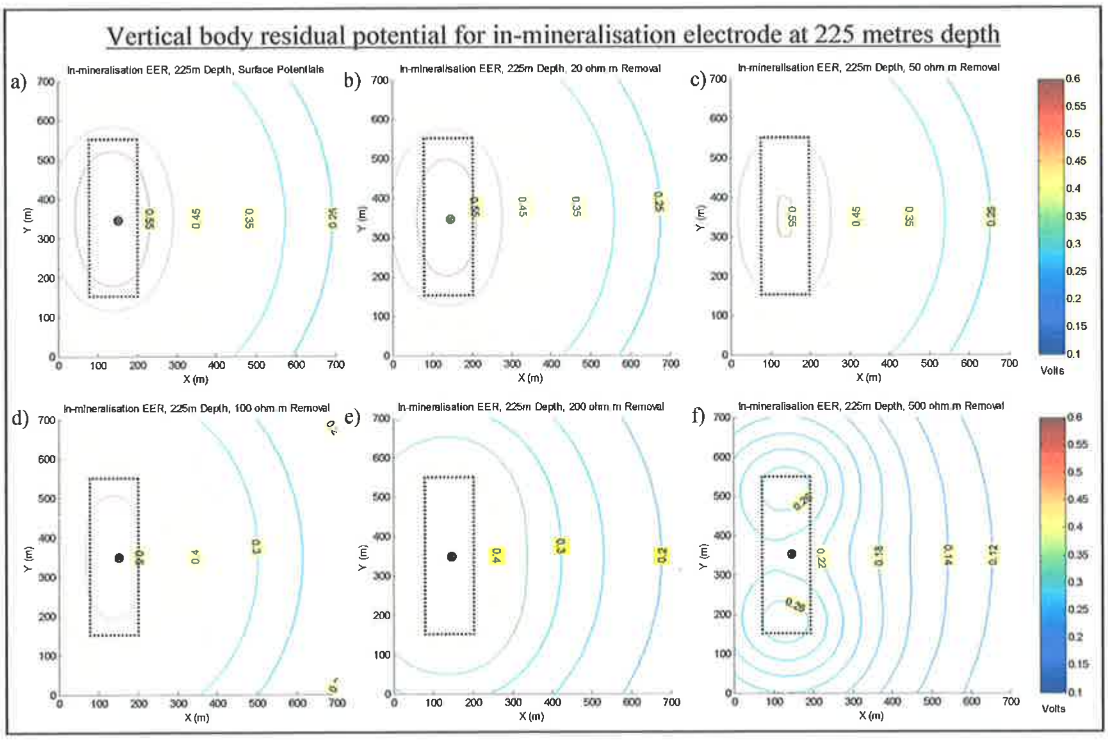

Figure 4.11: a) is the modelled surface potentials. b), c), d), e) and f) are residual potentials for a vertical body using the EER function with resistivities of 20, 50, 100, 200 and 500 ohm.m respectively. The black dashed outline and black dot demarcate the positions of the body and electrode respectively. Contour intervals are 0.05 V, the colour scale is 0.1 – 0.6 V.

With a 100 or 200 ohm.m EER, the hump seen in the surface potentials (red dashed line Figure 4.12 and Figure 4.13) is removed, with the residual potentials across the middle of the body being a near constant value of 0.52 volts (green curve Figure 4.13). This corresponds well with the modelled body as it is parallel to the upper surface of the body, therefore more accurately portraying the modelled geology.

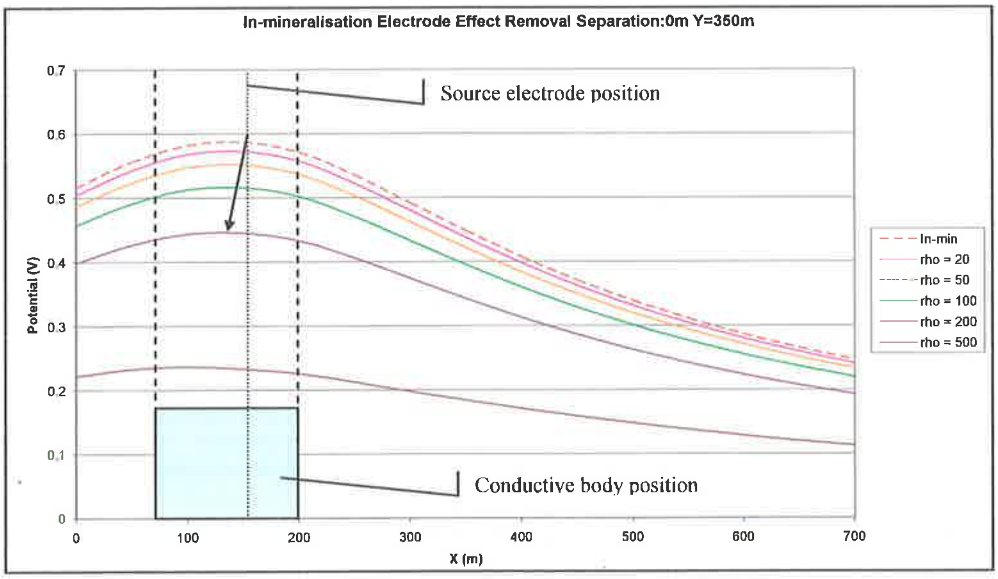

Figure 4.12: E-W profiles of in-mineralisation EER for resistivities 20, 50, 100, 200 and 500 ohm.m along Y=350m. The peak amplitude decreases with increased electrode removal, whilst there is a slight shift of the peak residual potentials towards the centre of the body. The blue rectangle marks the position of the body.

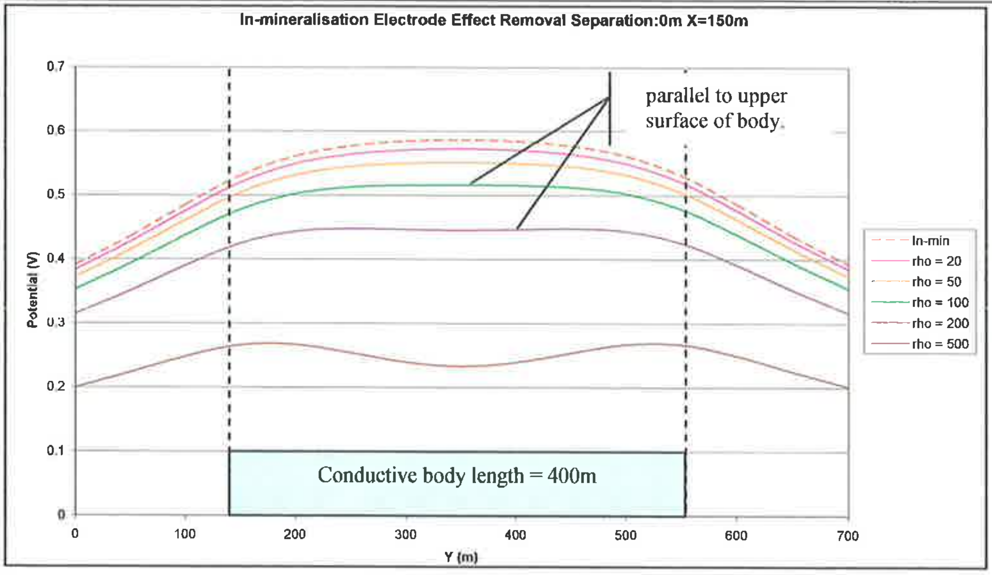

Figure 4.13: N-S profiles of in-mineralisation residual potentials after EER resistivities 20, 50, 100, 200 and 500 ohm.m along X=150m (i.e. the X position of the source electrode). Note profiles the artificial double peaks forming when the EER is applied with $\rho_{halfspace}$ = 500 ohm.m.

Dipping conductor models

An in-mineralisation electrode in a dipping conductor has the anomaly peak offset from the electrode position and occurs over the upper surface of the conductive structure. This was seen in the 30 degree and 45 degree conductive bodies. In this scenario, the EER function does little except for a reduction in the overall residual potentials (Figure 4.14). There were only minor changes in the shape of the anomalies that were already well defined in the MALM surface potentials.

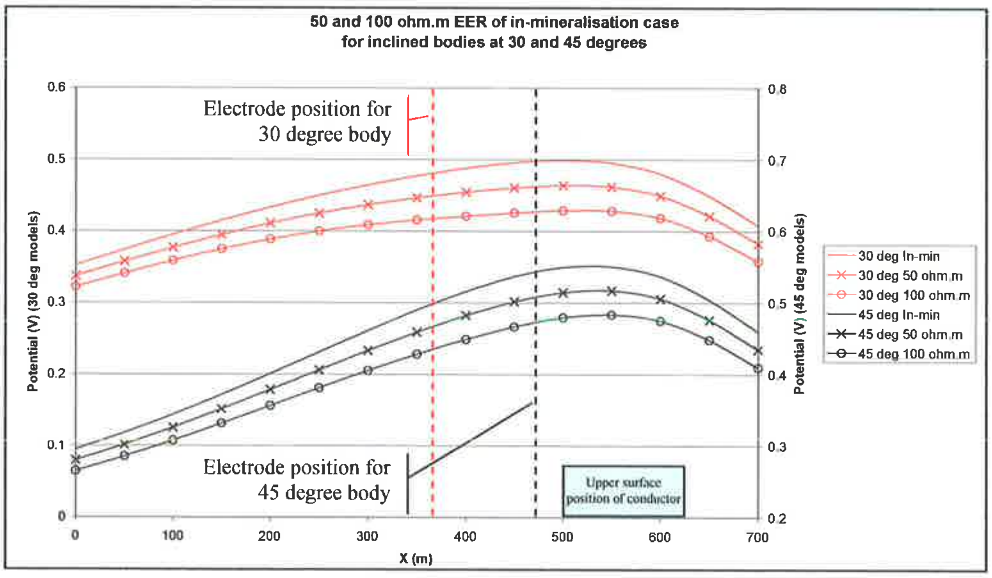

Figure 4.14: Residual potentials of dipping bodies of 30 and 45 degrees after EER of 50 and 100 ohm.m half-space. The removal of small electrode effects has minimal effect on the MALM potentials about the electrode position. Note that the profiles for the 30 degree body are plotted on the left vertical scale and the 45 degree body profiles are plotted according to the right vertical scale.

Two body models - depth/separation of a second body

Removing the electrode effect in the presence of multiple bodies can further elucidate the non-energised conductive bodies by suppressing the electrode peak generated by the energised body.

For models investigating the effects of the depth of a second body, the EER function successfully enhanced the position of a close proximity, non energised body. When the two bodies are of equal depth (i.e. source electrode energised second body at 100m), the surface potential profiles have an asymmetry situated directly above the position of the first body. This deviation in the profiles was enhanced with removal of an increasingly greater electrode effect (Figure 4.15). The residual potentials define the position of the first body when the electrode effect is removed using a 400 ohm.m half-space resistivity. With the second body at a depth of 250 metres, the surface potentials already indicate the presence of another conductive structure. With the EER function applied, the residual potentials do not show two separate bodies, but an amalgamation of the response for both, with a wide, flat-topped peak that encompasses both conductive body positions (Figure 4.15).

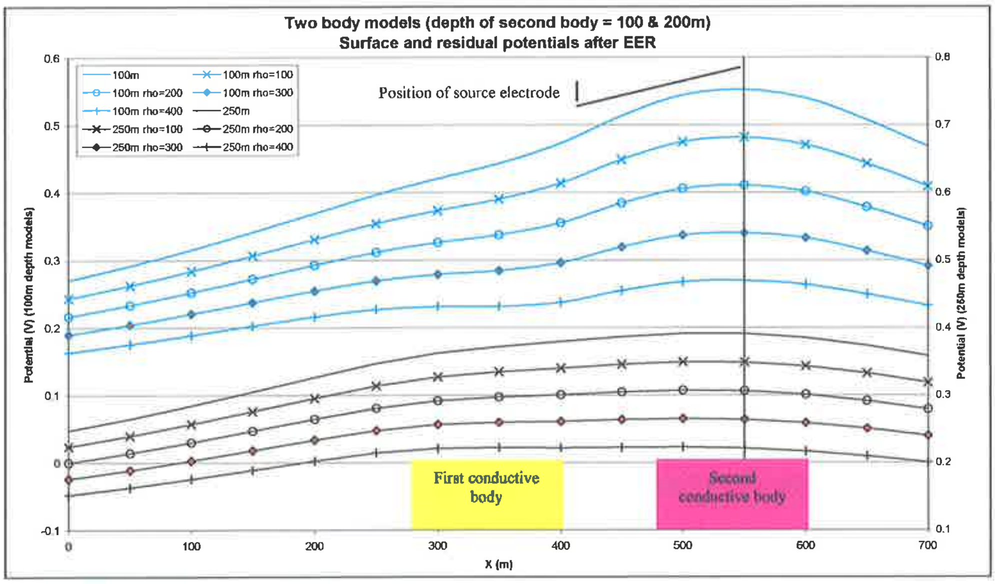

Figure 4.15: Two body models with the electrode in the second body. The two sets of curves shown are the second body at 100 and 250m depths. With increasing EER, the presence of the first body becomes more evident. The left vertical scale is for the 100m depth body, the right vertical scale is for the 250m depth body.

The results from the lateral separation of two conductive structures (see two body FEM models, p40) show that it is possible for the EER to enhance the response from a non-energised conductive body. At small separations, the surface potential response of the second body merges with that of the energised primary body, making it difficult to distinguish the presence of the non-energised body. When the EER is applied, the distortion in the residual potential profile better indicates the occurrence of a second body in comparison to the unprocessed MALM data (Figure 4.16). At larger separations (125m), there is less response from the non-energised conductive body. The residual potentials do not enhance the presence of a second body (Figure 4.16).

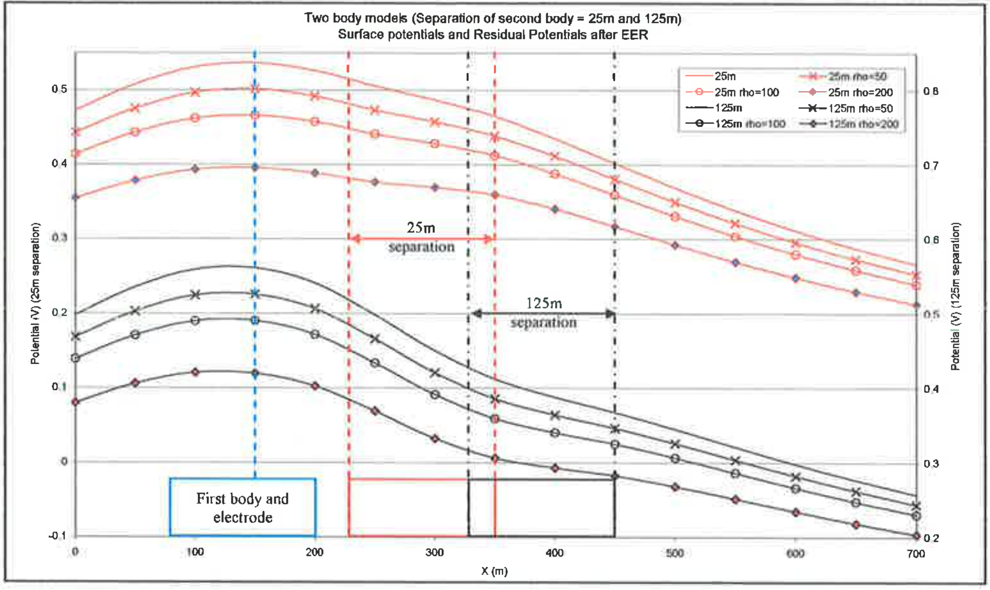

Figure 4.16: Two body models, separation of second body. The first body contains the current electrode. With increasing separation the second body is less evident in the profiles. With the EER applied the second body becomes more apparent. This occurs even at the larger separation of 125m.

Near-miss models

Near-miss vertical body models

Models with near-miss electrode positions were thoroughly investigated as the forward modelling has shown these models to have a combined surface potential pattern consisting of both the modelled body and the electrode response (FEM near-miss electrode positions, p43). By removing the electrode effect from the near-miss response, the residual potentials better reveal the position of the mineralisation.

Figure 4.17a shows the surface potentials of an in-mineralisation response of a shallow electrode position at 110 metres depth. In comparison the response for the 25 metre near-miss electrode position for the same depth (Figure 4.17b) has a distinctly different response with the peak centred over the electrode position. The residual potentials are distorted with the removal of increasing electrode effect, and to some extent delineate the position of the body. For a $\rho_{halfspace}$ of 200 ohm.m, the residual potentials (Figure 4.17c) show only a small change to the west of the electrode position where the potentials are elongate in the north-south direction. This elongation in the N-S direction increase when greater resistivities are specified for the EER function. At 500 ohm.m $\rho_{halfspace}$, the residual potentials over the body have a four peak pattern in the residual potential contours, one situated at the electrode position, another over the centre of the body and two more at either end of the body (Figure 4.17f). At shallow depths for a vertical body it is possible for the EER function to recover additional information that is otherwise not apparent in the unprocessed shallow near-miss surface potentials.

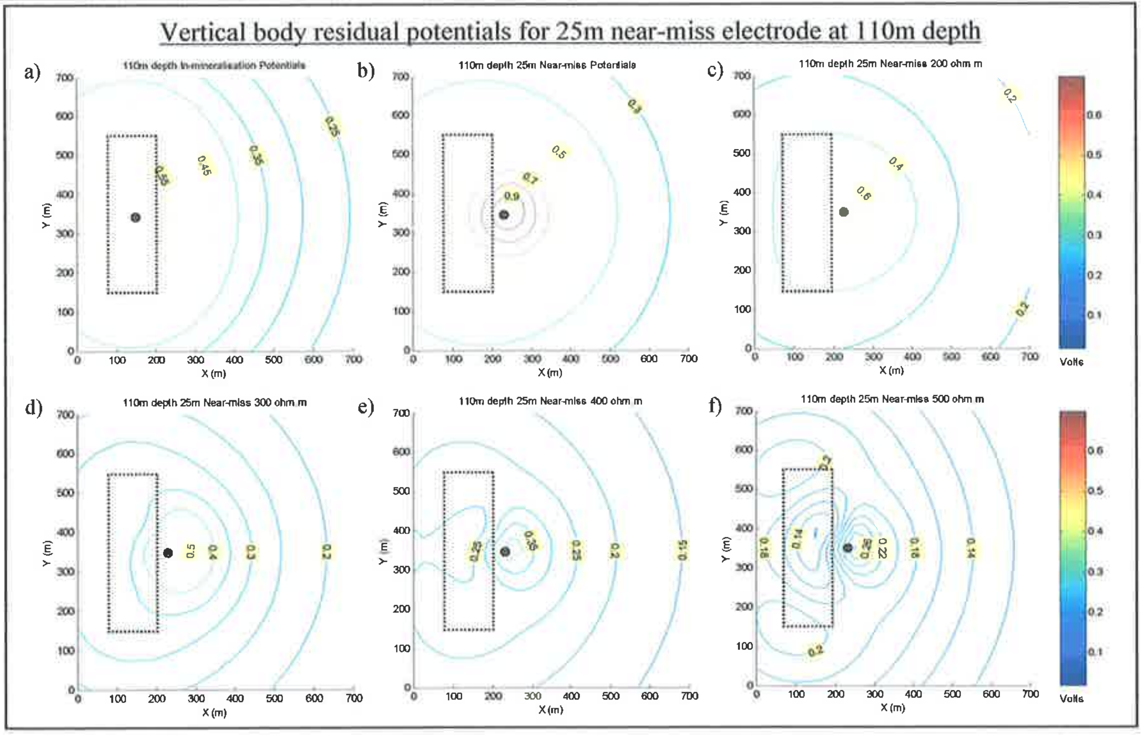

Figure 4.17: EER for near-miss electrode at 110m depth, 25m from the body. For comparison, a) is the in-mineralisation response and b) is the near-miss surface potentials. c), d), e) and f) are the residual potentials from the EER function with resistivities 200, 300, 400 and 500 ohm.m respectively. The black dot is the position of the source electrode and the black outline is the position of the conductive body.

For an electrode at 225 metres depth, the 25 metre near-miss surface potentials show anomaly contours that are elongate along the strike of the conductive body to the west of the electrode position. The peak of the surface potentials is not over the conductive body position or over the electrode position, but in-between the two (Figure 4.18a). With increased EER by specifying larger values for $\rho_{halfspace}$, the residual potential peak is shifted west, such that it is over the modelled mineralisation (Figure 4.18b and c).

At a separation of 75 metres from the body the near miss response is unlike that of the 25 metre separation (Figure 4.18d). The surface potentials are centred over the near-miss electrode. However, for the same $\rho_{halfspace}$ values in the EER function (200 and 400 ohm.m) as was used for the 25 metre separation, the residual potentials have a distinct contours that can be associated with the position of the conductive body (Figure 4.18e and f).

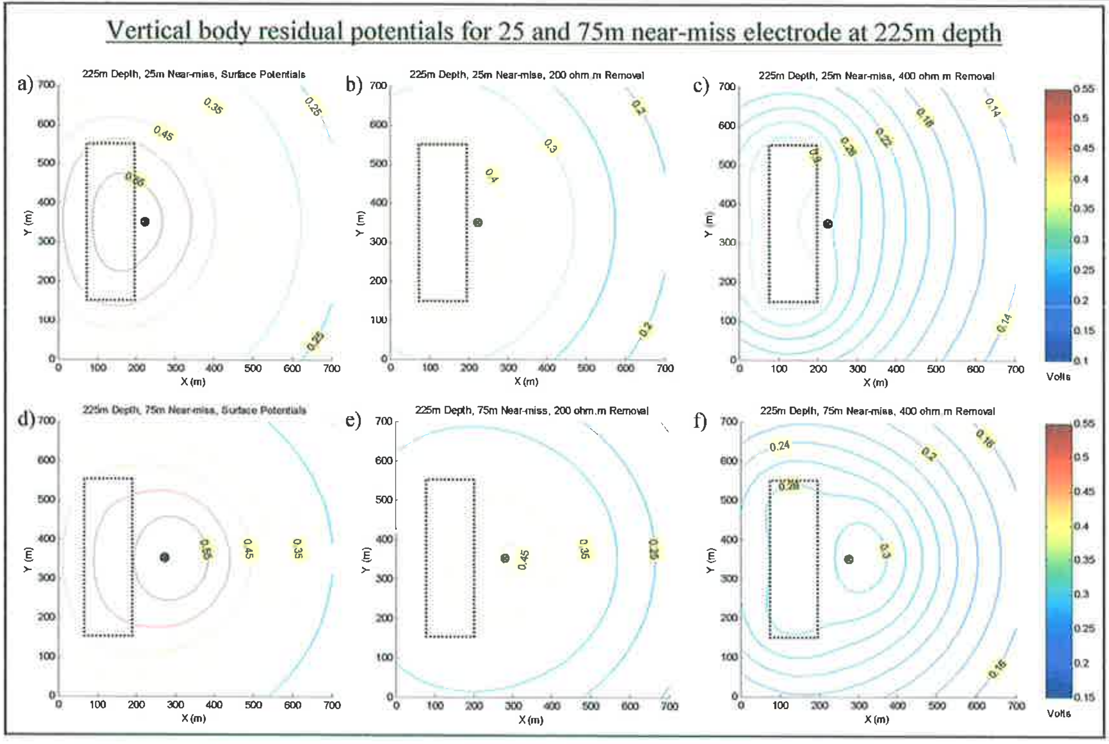

Figure 4.18: a) and d) surface potentials for near-miss electrodes at 225m depth and 25 and 75m separation from body respectively. b) and c) residual potentials for 25m near-miss with EER $\rho_{halfspace}$ = 200 and 400 ohm.m. e) and f) residual potentials for 75m near-miss with EER $\rho_{halfspace}$ = 200 and 400 ohm.m respectively. CI=0.05 V.

From the FEM modelling of near-miss electrodes (p43) it was found that deeper electrodes can be separated further from the body whilst still creating a mineralisation response. Figure 4.19a is the near-miss electrode surface potentials of a 325 metre deep electrode situated 75 metres from a vertical body, the response clearly indicates the presence of the conductive body to the west of the electrode position, with the peak situated in-between the body and the electrode.

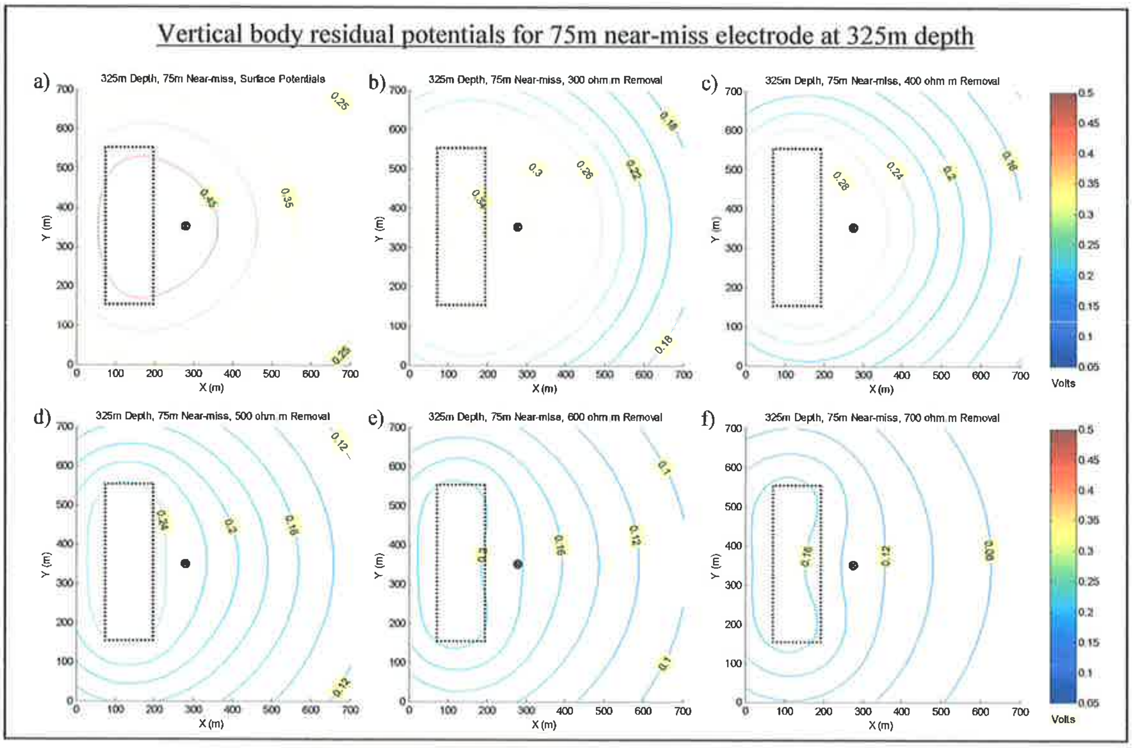

Figure 4.19: a) surface potentials for near-miss of 75m at source depth of 325m. b), c), d), e), and f) are residual potentials after application of the EER where $\rho_{halfspace}$ = 300, 400, 500, 600 and 700 ohm.m respectively. CI=0.02V, colour scale is 0.05 to 0.5 V.

With increasing $\rho_{halfspace}$ values used in the EER function (300, 400 and 500 ohm.m), the residual surface potentials further reveal the position of the conductive body (Figure 4.19b, c and d). Specifying even greater values of 600 and 700 ohm.m have the detrimental effect of artificially distorting the residual potentials such that they are no longer representative of the conductive body (Figure 4.19e and f).

Placing the electrode at 150 metres from the body for the same depth of 325 metres results in a similar pattern to the 75 meter separation at 160 metres depth and the EER function reveals comparable residual potentials (c.f. Figure 4.20a, b and c with Figure 4.18d, e and f). The peak of the residual potentials is still situated over the electrode position. The residual potentials are an improvement over the original surface potentials as the potentials over the conductive body are more diagnostic of its presence and position. Using an even greater value for $\rho_{halfspace}$ (600 ohm.m) in the EER function results in a double peak anomaly, with the second peak situated over the conductive body position (Figure 4.20).

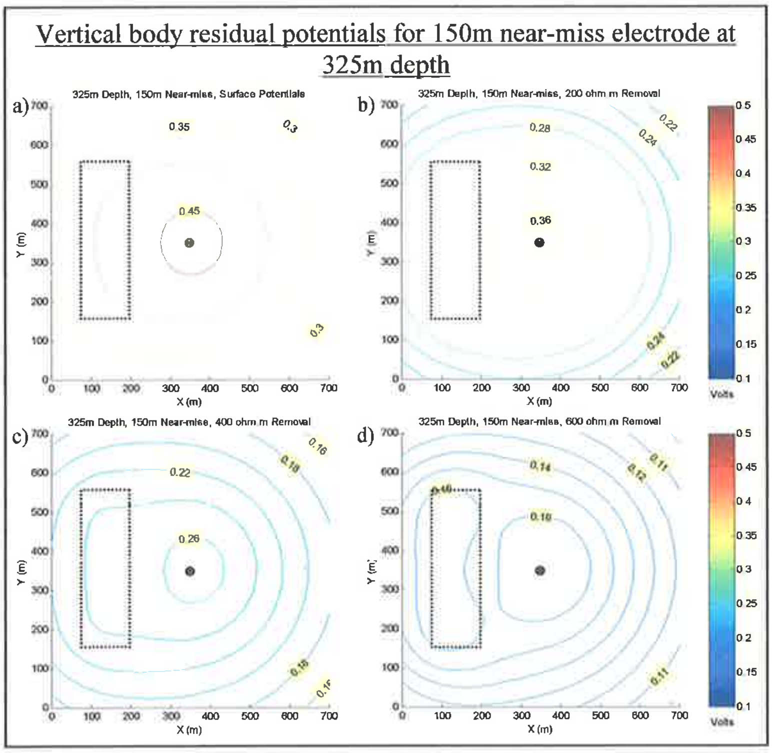

Figure 4.20: a) surface potentials for a 150m near-miss electrode at 325m depth. b), c) and d) residual potentials after 200, 400 and 600 ohm.m EER. Contour interval is 0.05 for a) and 0.02 for b), c) and d). Colour scale is 0.1 to 0.5 for all figures.

The last series of results of the near-miss electrode positions about a vertical body are those for the 375 metre depth near-miss positions. Displayed are the unaltered surface potentials (Figure 4.21a, b and c), the residual potentials for the EER function with $\rho_{halfspace}$ equal to 400 ohm.m (Figure 4.21d, e and f) and the residual potentials when $\rho_{halfspace}$ equals 600 ohm.m (Figure 4.21g, h and i). The unaltered surface potentials show that the near-miss effect dominates the 25 and 75 metre separations. The presence of the body is still evident in the 150 metre separation, although the maximum surface potentials are situated over the electrode position. With the removal of the electrode effect using a 400 ohm.m resistivity, the maximum residual potentials are situated over the conductive body position for the 25 and 75 metre near-miss electrodes (Figure 4.21d, and e). The residual potential contours for the same $\rho_{halfspace}$ at the 150 metre separation are distended westwards to the position of the conductive body (Figure 4.21f). Using a $\rho_{halfspace}$ value of 600 ohm.m produced a residual anomaly in the 150 metre separation which is indicative of the conductive structure compared with the unaltered near-miss potentials for the same separation.

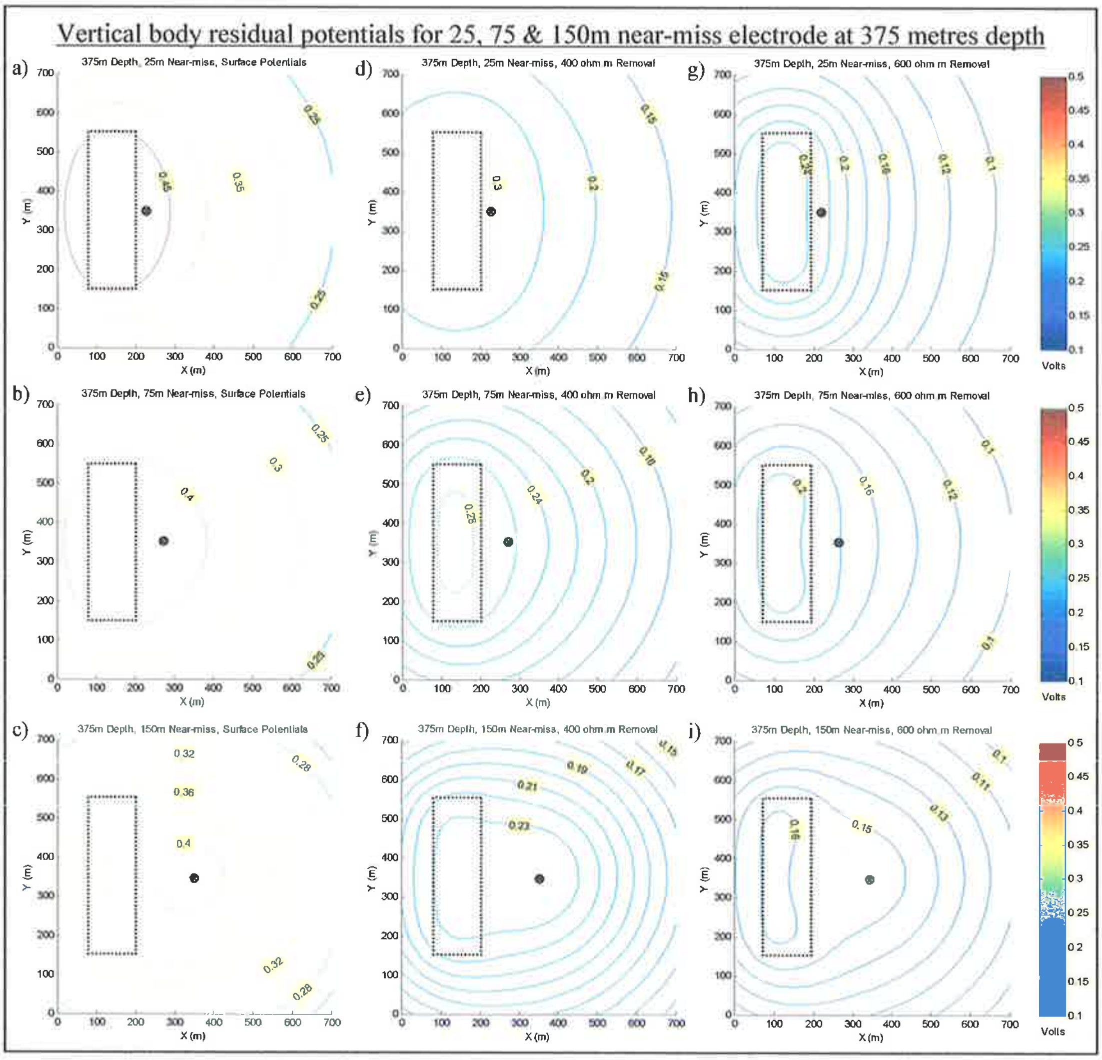

Figure 4.21: a), b) and c) are the surface potentials for near-miss electrodes with separations 25, 75 and 150m at a depth of 325m. d), e) and f) are residual potentials after a 400 ohm.m EER for the electrode positions 25, 75 and 150m. g), h) and i) are residual potentials after a 600 ohm.m EER for the electrode positions 25, 75 and 150m. Colour scale is 0.1 to 0.5 V.

Near-miss dipping body models

The effects of a near-miss electrode about a vertical or near vertical body are more readily interpreted than those about a dipping structure. For the 30 degree body dipping to the west, the use of the EER at resistivities of 100, 200 and 300 ohm.m, reduced the surface potentials directly above the electrode and shifted the peak of the residual potentials back towards the position of the upper surface of the conductive body (Figure 4.22a). This was of benefit as the original surface potentials had a broad anomaly compared to the residual potentials (Figure 4.22b). The EER function on the shallow near-miss 45 degree body had the same effect, although a higher $\rho_{halfspace}$ value was needed for a similar shift in the residual potentials (Figure 4.22c).

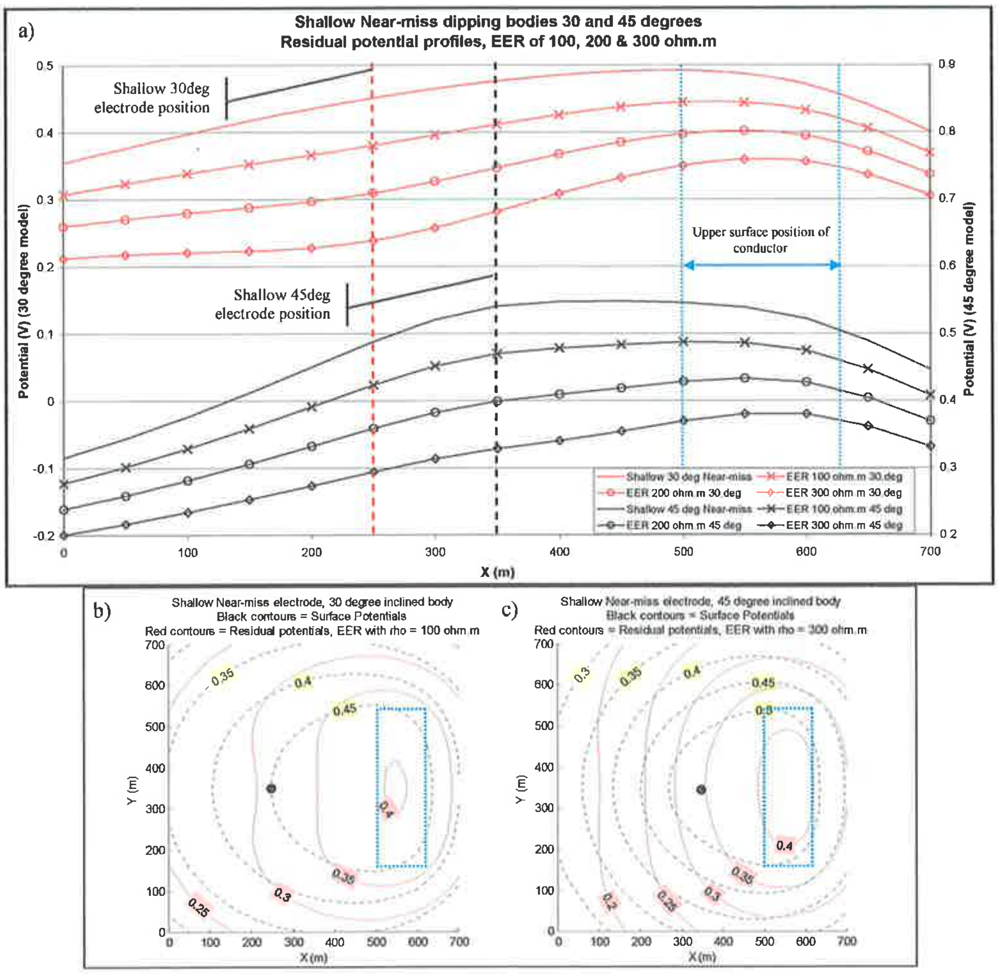

Figure 4.22: a) shallow near-miss profiles of 30 and 45 degree dipping bodies. The EER function has been applied with resistivity values of 100, 200 and 300 ohm.m. b) is the 30 degree body shallow near-miss surface potentials (black contours) compared to the 100 $\rho_{halfspace}$ EER residual potentials (red contours). c) is the 45 degree body shallow near-miss surface potential (black contours) compared to the 300 ohm.m $\rho_{halfspace}$ EER residual potentials (red contours).

Residual potentials of the shallow near-miss electrode for the 60 degree body using EER resistivity values of 300, 400 and 500 ohm.m had similar effects as the electrode removal for the shallow dipping bodies. The maximum surface potentials are recorded over the electrode position. With the increased removal of the electrode effect the position of the conductive structure is unobscured and the peak of the residual potentials is migrated back towards the position of the upper surface of the modelled mineralisation (Figure 4.23a and b). The 90 degree body has already been discussed and is used as a comparison for the resistivity values required to obtain a usable residual potential anomaly. In summary, the value for the EER resistivity to uncover the position of the body from a shallow near-miss electrode position about a dipping conductor increases with a steeply dipping body.

The surface potential response for a deep near-miss electrode about a dipping body has been shown to respond in a similar manner to the in-mineralisation response ("Dipping Near-miss models", p47). Using high resistivity values (>300 ohm.m) for the EER results in residual potentials with no additional information about the 30 or 45 degree bodies (Figure 4.24). With such high values, the residual potential anomaly for the 45 and 60 degree body (Figure 4.25) is displaced away from the position of the upper surface of the conductive body. Small $\rho_{halfspace}$ values of 100 or 200 ohm.m have less detrimental effects, but does not resolve the body any further than the unaltered deep near-miss surface potentials.

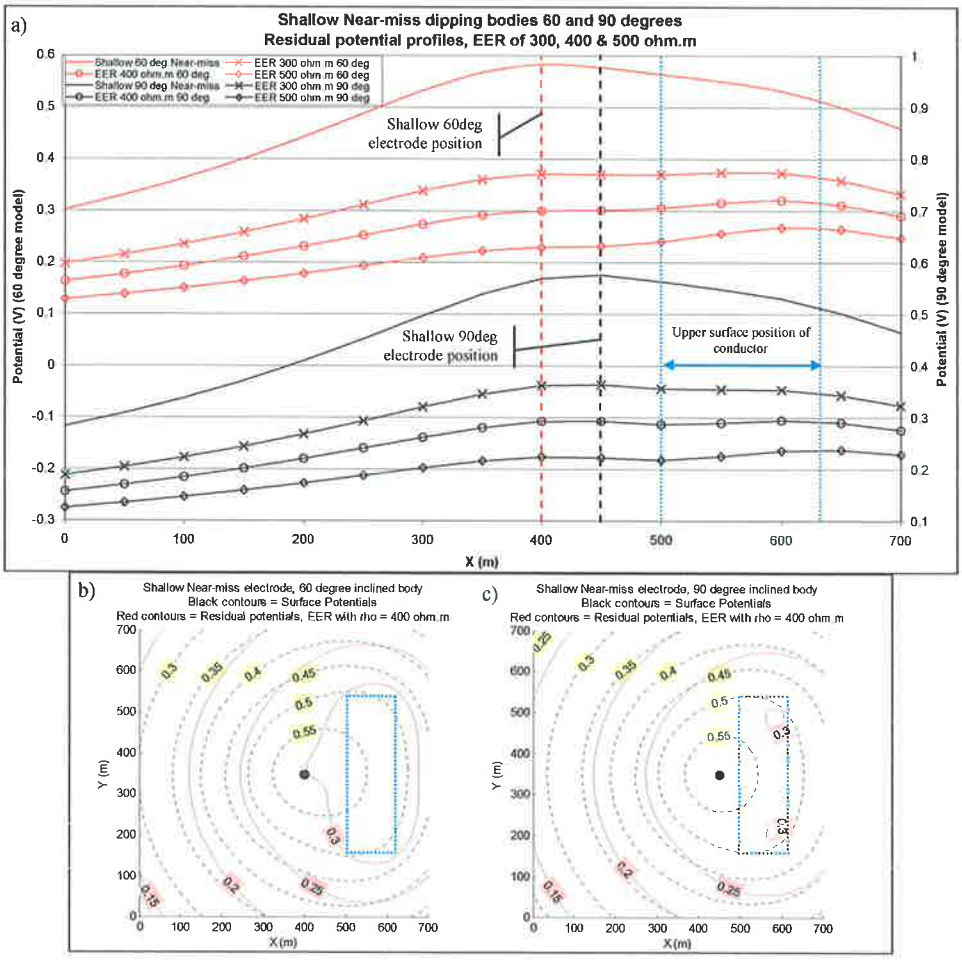

Figure 4.23: a) shallow near-miss profiles of 60 and 90 degree dipping bodies. The EER function has been applied with resistivity values of 300, 400 and 500 ohm.m. b) is the 60 degree body shallow near-miss surface potentials (black contours) compared to the 400 $\rho_{halfspace}$ EER residual potentials (red contours). c) is the 90 degree body shallow near-miss surface potential (black contours) compared to the 400 ohm.m $\rho_{halfspace}$ EER residual potentials (red contours).

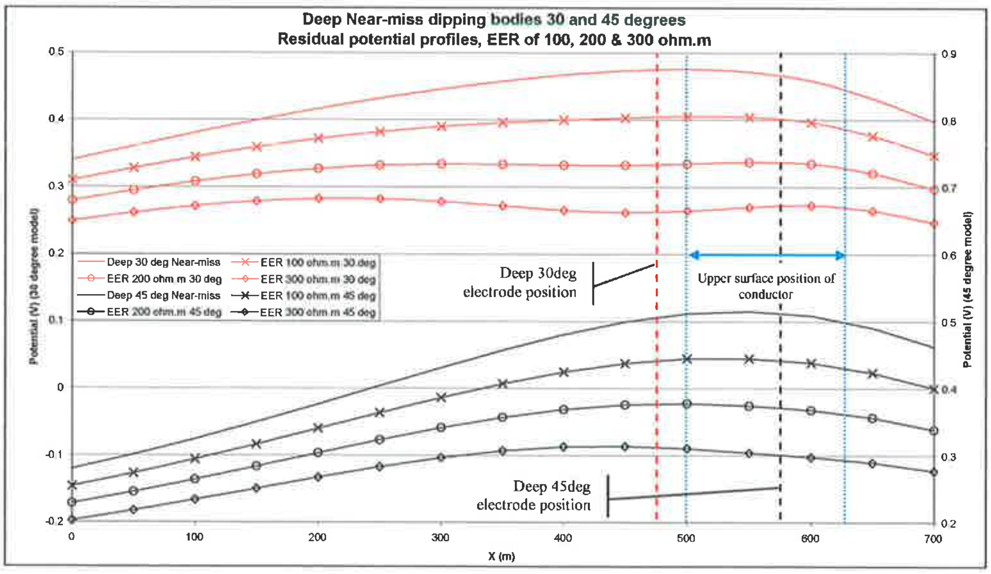

Figure 4.24: Profiles for the deep near-miss electrode position for 30 and 45 degree dipping models. The left vertical scale is for the 30 degree body residual potentials and the right is for the 45 degree body.

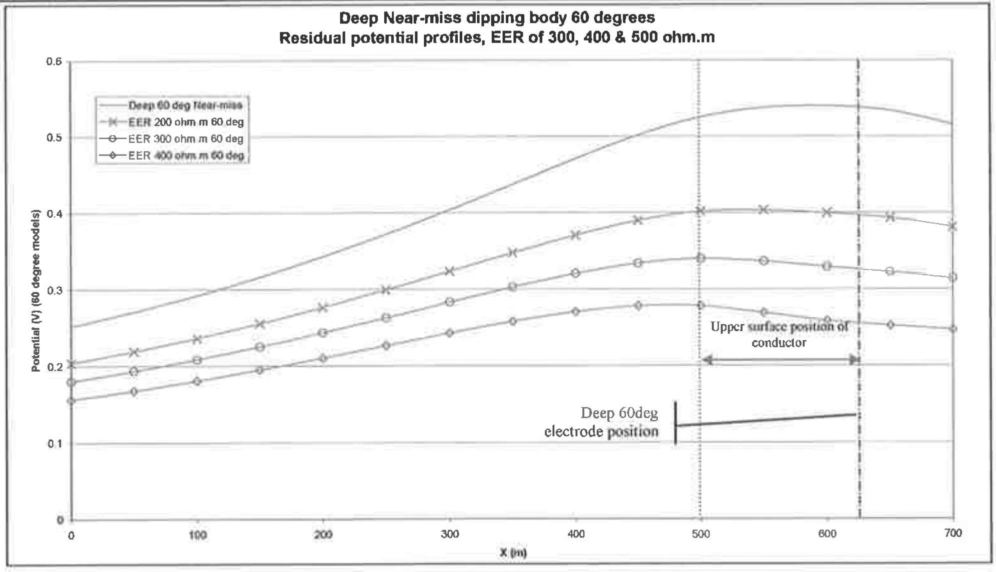

Figure 4.25: 60 degree deep near-miss surface potential profile and residual potential profile with EER resistivities of 200, 300 and 400 ohm.m. The EER does not contribute any addition information in this instance.

FEM field site models

Catalpa mdoels

The testing of the EER function on FEM field site models is a prelude to its application to the observed MALM data. Synthetic surface potentials for the in-mineralisation models of RHDD018 and RHDD020 are similar (Figure 4.26a and Figure 4.27a). However, the electrode positions of both models are unique and produce subtle differences in the residual responses for the same $\rho_{halfspace}$ values of 25, 45 and 65 ohm.m (c.f. Figure 4.26b, c and d with Figure 4.27b, c and d).

The EER function is applied to the modelled surface potential responses for RHDD020 Setup B and C. These are the near-miss electrode positions for the Catalpa area. The shallow near-miss surface potential response of RHDD020 Setup B is different to the deep near-miss response of RHDD020 Setup C (Figure 4.28a and Figure 4.29a). Residual potentials from the 25 ohm.m EER are migrated to the position of the upper surface of the modelled conductive body for the shallow near-miss position (Figure 4.28b). With increasing $\rho_{halfspace}$ values, the position of the body is enhanced in the residual potentials for the shallow near-miss (Figure 4.28c). However, too much EER renders the residual potentials useless (Figure 4.28d).

As identified in the idealised modelling for the near-miss electrodes positioned around a dipping conductor, the residual potentials of the deep near-miss position for the model (i.e. RHDD020 Setup C) does not show additional information. With increasing values for $\rho_{halfspace}$ (50, 75 and 100 ohm.m) the residual potentials highlight the position of the upper surface of the modelled conductive body (Figure 4.29b, c and d respectively).

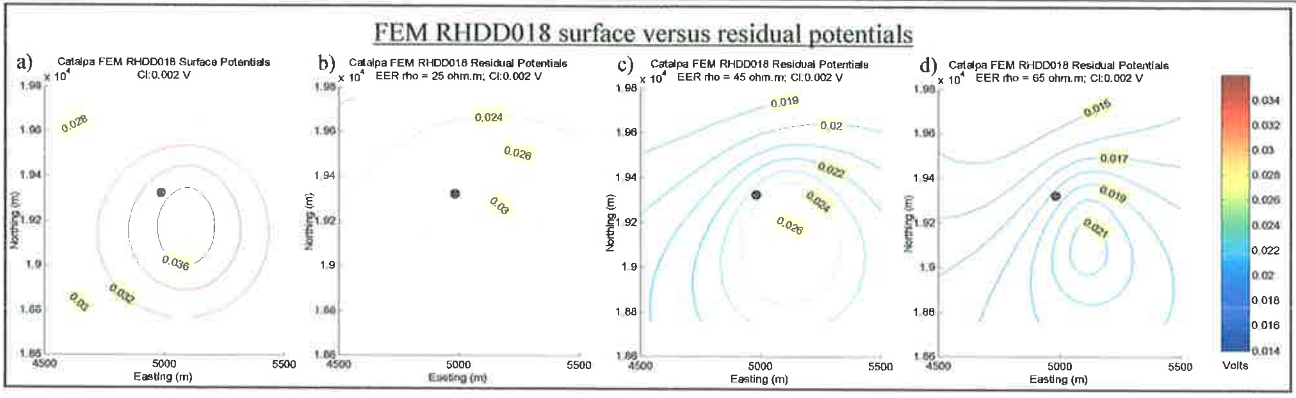

Figure 4.26: a) surface potentials for RHDD018 model, b) residual potentials for EER $\rho_{halfspace}$ = 25 ohm.m, c) residual potentials for EER $\rho_{halfspace}$ = 45 ohm.m, and d) residual potentials for EER $\rho_{halfspace}$ = 65 ohm.m. Colour scale from 0.014 to 0.036V.

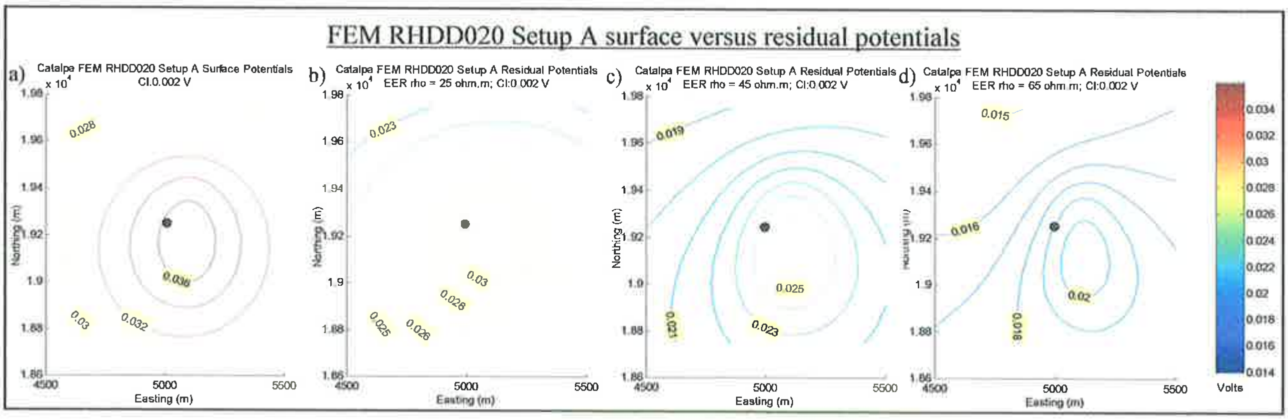

Figure 4.27: a) surface potentials for RHDD020 Setup A model, b) residual potentials for EER $\rho_{halfspace}$ = 25 ohm.m, c) residual potentials for EER $\rho_{halfspace}$ = 45 ohm.m, and d) residual potentials for EER $\rho_{halfspace}$ = 65 ohm.m. Colour scale from 0.014 to 0.036V.

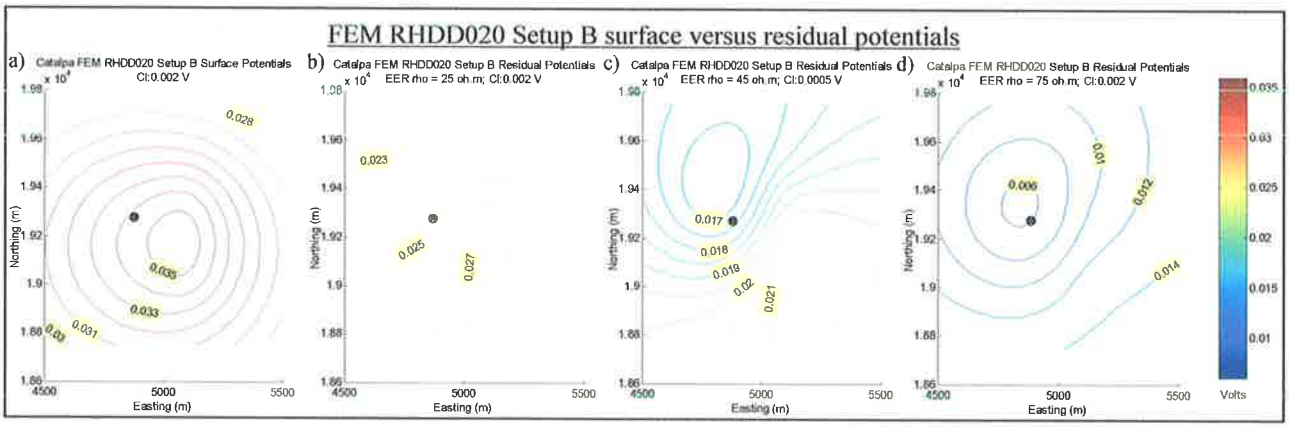

Figure 4.28: a) surface potentials for RHDD020 Setup B model, b) residual potentials for EER $\rho_{halfspace}$ = 25 ohm.m, c) residual potentials for EER $\rho_{halfspace}$ = 45 ohm.m, and d) residual potentials for EER $\rho_{halfspace}$ =75 ohm.m. Colour scale from 0.006 to 0.036V.

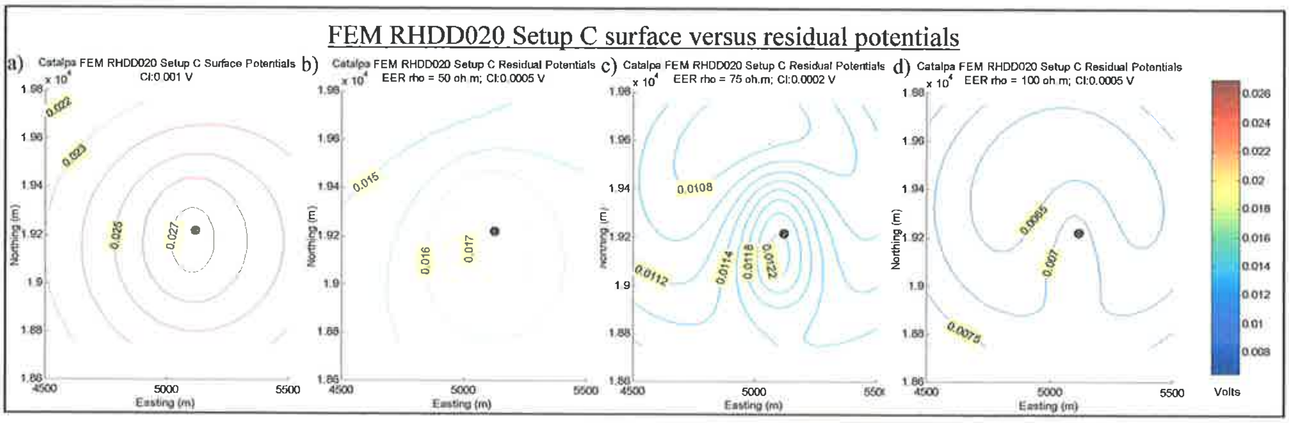

Figure 4.29: a) surface potentials for RHDD020 Setup C, b) residual potentials for EER $\rho_{halfspace}$ = 50 ohm.m, c) residual potentials for EER $\rho_{halfspace}$ = 75 ohm.m, and d) residual potentials for EER $\rho_{halfspace}$ = 100 ohm.m. Colour scale from 0.0065 to 0.027V.

Prominent Hill models

The Prominent Hill field data consisted of a single in-mineralisation survey, but the FEM near-miss models provided the opportunity to examine the MALM data for a non-intersecting/barren drill hole. The two near-miss cases modelled at Prominent Hill were situated about the chalcocite breccia target, one shallower and one deeper than the in-mineralisation case to simulate the downhole positions in RP017. These three FEM responses were passed through the EER function.

The in-mineralisation position (Figure 4.30a) shows the peak potentials to the south over the position of the conductive haematite rock (Figure 3.41, p65). With increasing removal of $\rho_{halfspace}$ at 25 and 35 ohm.m, the residual potentials are increasingly concentrated to the south over the haematite rock (Figure 4.30b and c respectively).

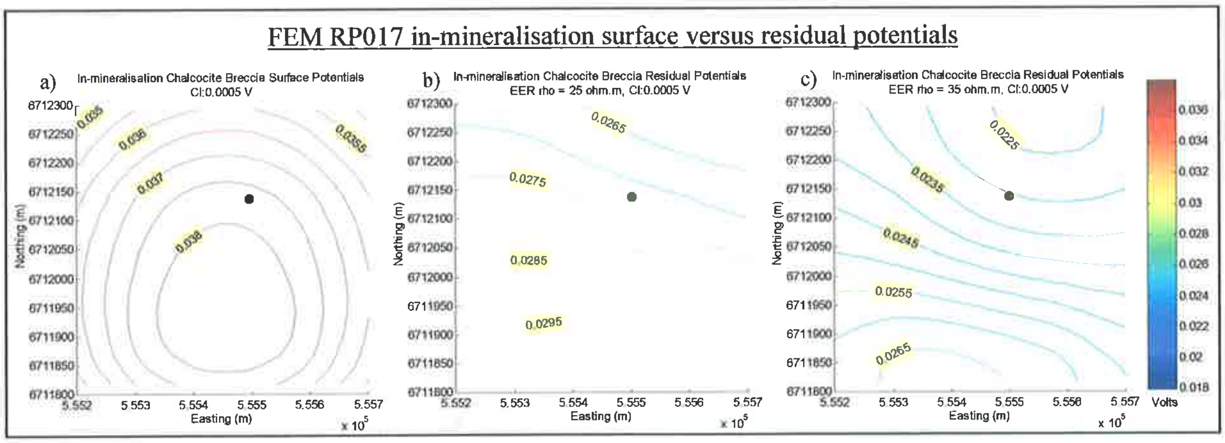

Figure 4.30: EER function applied to a) modelled in-mineralisation surface potentials, results in b) 25 ohm.m $\rho_{halfspace}$ EER residual surface potentials and c) 35 ohm.m $\rho_{halfspace}$ EER residual surface potentials. Colour scale is 0.018 to 0.038 V.

For the shallow near-miss potentials (Figure 4.31a), the peak of the anomaly is not situated over the haematite rock, but over the position of the haematite breccia north of the chalcocite breccia (Figure 3.41, p65). Applying the EER function with 25 ohm.m $\rho_{halfspace}$ (Figure 4.31b) shifts the residual potentials south, towards the less resistive haematite rock. This is the same for the 35 ohm.m $\rho_{halfspace}$ EER function (Figure 4.31c).

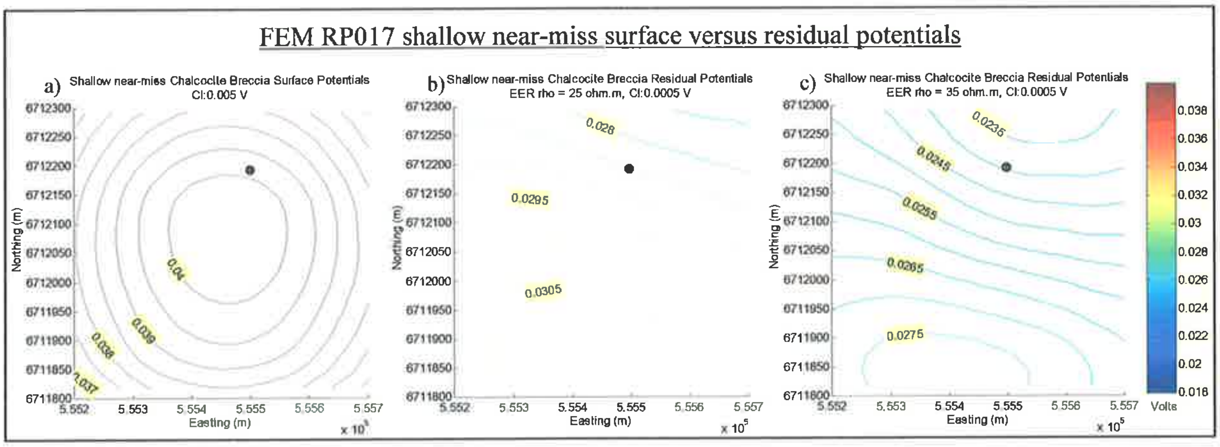

Figure 4.31: EER function applied to a) modelled shallow near-miss surface potentials, results in b) 25 ohm.m $\rho_{halfspace}$ EER residual surface potentials and c) 35 ohm.m $\rho_{halfspace}$ EER residual surface potentials. Colour scale is 0.018 to 0.04 V.

The deep near-miss surface potentials already highlight the conductive haematite rock to the south (Figure 4.32a). The residual potentials are more elongate along the strike of the modelled body (east-west) with increasing $\rho_{halfspace}$ (Figure 4.32b and c).

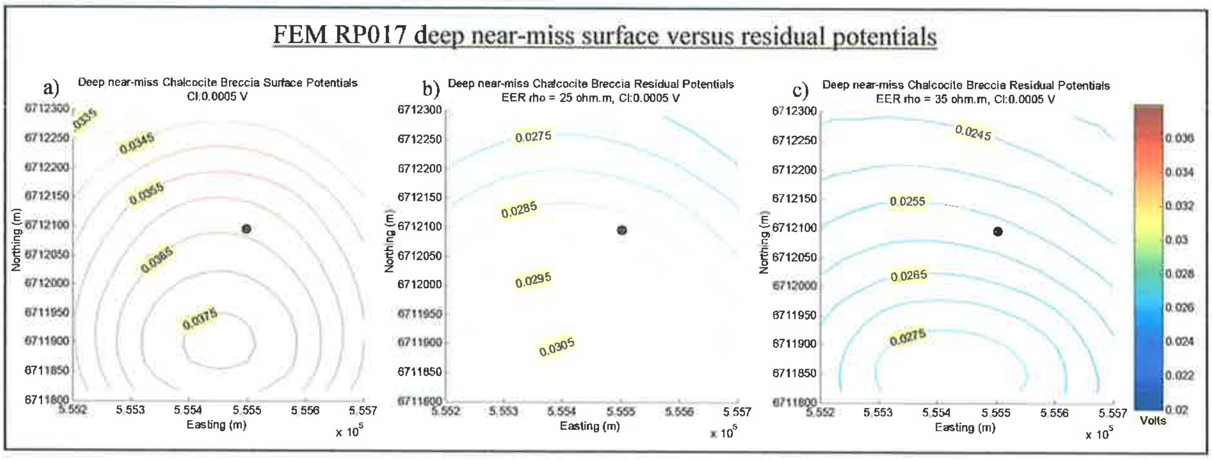

Figure 4.32: EER function applied to a) modelled deep near-miss surface potentials, results in b) 25 ohm.m $\rho_{halfspace}$ EER residual surface potentials and c) 35 ohm.m $\rho_{halfspace}$ EER residual surface potentials. Colour scale is 0.02 to 0.038 V.

Field MALM data

Whilst the surface potentials for all of the MALM surveys have been presented in large format in Section 4.1 (p85), these are presented again at the same scale as the residual potentials for ease of comparison. Colour scales are marked by the minima and maxima of the colour bar.

Catalpa

The source electrode position used in the EER for the Golden Grove data was derived from the drill logs (and the *dlog.m* program). For the in-mineralisation cases for RHDD018 (Figure 4.33a) and RHDD020 Setup A (Figure 4.34a), the peaks are in a similar position and remain so for residual potentials of increasing $\rho_{halfspace}$ of 50 and 100 ohm.m for the EER function.

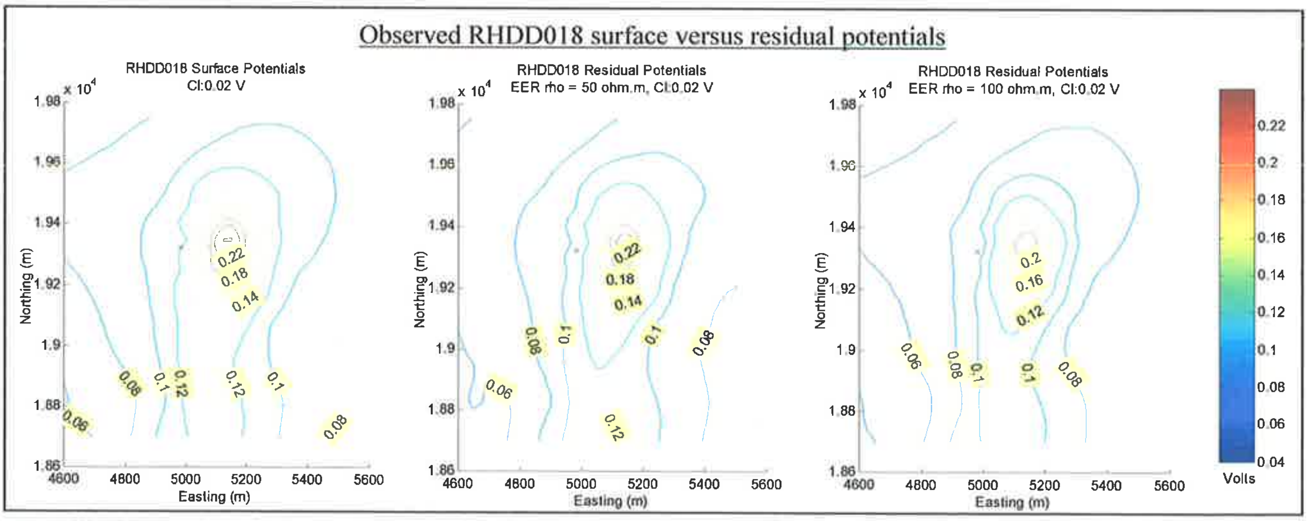

Figure 4.33: EER on RHDD018 MALM data. a) surface potentials, b) residual potentials with 50 ohm.m EER, c) residual potentials with 100 ohm.m EER. Colour scale is 0.04 to 0.24 V, contour interval is 0.02V.

The residual potentials for the 50 ohm.m $\rho_{\text{halfspace}}$ enhance the sharpness of the anomaly for both in-mineralisation electrode positions (Figure 4.33b and Figure 4.34b). At 100 ohm.m $\rho_{\text{halfspace}}$, the residual potentials for both RHDD018 and RHDD020 Setup A have a persistent continuation of equipotentials to the south and northeast. The southern residual potentials suggest a link to the Gossan Hill mineralisation (See longitudinal section, Figure 1.5, p8).

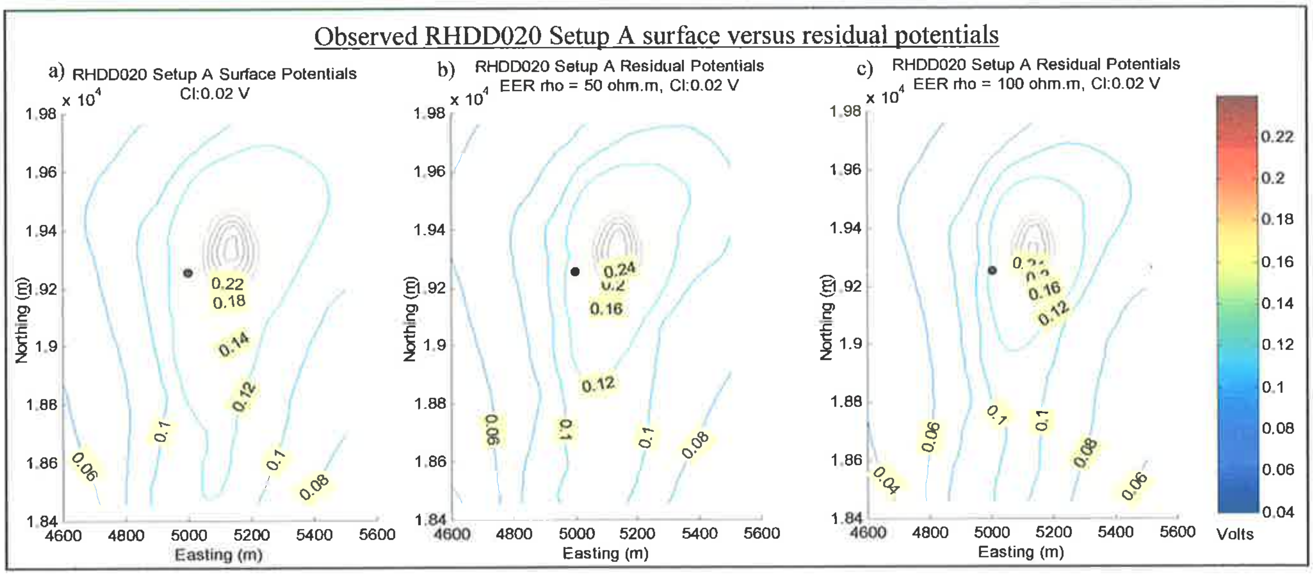

Figure 4.34: EER on RHDD020 Setup A MALM data. a) surface potentials, b) residual potentials with 50 ohm.m EER, c) residual potentials with 100 ohm.m EER. Colour scale is 0.04 to 0.24 V, contour interval is 0.02V.

The shallow near-miss case for RHDD020 (Setup B) has a large electrode effect due to the depth of the source electrode (Figure 4.35a). This is removed with increasing EER half-space resistivity values of 100 and 250 ohm in Figure 4.35b and c respectively. The residual potentials are trending towards the pattern seen in the in-mineralisation surveys with the residual equipotentials continuing to the south and the northeast. These northeast extensions of the potentials are similar to that seen in the MALM survey for Catalpa North for RHDD040 Setup 2 (Figure 4.8).

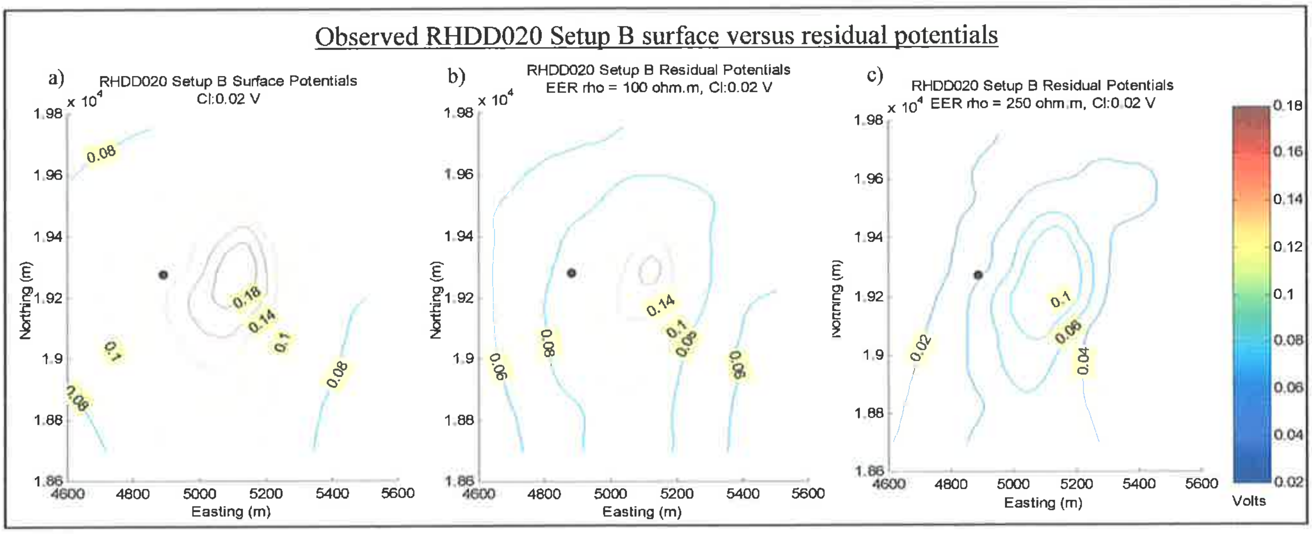

Figure 4.35: EER on RHDD020 Setup B MALM data. a) surface potentials, b) residual potentials with 100 ohm.m EER, c) residual potentials with 250 ohm.m EER. Colour scale is 0.02 to 0.18 V, contour interval is 0.02V.

The deep near-miss electrode (RHDD020 Setup C) is similar to the in-mineralisation set up but due to the electrode depth and the shading effect of the overlying conductive body as discussed in the FEM modelling for this position (p59), there is no electrode effect evident (Figure 4.36a). The position of the peak and the electrode position are coincidental as the upper surface of the dipping conductive body is positioned over the electrode at depth. EER using 100 and 300 ohm.m $\rho_{halfspace}$, have residual potentials which emphasise the electrical continuation towards Gossan Hill (Figure 4.36b and c respectively).

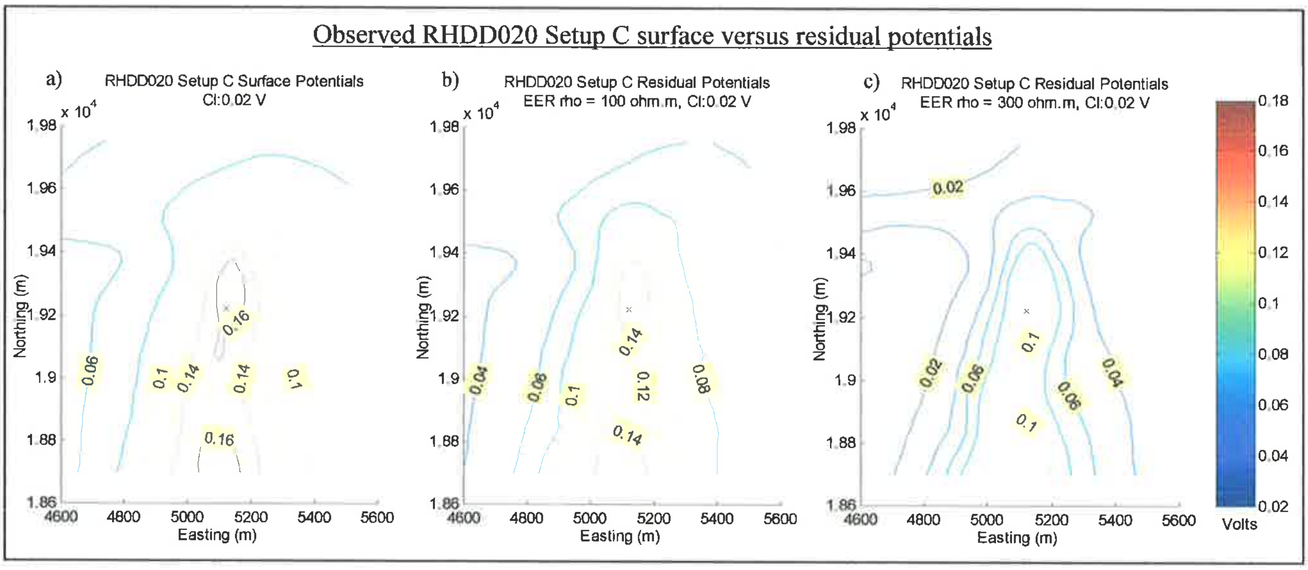

Figure 4.36: EER on RHDD020 Setup C MALM data. a) surface potentials, b) residual potentials with 100 ohm.m EER, c) residual potentials with 300 ohm.m EER. Colour scale is 0.02 to 0.18 V, contour interval is 0.02V.

Catalpa North

The EER for the Catalpa North MALM surveys yielded very interesting results that garner more information on the geology of the area than was available through the unprocessed MALM data. RHDD010 surface potentials (Figure 4.37a) have a double peak anomaly that persists in the residual potentials. Figure 4.37b is the residual potentials for an EER with $\rho_{halfspace}$ of 50 ohm.m. The peaks are further separated in Figure 4.37c with the residual potentials with a 100 ohm.m $\rho_{halfspace}$ removed. The southern peak in both residual potential results is an extension to the south towards the position of the peaks seen in other MALM data for the area (i.e. RHDD038 and RHDD040 Setup 2).

In Figure 4.38, the surface potentials for RHDD038 (a), RHDD040 Setup 1 (b) and RHDD040 Setup 2 (c) are distinct and dissimilar as discussed in Section 4.1. However, with the application of the EER function, the residual potentials are strikingly similar, suggesting a relationship to the geology. Figure 4.38d is the residual potentials for RHDD038 at 125 ohm.m $\rho_{halfspace}$. It shows the continuation of the residual surface potentials from the peak position in the south to the northeast.

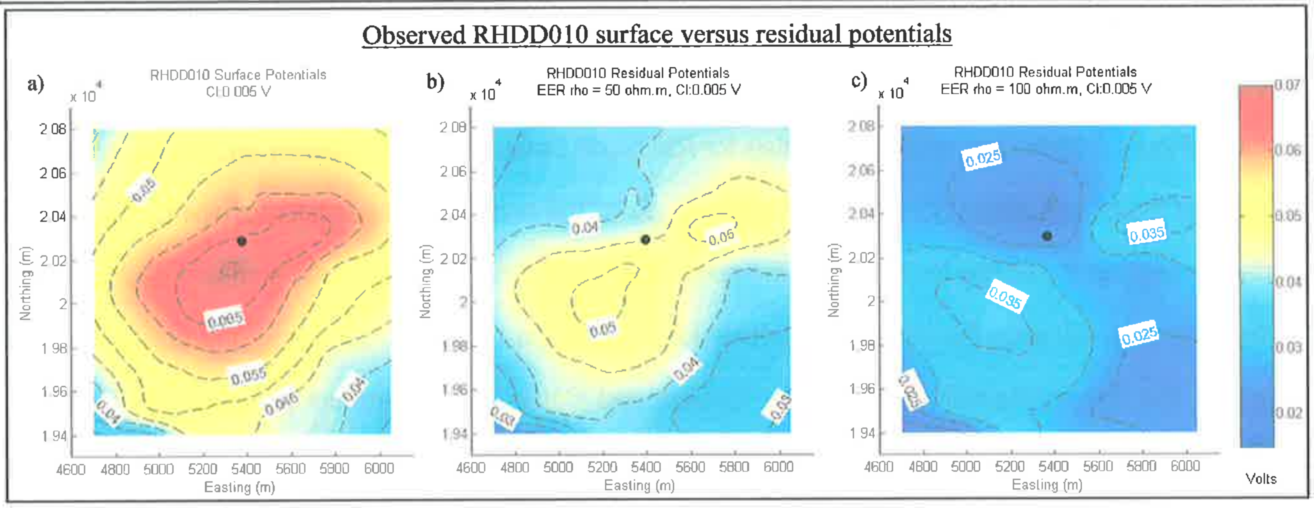

Observed RHDD010 surface versus residual potentials

Figure 4.37: EER on RHDD010 MALM data. a) surface potentials, b) residual potentials with 50 ohm.m EER, c) residual potentials with 100 ohm.m EER. Colour scale is 0.015 to 0.07 V, contour interval is 0.005V.

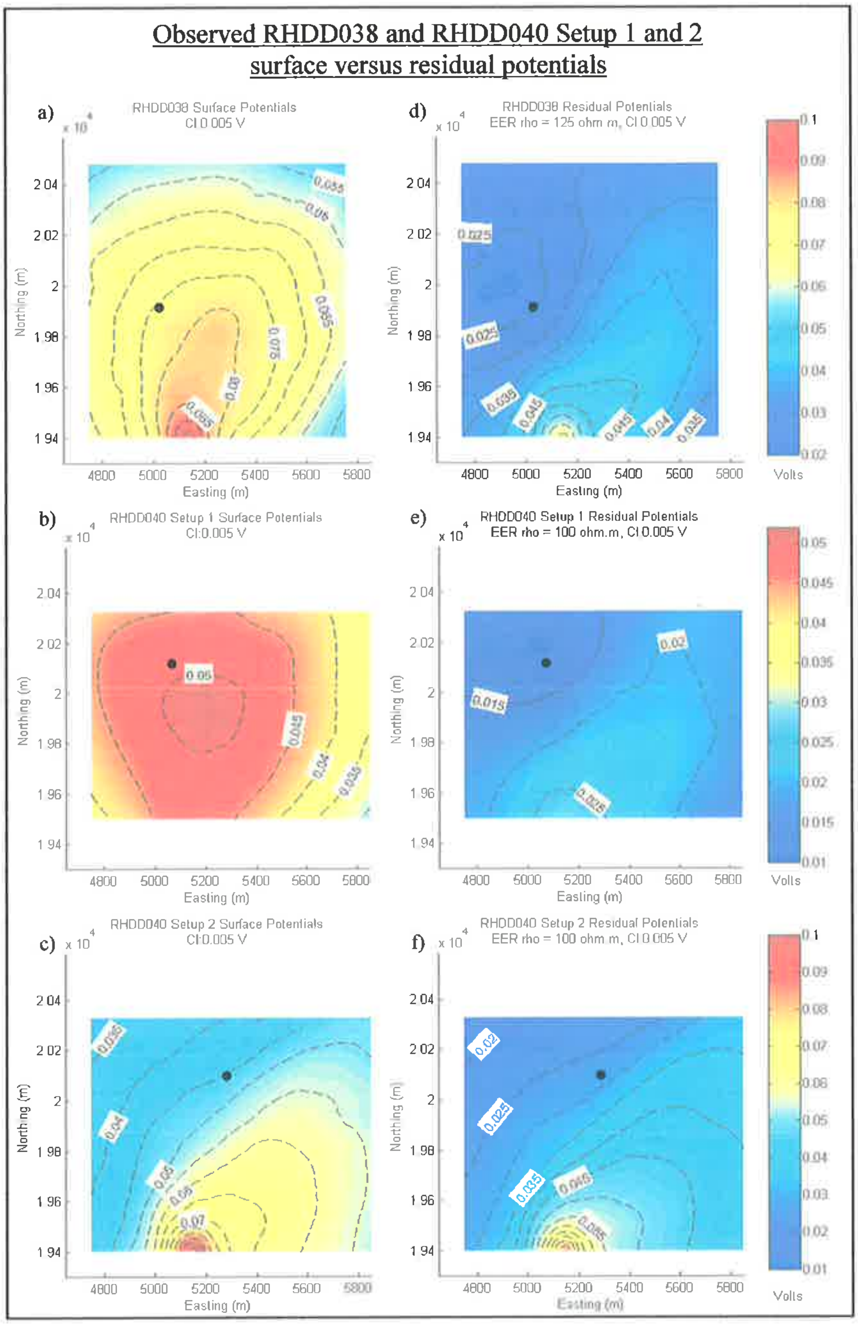

Observed RHDD038 and RHDD040 Setup 1 and 2 surface versus residual potentials

Figure 4.38: Surface potentials for a) RHDD038, b) RHDD040 Setup 1 and c) RHDD040 Setup 2 are compared to their residual surface potentials d) RHDD038 with 125 ohm.m $\rho_{halfspace}$ EER, e) RHDD040 Setup 1 with 100 ohm.m $\rho_{halfspace}$ EER and f) RHDD040 Setup 2 with 100 ohm.m $\rho_{halfspace}$ EER. Contour interval is 0.05V.

This is the same for the residual potentials of RHDD040 Setup 1 in Figure 4.38e, using a $\rho_{halfspace}$ of 100 ohm.m. Both are unlike their surface potentials and more akin to the surface potentials for RHDD040 Setup 2 (Figure 4.38c). The residual potentials for RHDD040 Setup C remain relatively unchanged compared to those of the other Catalpa North for the same $\rho_{halfspace}$ of 100 ohm.m. The persistent shape of the residual surface potentials at Catalpa North (that is the continuation to the northeast from the southern peak position) follows the patterns seen the residual potentials for the Catalpa region for the same grid positions. This suggests that the commonality between the Catalpa and Catalpa North residual potentials is due to the underlying geology and its associated geoelectrical connections.

Prominent Hill

The MALM data acquired at Prominent Hill was a magnitude lower in overall potential amplitude compared to the Golden Grove surveys. This implies that half-space resistivities used in EER are lower. For the single in-mineralisation survey in drill hole RP017, the surface potentials are to the south of the electrode position (Figure 4.39a). Using a $\rho_{halfspace}$ of 2.5 ohm.m, the residual potentials separate the peak into two (Figure 4.39b). This is exaggerated when 5 ohm.m is used for $\rho_{halfspace}$ (Figure 4.39c). The residual potentials highlight the haematite rock as the shallowest conductive body near the electrode position.

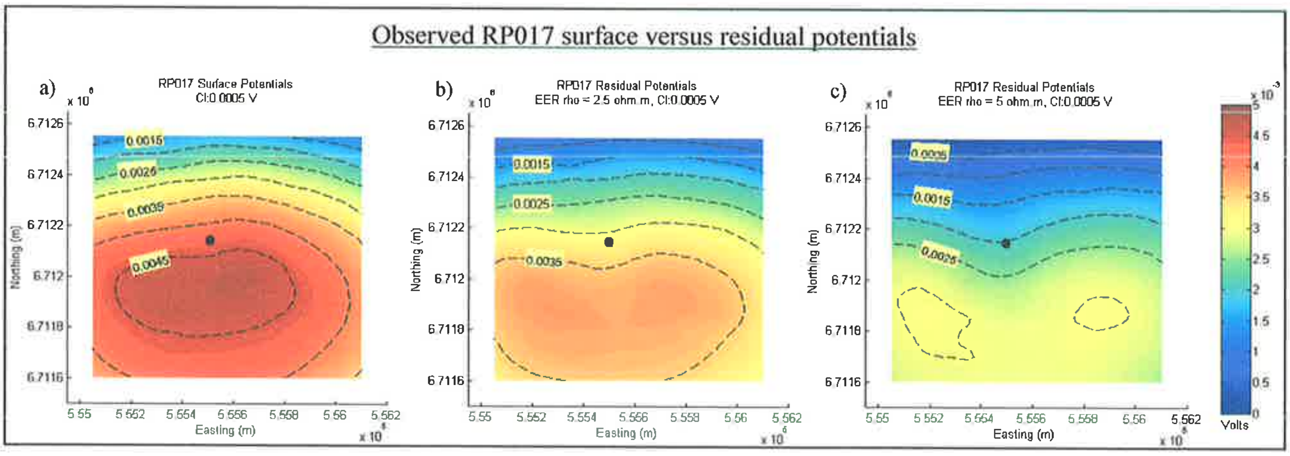
Observed RP017 surface versus residual potentials

Figure 4.39: EER on RP017 MALM data. a) surface potentials, b) residual potentials with 2.5 ohm.m EER and c) residual potentials with 5 ohm.m EER. Colour scale is 0.015 to 0.07 V, contour interval is 0.0005V.

4.3 SUBSURFACE APPROXIMATION ALGORITHM RESULTS

The SSA assists in the visualisation of the idealised FEM models or known geology by generating three dimensional volumes of data from the surface MALM data. By selecting an appropriate correlation value, the visualiser generates isosurfaces that encompasses regions of equal or greater correlation. The higher the correlation, the more likely the algorithm pinpoints regions in the volume which are associated with points of charge that contribute to a surface MALM anomaly. These points of charge relate to either the energised conductor in the modelling, or in most cases, to the mineralisation in the field. Along with *a priori* geological information, the SSA algorithm can aid to image the subsurface from just the surface potentials derived from a MALM survey.

Idealised FEM models

The SSA algorithm outputs a three dimensional matrix of correlation values. Isosurfaces representing equal correlation values are used to signify different levels of correlations. Surfaces which best approximate the modelled mineralisation are often a high correlation value (> 0.950 correlation); this is due to the concentration of good correlation elementary point sources identified by the algorithm. Depth from the surface to the mineralisation is a comparably lower correlation value. Figure 4.40 is the resistivity contrast model (p26) with 5 correlation isosurfaces. The 0.985 value is localised on the position of the conductive structure, whereas the 0.900 surface identifies the depth from surface of the conductive body (in this case 100 metres). Where contours of equal correlation are displayed, the contours mark the values 0.95 to zero correlation at intervals of 0.05 correlation.

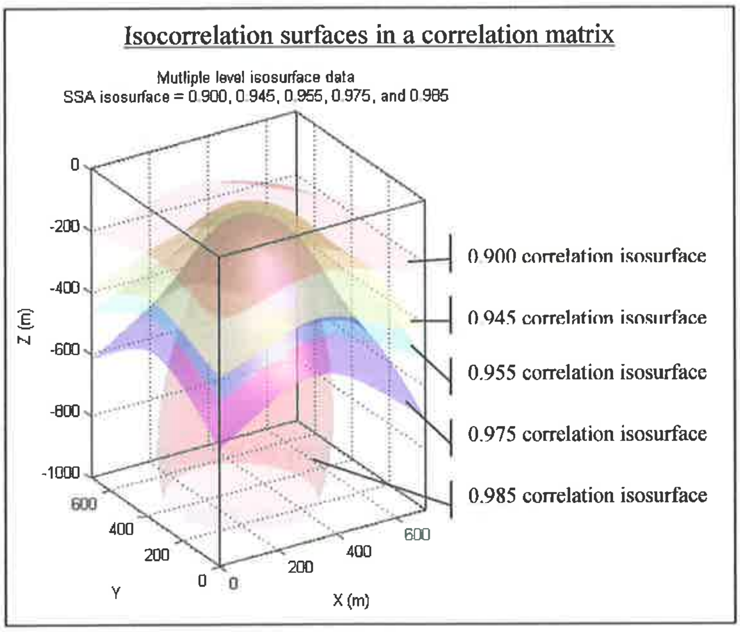

Figure 4.40: Resistivity contrast model with conductive body of 1 ohm.m resistivity and half-space of 1000 ohm.m resistivity. This diagram shows the various isosurfaces 0.900, 0.945, 0.955, 0.965, 0.975 and 0.985. The colours are arbitrary to aid identification.

Resistivity contrast models

Applying the SSA algorithm to models in which the conductive body has differing resistivities, it was found that there was little change in the correlation values with changing surface potential amplitude (Figure 4.41). With the conductive body at 100 ohm.m resistivity, the synthetic surface potentials are almost a homogeneous electrode response due to the low contrast in resistivities between the host-rock and the modelled mineralisation (Figure 3.3b, p36). With increased contrast of resistivities, the surface potentials are elongated along the length of the mineralisation. This is reflected in the correlation values of the SSA algorithm as the output from the SSA algorithm is predominantly affected by the spatial distribution of the surface potentials. Figure 4.41b, c and d have surface potentials that exhibit elongation along the length of the mineralisation (Figure 3.3). The mean surface potentials decrease with increasing resistivity contrast, but there is little change to be observed in the 0.985 correlation isosurface in comparison to the 0.985 correlation isosurface of the 100 ohm.m conductive body with surface potentials that are a near-homogenous response.

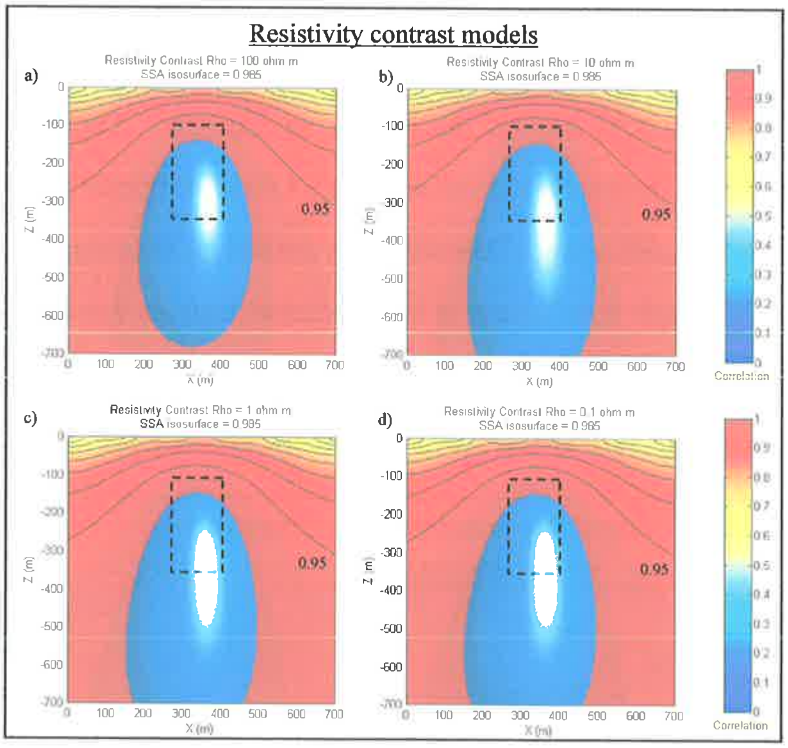

Figure 4.41: The resistivity contrast model with isocorrelation surfaces of 0.985 correlation (blue body), the dashed line is the modelled conductive body location. The conductive structure has 100, 10, 1 and 0.1 ohm.m resistivity in a), b), c) and d). There is little change as the isosurfaces of the SSA algorithm are dependent on changes in the pattern of the surface potential anomaly.

Effect of depth from surface models

The shallow body has a well defined surface potential anomaly of a sharp peak potential, with low surrounding background potentials (Figure 3.5). The SSA output of a shallow body shows high correlation values associated with the mid to lower sections of the conductive body (Figure 4.42a). With increasing depth the amplitude of the surface potential anomaly is decreased and broadened. This is echoed in the correlation values of the SAA algorithm with the 0.985 isosurface expanding with increasing depth of the body.

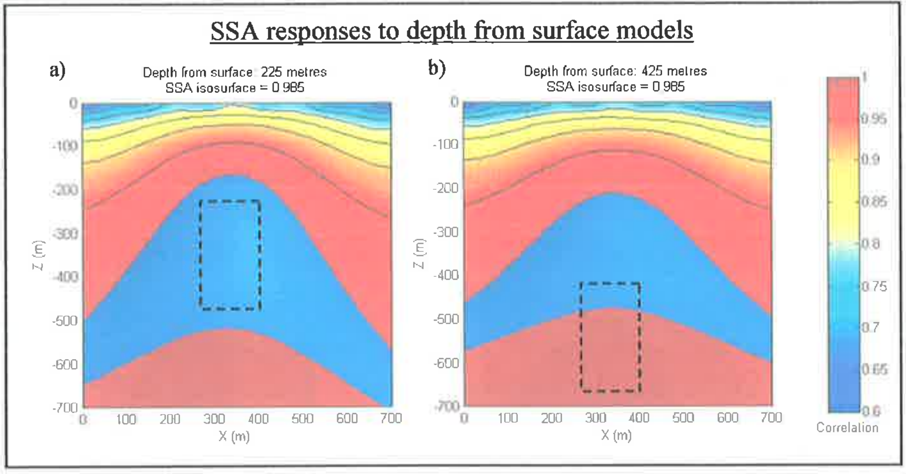

Figure 4.42: With increasing depth of the body (left to right), the 0.985 correlation isosurface has a small change in the minimum depth of the isosurface across the 2 models. As the surface potentials broaden, the isosurface broadens as well.

Effect of different body volumes models

As the volume of a conductive body increases the correlation values from the SSA algorithm changes in shape (Figure 4.43). Small volumes result in a closed isosurface as seen in Figure 4.43a with an isosurface of 0.980 correlation, whilst the same isosurface for a larger volume body (with the associated broadened surface potentials) is much broader and opens at depth (Figure 4.43b and c).

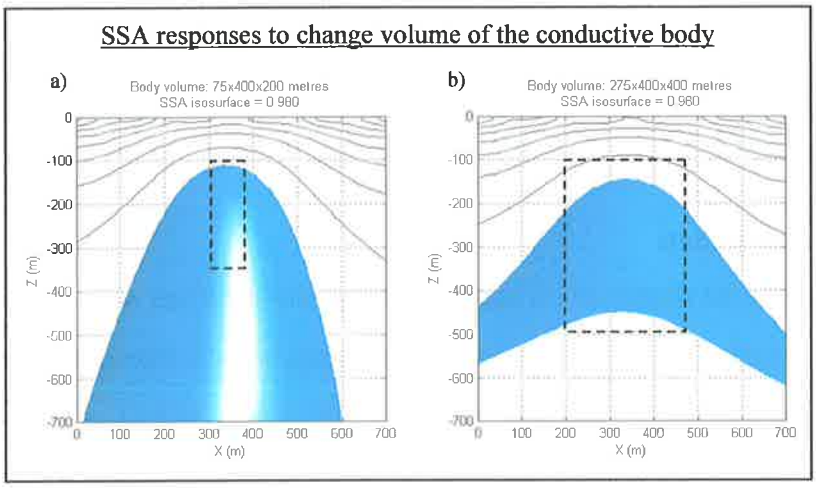

Figure 4.43: Isosurfaces = 0.980 correlation. a) small conductive volumes have a closed isosurface. and b) with increasing volume the isosuface opens at depth. The shape of the isosurface is determined by the pattern on the surface potentials. X-Z correlation contours at Y = 350m

In-mineralisation dipping models

Correlation values for dipping models shift towards the upper surface of the conductor with increasing dip. The 30 degree body with a broad surface potential anomaly has the 0.990 correlation isosurface situated under the bulk of the conductive structure (away from the position of the upper surface of the conductor) and trends to the east and down (as indicated by the arrow in Figure 4.44a).

This is repeated for the 45 degree body. With increasing dips of 60 and 90 degrees, the isosurface shifts so that it is located under the upper surface of the conductive body since the body tends towards a vertical orientation (Figure 4.44c and d). The response of the vertical body in this case is skewed towards the east due to the peak surface potential response being close to the edge of the model area.

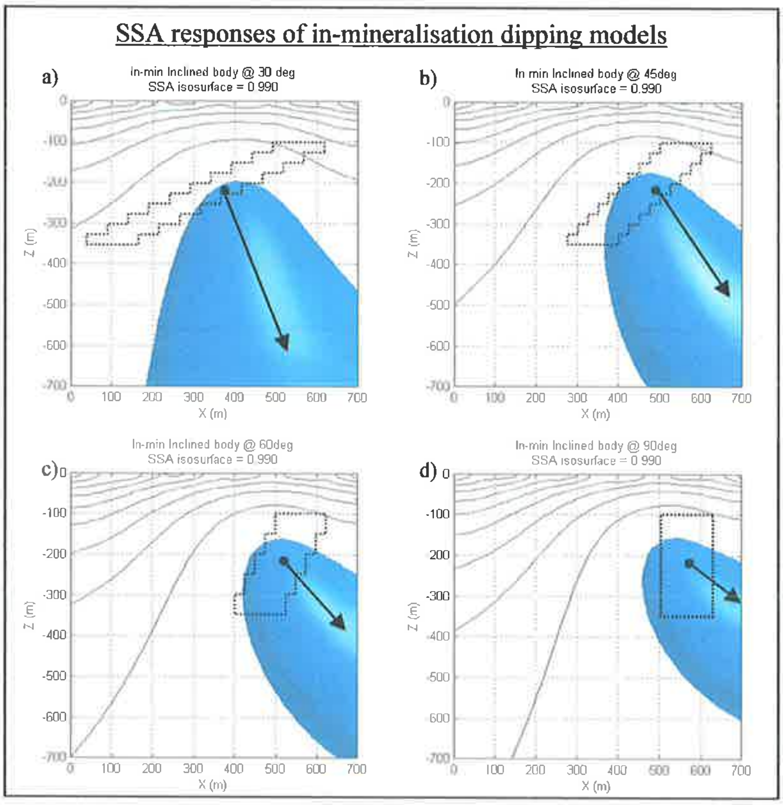

Figure 4.44: Isosurfaces = 0.990 correlation. a) 30 degree model, b) 45 degree model, c) 60 degree model and d) vertical body model. The dipping bodies have the isosurface located beneath the bulk of the body X-Z correlation contours at Y = 350m

Two body models

Depth of second body models

The SSA algorithm locates the position of the uppermost conductive structure when multiple conductive bodies are present. As the conductive body containing the source electrode is placed at an increasing depth, the SSA isocorrelation surface (of 0.960 correlation) is first centred over the shallow energised body at 100 metres (Figure 4.45a). With increasing depth of the energised body (250 and 350 metres) the isosurface is repositioned over the non-energised conductive body as its induced charges at resistivity boundaries are closer to the surface and dominate the surface potentials (Figure 4.45b, and c).

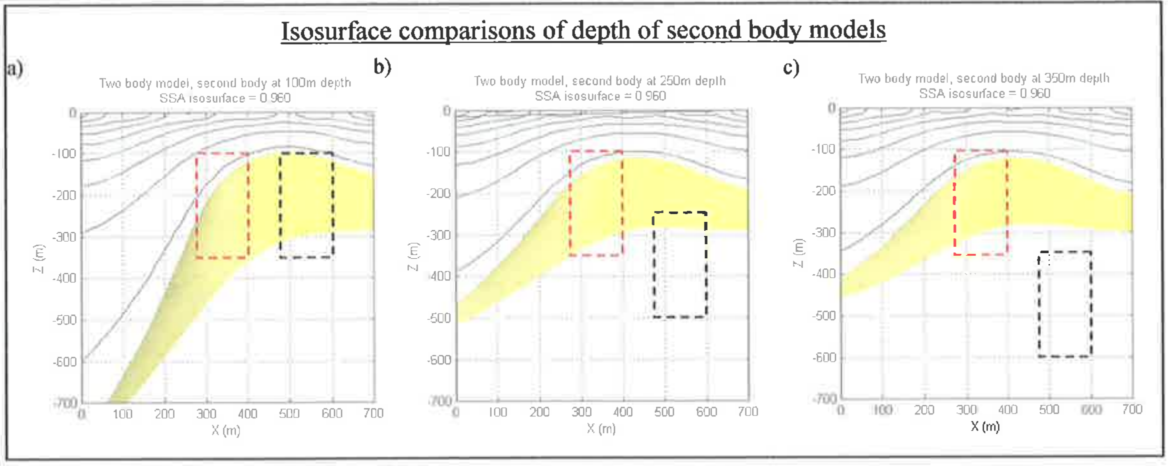

Figure 4.45: As the depth of the second body (black dashed outline) containing the source electrode increases (from a to c), the isosurface of 0.960 correlation (yellow) repositions towards the non-energised body in centred in the model space (red dashed outline). X-Z correlation contours at Y = 350m.

Separation of second body models

With increasing separation of two conductive bodies, the correlation values demarcate the position of the energised conductive body (Figure 4.46). At small separations, the surface potentials are much broader than a single body model. This is seen in the location of the high correlation elementary sources across both conductive bodies (Figure 4.46a). At 125 metre separation, the concentration of point sources is only about the energised body (Figure 4.46b), but the isosurface is much broader than that of Figure 4.46c, where the non-energised body is 225 metres from the conductive body containing the source electrode.

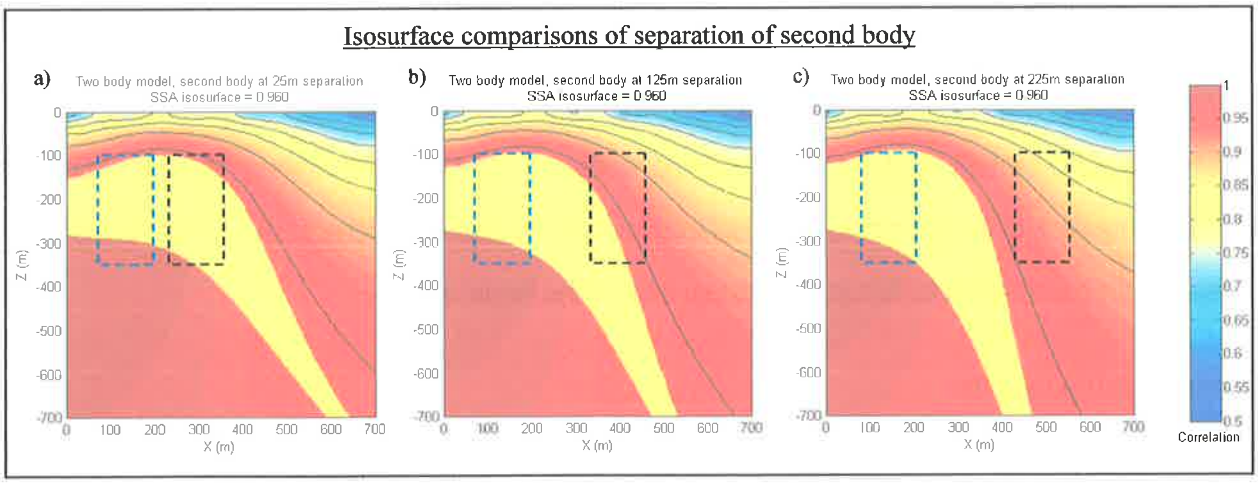

Figure 4.46: Isosurfaces = 0.960 (yellow). a) For small separations of 25 m between two bodies the isocorrelation surface is broad, encompassing both bodies, as the non-energised body (right) is increasingly separated from the energised body (left), the isosurfaces do not show the position of the non-energised body. b) 125m separation and c) 225m separation. X-Z coloured slice and correlation contours at Y = 350m.

Basement/regolith models

The results from the SSA algorithm so far present show that the algorithm can aid in spatially locating the upper surface of the conductive structure in models with no regolith. The inclusion of a high resistivity contrast regolith wedge (p54) has resulted in a significant difference in the surface potentials of otherwise similar models. The RBA model has the conductive body beneath the surface expression of the basement/regolith contact. The resultant SSA output of the RBA surface potentials has the location of high correlation charges to the west of the conductive body position (Figure 4.47, left).

The high correlation values of the RBB model shifted away from the conductive regolith wedge relative to the modelled mineralisation body. The shape of the RBB 0.960 isosurface is very different to that of the RBA model despite being in the same distance from the edge of the model volume. The higher correlation isosurface of 0.995 is still west of the of the conductive body position (Figure 4.47, right).

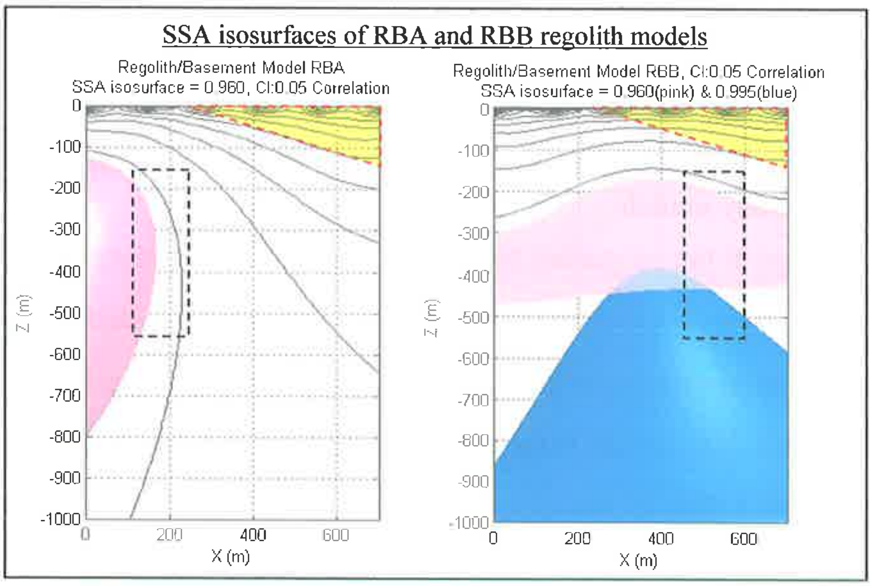

Figure 4.47: (left) the RBA model with a 0.960 (pink) isosurface calculated from the modelled surface potentials. (right) the RBB basement/regolith model with two isosurfaces 0.960 (pink) and 0.995 (blue). The yellow wedge represents the 15 ohm.m regolith wedge. Correlation contours at Y = 350m.

In summary, the westward offset from the conductive body of point sources with high correlation to the synthetic surface potentials, is due to the modelled wedge of conductive saprolith or alluvium against the basement. The peak of the isosurface was displaced towards the region of higher resistivity (i.e. to the west in this case as the basement outcrops on the western edge of the model space).

Regolith/regolith models

There is only a subtle change in the isocorrelation surfaces of 0.960 and 0.995 correlation (Figure 4.48) when the resistivities of the two regolith wedges are swapped in the "Figure 3.31b the contact is not as readily apparent when the body is placed beneath the bulk of the regolith wedge, the peak surface potentials are also shifted in the up-dip direction of the regolith/basement contact. The RBB potential profile curve in Figure 3.30 does not distinguish the position of the regolith/basement contact readily. In comparison, the contact is easily identified in the plan view of the surface potentials. This is due in part to the simplicity of the models and the sharp contrast of resistivities. This would not be as simple to identify in field data due to more complex geometries and gradational resistivity transitions from regolith to basement.

Regolith/regolith contact models" (WMA and WMB, p55). The isosurface peaks are shifted east of the conductive body position, located beneath the angular contact between the two modelled regolith materials of 10 and 15 ohm.m.

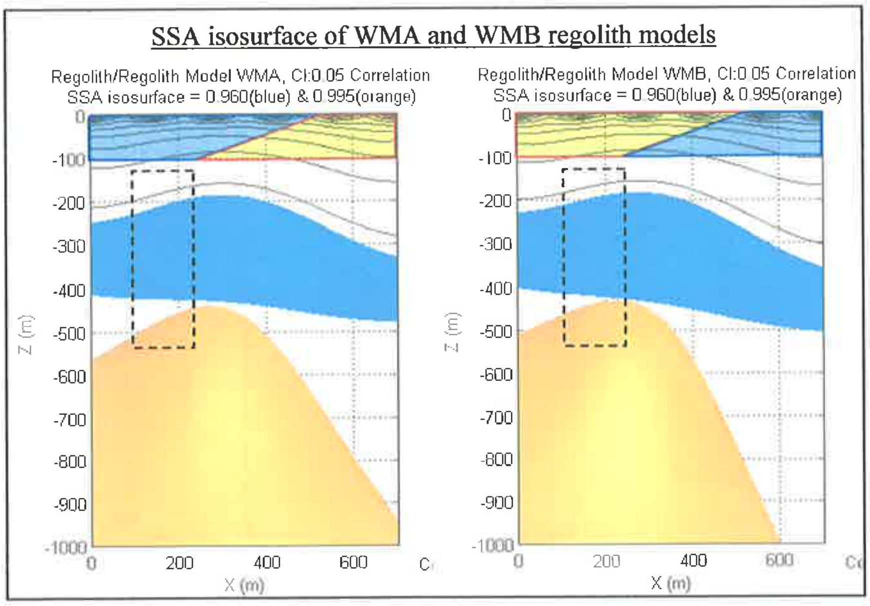

Figure 4.48: There is minimal change by switching the resistivities of the regolith wedges. The WMA model (left) has the peak of the isosurface to the east of the conductive body as does the WMB model (right). The black outline is the conductive body. The blue polygon denotes the 10 ohm.m regolith layer, the yellow polygon is the 15 ohm.m regolith layer. Correlation contours at Y = 350m.

The correlation values for the WMA model (Figure 4.48, left) exhibits a small change in isosurface peak position relative to the WMB model (Figure 4.48, right) where the isosurfaces are closer to the body position as the 15 ohm.m resistivity layer is above the conductive body. This was also seen in the basement/regolith scenario where the isosurface peak was distorted towards the more resistive material host-rock.

FEM field site models

Catalpa models

The surface potentials from the Catalpa FEM models were passed though the SSA algorithm to investigate its response to more complex models. The surface potentials of RHDD018 and RHDD020 were similar, hence the SSA algorithm response for RHDD018 (Figure 4.49a) is similar to RHDD020 Setup A (Figure 4.49b). For both the in-mineralisation cases the 0.950 correlation surface marks the top of the conductive body at 125m.

Isosurfaces for the shallow near-miss electrode position of the RHDD020 Setup B model (Figure 4.49c) is different compared with the two in-mineralisation models due to the association of surface potentials with the current electrode position. The isosurfaces for the deep near-miss model of RHDD020 Setup C (Figure 4.49d) is similar to the in-mineralisation scenario. Each of the four responses has the peak of the 0.990 correlation isosurface in approximately the same position.

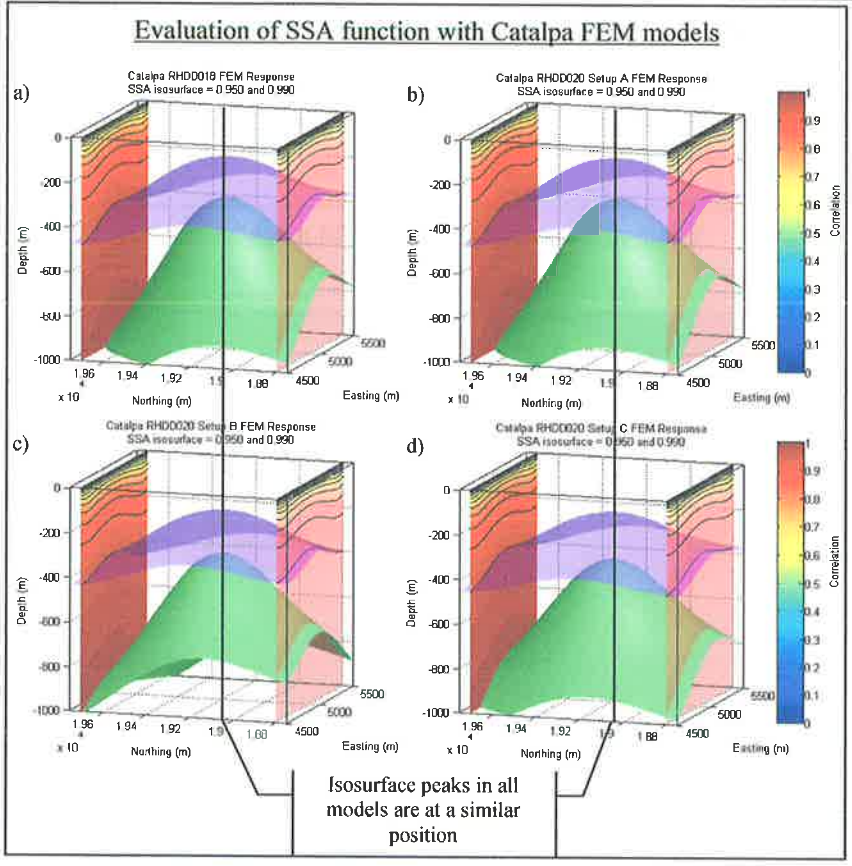
Evaluation of SSA function with Catalpa FEM models

Isosurface peaks in all models are at a similar position

Figure 4.49: Catalpa FEM models with two isosurfaces of 0.950 (purple) and 0.990 (green) correlation. SSA result for a) the in-mineralisation RHDD018 FEM surface potentials, are similar to b) RHDD020 Setup A. c) the shallow near-miss survey RHDD020 Setup B has an SSA response which is unlike the other 3, with d) the SSA result for RHDD020 Setup C (deep near-miss position) being similar to a) and b). The coloured slices show the X-Z correlation values at the northern and southern sections of the model space.

4.4 COMBINED EER AND SSA RESULTS

Idealised FEM models

Vertical near-miss models

Using a combination of the residual potentials and the imaging capabilities of the SSA algorithm allows for a realisation of the effectiveness of the EER algorithm for enhancing the MALM data. The vertical near-miss electrode positions were passed through both functions and the correlation isosurfaces for the unprocessed modelled surface potentials and the EER residual potentials were compared. For the electrode depth of 110 metres, Figure 4.50a shows the in-mineralisation correlation isosurface of 0.970 correlation. This is compared to Figure 4.50b, which is the same isocorrelation surface for the 25 metre near-miss electrode position. With the EER applied using a 400 ohm.m $\rho_{halfspace}$, the SSA isocorrelation surface for the near-miss electrode is similar to that of the in-mineralisation isosurface (Figure 4.50c).

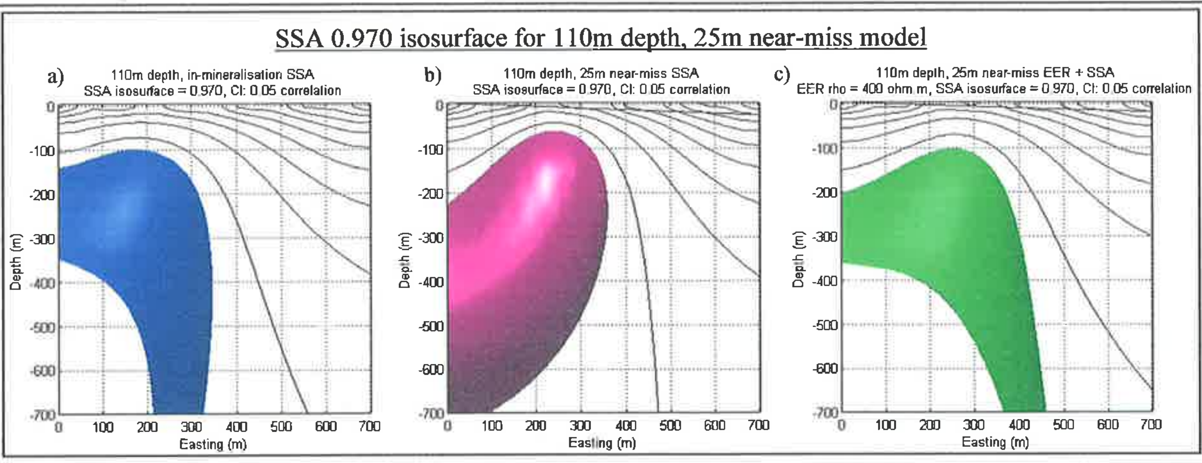

Figure 4.50: At 110m depth and 25m separation a) is the in-mineralisation 0.970 correlation isosurface, b) is the 25m near-miss 0.970 isosurface and c) is the 0.970 isosurface of the residual potentials from a 400 ohm.m EER for the near-miss model. Contours are at the X-Z slice of Y = 350 m.

As identified in the results for the FEM modelling of the near-miss electrode about a conductive vertical body, the in-mineralisation surface potentials vary only slightly (Figure 3.15, p44) and differences in the SSA correlation values are very small. Therefore only the in-mineralisation isosurface of 0.975 correlation for the depth of 225 metres has been present for comparison (Figure 4.51a). With increasing depth and separation from the conductive body, the SSA algorithm response of the near-miss electrodes for the 225, 325 and 375 metre depth electrodes at the corresponding separations of 25, 75 and 150 metres from the body, are increasingly less like the in-mineralisation isosurface of 0.975 correlation (Figure 4.51b, c and d). However, with the EER from these near-miss surface potentials, the residual potential isosurfaces are migrated back towards the conductive body and are similar to the in-mineralisation response. The correlation surface for the 400 $\rho_{halfspace}$ EER residual potentials of the 225 metre depth, 25 metre near-miss (Figure 4.51e) is a refinement of the unaltered surface potentials. Both Figure 4.51f and g are better comparisons to the in-mineralisation isosurface when 500 and 800 ohm.m $\rho_{halfspace}$ are used respectively in the EER function.

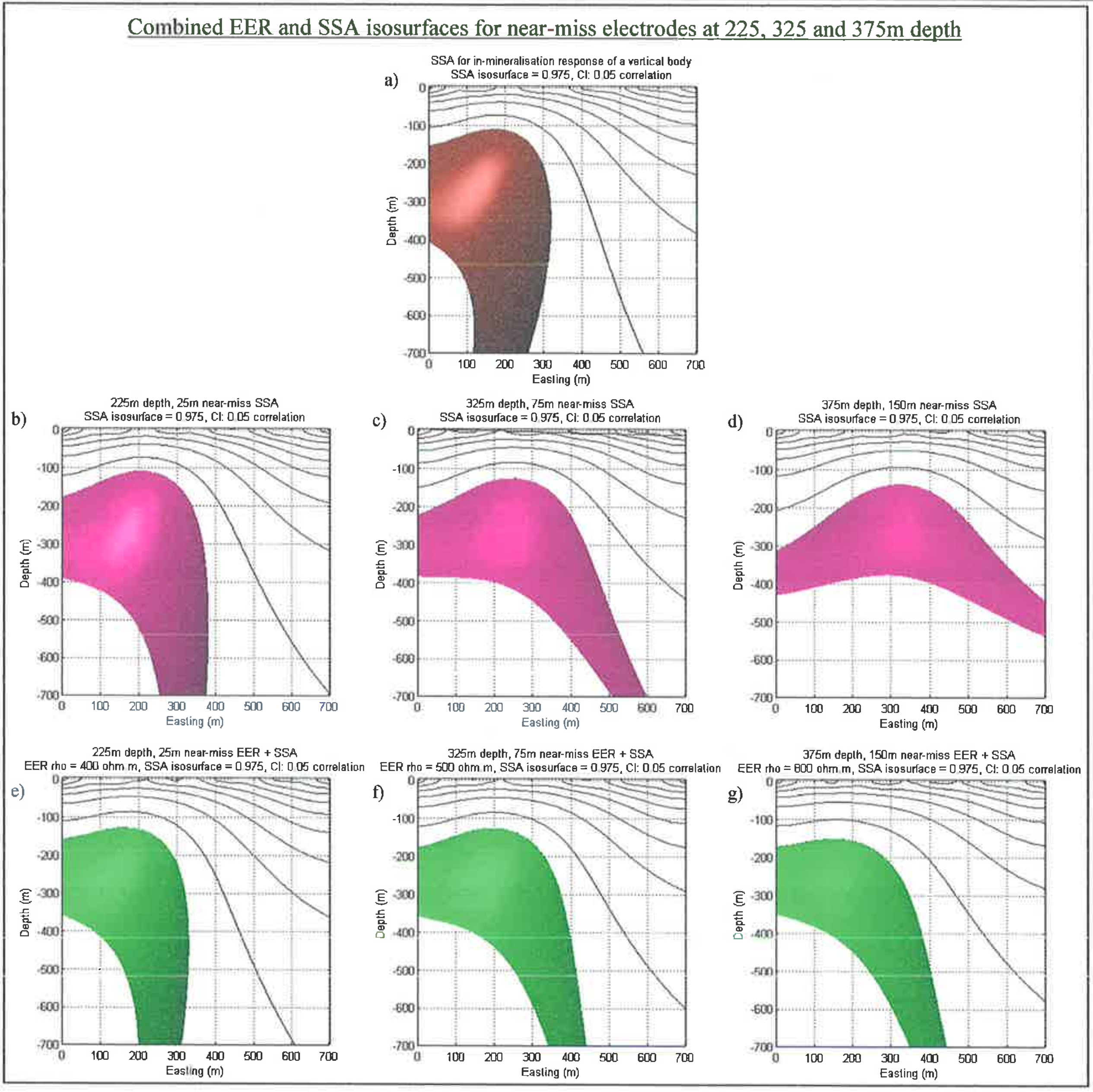
Combined EER and SSA isosurfaces for near-miss electrodes at 225, 325 and 375m depth

a) SSA for in-mineralisation response of a vertical body
SSA isosurface = 0.975, CI: 0.05 correlation

b) 225m depth, 25m near-miss SSA
SSA isosurface = 0.975, CI: 0.05 correlation

c) 325m depth, 75m near-miss SSA
SSA isosurface = 0.975, CI: 0.05 correlation

d) 375m depth, 150m near-miss SSA
SSA isosurface = 0.975, CI: 0.05 correlation

e) 225m depth, 25m near-miss EER + SSA
EER rho = 400 ohm.m, SSA isosurface = 0.975, CI: 0.05 correlation

f) 325m depth, 75m near-miss EER + SSA
EER rho = 500 ohm.m, SSA isosurface = 0.975, CI: 0.05 correlation

g) 375m depth, 150m near-miss EER + SSA
EER rho = 800 ohm.m, SSA isosurface = 0.975, CI: 0.05 correlation

Figure 4.51: All isosurfaces are isosurface 0.975 correlation. a) is the common in-mineralisation response of the SSA function. b) is the 225m depth 25m near-miss electrode position, c) is the 325m depth, 75m near-miss electrode position, d) is the 375m depth, 150m near-miss electrode position. e), f) and g) are the corresponding isosurfaces for the b), c) and d) using 400, 500 and 800 ohm.m $\rho_{halfspace}$ respectively. Contours are at the X-Z slice of Y = 350 m.

FEM field site models

Catalpa models

The combined use of the EER and SSA algorithms for the Catalpa FEM models show that, with the EER, the correlation isosurfaces of the residual potentials all open towards the south, which is a better representation of the modelled conductive body than the unaltered surface potential responses of the SSA algorithm (c.f Figure 4.52 with Figure 4.49, p118).

In comparing the residual versus surface potentials isosurfaces for RHDD018 (Figure 4.52a c.f. Figure 4.49a, p118), the isosurfaces of the residual potentials (using 45 ohm.m $\rho_{halfspace}$) are inclined to the north more so than the isosurfaces of the unaltered surface potentials. This is the same for the RHDD020 Setup A isosurfaces after an EER of 65 ohm.m $\rho_{halfspace}$. For RHDD018, RHDD020 Setup A and B, the 0.990 isosurface of the residual potentials stop short of the 19600m northing. Both isosurfaces for the RHDD020 Setup B residual potentials (Figure 4.52c) are more asymmetric in the y-axis as opposed to those in Figure 4.49c and is more like the in-mineralisation residual potentials. This suggests that the dip of the body is more effectively represented by residual potentials isosurface. There is only a small change in the RHDD020 Setup C isosurfaces (Figure 4.52d), with the residual potential isosurfaces opening to the south (c.f. Figure 4.49d).

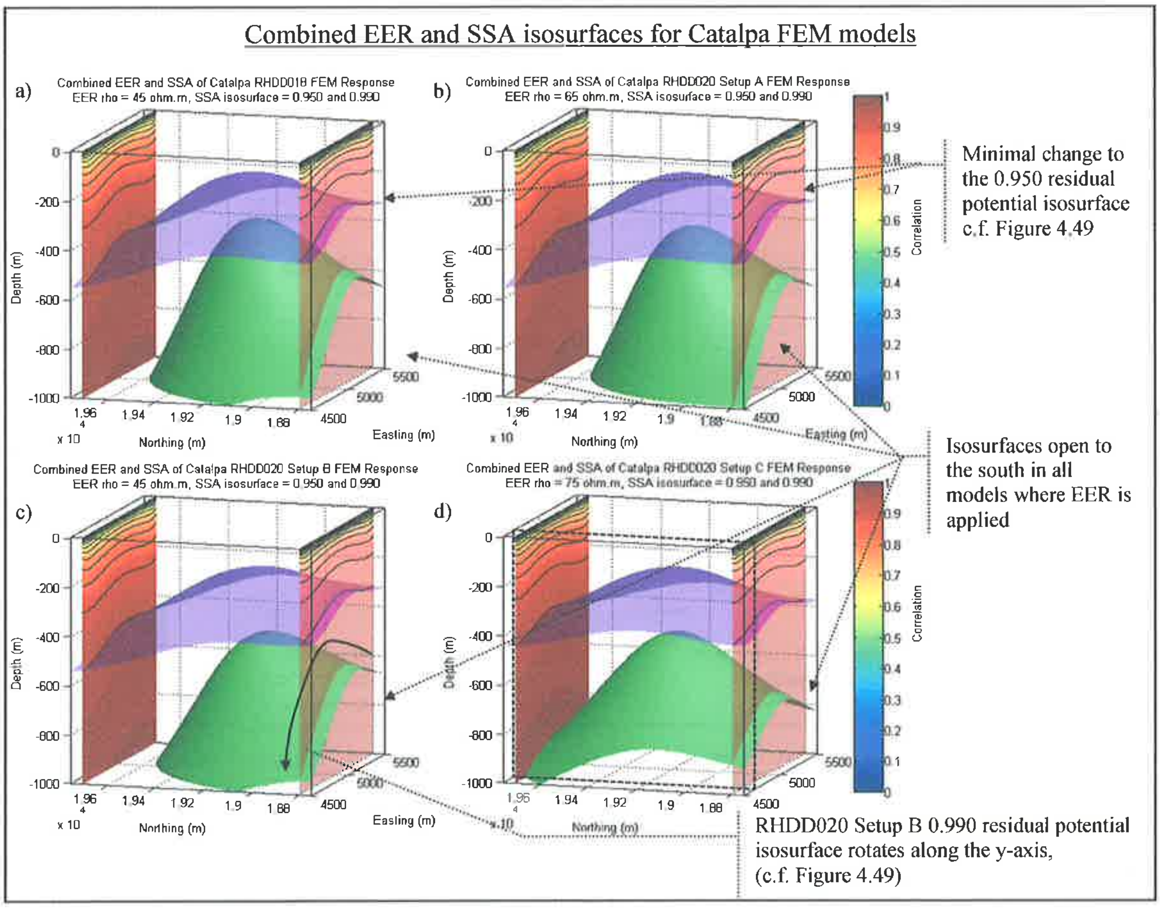

Minimal change to the 0.950 residual potential isosurface c.f. Figure 4.49

Isosurfaces open to the south in all models where EER is applied

RHDD020 Setup B 0.990 residual potential isosurface rotates along the y-axis, (c.f. Figure 4.49)

Figure 4.52: Purple and green isosurfaces are 0.950 and 0.990 correlation respectively. a) the SSA of residual potentials using a 45 ohm.m $\rho_{halfspace}$ for RHDD018, b) SSA of residual potentials with a 65 ohm.m $\rho_{halfspace}$ removal for RHDD020 Setup A, c) isocorrelations surfaces for RHDD020 Setup B using $\rho_{halfspace}$ of 45 ohm.m and d) isosurfaces of the deep near-miss RHDD020 Setup C residual potentials using a 75 ohm.m $\rho_{halfspace}$.

Prominent Hill models

The EER from the Prominent Hill FEM models and the subsequent correlation matrices generated, show that the high correlation source points are situated to the south, over the modelled conductive haematite rock. The in-mineralisation and shallow near-miss 0.985 isosurface are different from each other (Figure 4.53a c.f. Figure 4.53c). However, with the EER using 35 ohm.m $\rho_{halfspace}$, both the residual potentials for each electrode position (Figure 4.30b and Figure 4.31b, p105) are similar. Hence the isocorrelation surfaces share the same shape (Figure 4.53b and d).

As with the SSA isosurface comparisons of the surface and residual potentials for the Catalpa models, there is little change in the lower correlation isosurface (purple isosurface) between the surface potentials and the residual potentials. A greater change is observed between the higher correlation isosurface (green) of the surface potentials and residual potentials.

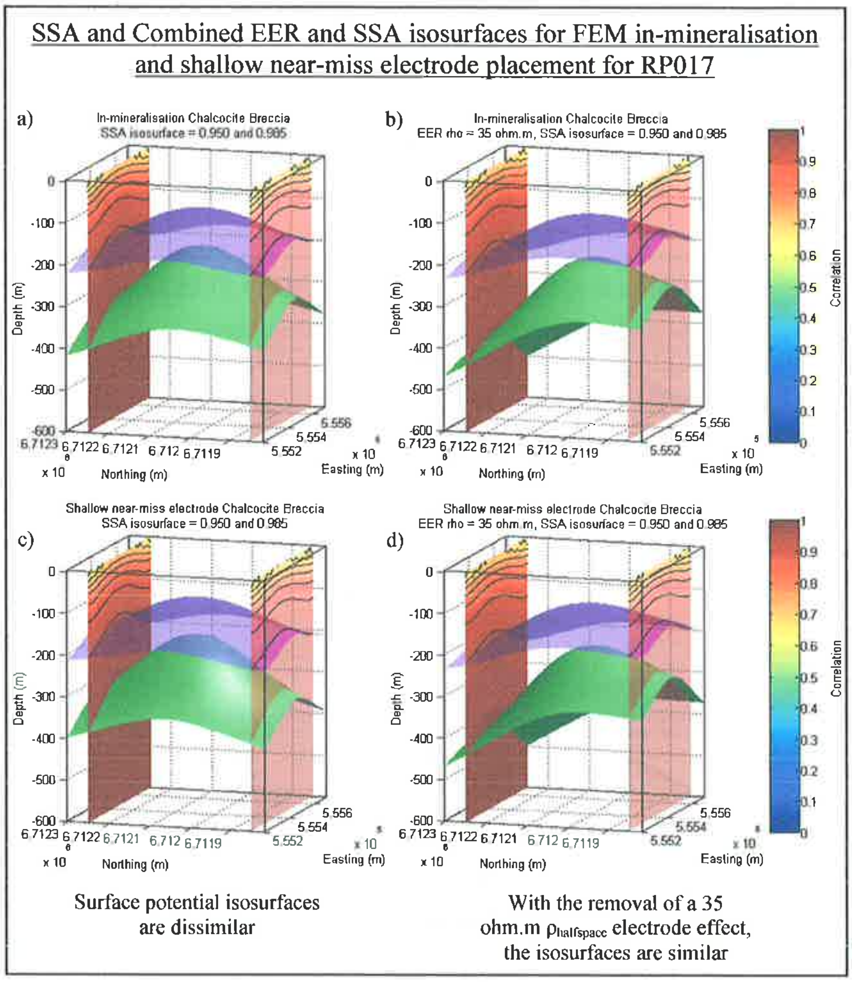
SSA and Combined EER and SSA isosurfaces for FEM in-mineralisation and shallow near-miss electrode placement for RP017

Surface potential isosurfaces are dissimilar

With the removal of a 35 ohm.m $\rho_{halfspace}$ electrode effect, the isosurfaces are similar

Figure 4.53: Purple and green isosurfaces are 0.950 and 0.985 correlation respectively a) SSA response from the in-mineralisation model for RP017, in the chalcocite breccia, b) the SSA response of the residual potentials for the in-mineralisation model, and c) the shallow near-miss model for RP017 and d) the residual potentials of that mode after a 35 ohm.m EER.

Field MALM data

Golden Grove

Catalpa

The SSA algorithm, using the Catalpa MALM data sets, has generated distinct isosurfaces for each set of surface potential data. The two in-mineralisation electrode positions of RHDD018 and RHDD020 Setup A have given rise to differently shaped isosurfaces for 0.920 and 0.950 correlation (Figure 4.54a and Figure 4.55a). In comparison, the isosurfaces for the shallow and deep near-miss position (RHDD020 Setup B and C respectively) have individually shaped isosurfaces that do not resemble each other or the in-mineralisation surfaces (Figure 4.56a and Figure 4.57a for RHDD020 Setup B and C respectively).

In using the EER function, the isosurfaces of the residual potentials for the respective surveys become more similar, suggesting that the shape of the isocorrelation is dependent on the geology. Using a low $\rho_{halfspace}$ for the EER function obtains the residual potentials seen in Figure 4.33 to Figure 4.36b (p106) for RHDD018, RHDD020 Setup A, B and C respectively.

These low $\rho_{halfspace}$ EER alter the residual potentials anomalies such that the residual potential isosurface for RHDD018 using a 50 ohm.m $\rho_{halfspace}$ (Figure 4.54b) shares some similarities to the surface potential isosurfaces for RHDD020 Setup A (Figure 4.55a). The residual potential isosurface for the near-miss electrode positions using a low $\rho_{halfspace}$ EER (100 and 50 ohm.m $\rho_{halfspace}$ for RHDD020 Setup B and C, Figure 4.56b and Figure 4.57b, respectively), are still very different to the other isosurfaces.

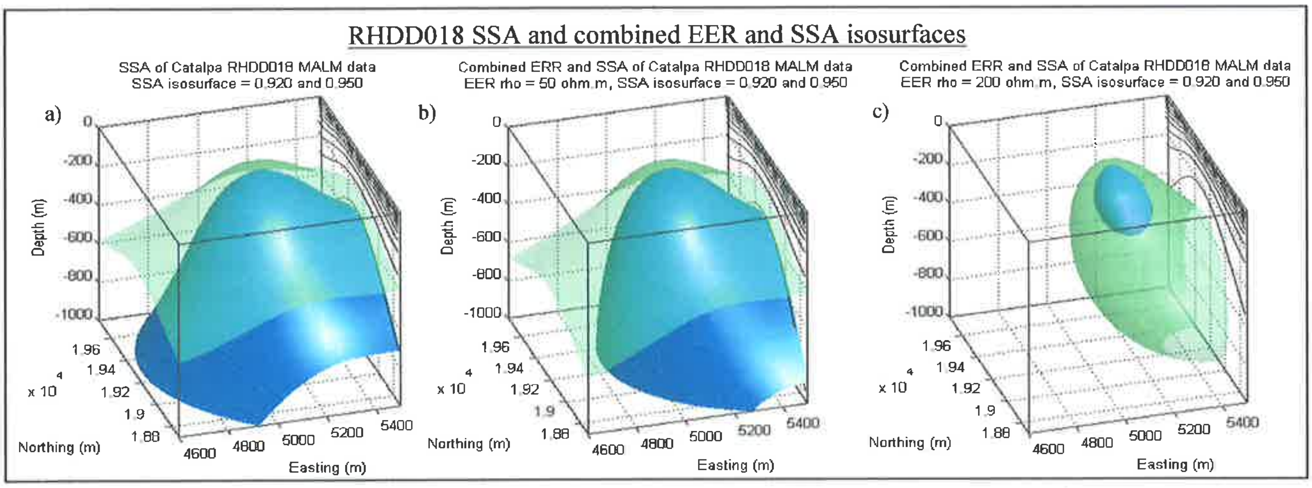

Figure 4.54: a) RHDD018 MALM surface potentials using the SSA function, b) RHDD018 isosurfaces of low EER residual potentials using 50 ohm.m $\rho_{halfspace}$ and c) isosurfaces of high EER residual potentials using 200 ohm.m $\rho_{halfspace}$. Green and blue isosurfaces represent the 0.920 and 0.950 correlation surfaces respectively.

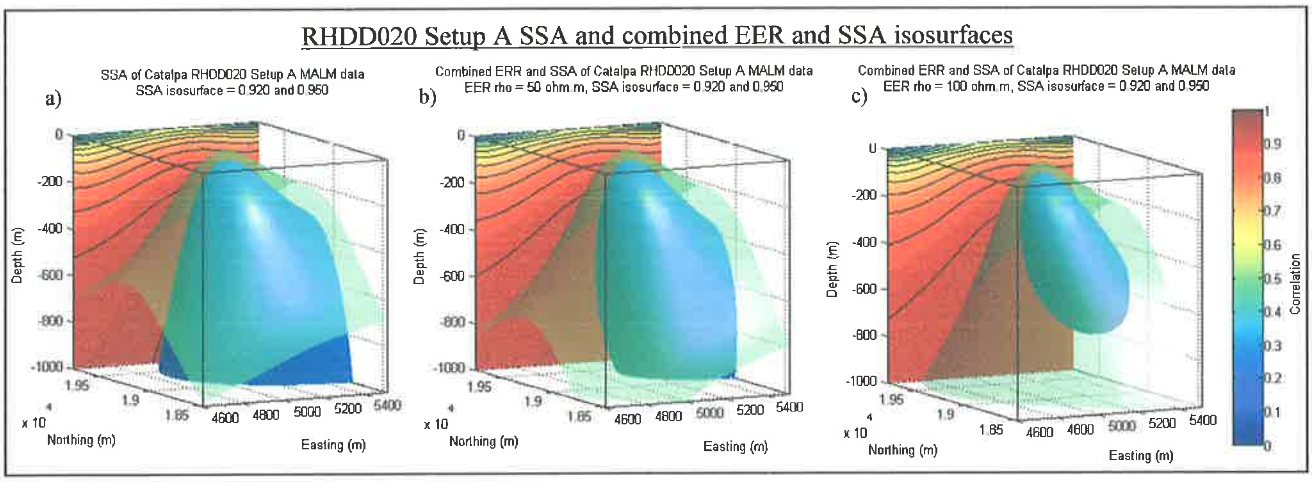

Figure 4.55: a) RHDD020 Setup A MALM surface potentials using the SSA function, b) RHDD020 Setup A isosurfaces of low EER residual potentials using 50 ohm.m $\rho_{halfspace}$ and c) isosurfaces of high EER residual potentials using 100 ohm.m $\rho_{halfspace}$. Coloured plane represents the X-Z slice through the correlation matrix at the northern end of the survey area. Green and blue isosurfaces represent the 0.920 and 0.950 correlation surfaces respectively.

The isosurfaces from the higher EER residual potentials share more similarities with each other than the isosurfaces of the unaltered surface potentials for each of the surveys. The position of the upper portion of the 0.950 isosurface is approximately the same for each survey. Using higher $\rho_{halfspace}$ for the EER removal gives the residual potentials seen in Figure 4.33 to Figure 4.36c (p106). The 200 ohm.m $\rho_{halfspace}$ residual potential isosurface (Figure 4.54c) is comparable to the residual potential isosurface for the shallow near-miss electrode of RHDD020 Setup B (Figure 4.56c) for the same $\rho_{halfspace}$ and to the RHDD020 Setup A isosurface (Figure 4.55c) using a 100 ohm.m $\rho_{halfspace}$. The high EER residual potential isosurface for RHDD020 Setup C extends to the south back towards the Gossan Hill Mine (Figure 4.57c) and falls off past the 19500m northing. This trend is seen in the other surveys as well as those of the Catalpa North surveys.

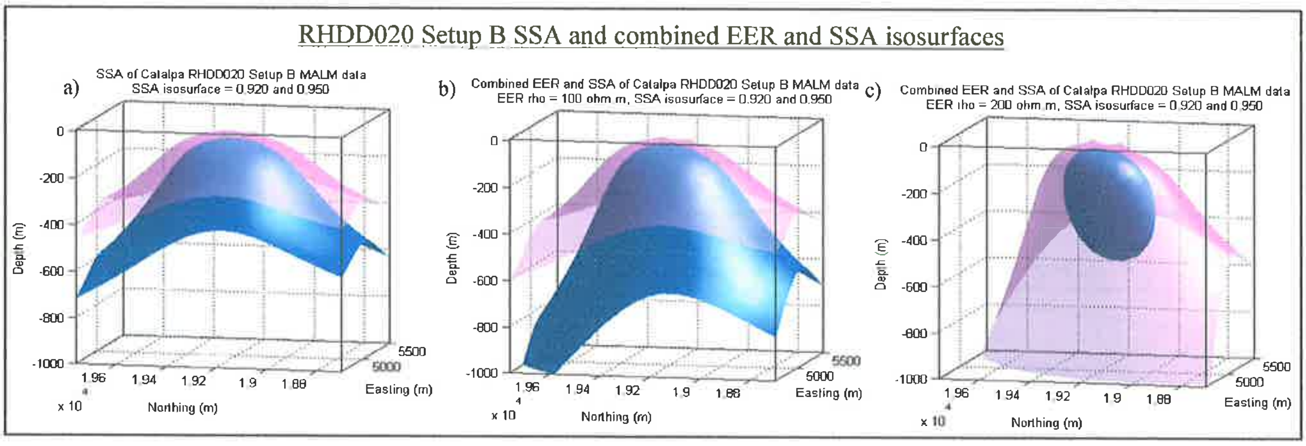

Figure 4.56: a) RHDD020 Setup B MALM surface potentials using the SSA function, b) RHDD020 Setup B isosurfaces of low EER residual potentials using 100 ohm.m $\rho_{halfspace}$ and c) isosurfaces of high EER residual potentials using 200 ohm.m $\rho_{halfspace}$. Pink and blue isosurfaces represent the 0.920 and 0.950 correlation surfaces respectively.

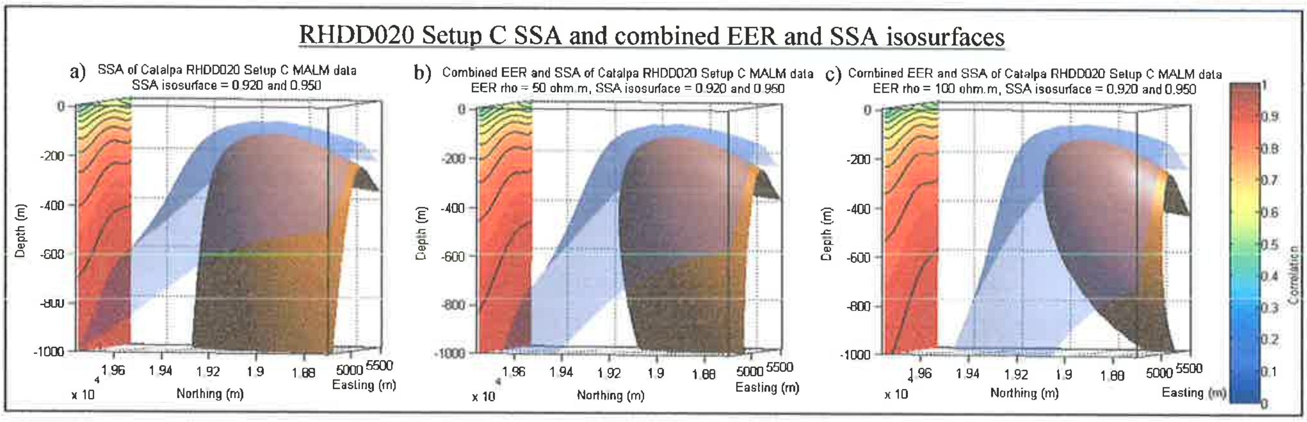

Figure 4.57: a) RHDD020 Setup C MALM surface potentials using the SSA function, b) RHDD020 Setup C isosurfaces of low EER residual potentials using 50 ohm.m $\rho_{halfspace}$, and c) isosurfaces of high EER residual potentials using 100 ohm.m $\rho_{halfspace}$. Coloured plane represents the X-Z slice through the correlation matrix at the northern end of the survey area. Blue and orange isosurfaces represent the 0.920 and 0.950 correlation surfaces respectively.

Catalpa North

The combined EER and SSA isosurfaces for RHDD010 at Catalpa North do not look like any of the other responses for the same area. The low correlation surface (blue isosurfaces, Figure 4.58) exhibits an anomaly generated by the code, as the areas of poor or no data coverage within the survey region (Figure 3.51 (left), p82) has led to the up-turn of the 0.990 correlation surface at the western and eastern edges. This affects both the surface potentials and the residual potentials (Figure 4.58a and b). The high correlation isosurface shows a disparity in the depths between the surface potential isosurface and residual potential isosurface (magenta isosurfaces in Figure 4.58). This suggests that the surface potentials are predominately caused by the electrode. Application of the EER migrates the RHDD010 residual potential isosurfaces to a greater depth, perhaps corresponding to some deeper geology.

The surface potential isosurfaces of RHDD038 and RHDD040 Setup 1 share a similar upper surface position in all three levels of correlation isosurfaces (Figure 4.59a and c). However, these are very different from the surface potential isosurfaces of RHDD040 Setup 2 (Figure 4.59e) which emanates from the south-eastern corner.

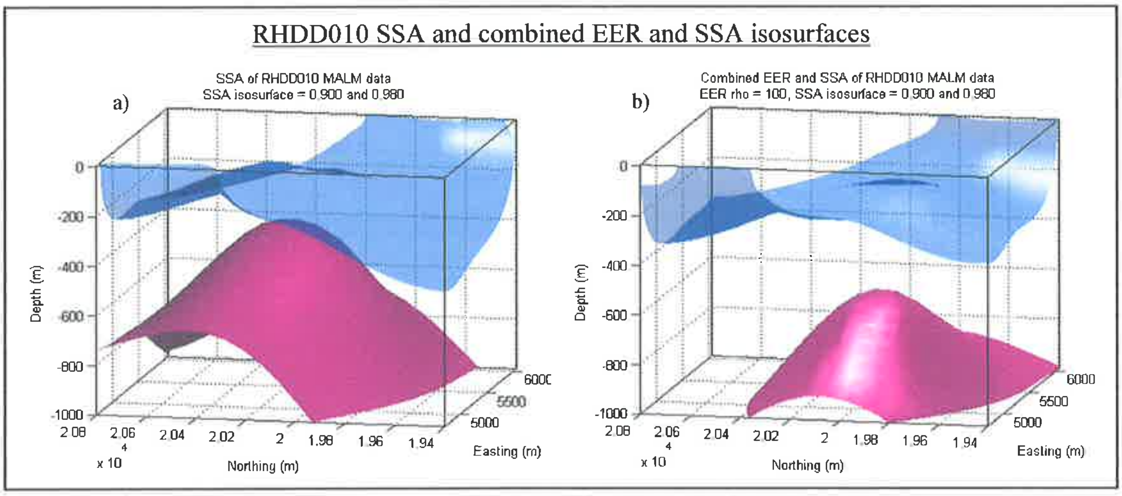

Figure 4.58: a) SSA of RHDD010 surface potentials and b) SSA of residual potentials after EER of 100 ohm.m $\rho_{halfspace}$. The "wings" to the east and west of the low correlation isosurfaces indicate no surface potential measurement stations. Blue and magenta isosurfaces are 0.900 and 0.950 correlation surfaces respectively.

Removing a 125 and 100 ohm.m $\rho_{halfspace}$ EER from RHDD038 and RHDD040 Setup 1 respectively, results in the residual potential isosurfaces (Figure 4.59b and d) which strongly resemble the isosurfaces for the surface potentials in RHDD040 Setup 2. The residual potential isosurfaces for RHDD040 Setup 2 migrate further into the south east corner in comparison to the surface potential isosurfaces. This implies that the genesis of the residual potential response is from the south east of the survey area.

The combined EER and SSA responses of the Catalpa North surveys concur with those of the Catalpa surveys. The Catalpa North residual potential isosurface are mapping the northern tip of the Catalpa residual potential isosurfaces (Figure 4.54 to Figure 4.57) which emanate from the eastern side of the unaltered Catalpa surface potential isosurfaces. The combination of the EER and SSA is able enhance the geological interpretation of the Catalpa/Catalpa North area by de-convoluting the MALM data.

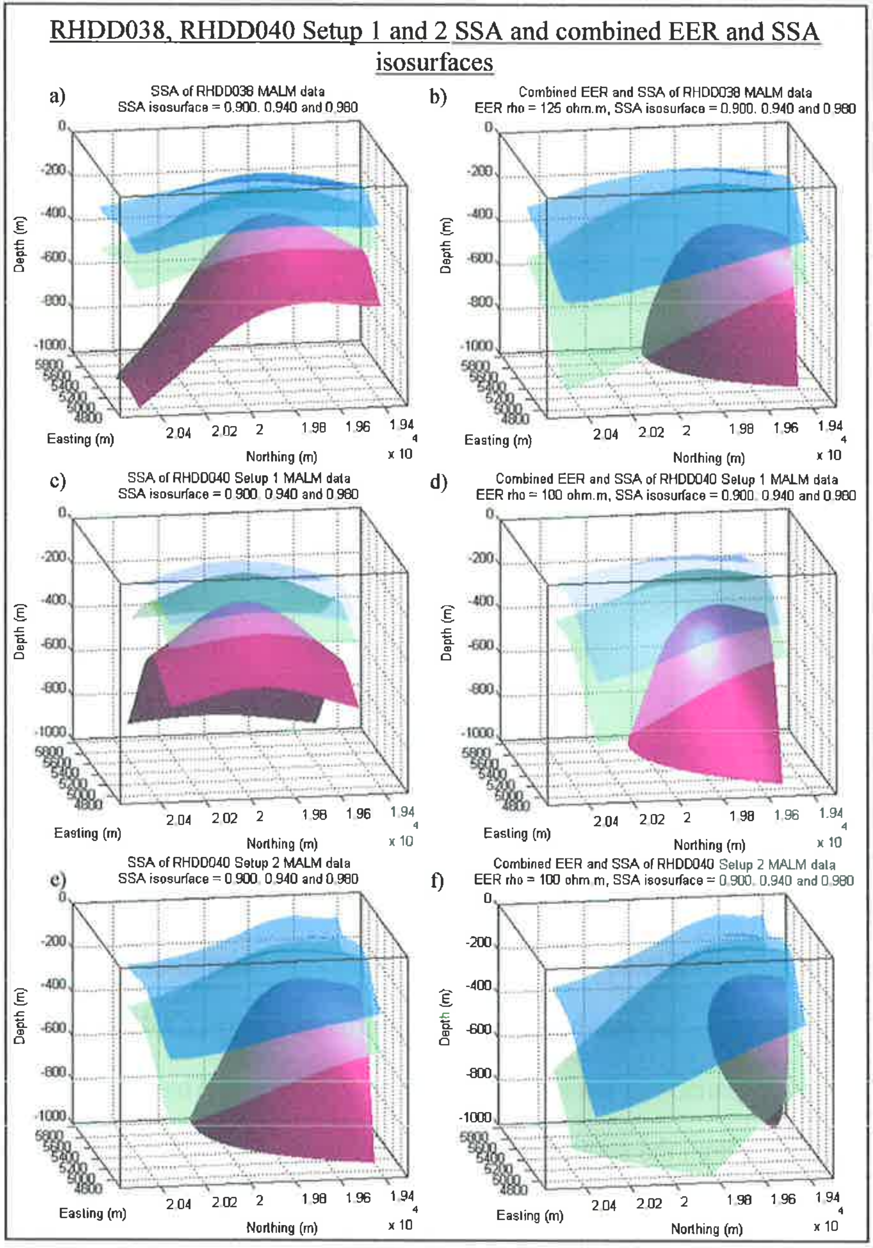

Figure 4.59: a), c) and e) are the SSA response for RHDD038, RHDD040 Setup 1 and 2 respectively. b) is the SSA isosurface for RHDD038 residual potentials using 125 ohm.m $\rho_{halfspace}$. d) and f) are the residual potential isosurfaces for RHDD040 Setup 1 and 2 respectively using a 100 ohm.m $\rho_{halfspace}$. Blue, green and magenta isosurfaces are 0.900, 0.940 and 0.980 correlation surfaces respectively.

Prominent Hill

Isosurfaces of the surface potentials for the RP017 MALM survey extend from the south to the north (Figure 4.60a). With increasing EER using 2.5 and 5 ohm.m $\rho_{halfspace}$, the residual potential isosurfaces are migrated back to the source, towards the south (Figure 4.60b and c). The depth slice of the correlation matrix at the electrode depth of 350 metres (Figure 4.60d), identifies that the electrode is not the dominant source in the surface potentials. Since the electrode is connected to the chalcocite breccia, the high correlation to the south of the electrode's position is due to a higher concentration of source points about the southern conductive haematite body. The depth slices for the residual potential correlation matrices (Figure 4.60e and f) have the high correlation elementary source points increasingly moved to the south and intrinsically associated with the haematite body rather than the chalcocite breccia. The combination of the EER and SSA algorithms have allowed an enhanced interpretation of the MALM survey.

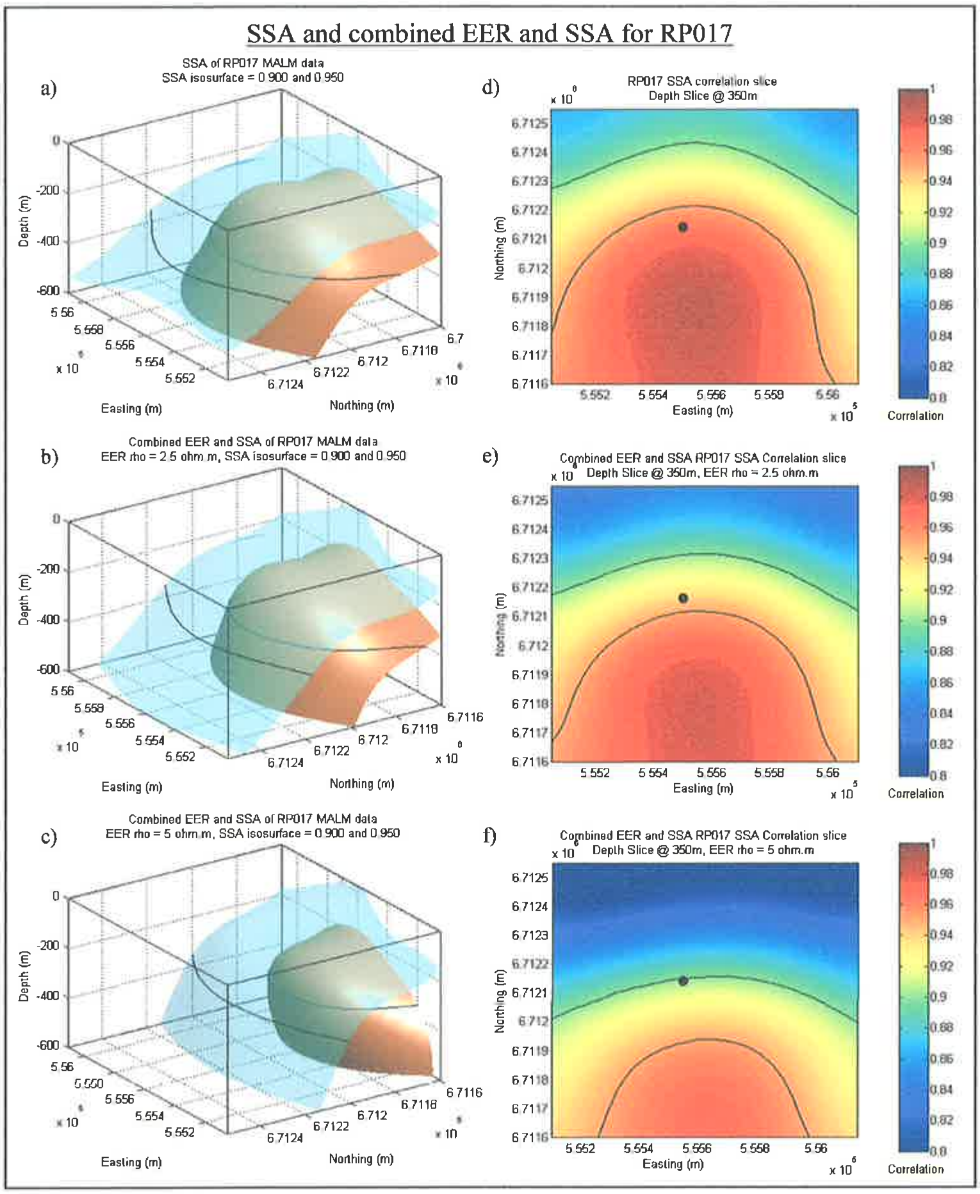

Figure 4.60: a) SSA response of the surface potentials for RP017, b) residual potential isosurfaces using a 2.5 ohm.m $\rho_{halfspace}$, *c) residual potential isosurfaces using a 5 ohm.m* $\rho_{halfspace}$. *Blue and orange isosurfaces are 0.900 and 0.950 correlation respectively. The 350m depth slices d), e) and f) which correspond to the correlation matrices used in a), b) and c), with the 0.900 and 0.950 correlation contours shown (where the isosurfaces intersect the slice). Colour scale is 0.8 to 1 correlation. Black dot marks the electrode position at 350m depth.*

CHAPTER 5 - DISCUSSIONS AND CONCLUSIONS

5.1 MALM FIELD DATA

The use of the MALM method in both field areas has shown that the MALM method can differentiate regions of different resistivities and as such allow for the mapping of conductive bodies within the subsurface. The position of the peak surface anomaly is associated with the position of the upper surface of the conductive structure. The shape of the anomaly is related to extent and geometry of the conductive body as well as the geoelectric connections of conductive bodies within the earth. However, the method does not always indicate the presence of the target to which the source electrode is connected.

Golden Grove

Catalpa

The four surveys at Catalpa can be subdivided into two categories; the in-mineralisation and the near-miss cases. Whilst the in-mineralisation electrode placements appear to be mapping the potentials generated by more or less the same conductive structure (Figure 4.1 and Figure 4.2, p86), the deep near-miss position of RHDD020 Setup C (Figure 4.4, p87) highlights yet another peak to the south of the electrode position. The shallow near-miss position of the RHDD020 Setup B has a different shape to the rest of the surveys. This is due to the position and depth of the electrode, allowing for an electrode effect to be present in the surface potentials. The peaks of all the surveys are in the vicinity of 5100mE, 19300mN.

Catalpa North

The Catalpa North data covers the eastern upper third of the Catalpa area. The electrode positions at Catalpa North are all classified as out-of-mineralisation positions as the electrodes have not been positioned in contact with any massive conductive targets such as the RHDD018 and RHDD020 Setup A surveys. However, this does not negate the value of the data derived from these surveys. The RHDD010 is the most northerly of these surveys and has the least similarities with the southern Catalpa surveys. The low amplitude double peak and broad anomaly suggest that it is dominated by the presence of the shallow source electrode. Given the ENE-WSW faulting in the area, the elongation in this direction could be associated with the faults.

The out-of-mineralisation MALM surface potentials of RHDD038 and RHDD040 Setup 2 (deep source position) both share a peak potential to the south of the survey area at approximately the 5150m easting. This is only seen as opening of the equipotentials to the south in RHDD040 Setup 1 (shallow source position) rather than the peak. The relative positions of RHDD038 and RHDD040 (Table 1-2 and Figure 1.7, p10) show that the easting and depth of RHDD038 and RHDD040 Setup 1 are approximately the same, but RHDD038 is 200 metres to the south, yet it generates a different peak position.

The peak position of RHDD038 and RHDD040 Setup 2 is the same approximate location as the Catalpa surveys. Despite the faulting in the area and the distance from the source to the peak, the surveys conducted in RHDD038 and RHDD040 Setup 2 are able to show an electrical connection to mineralisation that is over 500 metres to the south.

Deep source electrodes

The two deep electrode positions of RHDD020 Setup C and RHDD040 Setup 2 appear to be energising conductors that are further from the source. Roach and Fitzpatrick (2003) found that with increased separation between the electrodes, the resistivity of their mineralisation samples decreased both in the laboratory and *in situ* resistivity measurements. This was thought to be due to a greater connectivity between the conductive phase of the mineralisation (Roach and Fitzpatrick, 2003). Perhaps with increased depth there is greater connectivity, which manifests itself as lower resistivity but also extends the influence of the MALM method.

Prominent Hill

The single MALM survey in the RP017 drill was connected to a deep chalcocite breccia conductor that was bounded to the north and south by shallower conductive bodies. The peak of the MALM surface potentials in this instance was over the more conductive haematite rock to the south of the intended target position. Despite not mapping the location of the target mineralisation, the method aided the imaging of the subsurface by revealing the strike direction of the mineralisation and therefore increasing the understanding of the geology in the region. The price of a MALM survey is cheaper than cost of the multiple drill holes required to arrive at the same conclusion.

5.2 FEM MODELLING

Idealised modelling

The idealised FEM models were generated for two purposes; to understand the changes in the surface potentials by incrementally varying a specific parameter in a model, and to synthesise simplified models with which to test the EER and SSA algorithms.

The models have reiterated results found in the literature that the primary controls on MALM anomalies are predominately the resistivity contrast, depth from surface, dimensions and orientation of the conductive structure. Other factors include the presence of other conductive structures (hence their physical attributes) and their separation from the charged conductive body.

Models which explore the changes in resistivity contrasts, the volume of the body, or the depth of the body *etcetera*, provide a basis for control models as they were comparable with examples from Eloranta's publications (1985, 1986 and 1988) and others. Hence these idealised models have provided an invaluable aid to refine and understand the responses of the EER and SSA algorithms. Since the physical properties of the conductive structure in the FEM models is known, interpretations of the output from the algorithms using these models have been simplified. Both programs were thoroughly tested using the control models.

Idealised near-miss modelling

This set of models emphasises the interaction between depth of a conductive body and that of a near-miss electrode and its separation from the conductive target. The relationship between these three variables is the primary control between a near-miss and a complete miss electrode placement. With increased depth of the source electrode, the electrode can be positioned further away from the body whilst still generating surface potentials which delineate the position of the body.

The addition of dip to the conductive structure in the near-miss models shows that shallow dipping conductive bodies are less affected by the placement of the near-miss electrode. Steeply dipping conductors show a greater disparity between the surface potentials of a near-miss electrode than those of an in-mineralisation source. There is also a difference between a shallow source electrode that is above the conductive body, and a deep source electrode which is below the body. Surface potentials of shallow source electrode positions are dominated by the potentials of the source electrode

Forward regolith models

The regolith models which take after the AEM models used by Macnae et al. (2001), show that small changes in near-surface resistivities can affect the MALM surface potentials. The thickness of the weathered layer effectively increases the depth from surface of the conductive body hence the response of the body is correspondingly subdued. Whilst not modelled in this study, Butt (1981) surmises the lateral variation in regolith thickness can also generate false anomalies in electrical and EM methods. Wedging regolith models shows that a greater resistivity contrast between the regolith and basement materials causes a greater disturbance in the surface potential due to near-surface resistivity inhomogeneities. This is of particular importance with transported regolith cover since the resistivity contrast contact between basement and overburden is sharper than that of *in situ* weathering profiles (Doyle, 1981; Macnae et al., 2001). The models show that it is not possible to resolve a low resistivity contrast regolith contact (regolith/regolith models, p55), as there is no great disparity in the surface potentials of the models, only a shift in the surface potentials which can misplace the peak of the potential anomaly, in the case of the models, by 50 metres.

FEM field site models

The parameterisation for these models was interpreted from known geology into an idealised resistivity model to aid interpretation of the subsequent synthetic potentials. The models do not exhibit the same amplitudes compared to the observed MALM data. This may be caused by more complex geoelectrical scenarios within the earth which are not dealt with due to the simplicity of the models. However the qualitative trends seen in the Catalpa and Prominent Hill models, suggest that models can effectively replicate the same trends in the MALM field data. It was never a goal of this study to duplicate every nuance of the MALM data, but rather to understand the electrical potential fields that occur in the subsurface and how these affect the surface potentials.

Unfortunately, the modelling of the Catalpa North geology did not match the field results. The FEM models are idealised block models with sharp resistivity contrasts with macro scale electrical interconnections. It was not possible to model the minute electrical connectivity associated with a disseminated mineralisation halo or stringer vein deposits surrounding the massive sulphide mineralisation. Despite not being the ideal representation of the Catalpa North data, the models were still used to investigate the EER and SSA functions with their results (not presented) being comparable to those of Catalpa and Prominent Hill.

5.3 ELECTRODE EFFECT REMOVAL

The numerical calculation of the electrode effect from a homogeneous, isotropic half-space and its removal from the surface potentials, of both synthetic and acquired MALM data, was capable of delineating more information associated with resistivity contrast boundaries within subsurface. This residual potential information was intrinsically related to the geology, whether it was synthetic or real.

Idealised FEM models

Residual potentials for the in-mineralisation models are better representations of the conductive structure than unaltered surface potentials, providing the correct values for the EER are used. The EER results show that peaks are centred over the conductive body rather than the electrode position (Figure 4.12, p93). However, too high a $\rho_{halfspace}$ has an unfavourable effect on the surface potentials. For dipping structures, the EER function appeared to provide no advancement in interpretations using the residual potentials.

Where multiple bodies are concerned, the residual potentials increasingly identified the non-energised conductive body with increased $\rho_{halfspace}$, when both bodies are at an equal depth, or if the energised body is at a greater depth. This result implies that the residual potentials are able to define the position of the shallowest conductive body. However this is only the case if the non-energised body is close to the energised conductor as the EER results of the two body separation models (p94) show. With increased separation, the presence of the non-energised conductor is diminished from the surface potentials. The use of EER can recover the position information on the second conductor with increasing $\rho_{halfspace}$. However, a $\rho_{halfspace}$ which is too large will result in nonsensical residual potentials. At large separations of 225 metres the non-energised body is not present in either surface potentials or residual potentials.

The EER was most effective for the models that dealt with near-miss electrode placements about a vertical body or shallow near-miss electrode placements about a dipping body. The values for $\rho_{halfspace}$ used in the EER of a near-miss source position are associated with the principal parameters which determine a near-miss electrode position as already discussed; that is the relationship between the separation of the electrode from the body and the ratio of depths of the body and source electrode. With increased depth and separation, increasing values of $\rho_{halfspace}$ had to be used in order for the residual potentials to reveal the position of the conductive body (Figure 4.17 c.f. Figure 4.21). The $\rho_{halfspace}$ used are lower than that of the modelled host rock. This is due to the presence of the conductive body and its effect of lowering the bulk resistivity for the modelled volume.

For a dipping conductor the electrode effect was most prominent when the electrode was above the conductor in a shallow near-miss position. This is due to the conductive body masking or shading the electrode effect when the electrode is positioned deeper than the body. With increasing dip, the value of $\rho_{halfspace}$ had to be increased to reveal the position of the upper surface of the conductive body. When applied to the deep near-miss positions about a dipping body, the residual potentials did not aid in the interpretation of the modelled MALM data.

FEM field site models

The more complicated FEM models of the field sites allowed for a qualitative association of residual potential results to the observed field data. The results from the idealised FEM models aided in choosing the correct values for $\rho_{halfspace}$ for the FEM field models with trends in depth and separation of the electrode from the conductive bodies being similar. However the biggest difference between the idealised models and that of the FEM models was the inclusion of a conductive weathered layer which reduced the peak amplitudes of the FEM field site models. The $\rho_{halfspace}$ values for the FEM field site models were significantly lower than that of the idealised models because of the addition of a conductive layer which subdues the amplitudes of the surface potentials.

The EER responses for the Catalpa FEM models (Figure 4.26 to Figure 4.29, p104) showed that the peak in the synthetic surface potentials remains a consistent presence in the residual potentials and is associated with the upper surface of the conductive body. Of interest is that the FEM surface potentials do not show any continuation to the south, although the conductive body is modelled such that it extends to the south (Figure 3.35, p59). The residual potentials for each of the models reveal this southward continuation of the modelled mineralisation (Figure 4.26 to Figure 4.29, p104), thus providing additional information that would otherwise be missed in the unaltered surface potentials.

The Prominent Hill models allowed for the investigation of two near-miss scenarios about the chalcocite breccia target as well as the in-mineralisation case. Residual potentials for the three Prominent Hill models identify that the conductive haematite rock (Figure 3.41, p65) is the dominant shallow source in the models despite being a non-energised body. The results are similar to those of the two-body idealised models where current is channelled closer to the surface by the more conductive haematite rock which is only 48 metres from the deeper, chalcocite breccia target. The potential contribution of the haematite rock is still present in the shallow near-miss position which has a peak anomaly over the haematite breccia north of the target (see Prominent Hill model, p65).

Field MALM Data

The use of the EER upon the acquired MALM data and the interpretations made from the residual potentials are a primary goal of this study. As with the results of the idealised modelling, the choice of the $\rho_{halfspace}$ for the EER is significantly lower than the lab measured resistivity of the host rock. With *a priori* geological information, the choice of the $\rho_{halfspace}$ that would best fit a MALM survey does not require prior modelling. If this is not available, modelling of possible geometries and the application of the EER to those models would aid the application of the EER to field data.

The most important condition to satisfy when trying to find an appropriate $\rho_{halfspace}$ is that only positive values residual potentials should occur. Negative potentials are caused by an inappropriately large $\rho_{halfspace}$, hence the algorithm is removing potentials that are not associated with just the electrode. With prior knowledge of the geology under investigation, a range of $\rho_{halfspace}$ values can be used to generate residual potentials which best agree with the known geology. If used in as a primary exploration method, as mentioned, modelling is required to anticipate the possible residual potential patterns and possible range of $\rho_{halfspace}$.

The peak at the position 5100mE, 19350mN seen in all 4 electrode positions for the region at Catalpa is prevalent throughout the residual potentials (Figure 4.33 to Figure 4.36, p106). The residual potentials for surveys enhanced the continuity of potentials to the south. This is most evident in EER of 250 ohm.m $\rho_{halfspace}$

for RHDD020 Setup B (Figure 4.35c). The residual potentials for this EER of the shallow near-miss electrode position resemble that of the in-mineralisation surface potentials of RHDD018 and RHDD020 Setup A. As with the FEM models for the Catalpa area, the half-space resistivities used for the EER are lower than those of the idealised models without a modelled overburden layer.

The trend in lower values of $\rho_{halfspace}$ used in the EER function also holds for the Catalpa North surface potentials. The peak in the southern residual potentials of RHDD038 and RHDD040 Setup 2 are associated with the geology and its inherent resistivity contrasts which generate the surface potential peaks seen in the Catalpa surveys. The southern third of the Catalpa North surveys cover the same ground as the Catalpa surveys, but the source electrodes are placed to the north, with faults lying in-between. Residual potentials of RHDD038, RHDD040 Setup 1 and 2 all have a similar residual potential pattern of a southerly peak at the position of 5100mE, 19400mN, which extends towards the northeast. This southern third of the residual potentials of RHDD038, RHDD040 Setup 1 and 2 reflects the same residual potential patterns seen in the northern third of the 4 Catalpa surveys.

RHDD010 is harder to interpret since it is the most northerly of electrode placements and it also has no similarities to the other surveys. With the electrode effect the double peaks are sharpened and separated from each other. The orientation of these double peaks along ENE-WSW line suggests an association with faulting in the area that is orientated in that direction as well. Alternatively, it maybe associated with varying regolith thickness or near-surface resistivity inhomogeneities. The Catalpa North FEM models investigated the latter but it was not successful.

The Prominent Hill mineralisation was very similar to the in-mineralisation FEM model for the same area, but the potential amplitudes were significantly lower than the FEM models (Figure 3.42, p66). Due to this, the values for $\rho_{halfspace}$ were an order of magnitude lower as well. The most prevalent structure in the residual potentials is to the south which appears to be associated with the barren haematite rock (Figure 1.9, p12) to the south of the in-mineralisation electrode position and the chalcocite breccia target.

The residual potentials generated by the EER method appear to elucidate more information from the MALM surface potentials on the geology of the area. For the purposes of this study, the parameterisation of the EER function has been simplified to a single variable of half-space resistivity, $\rho_{halfspace}$. From the FEM models, this value is dependent on many factors including the position and depth of the electrode and the conductive target, a near-miss versus in-mineralisation electrode, distance of separation from the body and the near-miss electrode, as well as the physical properties of the conductive structure (dip, resistivity, volume, etc.). An algorithm to find the optimal $\rho_{halfspace}$ is beyond the scope of this particular study.

The other variable that could be changed is the current for an electrode in a homogenous, isotropic half-space, or the value of the total current, tc, used in the EER code (Code 3.1, p68). This was set to a value of 1 ampere as all potentials passed through the EER are current normalised. This study does not investigate the relationship between the geologic/geophysical parameters and the current variable of the EER function. It was primarily concerned with the advancements of MALM interpretation and additional information that can be obtained by removing differing levels of electrode effect.

5.4 SUBSURFACE APPROXIMATION AND COMBINATION WITH EER

The modification of the Hämmann et al. (1997) algorithm into the 3D subsurface approximation algorithm allows for the rapid assessment of the surface potentials of a MALM survey. Whilst these are approximations to the actual resistivity contrasts within the earth, the method is quicker than the 3D inversion of electrical potential data, allowing for a 3D image of the data to be produced in a matter of minutes as opposed to hours. The EER function has demonstrated that the residual potentials can be a better representation of the resistivity structure of the subsurface; therefore the SSA algorithm was used to compare the correlation values of the surface potentials and their corresponding residual potentials.

Idealised FEM models

Manipulating the basic geologic/geophysical parameters of a model (resistivity contrast to half-space, depth, volume, etc.) changes the surface potentials and therefore changes in the correlation values of the SSA algorithm are also seen. Changing the resistivity contrast noticeably affects the SSA if there is a change in the distribution of surface potentials such as the change from a 100 ohm.m to 10 ohm.m conductive body (Figure 4.41a and b, p112). A change in mean amplitude of the same patterned anomalies does not appreciably change the shape of the SSA correlation isosurfaces (i.e. increasing the contrast of the conductive body).

Increasing the depth of a conductive body changes the downwards distance of isosurfaces of the same value (Figure 4.42, p113), but it is not a linear change changes of the conductive body. The depth of the isosurface is also affected by the volume of the conductive body. Figure 4.43 (p113), shows that the increases in depth of the isosurfaces occurs with increased volume. This is due to a high correlation associated with the position of the centre of the conductive mass since the models are symmetric.

The link between the isosurfaces with the centre of the conductive mass is also observed in the SSA response of in-mineralisation conductive structures. In this case the position of the electrode is coincident with the placement of the isosurface (Figure 4.44, p114), as modelling of the in-mineralisation case has shown that for the FEM models, the position of the electrode within the model does not have a large effect (Figure 3.15, p44). However, the orientation of the isosurface is directly associated with the dip angle of the conductive body. It must be noted that the algorithm skews the shape of a vertical body when its surface potentials are close the edge of the model area, this is of importance to the Prominent Hill data.

The SSA algorithm is capable of identifying the position of the uppermost conductive body, regardless whether it is energised or otherwise. With increased depth of the energised body, non-energised body is relatively shallower and hence induced charges at its resistivity boundaries eclipses those of the deeper energised body. Using the EER function emphasises this effect in the isosurfaces of the residual potentials (not presented). At small separation the isocorrelation surfaces are a composite of the elementary source points about the energised body and those of the non-energised body. However, with increased separation of the non-energised body, the SSA response does not encompass both bodies, just the energised body (Figure 4.46, p115).

Regolith models

The regolith models, in particular the high contrast basement/regolith models, show that the SSA algorithm is sensitive to both large and small changes in surface potential anomaly location. In both regolith models, the dip of near-surface resistivity contrast displaces the position of the isosurfaces (Figure 4.47 and Figure 4.48). The displacement of the isosurfaces is opposite to the dip direction. In addition to this displacement, the change in the near-surface resistivities also repositions the upper portion of the isosurface towards the material of higher resistivity.

Residual potential isosurfaces for the vertical near-miss body

Using the residual potentials from the EER function has recovered a subsurface isocorrelation shape that is more similar to the in-mineralisation isosurface than the near-miss isosurface (Figure 4.50 and Figure 4.51). This combination of the SSA and the appropriate EER consistently images an idealised vertical body with a near-miss source position.

FEM field site models

The SSA response of the synthetic surface potentials of the FEM field site models has isosurfaces associated with the position of the conductive body modelled and isosurfaces corresponding to the depth of the conductive body (Figure 4.49 and Figure 4.52). In both the Catalpa and Prominent Hill FEM models the application of the EER significantly affects the SSA response. The residual potential isosurfaces are a much better approximation of the 3D models than the unaltered surface potentials.

The Catalpa residual potential isosurfaces are more alike as well, with the synthetic residual potential isosurface for RHDD020 Setup B (Figure 4.52c) having a likeness to that of the in-mineralisation residual potential isosurfaces for RHDD018 and RHDD020 Setup A (Figure 4.52a and b). The residual potential isosurfaces are also dipping to the east, which from the isosurfaces of dipping FEM models imply that the structure dips to the west; as was parameterised. For Prominent Hill, the residual potential isosurfaces for the in-mineralisation and shallow near-miss modelled positions are similar to each other (Figure 4.53b and c).

Field MALM Data

The residual potential isosurfaces reflect the results of the residual surface potentials for the individual field sites. At Catalpa the use of residual potentials in the SSA function results in isosurfaces that are all centred underneath the peak residual potential position. The residual potential isosurface resemble each other except the 0.950 correlation isosurface for RHDD020 Setup C opens to the south (Figure 4.57c, p124). The inclinations of the residual potential isosurfaces suggest that the conductive body is steeply dipping to the west which concurs with the known geology.

Although the surface potential isosurfaces of Catalpa North do not share similarities, the residual potential isosurfaces mark the southeast corner of the survey area as the region of highest correlation in the elementary point sources in the RHDD038, RHDD040 Setup 1 and 2 surveys. The shapes of the Catalpa North residual potential isosurfaces share an affinity with each other and the deep electrode position of RHDD040 Setup 2. The position of the SSA residual potential isosurfaces in the south suggests that the resistivity contrasts in Catalpa North are associated with the MALM anomaly seen in the Catalpa surveys to the south. However, the inclination of the isosurface points to a shallower dip of the conductive body occurring in both survey areas as the mineralisation extends further the north.

The residual potential isosurfaces for Prominent Hill reaffirm the conclusion that the MALM data is indeed mapping the haematite rock to the south of the targeted chalcocite breccia. The residual isosurfaces are a better approximation of the known geology than the isocorrelations generated by the unaltered surface potentials.

The algorithm suffers from the limitations identified by Hämmann et al. (1997), that subsurface approximations are meaningless if the basic assumptions of background resistivity or elementary point source super-positioning are not abided. The SSA results require that the interpretation of the isosurfaces to be made in combination with *a priori* information such as the known geology and its associated resistivity structure as the FEM modelling has shown the isosurfaces are non unique.

However, the SSA algorithm does allow for the qualitative interpretation and identification of possible source position for the MALM data at Golden Grove and Prominent Hill. In tandem with the EER function, the SSA algorithm is effective at quickly imaging the secondary potential contributions (i.e.residual potentials); but the results do not distinguish the individual conductive bodies.

5.5 FURTHER WORK

With ever increasing computational resources, the definition of the FEM models would increase, allowing for greater detail and complexity to be modelled. The resolution of the SSA algorithm has been a conciliation between mesh resolution (of the elementary source points) and computation time required to calculate the approximations. In future, faster processing would allow the SSA algorithm to use finer mesh grids in less time.

The MALM data sets investigated in this study have been surface data sets. As noted in the literature and in the FEM modelling, near-surface resistivity contrasts affect the surface potentials. Using 3D MALM data by obtaining underground potential measurements in adjacent drill holes would give an insight into the potential field in the subsurface surrounding the conductive structure. Both the EER and SSA algorithms could be readily adapted for 3D data sets and having subsurface points with which to constrain the correlation values at depth would increase the performance and accuracy of the SSA algorithm.

The choice of half-space resistivities values for the EER function can be a time consuming process. Further investigations could identify a method of automating the selection of the $\rho_{halfspace}$ value. This implies that the relationship of $\rho_{halfspace}$ to the position of the source electrode in relation to the geology needs to be identified. The adaptation for the EER to accommodate for a two or multiple layered earth model can also be implemented, but the use of the method of images would be an inelegant means of doing so.

The current incarnations of both algorithms do not account for topography since both survey areas and FEM models had no surface relief that would affect the surface potentials. The SSA algorithm can be augmented to account for topography variations (Patella, 1997b) as can the calculations for the electrode effect (Telford et al., 1990). These changes would allow the use of both algorithms in highly variable terrains.

The data sets and models obtained or generated for this study are associated with conductive mineralisations. It would be of interest to carry these investigations into environment orientated studies, such as contaminant plume delineation, coal seam mapping (Rodríguez and Rodríguez, 2000) or conductive hydrology mapping. The near-miss electrode position would not necessarily require a direct connection to a contaminant plume as this study has shown for massive sulphides.

5.6 CONCLUSIONS

This study has obtained MALM data from the two field sites of Golden Grove, Western Australia and Prominent Hill, South Australia. The two locations have different forms of conductive mineralisation, and the method has effectively delineated subsurface resistivity structures at both locations. The main outcomes of this study are as follows;

- FEM models were generated to investigate the response of the MALM method to systematic changes in the model parameters. These included models that examined changes in the position, orientation and physical properties of a conductive body. The near-miss models identified a relationship between the separation of a source electrode from a conductive body and the ratio of depths of the electrode and body. FEM models of the field sites were also generated with the synthetic surface potential responses of two field site models having qualitative success at matching the acquired field data. Models of near-surface resistivity variations elucidated the effects of the regolith on MALM responses.
- The EER algorithm strives to remove the effect of the electrode by calculating the potential contributions of the electrode from the equation for a source electrode in a homogeneous, isotropic half-space. The residual potentials generated by the EER algorithm was successful in enhancing the interpretations of the MALM data by unshrouding the surface potentials associated with resistivity contrasts and hence the geology. Through modelling, this was shown to be especially effective with near-miss electrodes about a vertical body or shallow near-miss electrodes above a dipping conductive body. Application to observed field data followed the successes in the modelling; the shallow near-miss electrode position of RHDD020 Setup B is an example (Figure 4.35, p107). The residual potentials for the surveys at Golden Grove demonstrated the MALM data, from the two survey areas Catalpa and Catalpa North, were inherently linked by the geology of the area.
- The modification and development of the IR algorithm (Hämmann et al., 1997) into the SSA algorithm, proved to be capable of approximating the subsurface in 3D using the super-positioning and correlation of elementary point sources to the surface potentials and the residual potentials. The approximations made by using the residual potentials were superior to those using the surface potentials.

The use of near-miss electrode positions and these techniques expand the abilities of MALM to investigate the earth using drill holes that do not intersect mineralisation. This makes MALM a cost effective solution to map conductive structures using a barren drill hole. The methods investigated and developed over the course of this project can enhance and aid the interpretations of MALM data to delineate subsurface resistivity contrasts both in two and three dimensions.

Bibliography

Alfano L., 1959. *Introduction to the interpretation of resistivity measurements for complicated structural conditions. Geophysical Prospecting,* ***7****, pp 311-366.*

Ascough G. L., 1999, *Geophysical characteristics of Volcanogenic Massive Sulphide deposits. Geophysics in mineral exploration: Fundamentals and case histories, short course notes, Geological Association of Canada,* ***14****, pp 41 – 62.*

Ashley P. M., Dudley R. J., Lesh R. H., Marr J. M. and Ryall A. H., 1988. *The Scuddles Cu-Zn Prospect, an Archaean volcanogenic massive sulphide deposit, Golden Grove District, Western Australia. Economic Geology,* ***83****, pp 918-951.*

Asten M. W., 1974. *The influence of Electrical Anisotropy on Mise-à-la-Masse Surveys. Geophysical Prospecting,* ***22****, pp 238-345.*

Beasley C. W. and Ward S. H., 1986. *Three-dimensional mise-à-la-masse modelling applied to mapping fracture zones. Geophysics,* ***51(1)****, pp 98-113.*

Belperio T. 2002. *Prominent Hill: Exploration Strategies for world class Iron-oxide Cu-Au deposits.* ***Extended Abstracts****, 16th Australian Geological Convention.*

Bishop J., Sattel D., Macnae J. and Munday T., 2001. *Electrical Structure of the Regolith at Lawlers. Exploration Geophysics,* ***32****, pp 20-28.*

Bhattacharya B. B., Gupta D., Banerjee B., and Shalivahan, 2001, *Case History: Mise-a-la-masse survey for an auriferous sulphide deposit. Geophysics,* ***66(1)****, pp 70-77.*

Bowker A., 1987. *Size determination of slab-like ore bodies – an interpretation scheme for mise-à-la-masse anomalies. Geoexploration,* ***24****, pp 207-218.*

Bowker A., 1991. *Quantitative interpretation on three-dimensional mise-à-la-masse data: A case history from Gairloch, northwest Scotland. Geoexploration,* ***28****, pp 1-22.*

Boyd G. and Frankcombe K. F., 1994. *Geophysical Responses over the Scuddles VMS deposit. Geophysical Signatures of Western Australian Mineral Deposits, ASEG Special Publication,* ***26****, pp 133-144.*

Butt C. R. M., 1981. *The nature and origin of the lateritic weathering mantle, with particular reference to Western Australia. Geophysical prospecting in deeply weathered terrains, ASEG seminar summary,* ***6****, pp 11-29.*

Craven B. L., Hayden W. B. and Smith M. J., 1985. *A Comparison of electromagnetic prospecting results at the Scuddles Cu-Zn massive sulphide deposit, Golden Grove, Western Australia. Exploration Geophysics,* ***16****, pp 194-197.*

Daly S. J., Fanning C. M. and Fairclough M. C., 1998. *Tectonic evolution and exploration potential of the Gawler Craton, South Australia. AGSO Journal of Australian Geology and Geophysics,* ***17****, pp 145-168.*

Daniels J. J., 1983. *Hole-to-surface resistivity measurements. Geophysics,* ***48(1)****, pp 87-97.*

Dey A. and Morrison H. F., 1979. *Resistivity modelling for arbitrarily shaped three-dimensional structures. Geophysics,* ***44(4)****, pp 753-780.*

Di Maio R. and Patella D., 1994. *Self-potential anomaly generation in volcanic areas. The Mt. Etna case history. Acta Vulcanologica,* ***4****, pp 119-124.*

Doyle H. A., 1981. *Comments on geophysical exploration in Australia, geophysical problems in deeply weathered terrains. Geophysical prospecting in deeply weathered terrains, ASEG seminar summary,* ***6****, pp 1-10.*

Ellis R. G. and Oldenburg D. W., 1994. *The pole-pole 3-D DC-resistivity inverse problem: a conjugate-gradient approach. Geophysical Journal International,* ***119****, pp 187-194.*

Eloranta E. H., 1985. *A Comparison between Mise-à-la-Masse Anomalies Obtained by Pole-Pole and Pole-Dipole Electrode Configurations. Geoexploration,* ***23****, pp 471-481.*

Eloranta E. H., 1986. *The behaviour of mise-à-la-masse anomalies near a vertical contact. Geoexploration,* ***24****, pp 1-14.*

Eloranta E. H., 1988. *The Modelling of Mise-à-la-Masse Anomalies in an Anisotropic Half-Space by the Integral Equation Method. Geoexploration,* ***25****, pp 93-101.*

Emerson D., Macnae J. and Sattel D., 2000. *Physical properties of the regolith in the Lawlers area, Western Australia. Exploration Geophysics,* ***31****, pp 229-235.*

Foley A., 1999. *Technical Memorandum, ref # 69268*, published by Normandy Exploration Limited.

Fox R. C., Hohmann G. W., Killpack T. J. and Rijo L., 1980. *Topographic effect in resistivity and induced-polarization surveys. Geophysics,* ***45****, pp 75-93.*

Frater K. M., 1983. *Geology of the Golden Grove Prospect, Western Australia: A Volcanogenic Massive Sulphide-Magnetite Deposit. Economic Geology,* ***78****, pp 875-919.*

Giancoli D. C., 1991. *Physics, Third Edition.* ***Prentice-Hall****, Australia.*

Greenhalgh S. and Cao S., 1998. *Applied potential modelling of simple orebody structures. Exploration Geophysics,* ***29****, pp 391-395.*

Halliday D., Resnick R. and Walker J., 1993. *Fundamentals of Physics: Extended Fourth Edition.* ***John Wiley and Sons****, Australia.*

Hämmann M., Maurer H. R., Green A. G. and Horstmeyer H., 1997. *Self-Potential Image Reconstruction: Capabilities and Limitations. Journal of Environmental and Engineering Geophysics,* ***2(1)****, pp 21-35.*

Hart J. and Freeman H., 2003a. *Geophysical response of the Prominent Hill Fe-Cu-Au-U Deposit.* ***Digital Extended Abstracts****, ASEG 16th Geophysical Conference and Exhibition.*

Hart J. and Freeman H., 2003b. *Geophysics of the Prominent Hill prospect, South Australia. Geophysical signatures of South Australia Mineral Deposits, ASEG Special Publication,* ***12****, pp 93-100*

Hattula A. and Rekola T., 2000. *Exploration geophysics at the Pyhäsalmi mine and grade control work of the Outokumpu Group. Geophysics,* ***65(6)****, pp 1961-1969.*

Kearey P. and Brooks M., 1991. *An Introduction to Geophysical Exploration, Second Edition.* ***University Press****, Cambridge.*

Keller G. V. and Frischknecht F. C., 1966. *Electrical Methods in Geophysical Prospecting. International Series of Monographs in Electromagnetic Waves,* ***10****,* ***Pergamon Press****, Oxford.*

Ketola M., 1972. *Some points of view concerning Mise-à-la-masse measurements. Geoexploration,* ***10(1)****, pp 1-21.*

Le Masne D. and Poirmeur C., 1988. *Three-dimensional model results for an electrical hole to surface method: Application to the interpretation of a field survey. Geophysics,* ***53****, pp 85-103.*

Leney G. W., 1966. *Field Studies in iron ore geophysics. Mining Geophysics,* ***1****, pp 391-428.*

Li P. and Uren N., 1997a. *The modelling of direct current electric potential in an arbitrarily anisotropic half-space containing a conductive 3-D body. Journal of Applied Geophysics,* ***38****, pp 57-76.*

Li P. and Uren N., 1997b. *The electrical potential arising from a point source in an arbitrarily anisotropic half-space with regolith cover. Exploration Geophysics,* ***28****, pp 361-362.*

Li X. and Pedersen L. B., 1991. *The electromagnetic response of an azimuthally anisotropic half-space. Geophysics,* ***56****, pp 1462-1473.*

Lindell I. V., Ermutlu M. E., Nikoskinen K. I. and Eloranta E. H., 1993. *Static image principle for anisotropic conducting half-space problems: Impedance boundary. Geophysics,* ***59****, pp 1773-1778.*

Macnae J., Bishop J. and Munday T., 2001. *Simplified electrical structure models at AEM scales, Lawlers, Western Australia. Exploration Geophysics,* ***32****, pp 29-35.*

Mansinha L. and Mwenifumbo C. J., *1983. A mise-à-la-masse study of the Cavendish Geophysical Test Site. Geophysics,* ***48****, pp 1252-1257.*

Merkel R. H., 1971. *Resistivity analysis for plane-layer half-space models with buried current sources.* Geophysical Prospecting, **19**, pp 626-639.

Nimmer R. E. and Osiensky J. L., 2002. *Using Mise-à-la-Masse to Delineate the Migration of a Conductive Tracer in Partially Saturated Basalt.* Environmental Geosciences, **9(2)**, pp 81-87.

Oppliger, G. L., *1984. Three-dimensional terrain corrections for mise-à-la-masse and magnetometric resistivity surveys. Geophysics,* ***49****, pp 1718-1729.*

Osiensky J. L., *1997. Ground water modelling of mise-a-la-masse delination of contaminated ground water plumes. Journal of Hydrology,* ***197****, pp 146-165.*

Parasnis D. S., *1966. Mining Geophysics.* ***Elsevier,*** *Amsterdam.*

Parasnis D.S., *1967. Three-Dimensional electric Mise-a-la-Masse survey of an irregular Lead-Zinc-Copper Deposit in Central Sweden. Geophysical Prospecting,* ***15****, pp 407-437.*

Parasnis D. S., *1986. Principles of Applied Geophysics.* **Chapman and Hall,** London.

Patella D., *1997a. Introduction to ground surface self-potential tomography. Geophysical Prospecting,* ***45****, pp 653-681.*

Patella D., *1997b. Self-potential global tomography including topographic effects. Geophysical Prospecting,* ***45****, pp 843-863.*

Pietilä R., *1991. The Application of Drillhole Magnetometry and Mise-a-la-masse in the Exploration for Nickel Sulphides, Finland – Discovery of the Telkkälä Orebody. Exploration Geophysics,* ***22****, pp 299-304.*

Reynolds J. M., *1997. An Introduction to Applied and Environmental Geophysics.* ***John Wiley and Sons****, Australia.*

Roach M. and Fitzpatrick A., *2003. The Electrical Properties of the Scuddles VHMS Deposit.* ***Digital Extended Abstracts,*** *ASEG 16th Geophysical Conference and Exhibition.*

Robinson S.H. and Belford S. M., *1991. The Scuddles Massive Sulphide Discovery; An Exploration Case History. Exploration Geophysics,* ***22,*** *pp 315-320.*

Rodríguez R., and Rodríguez H. R., *2000. Applying the mise-à-la-masse method to coal mining problems. The Leading Edge,* ***19(7)****, pp 759-762.*

Sato M. and Mooney H. M., *1960. The electrochemical mechanism of sulphide self-potentials. Geophysics,* ***25(1)****, pp 226-249.*

Soininen H., *1987. Mise-à-la-Masse Modelling by Integral Equation with the Continuity Equation as a Constraint. Geoexploration,* ***24****, pp 455-460.*

Spiegel R J., Studivant V. R. and Owen T. E., *1980. Modeling resistivity anomalies from localized voids under irregular terrain. Geophysics,* ***41****, pp 997-1015.*

Synder D. D. and Merkel R. M., *1973. Analytic models for the interpretation of electrical surveys using buried current electrodes. Geophysics,* ***38(3)****, pp 513-529.*

Taylor G. and Eggleton R. A., *2001. Regolith Geology and Geomorphology.* ***John Wiley and Sons****, Australia.*

Telford W. M., Geldart L. P. and Sheriff R. E., *1990. Applied Geophysics: Second Edition,* ***Cambridge University Press****, Cambridge.*

Wang T., Stodt J. A., Stierman D. J. and Murdoch L. C., *1991. Mapping hydraulic fractures using a borehole-to-surface electrical resistivity method. Geoexploration,* ***28****, pp 349-369.*

Webster S. S., *1981. Interpretational Procedures for the IP Data in Weathered Terrains as Derived from Field Trials with Modern IP Equipment. Geophysical prospecting in deeply weathered terrains, ASEG seminar papers summary,* ***6****, pp 101-126.*

Zhou B. and Greenhalgh S. A., 2001. *Finite element three-dimensional direct current resistivity modelling: accuracy and efficiency considerations. Geophysical Journal International,* ***145****, pp 679-688.*

Zohdy A. A., Anderson L. A. and Muffler L. J. P., 1973. *Resistivity, Self-potential and Induced-Polarization surveys of a vapour-dominated geothermal system. Geophysics,* ***38(6)****, pp 1130-1144.*

APPENDIX A: MATLAB FUNCTIONS AND SCRIPTS

Dlog.m Function

A description of this function can be found on p7, “Electrode position and drill hole deviation logs”.

```
function [c1x,c1y,c1z,tc,rho,drill] = dlog(filename)
% Ver 1.4 08-07-03 Completed
% This program works to convert a drill trace interms of down-hole depth,
% azimuth from grid north and drill dip, into Easting, Northing and actual
% depth.  This will then be used to accurately position the current
% electrode for electrode removal.
% It reads the drilllog data from a *.log file of the same name
% as the data *.csv file.  In its current form the drilllog file contains 1
% header row and seven columns being (line,x,y,z,dh_depth,dh_azi, dh_dip).
% The only three columns necessary are the dh_depth, dh_azi and dh_dip, so
% make modifications as required.  when the dh_depth = 0, this is the drill
% collar location (collarx,collary).  From this location the program looks at the next row's
% down-hole depth and subtracts it from the current row's depth to get a
% down-hole distance, h.  From the current ros'w abs(dip) it calculates the
% actual depth dz = h*sin(abs(dip)), and the surface distance L = h*cos((abs(dip)).
% Using L and the azi reading for the current row, the current row's
% surface position, is dx = ((L*sin(azi))+collarx) and dy =
% ((L*cos(azi))+collary).

log = importdata(filename,',');
dh_depth = log.data(:,4);
dh_azi = (log.data(:,5));
dh_dip = (log.data(:,6));

dx(1) = log.data(1,1);
dy(1) = log.data(1,2);
dz(1) = 0;
tz(1) = 0;

% all angles converted to radians only when needed.
h(1) = dh_depth(2) - dh_depth(1); % down-hole distance per increment
tz(2) = h(1);
dz(2) = h(1)*sin((pi/180)*(dh_dip(1)));
L(1) = h(1)*cos((pi/180)*(dh_dip(1)));
dx(2) = ((L(1)*sin((pi/180)*dh_azi(1)))+dx(1));
dy(2) = ((L(1)*cos((pi/180)*dh_azi(1)))+dy(1));


for i = 2:length(dh_depth)-1 %repeats for the entire file translate dip and azi into X,Y,Z format
   h(i) = dh_depth(i+1) - dh_depth(i);
   tz(i+1) = tz(i)+h(i); %test to see the total down-hole metres
   dz(i+1) = dz(i)+h(i)*sin((pi/180)*(dh_dip(i)));
   L(i) = h(i)*cos((pi/180)*(dh_dip(i)));
   dx(i+1) = ((L(i)*sin((pi/180)*dh_azi(i)))+dx(i));
   dy(i+1) = ((L(i)*cos((pi/180)*dh_azi(i)))+dy(i));
end

drill(1,:) = dx;    %drill matrix contains values in X,Y & Z for the drill trace.
drill(2,:) = dy;
drill(3,:) = dz;

% this next part of the program calculates the exact electrode position for
% the given down-hole depth.  This is found from filename for the log file
% which has the format 010430.log, where xxx430.log is the hole number and
% 010xxx.log is the depth of the electrode.

c1h = str2num(filename(1,4:6)); %reads the depth from the 4th to 6th characters of the filename

for j = 1:length(dh_depth-1)
```

```
    if tz(j) < c1h
        tz(j);
        continue
    elseif tz(j) >= c1h % < tz(j+1)
        delh = c1h - tz(j);
        c1z = dz(j)+delh*sin((pi/180)*(dh_dip(j)));
        delL = delh*cos((pi/180)*(dh_dip(j)));
        c1x = ((delL*sin((pi/180)*dh_azi(j)))+dx(j));
        c1y = ((delL*cos((pi/180)*dh_azi(j)))+dy(j));
        break
    else c1h > tz(j)
        disp('Electrode not on trace')
    end
end
disp('what is the input current?...');
tc = input('(mA)');
disp('what is the resistivity?...');
rho = input('(ohm.m)');
```

End of function.